BEILSTEIN JOURNAL OF NANOTECHNOLOGY

Noncontact atomic force microscopy

Edited by Udo D. Schwarz

Imprint

Beilstein Journal of Nanotechnology
www.bjnano.org
ISSN 2190-4286
Email: journals-support@beilstein-institut.de

The *Beilstein Journal of Nanotechnology* is published by the Beilstein-Institut zur Förderung der Chemischen Wissenschaften.

Beilstein-Institut zur Förderung der Chemischen Wissenschaften
Trakehner Straße 7–9
60487 Frankfurt am Main
Germany
www.beilstein-institut.de

Beilstein Journal of Nanotechnology

Noncontact atomic force microscopy

Udo D. Schwarz

Editorial

Open Access

Address:
Department of Mechanical Engineering and Materials Science, Yale University, P.O. Box 208284, New Haven, CT 06520-8284, USA

Email:
Udo D. Schwarz - udo.schwarz@yale.edu

Beilstein J. Nanotechnol. **2012,** *3,* 172–173.
doi:10.3762/bjnano.3.17

Received: 08 February 2012
Accepted: 16 February 2012
Published: 29 February 2012

This article is part of the Thematic Series "Noncontact atomic force microscopy".

Editor-in-Chief: T. Schimmel

No other method has opened the door to progress in nanoscience and nanotechnology as much as the introduction of scanning probe methods did in the 1980s, since they offer a way to *visualize* the nanoworld. For maximum impact, however, the ability to image and manipulate individual atoms is the key. Initially, scanning tunneling microscopy was the only scanning-probe-based method that was able to achieve this resolution. Atomic force microscopy (AFM), on the other hand, was quickly developed into a versatile tool with applications ranging from materials characterization in ultrahigh vacuum and nanofabrication under ambient conditions, to biological studies in liquids, but its resolution was limited to the nanometer scale.

The reason for this restriction resulted from the fact that the resolution in probe microscopy scales with the sharpness of the tip. In conventional AFM operational modes, a tip that is located at the end of a leaf spring (the so-called cantilever) is either dragged over the surface in permanent contact or gently taps the surface while vibrating, and, whichever mode is used, tips quickly blunt through either permanent or intermittent contact. Maintaining the atomic sharpness of an initially atomically sharp tip requires that the tip never touches the surface. But how can the tip know that the surface is there if it is not allowed to touch? This problem was solved in the 1990s through the realization that the attractive forces acting on the tip when it is in close proximity to the sample affect the resonance frequency of the cantilever even though it is not in actual contact with the surface. Noncontact atomic force microscopy (NC-AFM) makes use of this effect by tracking the shift of the cantilever resonance frequency due to the force field of the surface without ever establishing physical contact between the tip and sample. Much to the astonishment of many, changes induced by individual atoms turned out to induce frequency shifts that are large enough to be detected, and thus atomic-scale imaging with AFM became a reality.

Since the beginnings, almost two decades ago, NC-AFM has evolved into a powerful method that is able not just to image surfaces, but also to quantify tip–sample forces and interaction potentials as well as to manipulate individual atoms on conductors, semiconductors, and insulators alike. For the community to keep track of the rapid development in the field, a series of annual international conferences, starting in Osaka, Japan in 1998, has been established. The most recent conference from this series was held in Lindau, Germany, from September 18–22, 2011. Once again, substantial progress was presented;

NC-AFM is now able to quantitatively map three-dimensional force fields of surfaces with atomic resolution in ultrahigh vacuum as well as in liquids, and methodological developments add more information to the measurements, for example, through the driving of higher cantilever harmonics or the recording of tunneling currents. For this Thematic Series of the *Beilstein Journal of Nanotechnology*, many of the presenters from the Lindau conference agreed to submit contributions in order to assemble a series that showcases the present state of the art in the field. I would like to thank all authors who have contributed their excellent original work to this series, all referees whose promptly provided reports have provided valuable suggestions for further improvements while keeping the publication times short, and the entire NC-AFM community for supporting the open access policy of the *Beilstein Journal of Nanotechnology*.

Udo D. Schwarz

New Haven, February 2012

Beilstein Journal of Nanotechnology

Effect of the tip state during qPlus noncontact atomic force microscopy of Si(100) at 5 K: Probing the probe

Adam Sweetman*, Sam Jarvis, Rosanna Danza and Philip Moriarty

Full Research Paper

Open Access

Address:
School of Physics and Astronomy, University of Nottingham, Nottingham NG7 2RD, U.K.

Email:
Adam Sweetman* - adam.sweetman@nottingham.ac.uk;
Philip Moriarty - philip.moriarty@nottingham.ac.uk

* Corresponding author

Keywords:
force spectroscopy; image contrast; noncontact AFM; qPlus; Si(001); Si(100); tip (apex) structure

Beilstein J. Nanotechnol. **2012,** *3,* 25–32.
doi:10.3762/bjnano.3.3

Received: 25 July 2011
Accepted: 03 December 2011
Published: 09 January 2012

This article is part of the Thematic Series "Non-contact atomic force microscopy".

Guest Editor: U. D. Schwarz

Abstract

Background: Noncontact atomic force microscopy (NC-AFM) now regularly produces atomic-resolution images on a wide range of surfaces, and has demonstrated the capability for atomic manipulation solely using chemical forces. Nonetheless, the role of the tip apex in both imaging and manipulation remains poorly understood and is an active area of research both experimentally and theoretically. Recent work employing specially functionalised tips has provided additional impetus to elucidating the role of the tip apex in the observed contrast.

Results: We present an analysis of the influence of the tip apex during imaging of the Si(100) substrate in ultra-high vacuum (UHV) at 5 K using a qPlus sensor for noncontact atomic force microscopy (NC-AFM). Data demonstrating stable imaging with a range of tip apexes, each with a characteristic imaging signature, have been acquired. By imaging at close to zero applied bias we eliminate the influence of tunnel current on the force between tip and surface, and also the tunnel-current-induced excitation of silicon dimers, which is a key issue in scanning probe studies of Si(100).

Conclusion: A wide range of novel imaging mechanisms are demonstrated on the Si(100) surface, which can only be explained by variations in the precise structural configuration at the apex of the tip. Such images provide a valuable resource for theoreticians working on the development of realistic tip structures for NC-AFM simulations. Force spectroscopy measurements show that the tip termination critically affects both the short-range force and dissipated energy.

Introduction

It is now generally accepted that atomic resolution in NC-AFM imaging on semiconducting surfaces is due to the chemical force between the atoms of the surface and the last few atoms of the tip apex [1-4]. Even with well-prepared tips and surfaces, however, a wide range of imaging interactions are often observed, resulting in varying apparent topographic structures [5-7]. In cases where there has been debate as to the surface structure (for example TiO_2 [8] and Si(100) [9]) different imaging mechanisms can result in inconclusive, or even erroneous results. Consequently, there has been a considerable effort of late to model the tip–surface interaction in NC-AFM by using more-realistic tip structures [10-12], although this requires a considerable computational expense. These efforts are, however, often hampered as there can be a reticence to publish results showing imaging that cannot be easily understood, with a perhaps understandable preference to present data which fits accepted interaction models. In this paper, by highlighting a wide range of observed behaviours, we hope to provide valuable information to the modelling community that will lead to the investigation of more-realistic tip structures, and their respective tip–sample interaction and contrast mechanisms.

The role of the tip was investigated by imaging the well studied Si(100) surface. The Si(100) surface is now understood to form a stable c(4 × 2)/p(2 × 2) reconstruction at temperatures below 120 K [9,13-15], but enjoyed lively debate in the literature for some time due to conflicting results [9]. Si(100), while structurally well understood for some time, is unusually sensitive to the influence of temperature and, importantly, the probe [14] (especially the influence of tunnelling electrons during STM). While in principle NC-AFM can provide a "cleaner" system (i.e., imaging is possible without the presence of tunnelling electrons), a bias is often applied to null out the contact-potential difference (CPD) between tip and sample. This may, however, also perturb the system through the influence of the inelastic scattering of tunnelling electrons. In addition, it has recently been shown that the presence of significant tunnel currents can influence the tip–sample force during NC-AFM imaging of semiconductor surfaces [16,17], and hence significantly complicate the interpretation of the acquired images.

The silicon atoms terminating the Si(100) surface pair up into dimers in order to reduce the number of dangling bonds, and subsequently buckle, forming rows of alternately buckled dimers along the surface (Figure 1j). It has been shown that the structure of the rows may be locally manipulated by controlled tunnel-current injection [18], and we recently demonstrated that the buckling of the dimers can be toggled with atomic precision by direct application of mechanical force during NC-AFM [19,20]. In this paper we present imaging and force spectroscopy of the Si(100) surface at 5 K by qPlus [21] NC-AFM at zero applied bias, and investigate the influence of different apex types on the qualitative image appearance, and quantitative short-range tip–sample force and dissipation.

Experimental details

We used a commercial low-temperature (LT) STM/qPlus NC-AFM instrument (Omicron Nanotechnology GmbH) operating in UHV (base pressure $\leq 5 \times 10^{-11}$ mbar) cooled to 5 K. The sample and tip-preparation procedures are described in detail elsewhere [19,22]. Briefly, boron-doped silicon samples were prepared by standard flash-annealing to 1200 °C, and then slow cooling from 900 °C to room temperature before being placed into the scan head. We introduced commercial qPlus sensors (Omicron GmbH), with an electrochemically etched tungsten wire attached to one tine of the tuning fork, into the scan head without any ex situ tip treatment. The tips were prepared by standard STM methods (voltage pulses, controlled contacts with the sample) until good atomic resolution was obtained in STM feedback, at which point we made the transition to NC-AFM (i.e., Δf) feedback. As a result of our tip preparation procedures our tips are likely to be silicon- rather than tungsten-terminated, and this assumption is supported by a combined scanning electron microscopy (SEM)/energy dispersive X-ray spectroscopy (EDX) study on an STM tip prepared by similar methods. We imaged at constant Δf, maintaining a constant oscillation amplitude (A_0). All data presented were taken at close to zero bias (i.e., ~0 V applied to the tip, sample held at system ground), in order to eliminate the possibility of electronic crosstalk (Supporting Information File 1) and the effect of tunnelling electrons [19]. To ensure that this was the case, the tunnel current was recorded in parallel for all the results presented below. We detected no DC tunnel current within the noise level of our preamplifier for all images and spectroscopy presented in this paper, nor were we able to detect any AC displacement current (Supporting Information File 1).

Results and Discussion

Tip-induced imaging variation

At 5 K we routinely observe the c(4 × 2) reconstruction and associated surface defects (Figure 1a). Note that in order to avoid perturbation of the surface during scanning we typically image at a setpoint corresponding to low tip–sample interaction (i.e., at a frequency shift setpoint just after the onset of atomic resolution) [15,19]. In this "conventional" image the bright circular spots correspond to the "up" atoms of the buckled dimers.

It must be noted that here the word "conventional" is used in the sense of the contrast most commonly reported in the literature, and which most intuitively corresponds to the known topography of the surface, which is not that which is necessarily most commonly observed during experiments. In fact only a small proportion of the contrasts we observe are of this form. Statistical analysis of the relative prevalence of different contrast types is difficult as typically we attempt to coerce the tip state into producing "conventional" images before performing manipulation experiments, so as to simplify interpretation of our experiments. Therefore, simply counting the number of images of each type acquired over an experimental run (in which the purpose of the experiment is not simply to investigate the influence of the tip state) does not provide a good statistical measure as there is an inbuilt bias in the dataset. Nonetheless, an informal measure suggests that upon initial atomic resolution of the surface in NC-AFM (i.e., the first scans with a given apex producing atomic resolution), the probability of obtaining "conventional" resolution is on order of ~50%. Analysing the statistics from different forms of atomic resolution images is a topic under investigation by means of computer-aided tip preparation [23,24].

As stated, we also see a considerable number of additional characteristic image types, which are presented here to highlight the key role of the tip apex in contrast formation, even on well-

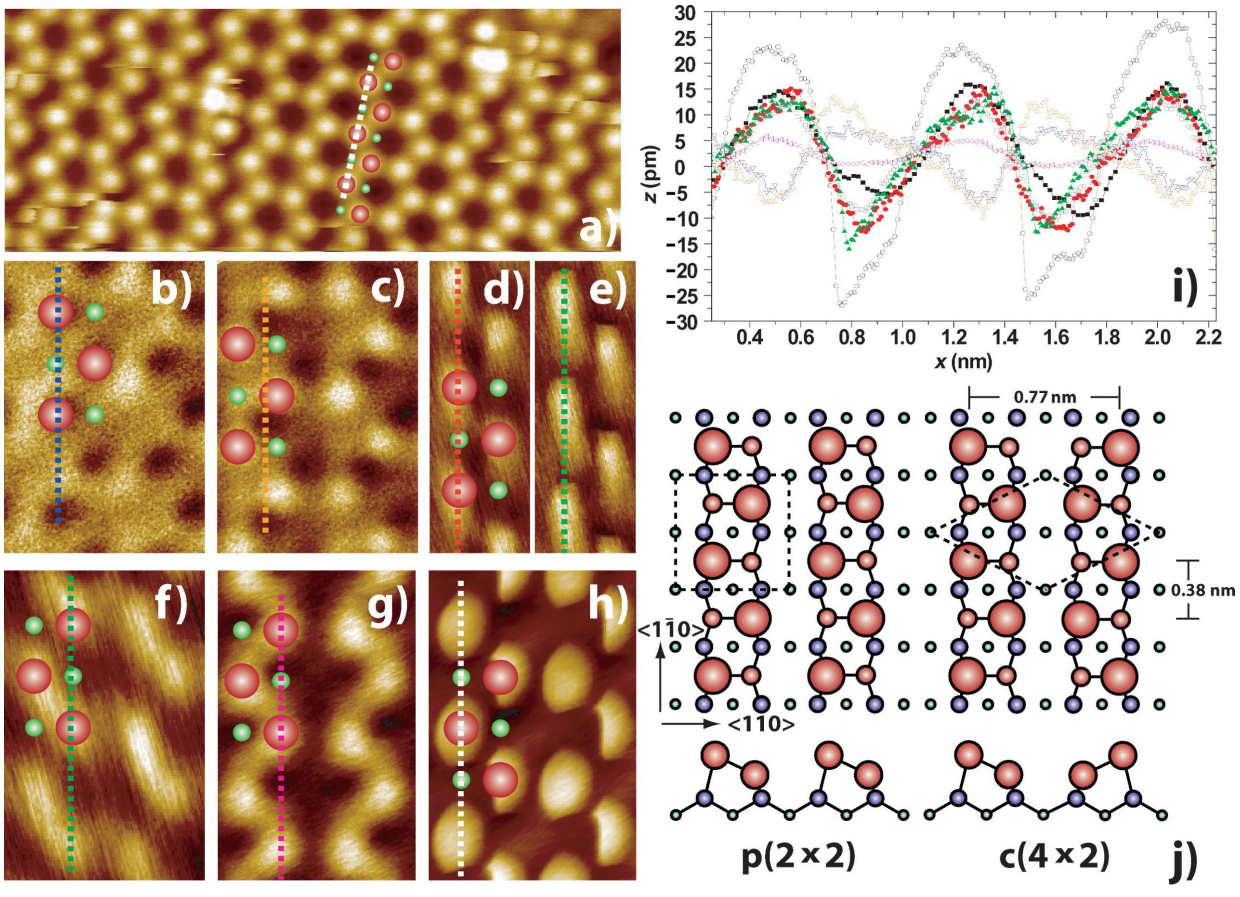

Figure 1: Topographs acquired in constant Δ*f* NC-AFM of Si(100) at 5 K, demonstrating different imaging mechanisms. Images have been rotated to align the direction of dimer rows. (a) High quality "conventional" image, "slicing" of some atoms indicates scan-induced dimer manipulation [19] Image size 8.9 nm × 3.5 nm. Δf_{set} = −46 Hz, A_0 = 0.25 nm. (b) "Inverted" image. Δf_{set} = −53 Hz, A_0 = 0.1 nm. (c) Subsequent scan of the same region as (b) with the same tip apex at higher Δ*f* setpoint showing a "depression/protrusion" double image. Δf_{set} = −54 Hz, A_0 = 0.1nm. (d) and (e) "Dimer"-type image showing the difference between the forward (d) and reverse (e) scan directions. Δf_{set} = −10 Hz, A_0 = 0.25 nm. (f) "Crescent"-type image. Δf_{set} = −40.5 Hz, A_0 = 0.25 nm. (g) "Wormlike" image. Δf_{set} = −10.4 Hz, A_0 = 0.25 nm. (h) "Discuslike" image. Δf_{set} = −44 Hz, A_0 = 0.25 nm. In each image the dotted line shows the location of the line profiles and the illustration shows the apparent position of the atoms in the c(4 × 2) reconstruction (large red - "up" atoms, small green - "down" atoms). Image size (b), (c) and (f)–(h) 1.4 nm × 2.1 nm, (d) and (e) 0.8 nm × 2.1 nm. (i) Line profiles from positions indicated in (a)–(h). (a) "Conventional" (black filled squares), (b) "Inverted" (empty blue triangles), (c) "Inverted high setpoint" (empty orange triangles), (d) "Dimer" forward (filled red circles), (e) "Dimer" back (filled green triangles), (f) "Crescent" (empty green squares), (g) "Wormlike" (empty pink triangles), (h) "Discuslike" (empty black circles), (j) Ball and stick model of the Si(100) surface reconstruction showing in-phase (p(2 × 2)) and out-of-phase (c(4 × 2)) dimer buckling.

defined surfaces. First, we consider the case of "inverted" images (Figure 1b). Although we refer to this contrast as "inverted" we also note that similar imaging can occur in the case of "enhanced-depression" images (where the height of the up atoms is reduced, and the dips associated with the down atoms are enhanced [25]). However, it appears that in this case the "up" atoms appear as dark depressions, as we have observed depressions corresponding to known defect-based protrusions on the surface with tips displaying similar inverted contrast over the clean surface (Supporting Information File 1). Inverted images have previously been reported during NC-AFM imaging of Si(111) [16], but in this instance this was likely due to the influence of significant tunnel currents [17], and also during the imaging of adsorbed molecules [4,26,27]. Here, however, an additional subtlety is revealed upon imaging the same region at slightly higher Δf setpoints (Figure 1c). It is now clear that, in addition to the depressions, a corresponding second set of protrusions is evident at a spacing of 0.56 ± 0.01 nm. This suggests an intriguing form of "double tip", where it appears one apex of the tip has an attractive interaction with the surface atoms, whilst the other (at the same tip–sample separation) is more repulsive.

The identification of the depressions as "up" atoms was performed by identifying characteristic structures and cross-comparing between the inverted image and the subsequent high setpoint image. This is demonstrated in Figure 2 in which we use a phason buckling defect (2 dimers in a row in the same buckling configuration). By using the defects to correlate the features between the two images it can be seen that in the high setpoint image (Figure 2b) the apex producing the "inverted" image and the apex producing the "conventional" image are offset by 0.56 ± 0.01 nm (c.f., the spacing of the dimer rows 0.77 ± 0.01 nm), which is suggestive of two atoms terminating the tip and exhibiting radically different interactions with the surface, either due to different elemental composition, or a structurally distorted charge density. It should be noted that thermal drift during these scans was negligible (much less than one atomic diameter per scan), and therefore drift is not an issue in the assignment of atomic position. This assignment is confirmed by analysis of other images with similar contrast in which the presence of dopant-related defects [22,28] allows unambiguous identification of true contrast inversion (Supporting Information File 1), we also stress that in the absence of tunnelling electrons this imaging must have a different origin to the image inversion that is due to a tunnel-current-induced force as recently reported by Weymouth et al. [17].

Another imaging type we commonly observe is the so-called "dimer-tip" type image [5,6]. Typically this is characterised by surface atoms appearing elongated and rectangular, and a degree of asymmetry in the imaging (c.f., Figure 1d and Figure 1e), and has been hypothesised to result from a silicon dimer-like termination of the tip apex.

In addition to these previously reported image types, we also observed at least three additional characteristic image types. Figure 1f shows pairs of "up" atoms that appear to be joined to form a "crescent" shaped curved protrusion. This is similar, yet distinct, from Figure 1g, which we term the "wormlike" topography. Here the "up" atoms are clearly resolved but joined together to form a long continuous undulating band along the row. The final image type is shown in Figure 1h. Here the "up" atoms are imaged as flattened discs. In addition we note intriguing, and well-defined, straight edges on some discs, suggestive of a complex polygonal tip apex.

This wide variety of tip apices may, in part, be due to our low temperature operation, which may allow a population of metastable tip structures to exist [29] that might only have short lifetimes at room temperature. Additionally, our STM-based tip

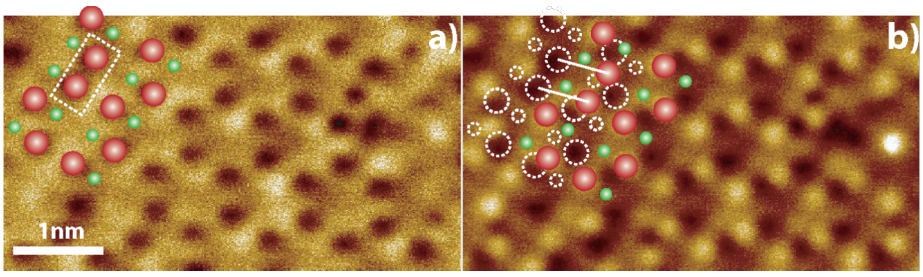

Figure 2: Larger scans of (a) inverted and (b) high-setpoint inverted images presented in Figure 1b and Figure 1c. In a) the large red (small green) circles indicate the apparent location of the up (down) atoms. In (b) the dotted outlines indicate the position of the atoms in the inverted image and the red (green) circles indicate the new apparent position of the up (down) atoms. Solid white lines link the inverted and noninverted images of the same atoms.

preparation may allow us to access a wider apex parameter space than is available from conventionally prepared silicon cantilever AFM tips. Moreover, it must be noted that although we strongly suspect our tips are bulk silicon terminated, at least four atomic species (W and O from the tip and Si and B from the surface) are, in principle, available to terminate the apex, each of which may result in a radically different tip–sample interaction [30].

In each image of Figure 1 the apparent positions of the "up" and "down" atoms of the dimers were assigned by checking the registry of the dimer rows against recognised surface features (such as defects). Line profiles were taken along the dimer row in each case, directly over the apparent positions of the atoms, with the exception of Figure 1c, where the line profile was taken in the same absolute position as Figure 1b to highlight the offset position of the normal and inverted atomic positions.

Analysis of line profiles taken along a dimer row in each topograph provides insight into the differences in tip–sample interaction (Figure 1i). Despite their asymmetry it is clear that both the "dimer" and "crescent" images show a similar corrugation to the "conventional" image. The "wormlike" image, despite looking superficially similar, actually shows a marked reduction in apparent corrugation. In contrast, the "discus-like" image shows a dramatically enhanced corrugation, suggesting (in light of significant dissipation observed during imaging; see Supporting Information File 1) that the tip may be deformed significantly during scanning. The "inverted" image shows a dip in apparent height over the atomic positions, but at higher setpoint the edge of the offset protrusion is evident, with a corrugation similar to that seen in the conventional image. It should be noted that variation in setpoint can also result in variation in measured corrugation. In each case, however, we imaged using a Δf setpoint just below that required to perturb the surface [19]. Consequently, we do not expect the imaging forces between different tips to be significantly different in each case, an assumption confirmed by force spectroscopy experiments (see discussion below). It is instructive to note that direct comparison of the frequency shift setpoints for each image is not a good measure of the site specific (short-range) tip–sample interaction, as the magnitude of Δf is highly dependent on the *macroscopic* radius of curvature of the tip (and indeed any CPD between tip and sample), as well as on the oscillation amplitude. The long-range forces can change dramatically after tip preparation by voltage pulsing or making contact with the surface. We find that regardless of the long range behaviour the maximum short range force (with the exception of "inverted" imaging) between tip and sample is usually in the range of 1–2 nN, with forces at the imaging position of ~0.1–0.5 nN. We find the onset of scan-induced dimer flipping provides a natural comparative measure of the (approximate) short-range interaction forces between different scans, as this occurs at a reasonably well-defined tip–sample interaction force.

Force spectroscopy

In order to further elucidate the differences in interaction between different apices, we performed experiments to measure the frequency shift versus z (i.e., $\Delta f(z)$) with a number of tip apices. The long-range van der Waals and electrostatic components were removed by fitting the long-range Δf curve to a power law of the form $a/(b+z)^c$ (a detailed discussion of the fitting is found elsewhere [5,19,31]). We inverted the resultant short-range Δf data by using the Sader–Jarvis algorithm [32] to determine the short-range force between the surface and tip apex. In particular we note that the removal of the long-range force by this method may result in significant errors, depending on the quality of the data, range of extrapolation, and determination of short-range cut-off point, amongst other factors. We intend to address in detail the uncertainties associated with short-range force extraction in an upcoming publication [33]. Here, however, we restrict ourselves to the estimation of uncertainties of up to ~30% in the final inverted forces, the main source of this error being the extrapolation required from the long-range power-law fit used to remove the long-range forces. This hinders rigorous quantitative comparison to simulations with different tip apices as the difference in force profiles between simulated force spectroscopy experiments (with different tip apices) are of the same order as the uncertainties associated with the technique for the long-range fitting. Nonetheless, we are able to state that the force profiles associated with the "inverted" image differ significantly from the "dimer" and "conventional" images, and that the observed dissipation varies strongly between different tip apices. The results of these experiments are presented in Figure 3. All of the data presented in Figure 3 were taken during the same experimental session with the same qPlus sensor, therefore only changes in the tip apex would appear to explain the changes in the observed contrast.

In Figure 3a we show typical force spectroscopy data obtained with a tip demonstrating a "conventional" image. Spectroscopy was performed over both "up" and "down" atoms of the dimers. In the case of the "down" atom, spectroscopy produced a correlated dimer-flip event as detailed previously [19]. This results in a significant hysteresis between approach and retract as the atom under the tip changes state. However, over the "up" atom the forward and retract curves overlap within the error of the measurement, indicating that no significant inelastic structural changes occurred on tip or surface. This assumption is supported by the negligible dissipation in both cases [7,34], and we note that the measured forces and behaviour are qualitatively similar to previous results on the same surface [19].

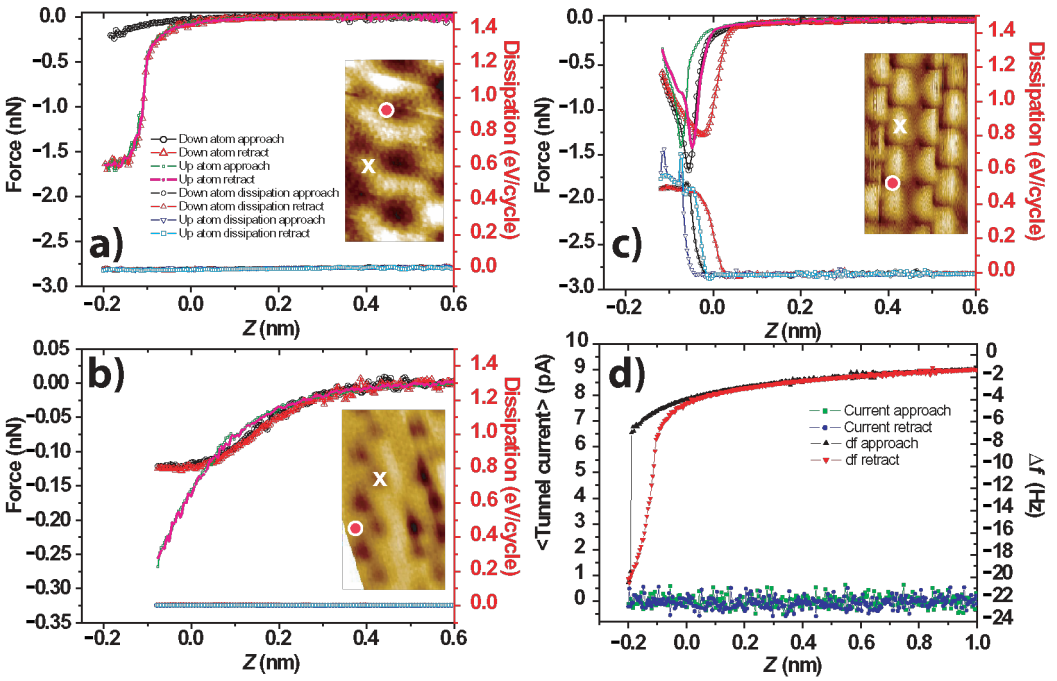

Figure 3: Experimental short-range force (nN) and dissipation (eV/cycle) as a function of relative tip–sample displacement for three different tip apices. The zero in the *z* scale indicates the feedback position. In each case spectroscopy was performed over the apparent location of both an "up' and "down" dimer atom. Results were obtained with the same probe in one experimental session. (a) Data acquired with a tip demonstrating "conventional" atomic resolution. Δf_{set} = −4.3 Hz, A_0 = 0.25 nm (3 × 3 median smoothing applied to inset figure). (b) Data acquired with a tip demonstrating "inverted" atomic resolution. Δf_{set} = −5.1 Hz, A_0 = 0.1 nm. (c) Data acquired with a tip demonstrating "dimer" atomic resolution. Δf_{set} = −8.4 Hz, A_0 = 0.25 nm. (d) Raw Δf and I_t data corresponding to the spectra in (a). We note that the tunnel current remains zero throughout, as was the case for the spectra in (b) and (c) (data not shown). Note that for (a) and (b) the dissipation signals for each of the spectra overlap within the noise of the data. Insets: Typical imaging for each tip type. Red dot: Location of spectra over "down" atom, White cross: Location of spectra over "up" atom. Keys are the same for each graph.

The inverted imaging demonstrates radically different behaviour (Figure 3b). Although the onset of the short-range force occurs over approximately the same range, the turn-around point (i.e., the minimum in the force–distance plot) is almost an order of magnitude smaller than that with the tip producing the "conventional" image. Similar to other reports of inverted contrast we also observe a crossover in the force curves taken over inverted and noninverted regions. In the third set of data, we performed the same experiment with a tip demonstrating "dimer"-type imaging (Figure 3c). Similar to the work of Oyabu et al. on Ge(111) [7], we observe significant dissipation, both at "up", and "down", atom positions. Also we note there is significant hysteresis in the force curves, even over the structurally stable "up" atoms, indicating that significant deformations occur at the tip apex during close approach. Interestingly, despite the dramatic differences between the three imaging types, analysis of the force curves reveals that the "imaging force" (i.e., the short-range force between tip and sample at the feedback position) was approximately 0.1–0.2 nN regardless of the image type. We stress that as these results are all obtained in the same session, and in the absence of any tunnel current (Figure 3d), only changes at the tip apex can be responsible for the altered tip–sample interaction.

Conclusion

In conclusion we have presented data demonstrating a wide range of stable image types in the small-amplitude NC-AFM of the Si(100) surface at 5 K. We have shown that the qualitative and quantitative behaviour of the tip–sample interaction can vary strongly with the same sensor, suggesting that the very apex of the tip dominates the short-range force, and hence the imaging. While we note that the elucidation of the tip structures that produce these contrasts is likely to be nontrivial, we hope that these results will inspire further debate in the modelling community, and help further understanding of contrast mechanisms in NC-AFM imaging of semiconductor surfaces. In particular we note that by operating at zero bias, the influence of tunnelling electrons is eliminated, highlighting the fact that the

different types of contrast arise from variations in the short-range covalent interaction between tip and surface. Future experiments related to the controlled functionalisation of the tip may allow us to selectively "tune" the interaction based on the identification of imaging and force-profile signatures, which will be critical for future chemically selective manipulation strategies.

Supporting Information

Supporting information is available highlighting that no tunnel current was measured during the experiments performed in this paper. We also discuss the assignment of atomic positions due to the double tip present in the high-setpoint "inverted" image presented in Figure 1.

Supporting Information File 1

Complete additional experimental detail and figures
[http://www.beilstein-journals.org/bjnano/content/supplementary/2190-4286-3-3-S1.pdf]

Supporting Information File 2

Representative tunnel current data during zero bias imaging
[http://www.beilstein-journals.org/bjnano/content/supplementary/2190-4286-3-3-S2.png]

Supporting Information File 3

Atomic position assignment
[http://www.beilstein-journals.org/bjnano/content/supplementary/2190-4286-3-3-S3.png]

Acknowledgements

The work described in this paper was funded by the UK Engineering and Physical Sciences Research Council (EPSRC) under grant EP/G007837. A. S. gratefully acknowledges J. Pethica for providing inspiration for the paper topic.

References

1. Giessibl, F. J. *Rev. Mod. Phys.* **2003,** *75,* 949–983. doi:10.1103/RevModPhys.75.949
2. Giessibl, F. J.; Hembacher, S.; Bielefeldt, H.; Mannhart, J. *Science* **2000,** *289,* 422–425. doi:10.1126/science.289.5478.422
3. Lantz, M. A.; Hug, H. J.; Hoffmann, R.; van Schendel, P. J. A.; Kappenberger, P.; Martin, S.; Baratoff, A.; Güntherodt, H.-J. *Science* **2001,** *291,* 2580–2583. doi:10.1126/science.1057824
4. Gross, L.; Mohn, F.; Moll, N.; Liljeroth, P.; Meyer, G. *Science* **2009,** *325,* 1110–1114. doi:10.1126/science.1176210
5. Sugimoto, Y.; Pou, P.; Custance, Ó.; Jelinek, P.; Morita, S.; Pérez, R.; Abe, M. *Phys. Rev. B* **2006,** *73,* 205329. doi:10.1103/PhysRevB.73.205329
6. Naitoh, Y.; Kinoshita, Y.; Li, Y. J.; Kageshima, M.; Sugawara, Y. *Nanotechnology* **2009,** *20,* 264011. doi:10.1088/0957-4484/20/26/264011
7. Oyabu, N.; Pou, P.; Sugimoto, Y.; Jelinek, P.; Abe, M.; Morita, S.; Pérez, R.; Custance, Ó. *Phys. Rev. Lett.* **2006,** *96,* 106101. doi:10.1103/PhysRevLett.96.106101
8. Enevoldsen, G. H.; Pinto, H. P.; Foster, A. S.; Jensen, M. C. R.; Kühnle, A.; Reichling, M.; Hofer, W. A.; Lauritsen, J. V.; Besenbacher, F. *Phys. Rev. B* **2008,** *78,* 045416. doi:10.1103/PhysRevB.78.045416
9. Uda, T.; Shigekawa, H.; Sugawara, Y.; Mizuno, S.; Tochihara, H.; Yamashita, Y.; Yoshinobu, J.; Nakatsuji, K.; Kawai, H.; Komori, F. *Prog. Surf. Sci.* **2004,** *76,* 147–162. doi:10.1016/j.progsurf.2004.05.015
10. Canova, F. F.; Foster, A. S. *Nanotechnology* **2011,** *22,* 045702. doi:10.1088/0957-4484/22/4/045702
11. Ghasemi, S. A.; Goedecker, S.; Baratoff, A.; Lenosky, T.; Meyer, E.; Hug, H. J. *Phys. Rev. Lett.* **2008,** *100,* 236106. doi:10.1103/PhysRevLett.100.236106
12. Pou, P.; Ghasemi, S. A.; Jelinek, P.; Lenosky, T.; Goedecker, S.; Perez, R. *Nanotechnology* **2009,** *20,* 264015. doi:10.1088/0957-4484/20/26/264015
13. Wolkow, R. A. *Phys. Rev. Lett.* **1992,** *68,* 2636–2639. doi:10.1103/PhysRevLett.68.2636
14. Yoshida, S.; Kimura, T.; Takeuchi, O.; Hata, K.; Oigawa, H.; Nagamura, T.; Sakama, H.; Shigekawa, H. *Phys. Rev. B* **2004,** *70,* 235411. doi:10.1103/PhysRevB.70.235411
15. Li, Y. J.; Nomura, H.; Ozaki, N.; Naitoh, Y.; Kageshima, M.; Sugawara, Y.; Hobbs, C.; Kantorovich, L. *Phys. Rev. Lett.* **2006,** *96,* 106104. doi:10.1103/PhysRevLett.96.106104
16. Arai, T.; Tomitori, M. *Applied Surface Science* **2000,** *157,* 207–211. doi:10.1016/S0169-4332(99)00527-9
17. Weymouth, A. J.; Wutscher, T.; Welker, J.; Hofmann, T.; Giessibl, F. J. *Phys. Rev. Lett.* **2011,** *106,* 226801. doi:10.1103/PhysRevLett.106.226801
18. Sagisaka, K.; Fujita, D.; Kido, G. *Phys. Rev. Lett.* **2003,** *91,* 146103. doi:10.1103/PhysRevLett.91.146103
19. Sweetman, A.; Jarvis, S.; Danza, R.; Bamidele, J.; Gangopadhyay, S.; Shaw, G. A.; Kantorovich, L.; Moriarty, P. *Phys. Rev. Lett.* **2011,** *106,* 136101. doi:10.1103/PhysRevLett.106.136101
20. Sweetman, A.; Jarvis, S.; Danza, R.; Bamidele, J.; Kantorovich, L.; Moriarty, P. *Phys. Rev. B* **2011,** *84,* 085426. doi:10.1103/PhysRevB.84.085426
21. Giessibl, F. J. *Appl. Phys. Lett.* **2000,** *76,* 1470. doi:10.1063/1.126067
22. Sweetman, A.; Gangopadhyay, S.; Danza, R.; Berdunov, N.; Moriarty, P. *Appl. Phys. Lett.* **2009,** *95,* 063112. doi:10.1063/1.3197595
23. Chen, C. J. *Nanotechnology* **2006,** *17,* S195. doi:10.1088/0957-4484/17/7/S16
24. Woolley, R. A. J.; Stirling, J.; Radocea, A.; Krasnogor, N.; Moriarty, P. *Appl. Phys. Lett.* **2011,** *98,* 253104. doi:10.1063/1.3600662
25. Sweetman, A.; Danza, R.; Gangopadhyay, S.; Moriarty, P. *J. Phys.: Condens. Matter* **2011**.
26. Kobayashi, K.; Yamada, H.; Horiuchi, T.; Matsushige, K. *Appl. Surf. Sci.* **2000,** *157,* 228–232. doi:10.1016/S0169-4332(99)00531-0
27. Rahe, P.; Bechstein, R.; Schütte, J.; Ostendorf, F.; Kühnle, A. *Phys. Rev. B* **2008,** *77,* 195410. doi:10.1103/PhysRevB.77.195410
28. Liu, Z.; Zhang, Z.; Zhu, X. *Phys. Rev. B* **2008,** *77,* 035322. doi:10.1103/PhysRevB.77.035322
29. Such, B.; Glatzel, T.; Kawai, S.; Koch, S.; Meyer, E. *J. Vac. Sci. Technol., B* **2010,** *28,* C4B1. doi:10.1116/1.3382230

30. Campbellová, A.; Ondráček, M.; Pou, P.; Pérez, R.; Klapetek, P.; Jelínek, P. *Nanotechnology* **2011,** *22,* 295710. doi:10.1088/0957-4484/22/29/295710
31. Sawada, D.; Sugimoto, Y.; Morita, K.; Abe, M.; Morita, S. *Appl. Phys. Lett.* **2009,** *94,* 173117. doi:10.1063/1.3127503
32. Sader, J. E.; Jarvis, S. P. *Appl. Phys. Lett.* **2004,** *84,* 1801. doi:10.1063/1.1667267
33. In preparation.
34. Ternes, M.; González, C.; Lutz, C. P.; Hapala, P.; Giessibl, F. J.; Jelínek, P.; Heinrich, A. J. *Phys. Rev. Lett.* **2011,** *106,* 016802. doi:10.1103/PhysRevLett.106.016802

License and Terms

Beilstein Journal of Nanotechnology

qPlus magnetic force microscopy in frequency-modulation mode with millihertz resolution

Maximilian Schneiderbauer*, Daniel Wastl and Franz J. Giessibl

Letter

Open Access

Address:
Institute of Experimental and Applied Physics, University of Regensburg, 93040 Regensburg, Germany

Email:
Maximilian Schneiderbauer* - maximilian.schneiderbauer@physik.uni-regensburg.de

* Corresponding author

Keywords:
hard disc; high-stiffness cantilever; magnetic force microscopy; qPlus

Beilstein J. Nanotechnol. **2012,** *3,* 174–178.
doi:10.3762/bjnano.3.18

Received: 07 November 2011
Accepted: 12 January 2012
Published: 29 February 2012

This article is part of the Thematic Series "Noncontact atomic force microscopy".

Associate Editor: E. Meyer

Abstract

Magnetic force microscopy (MFM) allows one to image the domain structure of ferromagnetic samples by probing the dipole forces between a magnetic probe tip and a magnetic sample. The magnetic domain structure of the sample depends on the alignment of the individual atomic magnetic moments. It is desirable to be able to image both individual atoms and domain structures with a single probe. However, the force gradients of the interactions responsible for atomic contrast and those causing domain contrast are orders of magnitude apart, ranging from up to 100 Nm^{-1} for atomic interactions down to 0.0001 Nm^{-1} for magnetic dipole interactions. Here, we show that this gap can be bridged with a qPlus sensor, with a stiffness of 1800 Nm^{-1} (optimized for atomic interaction), which is sensitive enough to measure millihertz frequency contrast caused by magnetic dipole–dipole interactions. Thus we have succeeded in establishing a sensing technique that performs scanning tunneling microscopy, atomic force microscopy and MFM with a single probe.

Introduction

Ferromagnetism is a collective phenomenon showing a parallel alignment of atomic magnetic dipole moments over macroscopic domains caused by a quantum-mechanical exchange interaction. Regions of aligned spins, called domains, are used, for example, to store bits of information on hard discs. Such ferromagnetic domains have much larger magnetic dipole moments, as many atoms contribute to the resulting moment. To probe magnetic structures on the atomic as well as on the domain-size scale in real space, variations of Scanning Tunneling Microscopy (STM) [1] and Atomic Force Microscopy (AFM) [2] are used. To explore spin structures on conductive samples, the Spin Polarized-STM (SP-STM) [3,4] is a powerful tool. The SP-STM measures the spin-dependent conductivity between a spin-polarized tip and the spin-depen-

dent local density of states of the sample (Figure 1b). STM is unable to probe insulating surfaces but AFM can be used: The antiferromagnetic surface structure of NiO (001) was imaged by Magnetic Exchange Force Microscopy (MExFM) [5]. In MExFM the magnetic exchange force between a tip atom with fixed spin orientation and a sample atom is measured (Figure 1c).

Imaging magnetic domains by Magnetic Force Microscopy (MFM) [6,7] is nowadays well-established. MFM images the magnetic-dipole interaction of a ferromagnetic tip and a domain-structured sample (Figure 1a). Typically, magnetically coated silicon cantilevers are used. These cantilevers are produced in large quantity by microfabrication techniques. Typical probe features are spring constants on the order of 10 Nm^{-1} and resonance frequencies of about 100 kHz. Another type of force sensor is made from a quartz (SiO_2) tuning fork. The qPlus sensor [8] is based on a quartz tuning fork, in which one prong is attached to a carrier substrate. The large spring constant of the qPlus, k = 1800 Nm^{-1}, allows one to overcome the snap-to-contact-problem in small-amplitude operation [9]. In this mode, the qPlus setup is customized for combined STM/AFM measurements with atomic resolution [10]. However, in standard MFM experiments, this large k, in combination with the resonance frequency $f_0 \approx 31000$ Hz, leads to very small frequency shifts (Equation 1).

Whereas MFM experiments employing quartz tuning forks, with both prongs oscillating, were previously conducted [11,12], the qPlus sensor has not yet proven its ability to detect weak long-range magnetic dipole interaction. In this article we show that the qPlus sensor is also capable of MFM experiments. We show imaging contrast of several millihertz in the large-amplitude regime, which is typically used for MFM. Therefore, we achieved a setup that is able to record a wide range of scanning-probe imaging signals; starting from domain-resolving MFM experiments, culminating in atomically resolved STM and AFM experiments (Figure 1).

Results and Discussion

In frequency modulation AFM (FM-AFM) the measured frequency shift Δf is proportional to an averaged force gradient $\langle k_{\mathrm{ts}} \rangle$ with $k_{\mathrm{ts}} = -\partial F_{ts}/\partial z$; F_{ts} is the force acting between tip and sample within one oscillation period; the z-direction is perpendicular to the sample surface. Within the gradient approximation, Δf is given by:

$$\Delta f = \frac{f_0}{2k} \langle k_{\mathrm{ts}} \rangle \tag{1}$$

To determine the sensitivity of the experimental setup, and thus the minimum detectable averaged force gradient $\langle k_{\mathrm{ts}} \rangle_{\mathrm{min}}$, one has to calculate the frequency noise of the setup $\delta(\Delta f)$. In

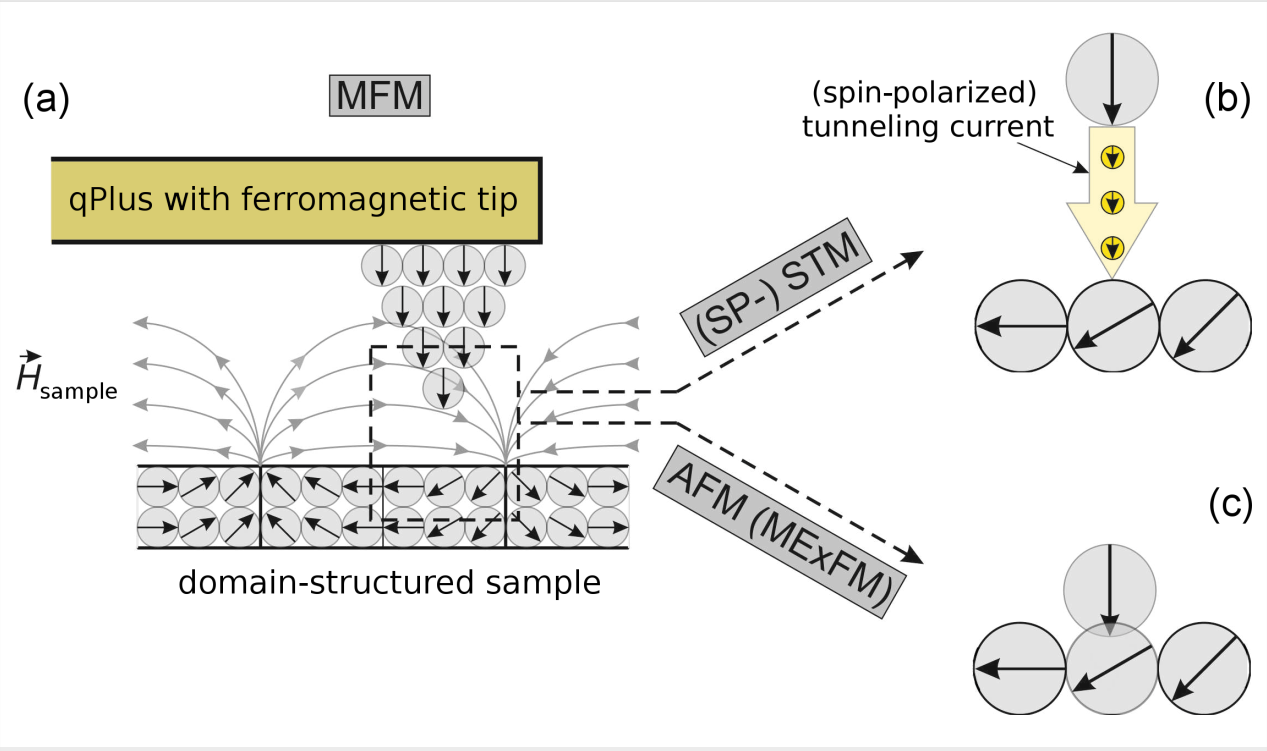

Figure 1: (a) MFM probes the force between the magnetic dipole moment of a probe tip and the magnetic stray field of a sample. With a qPlus sensor, the same probe can be used to perform (b) (SP-) STM and (c) AFM (MExFM) experiments.

FM-AFM setups $\delta(\Delta f)$ is a sum of three uncorrelated noise sources [13,14]: Thermal noise

$$\delta\left(\Delta f_{\text{thermal}}\right)=\frac{1}{A}\sqrt{\frac{f_0 k_{\text{B}} TB}{\pi kQ}}, \tag{2}$$

deflection-detector noise

$$\delta\left(\Delta f_{\text{detector}}\right)=\frac{1}{A}\frac{n_{\text{q}}B^{3/2}}{\pi} \tag{3}$$

and oscillator noise

$$\delta\left(\Delta f_{\text{oscillator}}\right)=\frac{1}{A}\frac{n_{\text{q}}}{Q}\sqrt{\frac{B}{2}}. \tag{4}$$

Here A is the cantilever amplitude, f_0 the undisturbed resonance frequency of the cantilever, k the spring constant, Q the quality factor of the oscillation, n_{q} the deflection-noise density, B the bandwidth of the measurement, k_{B} the Boltzmann constant and T the temperature.

In each term, the frequency noise is inversely proportional to the oscillation amplitude A of the force sensor. Thus, we can reduce frequency noise by using large amplitudes and therefore minimize the $\langle k_{\text{ts}}\rangle_{\text{min}}$. Moreover, one achieves the best signal-to-noise ratio by using an amplitude that is on the order of the decay length of the interaction being measured [15]. Here we take advantage of the large decay length of the magnetic dipole force, which is in the range of domain sizes, around 100 nm. Thus we chose oscillation amplitudes from 20 nm to 100 nm.

Typical values in our ambient qPlus setup are $f_0 \approx 31000$ Hz, $k \approx 1800$ Nm^{-1}, $Q \approx 2000$, $B \approx 50$ Hz, $n_{\text{q}} \approx 50$ fm/$\sqrt{\text{Hz}}$ and $A = 50$ nm. This yields a frequency noise of $\delta(\Delta f) \approx 0.5$ mHz. From Equation 1 we can now calculate the minimum detectable force gradient $\langle k_{\text{ts}}\rangle_{\text{min}} \approx 5 \times 10^{-5}$ Nm^{-1}. In comparison, commercial silicon-cantilever setups with a standard MFM probe, $f_0 \approx 75$ kHz and $k \approx 3$ Nm^{-1}, are sensitive to force gradients down to $\langle k_{\text{ts}}\rangle_{\text{min}} \approx 5 \times 10^{-7}$ Nm^{-1}.

All experiments presented here were performed under ambient conditions. For vibration isolation the microscope is mounted on a mechanical double damping stage [16]. We used the Nanonis SPM [17] control electronics and the Multipass configuration to perform lift-mode experiments for MFM. The lift mode is a two-pass technique that enables a separation of topographic and, here, magnetic signals. In the first pass, a line is scanned in FM-AFM to obtain the topography of the surface. With the second pass, this previously acquired topographic trace is used to track the probe over the surface at an elevated tip–sample distance. Thus, the short-range van der Waals force is kept constant, and any force change is caused by long-range interactions, including the magnetostatic interaction. To minimize the long-range electrostatic interaction we compensated for the contact potential difference (CPD) in both paths. We determined the CPD by taking Kelvin parabolas over the sample surface; typical values are 250 mV. The Nanonis Multipass configuration also allows us to vary the scan speed on different paths. For the second path, in which the frequency shift is detected, we lowered the scan speed to half of the value used for topography imaging, thus reducing the detection bandwidth. As already mentioned, the oscillation amplitude should always be adapted to the interaction of interest. Thus, the lift-mode technique could be improved by programming a small amplitude for the topographic path and a large one for the magnetic path. In our current setup, the same amplitude is used for both paths. For FM detection we utilized the Nanonis OC4 and Nanosurf Saphyr, both of which are fully digital, allowing lowest noise operation. As a reference sample we used a 41 GB hard disc from MAXTOR with a bit density of approximately 2 Gbit/in^2, resulting in a bit size of approximately (200 × 600) nm^2.

Assuming a rigid tip magnetization in the z-direction, the magnetostatic force is a function of the magnetic moment of the tip and the gradient of the magnetic stray field of the surface [18]:

$$\vec{F}_{\text{mag}}=\mu_0\left(\vec{m}_{\text{tip}}\cdot\nabla\right)\vec{H}_{\text{sample}}. \tag{5}$$

Here $\vec{m}_{\text{tip}}$ is the effective dipole moment of the probe and $\vec{H}_{\text{sample}}$ is the magnetic stray field of the sample. As $\vec{H}_{\text{sample}}$ primarily varies in the z-direction, perpendicular to the sample surface, the main contribution of F_{mag} is given by the partial derivative in the z-direction. By using the same sample one can therefore vary the interaction strength by means of the magnetic moment of the tip and the lift-mode height.

In a first attempt we used an electrochemically etched bulk-iron tip (see inset in Figure 2a) and magnetized it for scanning by means of a strong permanent magnet. With this tip, and with an amplitude of 20 nm in both paths and a lift height of 45 nm, we imaged the bit structure of the hard-disc sample. The topographic image shows the typical surface texture of a hard disc (Figure 2a). The sizeable drift in both images is due to long measuring times, which were necessary in order to reduce the noise by reducing the bandwidth. In Figure 2b the flattened raw

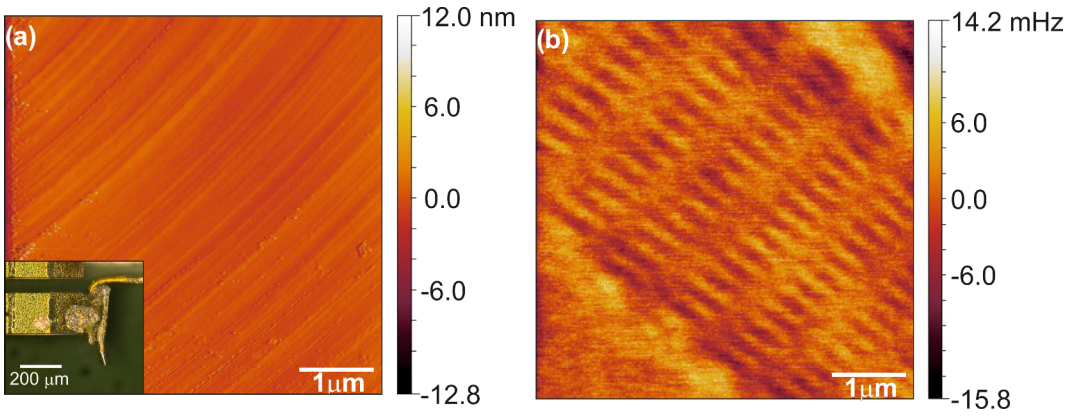

Figure 2: Lift Mode FM-MFM image using a qPlus sensor with an etched iron tip attached to it (see inset in a). Flattened raw data with imaging parameters f_0 = 24097 Hz, k = 1250 Nm^{-1}, Q = 1161, A = 20 nm and lift height 45 nm. (a) Topography and (b) lift-mode frequency shift.

data of the frequency-shift channel gathered in lift-mode show an image contrast of ±5 mHz along the bit tracks. According to the resonance frequency f_0 = 24097 Hz and spring constant k = 1250 Nm^{-1} of the sensor this contrast corresponds to a force gradient of ±520 µNm^{-1}. The flat contrast in the upper-right and lower-left corner in Figure 2b is a marker region as we could measure another bit track beside it. The magnetic contrast in Figure 2b was also confirmed by scanning the same sample with a commercial silicon MFM cantilever setup (Nanosurf Flex AFM). Moreover we measured the expected bit density of ≈1.9 Gbit/in^2 in Figure 2b.

As large magnetic moments of the probing tip can influence and even destroy the magnetic structure of the observed sample, a small magnetic moment is desirable. However, tips with a small magnetic moment reduce the interaction energy (Equation 5) and thus the signal strength, bringing the signal close to its noise floor. Here a trade-off has to be made between increased sensitivity due to decreased measurement bandwidth and large thermal drift at room temperature due to long acquisition times.

To benchmark our setup, we reduced the magnetic moment of the tip by attaching a commercial MFM cantilever tip (NanoWorld Pointprobe MFMR, coated with approx. 40 nm cobalt alloy) onto a qPlus sensor. This has been done before in tuning-fork setups in room-temperature ultrahigh-vacuum systems [19] and low-temperature systems [12,20,21]. For this sensor setup, see inset in Figure 3a, we found an amplitude of 25 nm in both paths and a lift height of 35 nm to be a good choice. The first-pass topography data set shows the expected surface structure (Figure 3a). The scan speed again had to be set to relatively slow values, allowing for a small bandwidth, but leading to sizeable drift, as seen in both sets of Figure 3. The frequency-shift data set in the second (MFM) path was flattened by applying a simple parabolic fit and shows an image contrast of ±10 mHz (Figure 3b). Along the magnetic tracks, the

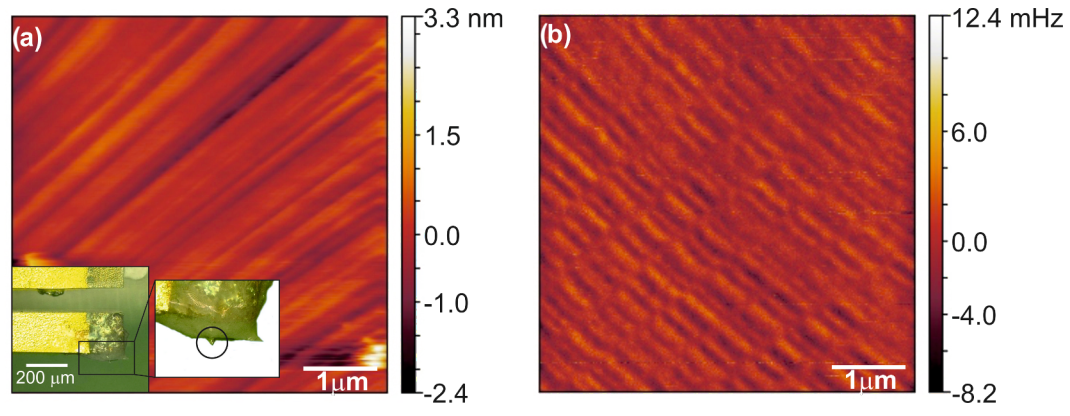

Figure 3: Lift Mode FM-MFM image employing a qPlus sensor with a commercial cobalt-coated MFM cantilever tip attached to it (see inset in a). Flattened raw data with imaging parameters f_0 = 32517 Hz, k = 1800 Nm^{-1}, Q = 1870, A = 25 nm and lift height 35 nm. (a) Topography and (b) lift-mode frequency shift.

frequency shift varies by ±2 mHz. Based on the properties of the sensor, f_0 = 32517 Hz and k = 1800 Nm^{-1}, this frequency shift corresponds to a force gradient of ±220 μNm^{-1}.

Conclusion

The key aim of this study was to find out if it is possible to observe the weak contrast caused by magnetic dipole interactions, with a qPlus force sensor that is optimized to detect the strong force gradients of chemical bonds. Chemical bonds show force gradients up to about 100 Nm^{-1}, while we have shown here that a sensor with a stiffness of 1800 Nm^{-1} can resolve force gradients from magnetic dipole forces with a magnitude of only ±220 μNm^{-1}. Therefore, we have clearly demonstrated that, although the relevant prefactor f_0/k (Equation 1) is only about 20 $Hz(N/m)^{-1}$ for the qPlus sensor versus 4000 $Hz(N/m)^{-1}$ for standard Si cantilevers with f_0 = 200 kHz and k = 50 Nm^{-1}, it is perfectly feasible to perform magnetic force microscopy with qPlus sensors, even under ambient conditions.

State-of-the-art low-temperature magnetic force microscopy has been applied to measure the Barkhausen effect, yielding a frequency-shift contrast of 0.7 Hz for a cantilever with f_0 = 195 kHz and k = 47 Nm^{-1} [22], which corresponds to a magnetic force gradient of 340 μNm^{-1}. At low temperatures we expect that the noise in our MFM measurements will decrease dramatically due to an increase in Q, a decrease in n_q (Equation 2–Equation 4), and a decrease in thermal frequency drift, therefore we trust that qPlus sensors will become a competitive alternative to Si cantilevers for performing MFM under such conditions. The key benefit of employing the qPlus sensor in MFM, however, is that atomically resolved STM and AFM as well as MFM is possible without changing the probe.

Acknowledgements

We thank the Deutsche Forschungsgemeinschaft for funding through Sonderforschungsbereich 689.

References

1. Binnig, G.; Rohrer, H.; Gerber, C.; Weibel, E. *Phys. Rev. Lett.* **1982,** *49,* 57–61. doi:10.1103/PhysRevLett.49.57
2. Binnig, G.; Quate, C. F.; Gerber, C. *Phys. Rev. Lett.* **1986,** *56,* 930–933. doi:10.1103/PhysRevLett.56.930
3. Wiesendanger, R.; Güntherodt, H.-J.; Güntherodt, G.; Gambino, R. J.; Ruf, R. *Phys. Rev. Lett.* **1990,** *65,* 247–250. doi:10.1103/PhysRevLett.65.247
4. Wiesendanger, R. *Rev. Mod. Phys.* **2009,** *81,* 1495–1550. doi:10.1103/RevModPhys.81.1495
5. Kaiser, U.; Schwarz, A.; Wiesendanger, R. *Nature* **2007,** *446,* 522–525. doi:10.1038/nature05617
6. Martin, Y.; Wickramasinghe, H. K. *Appl. Phys. Lett.* **1987,** *50,* 1455–1457. doi:10.1063/1.97800
7. Saénz, J. J.; García, N.; Grütter, P.; Meyer, E.; Heinzelmann, H.; Wiesendanger, R.; Rosenthaler, L.; Hidber, H. R.; Güntherodt, H.-J. *J. Appl. Phys.* **1987,** *62,* 4293–4295. doi:10.1063/1.339105
8. Giessibl, F. J. *Appl. Phys. Lett.* **2000,** *76,* 1470–1472. doi:10.1063/1.126067
9. Giessibl, F. J.; Hembacher, S.; Bielefeldt, H.; Mannhart, J. *Science* **2000,** *289,* 422–425. doi:10.1126/science.289.5478.422
10. Giessibl, F. J. Principle of NC-AFM. In *Noncontact Atomic Force Microscopy;* Morita, S.; Wiesendanger, R.; Meyer, E., Eds.; Springer: Berlin, 2002; Vol. 2, pp 11–46. Chapter 2.
11. Todorovic, M.; Schultz, S. *J. Appl. Phys.* **1998,** *83,* 6229–6231. doi:10.1063/1.367642
12. Kim, K.; Seo, Y.; Jang, H.; Chang, S.; Hong, M.-H.; Jhe, W. *Nanotechnology* **2006,** *17,* S201–S204. doi:10.1088/0957-4484/17/7/S17
13. Albrecht, T. R.; Grütter, P.; Horne, D.; Rugar, D. *J. Appl. Phys.* **1991,** *69,* 668–673. doi:10.1063/1.347347
14. Kobayashi, K.; Yamada, H.; Matsushige, K. *Rev. Sci. Instrum.* **2009,** *80,* 043708. doi:10.1063/1.3120913
15. Giessibl, F. J.; Bielefeldt, H.; Hembacher, S.; Mannhart, J. *Appl. Surf. Sci.* **1999,** *140,* 352–357. doi:10.1016/S0169-4332(98)00553-4
16. Park, S.-i.; Quate, C. F. *Rev. Sci. Instrum.* **1987,** *58,* 2004–2009. doi:10.1063/1.1139507
17. NANONIS, SPECS Zurich GmbH, Zurich, Switzerland. http://www.specs-zurich.com.
18. Hartmann, U. *Annu. Rev. Mater. Sci.* **1999,** *29,* 53–87. doi:10.1146/annurev.matsci.29.1.53
19. Rozhok, S.; Chandrasekhar, V. *Solid State Commun.* **2002,** *121,* 683–686. doi:10.1016/S0038-1098(02)00035-2
20. Seo, Y.; Cadden-Zimansky, P.; Chandrasekhar, V. *Appl. Phys. Lett.* **2005,** *87,* 103103. doi:10.1063/1.2037852
21. Callaghan, F. D.; Yu, X.; Mellor, C. J. *Appl. Phys. Lett.* **2005,** *87,* 214106. doi:10.1063/1.2132525
22. Schwarz, A.; Liebmann, M.; Kaiser, U.; Wiesendanger, R.; Noh, T. W.; Kim, D. W. *Phys. Rev. Lett.* **2004,** *92,* 077206. doi:10.1103/PhysRevLett.92.077206

License and Terms

Beilstein Journal of Nanotechnology

Quantitative multichannel NC-AFM data analysis of graphene growth on SiC(0001)

Christian Held[1], Thomas Seyller[2] and Roland Bennewitz[*1]

Full Research Paper

Open Access

Address:
[1]INM – Leibniz-Institute for New Materials, Campus D2 2, 66123 Saarbrücken, Germany and [2]Lehrstuhl für Technische Physik, Universität Erlangen-Nürnberg, 91058 Erlangen, Germany

Email:
Roland Bennewitz[*] - roland.bennewitz@inm-gmbh.de

* Corresponding author

Keywords:
FM-AFM; graphene; 6H-SiC(0001); KPFM; SPM

Beilstein J. Nanotechnol. **2012,** *3,* 179–185.
doi:10.3762/bjnano.3.19

Received: 22 November 2011
Accepted: 03 February 2012
Published: 29 February 2012

This article is part of the Thematic Series "Noncontact atomic force microscopy".

Guest Editor: U. D. Schwarz

Abstract

Noncontact atomic force microscopy provides access to several complementary signals, such as topography, damping, and contact potential. The traditional presentation of such data sets in adjacent figures or in colour-coded pseudo-three-dimensional plots gives only a qualitative impression. We introduce two-dimensional histograms for the representation of multichannel NC-AFM data sets in a quantitative fashion. Presentation and analysis are exemplified for topography and contact-potential data for graphene grown epitaxially on 6H-SiC(0001), as recorded by Kelvin probe force microscopy in ultrahigh vacuum. Sample preparations by thermal decomposition in ultrahigh vacuum and in an argon atmosphere are compared and the respective growth mechanisms discussed.

Introduction

Graphene grows epitaxially on the Si face of 6H-SiC(0001) by thermal decomposition in vacuum or an inert atmosphere. Recently, fundamental studies have led to an improvement of this process, now allowing for the production of almost wafer-size single-layer graphene coverage [1-3]. Understanding the interaction between the substrate and the epitaxial layer during the growth process is crucial for further optimization. Towards this goal, the graphene layer thickness has been determined by various methods including scanning tunnelling microscopy (STM) [4], Raman spectroscopy [5], low-energy electron microscopy [6,7], transmission electron microscopy [8], and atomic force microscopy (AFM) [9,10]. AFM also allows the identification of the graphene layer thickness from the local contact potential as determined by means of Kelvin probe force microscopy (KPFM) [11,12]. As a further advantage, KPFM determines step heights more accurately than STM or AFM with constant bias [13] and is therefore employed in this study to investigate the growth mechanisms of graphene on SiC(0001).

The carbon for graphene growth on SiC(0001) is obtained from thermal decomposition of the bulk substrate. Heating the sample to temperatures above 1100 °C leads to Si evaporation and to the formation of carbon-rich reconstructions [3]. At even

higher temperatures these processes lead to the growth of graphene. A high homogeneity of the graphene coverage was obtained in ultrahigh vacuum by cyclic heating to 1200 °C [2] and in an argon atmosphere by prolonged heating to 1650 °C [1]. On the Si face of the 6H-SiC(0001) wafers the thickness of the graphene layer is limited to two or three layers. The layer coverage is controlled by the growth temperature rather than by the duration of the heating cycle [14]. The determination of substrate step heights and of related changes in the graphene coverage has already provided interesting insight into the possible growth mechanisms. For example, Charrier et al. observed a preferred step height of one half of a unit cell of 6H-SiC(0001) after thermal decomposition [15]. Lauffer et al. correlated these steps with a change in the graphene coverage, based on the observation that one half of a unit cell has almost the same carbon density as one layer of graphene [16].

Experimental

Noncontact atomic force microscopy (NC-AFM) measurements were performed in ultrahigh vacuum (UHV, $p < 2{\cdot}10^{-10}$ mbar) by means of a home-built microscope similar to the one described in [17]. Kelvin probe force microscopy (KPFM) studies were performed in the frequency-modulation mode [18,19]. The modulation frequency was set to 1000 Hz with a bias amplitude of 200 mV. Polycrystalline diamond-coated tips (nanosensors) with a typical radius of 20 to 70 nm were used. Frequencies for the first normal mode of the cantilever were around 100 kHz. This choice of cantilever gives the opportunity to perform complementary contact-mode friction and noncontact KPFM experiments on the same surface areas [20].

Graphene grown in UHV

The substrate material for the study is the Si face of 6H-SiC(0001). The unit cell of 6H-SiC is composed of six bilayers of SiC(0001) each with a height of 0.25 nm. Wafers of 6H-SiC(0001) were purchased from SiCrystal AG. Polishing scratches were removed by hydrogen etching (grade 5.0, p = 1 bar, T = 1550 °C, t = 15 min) [1]. After insertion into UHV and heating to 120 °C for 10 h to remove adsorbed water, the surface was imaged by NC-AFM (Figure 1a). Flat terraces with a typical width of 500 nm were found. The surface of terraces is covered with irregular mounds of up to 0.5 nm in height. Smaller depressed islands decorate the steps between terraces (see white arrow in Figure 1a). The steps between terraces have a typical height of 1.5 nm, whereas the smaller steps towards the depressed islands have a height of roughly 0.25 nm (Table 1). The step heights match the height of the SiC

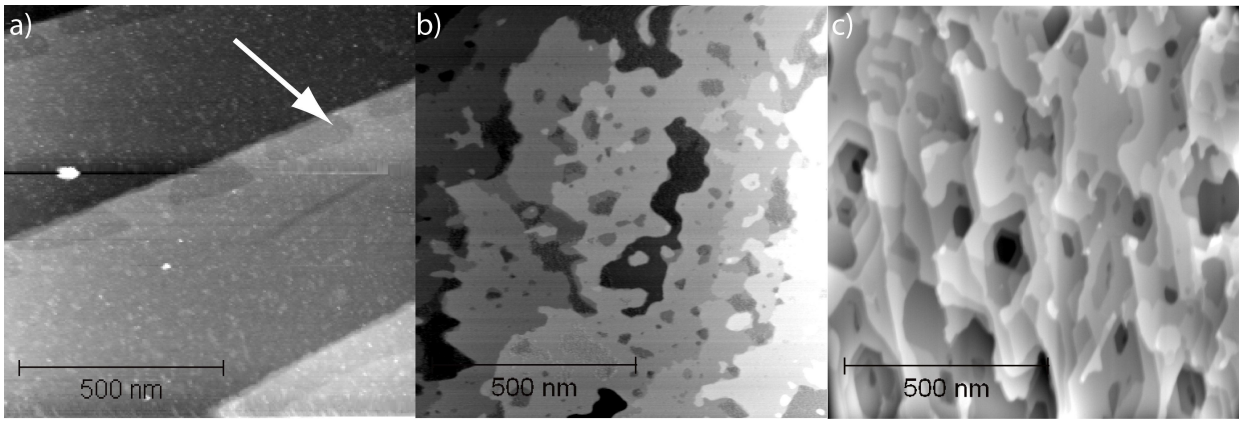

Figure 1: Topography images of the SiC(0001) sample (a) before annealing, (b) after oxide removal at 1000 °C, and (c) after graphene growth at 1300 °C. Step heights in (a) are 1.5 nm between the large terraces and 0.25 nm towards the small depressed islands (indicated by the arrow). Step heights in (b) are 0.25, 0.50 and 0.75 nm, evenly distributed. Step heights in (c) vary from 0.09 nm to 0.75 nm.

Table 1: Table of different step heights found before and after graphenization of 6H-SiC(1000). Dominant step heights are underlined. After graphenization the substrate step heights formed as multiples of the SiC(0001) bilayer height of 0.25 nm may vary by the graphene thickness of 0.33 nm.

Substrate	Step heights found	Figure
Wafer SiC as received	1.5 and 0.25 nm	Figure 1a
Graphenized in argon	0, 0.25, 0.5, 0.75 , 1, …, 2 nm ± 0.33 nm for each of the above.	Figure 2a, Figure 3a, Figure 4b
Wafer SiC heated to 1000 °C	0.25, 0.50, 0.75 nm	Figure 1b
Graphenized in UHV	0.75 nm ± 0.33 nm	Figure 1c, Figure 2a, Figure 4a

unit cell of 1.52 nm [21] and the SiC bilayer height of 1.52 nm/6 = 0.253 nm, respectively.

The surface oxide was removed in UHV by direct-current heating (T = 1000 °C, t = 6 min) [3]. The temperature was determined with an infrared pyrometer adjusted to an emissivity of 0.9. This oxide removal technique is known to change the SiC surface stoichiometry, as the oxide layer is removed by evaporation of SiO gas. Overall, the surface structure remains the same upon oxide removal (Figure 2b). The width of the large terraces is slightly reduced and a number of smaller and larger pits and islands with lateral extensions of only a few nanometers up to hundreds of nanometers are found. Except for a few remaining rough spots the surface is now atomically smooth. Step heights between the smooth terraces are mostly 0.25 nm, 0.5 nm and 0.75 nm, which again correspond to multiples of the SiC(0001) bilayer height (Table 1). The step height between rough spots and adjacent smooth terraces was found to be approximately 0.17 nm in good agreement with previous studies[10].

Graphene was grown by first heating the sample to 1000 °C for 6 min to remove contaminants and also to reduce the pressure burst during the subsequent graphenization step of heating to 1300 °C for 30 s [3]. This treatment changes the topography significantly (Figure 1c). The largest atomically flat areas now have a lateral extension of only 100 nm. The sample is covered with small pits of hexagonal shape. A large variety of step heights is found (Table 1).

Graphene grown in an argon atmosphere

The same starting material and sample preparation, i.e., wafer manufacturer, polishing, and hydrogen etching, were used for the graphenization in an argon atmosphere at 1650 °C following the procedure describe in [1]. After graphenization the sample was introduced into the UHV chamber and heated for 10 h at 120 °C in order to remove adsorbed water.

A direct comparison of samples prepared in UHV and in an argon atmosphere reveals huge differences in the surface topography (Figure 2a and Figure 2b). While the sample prepared in UHV exhibits the pitted structure described above, the sample prepared in an argon atmosphere shows only a few straight step bunches every several microns.

Results

KPFM measurements reveal variations in the graphene coverage as contributing to the different step heights observed. Figure 3 shows a typical step structure for a sample prepared in an argon atmosphere. Of the two topographic steps (Figure 3a) only one coincides with a change in contact potential (Figure 3b). The underlying surface structure is analyzed in Figure 3c and represented in an atomic ball-and-stick scheme in Figure 3d. The left step is a substrate step of three bilayers of SiC with a height of 0.75 nm, indicated by the three blue blocks representing the bilayers. The right step is a substrate bilayer step combined with a change in graphene coverage from single to double layer. The resulting topographic step height is 0.09 nm, the change in contact potential 130 mV. Such analysis is supported by the fact that steps with a height that is a multiple of the SiC bilayer height never coincide with a change in contact potential. The interface layer introduced in Figure 3c has been reported as a graphitic layer covalently bound to the SiC substrate [4,16]. While its influence on the electronic structure and contact potential is under discussion, it has no influence on the step heights between graphene-covered terraces.

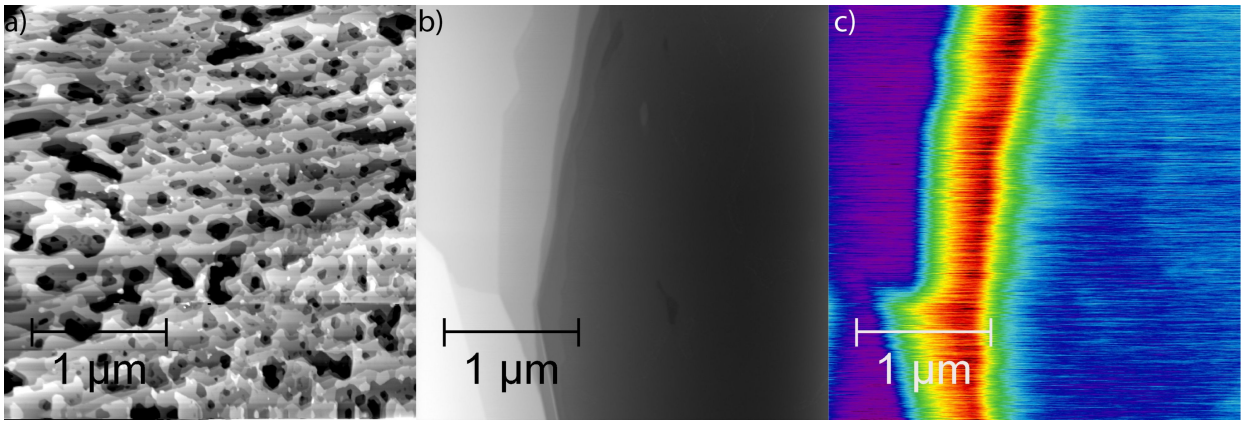

Figure 2: Topography images of graphene layers epitaxially grown on SiC(0001); (a) preparation in UHV, (b) preparation in an argon atmosphere. Step heights in (a) vary from 0.09 nm up to 0.75 nm. The total height of the step bunch in (b) is 3.25 nm. The contrast in the contact potential in (c) was recorded simultaneously with the topography in (b). Blue areas indicate single-layer graphene; red areas with 130 mV higher contact potential indicate double-layer graphene.

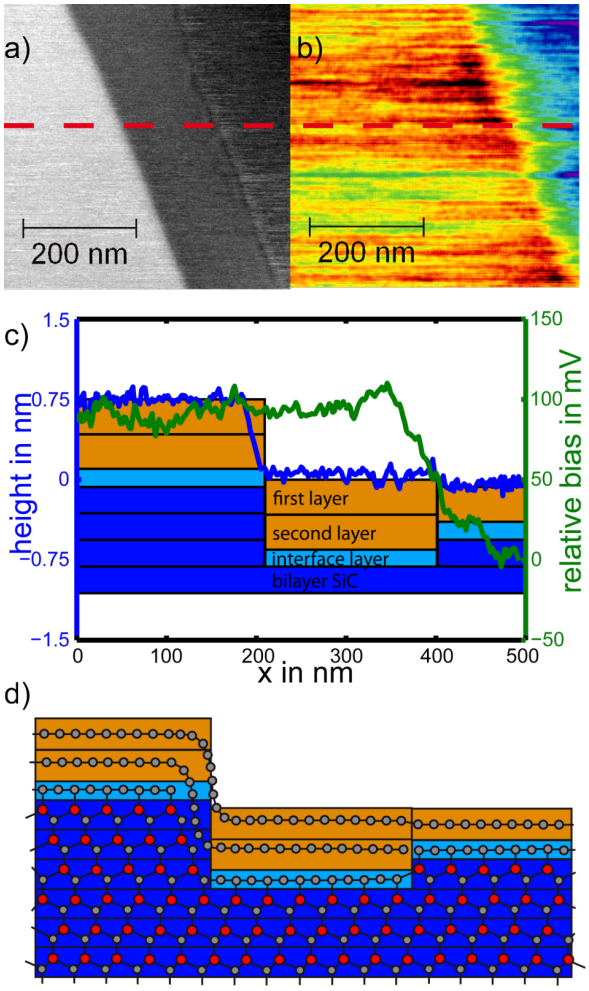

Figure 3: (a) Topographic image showing two steps found typically on samples prepared in an argon atmosphere. (b) Corresponding image of the contact potential difference. Note that only the small step in (a) coincides with a shift in contact potential. (c) Topography (blue) and contact-potential (green) profiles taken along the dashed line in (a). Underlying is a schematic illustration of the corresponding substrate composition. Different layers are drawn to their corresponding step height as SiC(0001) bilayer (0.25 nm, blue), interfacial layer (unknown height, light blue), and graphene layer (0.33 nm, orange). (d) Schematic atomic model of the surface structure, showing SiC bilayers, the carbon-rich interface layer, and single- and double-layer graphene.

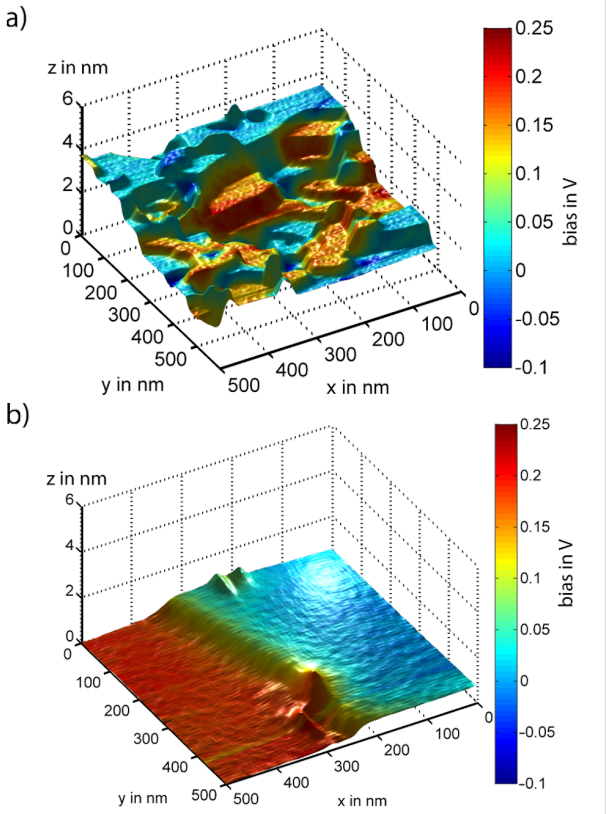

Figure 4: Rendered images of graphene layers on SiC(0001) prepared in (a) UHV and (b) an argon atmosphere. The colour represents the local contact potential. Bluish colour indicates single-layer graphene, reddish colour double-layer graphene.

Rendering the data sets into a pseudo-three-dimensional representation provides an intuitive understanding of the structure and composition of the sample [22]. Figure 4a shows results for a sample prepared in UHV. The topography data is rendered and overlayed with a colour scale representing the local contact potential. Most parts of the sample show a bluish colour indicating single-layer graphene coverage. Some smaller terraces exhibit a higher contact potential represented in red, which indicates double-layer graphene. Double-layer graphene spots are regularly observed to grow over a SiC bilayer substrate step. No change in contact potential is observed without a corresponding change in step height. The much simpler surface structure of samples prepared in an argon atmosphere is demonstrated in Figure 4b. The identification of surface areas such as the one in Figure 4b by KPFM allows subsequent experiments to be aimed at a direct comparison between single and double layer graphene, for example, in friction experiments.

While this visualization method allows for a quick identification of the surface structure, we will now introduce two-dimensional histograms as a complementary data representation. These histograms are very useful for a quantitative analysis of the complex structures of samples prepared in UHV.

Histograms represent the distribution of values in a given data set. Here we are using two-dimensional histograms to represent the data contained in multichannel NC-AFM frames. Several signal values are assigned to each pixel of a scanned frame, e.g., topography and contact-potential values. Using topography and contact potential as axes of a two-dimensional scatter plot, the frequency of occurrence of each pair of topography and contact-

potential values is represented by a colour scheme. In this way, topography and contact potential can be graphically correlated while their quantitative values can be directly read from the plot. In order to make two such histograms comparable, topography and contact-potential values are given with respect to the values found in one reference area of the scan frame. A scan frame recorded with 512 lines of 512 pixels provides 262144 data points for this scatter plot, enough for a distinct representation of the relationship between topography and contact potential. Figure 5 shows two-dimensional histograms based on the data sets already presented in the rendered images in Figure 4.

The sample prepared in UHV is analyzed in Figure 5a. Two distinct groups of clustered data points are lined up vertically, reflecting the coverage by single and double-layer graphene. Within each group, a distinct step height of 0.75 nm is dominant, which corresponds to half the unit cell of 6H-SiC(0001). The step height between single- and double-layer graphene terraces is typically 0.42 nm, indicated by green arrows in Figure 5a. It has been suggested that half a unit cell of SiC(0001) is consumed for the growth of one layer of graphene. This relation suggests itself as the density of carbon atoms is very similar for one half of a unit cell of SiC and one layer of graphene. The step height of 0.42 nm is then given as the difference between 0.75 nm for half a unit cell and 0.33 nm for the height of one layer of graphene.

The sample prepared in an argon atmosphere is analyzed in Figure 5b, its structure with wide terraces and few steps is reflected in the observation of only two narrow clusters of data points in the histogram. The two groups correspond to a height difference of 0.64 nm, i.e., about 0.33 nm less than four SiC(0001) bilayers, which is again the step height of the graphene layer. Therefore we conclude that the lower terrace is depressed by four SiC bilayers but is covered by one additional graphene layer compared to the upper terrace. The extra SiC bilayer decomposed for the structure in Figure 5b as compared to Figure 5a is indicated by the grey arrow.

Discussion

The results described above shed light on the growth mechanism of graphene on the Si face of 6H-SiC(0001). After oxide removal at 1000 °C in UHV, the step heights vary between one, two and three bilayers of the SiC(0001) structure. Subsequent graphenization at 1300 °C in UHV results in a preferred step height of three bilayers of SiC(0001). Two mechanisms leading

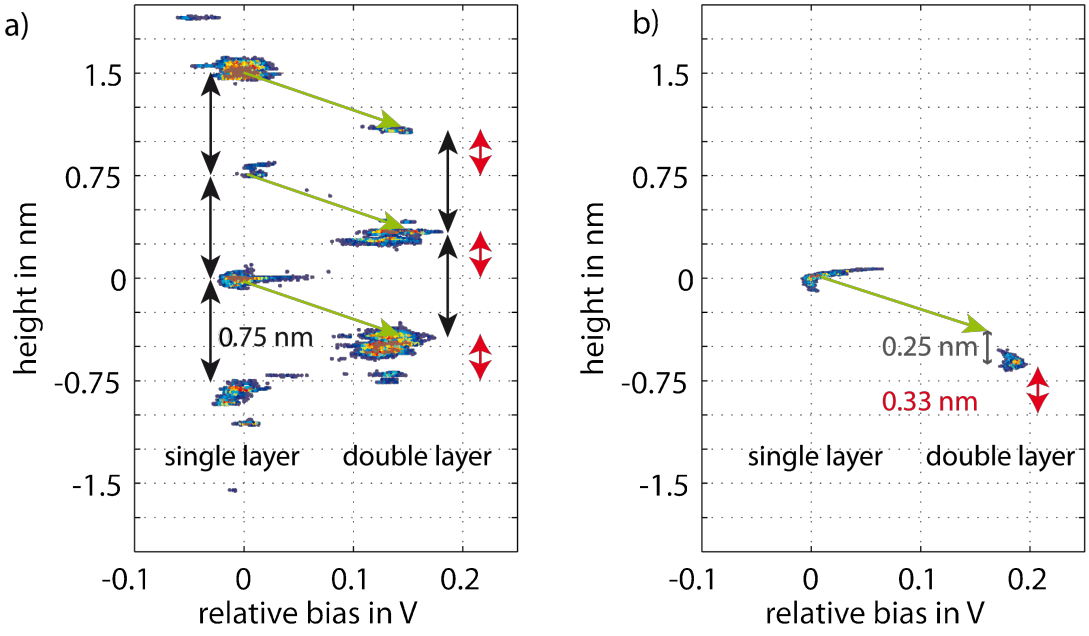

Figure 5: Two-dimensional histograms based on the data set for the rendered images in Figure 4. The colour scheme represents the number of data couples that fall into the respective topography and contact-potential bin; (a) sample prepared in UHV, (b) in an argon atmosphere. Black arrows indicate a height difference of 0.75 nm, equal to half a unit cell of 6H-SiC(0001), and the grey arrow a height of 0.25 nm, equal to one bilayer of SiC(0001). Red arrows indicate the step height of 0.33 nm corresponding to one graphene layer. Green arrows indicate a suggested graphene growth process, in which three SiC bilayers are consumed to produce one single graphene layer. Points with less than 5 counts are left transparent to enhance readability of the graph. The colour scale ranges from 5 (blue) to 70 (red) occurrences per 0.01 nm and 1.75 mV.

to this step height have been suggested. As discussed above, a little more than three bilayers SiC(0001) provide the carbon atoms required to form one graphene sheet [3]. This simple stochiometric argument is supported by our experimental results, as all spots for single-layer graphene coverage are connected to double-layer graphene spots by the corresponding green arrows in Figure 5. The contact potential difference between single- and double-layer graphene is always found to be close to 130 mV.

However, the stochiometric argument does not explain the preferred step height of 0.75 nm between single-layer graphene areas or between double-layer graphene areas. Hupalo et al. [2] have concluded that different SiC bilayers within the SiC(0001) unit cell have different Si evaporation rates, i.e., the first bilayer of each half unit cell evaporates fastest, followed by the second bilayer, whereas every third bilayer exhibits a low evaporation rate. In Figure 5a all height differences fit multiples of three SiC bilayers. Double layer graphene areas are shifted in height by exactly 0.33 nm, i.e., the thickness of one graphene layer. Therefore, single and double layers of graphene have grown on terraces defined by half unit cells of the 6H-SiC(0001) structure. Terraces not following this rule were found rarely, supporting the suggestion of Hupalo et al. for a mechanism of graphene growth in UHV.

Samples prepared in an argon atmosphere differ significantly in step structure. Atomically flat terraces extend over several microns. They are separated by bunches of steps reaching heights of up to 10 nm. The steps have heights that correspond to multiples of a bilayer of SiC(0001), varying from single up to seven SiC bilayers.

These results indicate that the mechanism described for growth in UHV is not the dominant mechanism for the step structure formation upon growth in argon. The terraces found after graphenization in argon are larger than those found on the starting material, excluding a simple carbon-maintaining transformation of the sample. Furthermore, step heights between the large terraces do not match the height of the half unit cell. The differences may be explained by enhanced diffusion at the elevated temperature of 1650 °C used for the preparation in argon as compared to 1300 °C for the preparation in UHV. Several studies have shown that the diffusion of carbon and silicon atoms differs significantly for the two temperatures, for which absolute values are still under discussion [23-25]. Diffusion of carbon atoms from areas with carbon excess to carbon-depleted areas appears to be a reasonable mechanism for the formation of larger terraces. Future models of the effect of diffusion will have to take into account the preferred nucleation of double-layer graphene at step bunches.

Samples prepared in argon show an interesting deviation of the contact potential difference between single and double layer graphene from the average value of 130 mV. Terraces that are separated by steps with a height other than a half unit cell of SiC(0001) exhibit contact potential differences of 130 ± 50 mV, examples are presented in Figure 2c and Figure 5b. We found no predictable relation between step height and contact potential difference in the available data. The origin of these deviations is not clear at present, but differences in the interface layer between graphene and SiC at different stacking positions within the unit cell are plausible candidates to explain the variations in contact potential. These differences could express themselves as a variation of the surface reconstruction (e.g., (5×5), (6×6) versus ($6\sqrt{3}\times6\sqrt{3}$)R30°) of the interface layer [4].

Finally, we add a few comments on the data quality in the two-dimensional histograms. The contact potential signal recorded in KPFM shows only a little noise and drift, and can be directly processed in the form of histograms. In contrast, the topography signal needs to be processed to correct for the effects of drift, piezo creep, and piezo hysteresis [26]. The goal, and the justification, for processing is to obtain a minimal curvature of atomically flat terraces. Most NC-AFM operating in UHV do not offer the opportunity to linearize the piezo actuators in a closed-loop scheme. However, for ambient conditions such linearized instruments are commercially available and provide suitable input data for two-dimensional histograms, in particular when the lift-mode KPFM is used [27].

Acknowledgements

We thank E. Arzt for continuous support of this project. This work was supported by the Deutsche Forschungsgemeinschaft within the European Science Foundation project FANAS.

References

1. Emtsev, K. V.; Bostwick, A.; Horn, K.; Jobst, J.; Kellogg, G. L.; Ley, L.; McChesney, J. L.; Ohta, T.; Reshanov, S. A.; Röhrl, J.; Rotenberg, E.; Schmid, A. K.; Waldmann, D.; Weber, H. B.; Seyller, T. *Nat. Mater.* **2009,** *8,* 203–207. doi:10.1038/nmat2382
2. Hupalo, M.; Conrad, E. H.; Tringides, M. C. *Phys. Rev. B* **2009,** *80,* 041401. doi:10.1103/PhysRevB.80.041401
3. Hass, J.; de Heer, W. A.; Conrad, E. H. *J. Phys.: Condens. Matter* **2008,** *20,* 323202. doi:10.1088/0953-8984/20/32/323202
4. Riedl, C.; Starke, U.; Bernhardt, J.; Franke, M.; Heinz, K. *Phys. Rev. B* **2007,** *76,* 245406. doi:10.1103/PhysRevB.76.245406
5. Shivaraman, S.; Chandrashekhar, M.; Boeckl, J. J.; Spencer, M. G. *J. Electron. Mater.* **2009,** *38,* 725–730. doi:10.1007/s11664-009-0803-6
6. Hibino, H.; Kageshima, H.; Maeda, F.; Nagase, M.; Kobayashi, Y.; Yamaguchi, H. *Phys. Rev. B* **2008,** *77,* 075413. doi:10.1103/PhysRevB.77.075413
7. Ohta, T.; El Gabaly, F.; Bostwick, A.; McChesney, J. L.; Emtsev, K. V.; Schmid, A. K.; Seyller, T.; Horn, K.; Rotenberg, E. *New J. Phys.* **2008,** *10,* 023034. doi:10.1088/1367-2630/10/2/023034

8. Norimatsu, W.; Kusunoki, M. *Physica E* **2010,** *42,* 691–694. doi:10.1016/j.physe.2009.11.151
9. Filleter, T.; Bennewitz, R. *Phys. Rev. B* **2010,** *81,* 155412. doi:10.1103/PhysRevB.81.155412
10. Vesapuisto, E.; Kim, W.; Novikov, S.; Lipsanen, H.; Kuivalainen, P. *Phys. Status Solidi B* **2011,** *248,* 1908–1914. doi:10.1002/pssb.201046368
11. Curtin, A. E.; Fuhrer, M. S.; Tedesco, J. L.; Meyers-Ward, R. L.; Eddy, C. R., Jr.; Gaskill, D. K. *Appl. Phys. Lett.* **2011,** *98,* 243111. doi:10.1063/1.3595360
12. Filleter, T.; Emtsev, K. V.; Seyller, T.; Bennewitz, R. *Appl. Phys. Lett.* **2008,** *93,* 133117. doi:10.1063/1.2993341
13. Sadewasser, S.; Lux-Steiner, M. C. *Phys. Rev. Lett.* **2003,** *91,* 266101. doi:10.1103/PhysRevLett.91.266101
14. Hass, J.; Feng, R.; Li, T.; Li, X.; Zong, Z.; de Heer, W. A.; First, P. N.; Conrad, E. H.; Jeffrey, C. A.; Berger, C. *Appl. Phys. Lett.* **2006,** *89,* 143106. doi:10.1063/1.2358299
15. Charrier, A.; Coati, A.; Argunova, T.; Thibaudau, F.; Garreau, Y.; Pinchaux, R.; Forbeaux, I.; Debever, J.-M.; Sauvage-Simkin, M.; Themlin, J.-M. *J. Appl. Phys.* **2002,** *92,* 2479–2484. doi:10.1063/1.1498962
16. Lauffer, P.; Emtsev, K. V.; Graupner, R.; Seyller, T.; Ley, L.; Reshanov, S. A.; Weber, H. B. *Phys. Rev. B* **2008,** *77,* 155426. doi:10.1103/PhysRevB.77.155426
17. Howald, L.; Meyer, E.; Lüthi, R.; Haefke, H.; Overney, R.; Rudin, H.; Güntherodt, H.-J. *Appl. Phys. Lett.* **1993,** *63,* 117–119. doi:10.1063/1.109732
18. Nonnenmacher, M.; O'Boyle, M. P.; Wickramasinghe, H. K. *Appl. Phys. Lett.* **1991,** *58,* 2921–2923. doi:10.1063/1.105227
19. Kitamura, S.; Iwatsuki, M. *Appl. Phys. Lett.* **1998,** *72,* 3154–3156. doi:10.1063/1.121577
20. Filleter, T.; McChesney, J. L.; Bostwick, A.; Rotenberg, E.; Emtsev, K. V.; Seyller, T.; Horn, K.; Bennewitz, R. *Phys. Rev. Lett.* **2009,** *102,* 086102. doi:10.1103/PhysRevLett.102.086102
21. Bauer, A.; Kräußlich, J.; Dressler, L.; Kuschnerus, P.; Wolf, J.; Goetz, K.; Käckell, P.; Furthmüller, J.; Bechstedt, F. *Phys. Rev. B* **1998,** *57,* 2647–2650. doi:10.1103/PhysRevB.57.2647
22. Sadewasser, S.; Glatzel, T.; Rusu, M.; Jäger-Waldau, A.; Lux-Steiner, M. C. *Appl. Phys. Lett.* **2002,** *80,* 2979–2981. doi:10.1063/1.1471375
23. Rüschenschmidt, K.; Bracht, H.; Stolwijk, N. A.; Laube, M.; Pensl, G.; Brandes, G. R. *J. Appl. Phys.* **2004,** *96,* 1458–1463. doi:10.1063/1.1766101
24. Alfieri, G.; Monakhov, E. V.; Svensson, B. G.; Linnarsson, M. K. *J. Appl. Phys.* **2005,** *98,* 043518. doi:10.1063/1.2009816
25. Bedoya-Martínez, B.; Roma, G. *Phys. Rev. B* **2010,** *82,* 134115. doi:10.1103/PhysRevB.82.134115
26. Moheimani, R. *Rev. Sci. Instrum.* **2008,** *79,* 071101. doi:10.1063/1.2957649
27. Ziegler, D.; Stemmer, A. *Nanotechnology* **2011,** *22,* 075501. doi:10.1088/0957-4484/22/7/075501

License and Terms

The definitive version of this article is the electronic one which can be found at:
doi:10.3762/bjnano.3.19

Beilstein Journal of Nanotechnology

Molecular-resolution imaging of pentacene on KCl(001)

Julia L. Neff[1], Jan Götzen[1,2], Enhui Li[1], Michael Marz[1,3] and Regina Hoffmann-Vogel[*1]

Full Research Paper

Open Access

Address:
[1]Physikalisches Institut and DFG-Center for Functional Nanostructures, Karlsruhe Institute of Technology, Wolfgang-Gaede-Str. 1, 76128 Karlsruhe, Germany, [2]Mechanical Engineering and Materials Science, Yale University, CT 06511, USA and [3]National Institute for Materials Science (NIMS), 1-2-1 Sengen, Tsukuba, Ibaraki, Japan

Email:
Regina Hoffmann-Vogel[*] - regina.hoffmann-vogel@kit.edu

* Corresponding author

Keywords:
KCl; molecular growth; pentacene; scanning force microscopy; self-assembly

Beilstein J. Nanotechnol. **2012,** *3,* 186–191.
doi:10.3762/bjnano.3.20

Received: 22 November 2011
Accepted: 03 February 2012
Published: 29 February 2012

This article is part of the Thematic Series "Noncontact atomic force microscopy".

Guest Editor: U. D. Schwarz

Abstract

The growth of pentacene on KCl(001) at submonolayer coverage was studied by dynamic scanning force microscopy. At coverages below one monolayer pentacene was found to arrange in islands with an upright configuration. The molecular arrangement was resolved in high-resolution images. In these images two different types of patterns were observed, which switch repeatedly. In addition, defects were found, such as a molecular vacancy and domain boundaries.

Introduction

To understand the functionalization of surfaces with molecular building blocks, an important step is to study the self-assembly of molecules. Scanning tunneling microscopy (STM) enables such studies on conductive surfaces [1,2]. On metallic surfaces, molecular growth is usually governed by strong adsorbate–substrate interactions. However, for some applications in the field of thin-film electronic devices, insulating substrates are required in order to decouple the molecular structure from the substrate. On insulators the interaction of the molecules with the substrate is much weaker than on metals because the partial transfer of electrons is expected to be weak, such that the interaction is dominated by van der Waals and electrostatic interactions, as opposed to chemical bonding. A unique tool to investigate the thin-film structure of molecules adsorbed on insulating materials is the scanning force microscope (SFM). To date only a limited number of molecules have been studied on insulating substrates, see for example [3-11]. Among the frequently studied organic molecules, pentacene has promising perspectives for thin-film electronic devices due to its high carrier mobility [12]. Besides its high carrier mobility, this π-conjugated organic molecule shows shape anisotropy, which leads to a preferential orientation with respect to the substrate in bulk

crystals and crystalline thin films. Shape anisotropy also causes a pronounced anisotropy of the electronic transport properties. Therefore, the electronic properties of pentacene are closely related to its structural order, and a precise control of the molecular packing and the crystalline orientation of thin films is of vital interest for the optimization of organic electronic devices [13].

The adsorption of pentacene on various substrates has been investigated with diffraction methods and STM [14-18]. On single crystalline metal surfaces such as, e.g., Cu(110), Au(111) and Ag(111) [19-24], pentacene forms a wetting layer of flat-lying molecules. These order in a commensurable superstructure with respect to the surface pattern. The growth of multilayers depends on the structural details of the substrate. A recent SFM study has shown the morphology of thin pentacene films on Cu(111) with molecular resolution [25]. On graphite, template-induced growth from one monolayer to thick films was studied by STM [18]. The molecular arrangement even on the top of islands with several nanometers in height appears to be commensurate with the graphite surface. On the more inert SiO_2, templating is not possible, due to the disordered substrate. The molecules crystallize in an upright configuration from the first layer onward [26]. In this configuration, the long edge of the molecule forms an angle of nearly 90° with the surface. In thin films, the molecules crystallize in a thin-film phase [27] that is similar to the bulk phases [28,29] but shows a different tilting angle. On alkali halides, diffraction measurements and ambient SFM measurements of thick pentacene films show similar phases [30-34]. Single flat-lying molecules on ultrathin NaCl films on Cu(111) have been examined by SFM with unprecedented resolution with the aid of a functionalized tip [35].

In this work, we describe the arrangement of pentacene adsorbed on the KCl(001) single-crystal surface. For submonolayer coverage the molecules form islands with upright ordering. In molecularly resolved images of these islands two different molecular patterns are observed. Furthermore, the high-resolution images show domain boundaries and a defect resulting from a molecular vacancy.

Experimental

Experiments were carried out in an ultrahigh-vacuum (UHV) variable-temperature SFM (Omicron NanoTechnology GmbH, Taunusstein, Germany) with a base pressure below 3×10^{-10} mbar. Terraces separated by atomic steps were obtained by cleavage of atomically clean KCl(001) (Kohrt, Altenholz, Germany). The cuboid KCl crystal was mounted such that its edges were aligned with the unturned slow and fast (x,y) scan directions. This alignment of the crystallographic [100] and [010] directions with the (x,y) directions was double-checked by looking at the KCl step edges. After cleavage of the KCl crystal in air, the crystal was immediately introduced into the UHV chamber. Subsequently it was heated to 400 K for about one hour in order to remove contaminations such as water as well as charge buildup produced during the cleavage process. Pentacene molecules (ABCR, Karlsruhe, Germany, purity >98%) were degassed for several hours at temperatures slightly below the evaporation temperature (508 K). Several angstroms of pentacene were deposited from a resistively heated Knudsen cell, while the surface was kept at room temperature. The rate was approximately 1 Å/min and was monitored by a quartz microbalance. Supersharp silicon cantilevers provided by Nanosensors (Neuchatel, Switzerland) were heated in vacuum to about 390 K to remove contaminants. Frequency-modulation dynamic SFM measurements were carried out by using a phase-locked-loop frequency demodulator from Nanonis (SPECS, Zürich, Switzerland). Typical resonance frequencies f_0 and spring constants k of the cantilevers were 160 kHz and 45 N/m, respectively. Samples were investigated at room temperature and afterwards at low temperatures. For the data shown here the sample was cooled to below 28 K and investigated under conditions of a nonconstant thermal drift smaller than 0.1 Å/s. The piezo-scanner calibration was double checked by performing high-resolution measurements on the Si(111) surface. To reduce the influence of long-range electrostatic forces, the tip–sample work-function difference was compensated by application of the appropriate bias voltage to the tip.

Results and Discussion

Figure 1a shows the KCl(001) surface with submonolayer coverage of pentacene molecules forming an extended island over several microns. The island displays an apparent height of

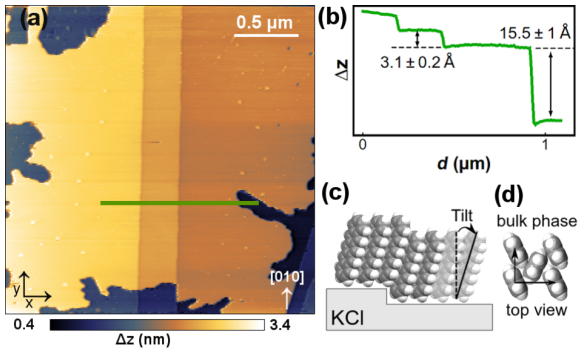

Figure 1: (a) SFM image showing part of a large pentacene island that overgrows two monoatomic substrate steps. f_0 = 160.440 kHz, Δf = −1.541 Hz, oscillation amplitude $A \approx 125$ nm, V_{bias} = −1.875 V. (b) Cross section along the line in (a) cutting two step edges and the island border. (c) Sketch of the upright alignment of the pentacene molecules. (d) Top view of the herringbone arrangement of pentacene in the bulk phase.

15.5 ± 1 Å which corresponds to the van der Waals length of the molecule, indicating an upright configuration (Figure 1b). The height of the molecular steps was cross-calibrated by comparison with single KCl steps. Another indication for an upright configuration of the molecules is their smooth growth over substrate step edges. The steps are clearly visible through the molecular film (Figure 1a), which also suggests a high crystallinity of the molecular islands. As mentioned before, pentacene films of several hundred nanometers in thickness order into crystalline layers on alkali halides [30,32-34]. Additionally, pentacene films of approximately 30 nm as well as 100 nm thickness have been found to grow epitaxially on KCl(001) in ambient-pressure SFM and diffraction studies [32,33]. Depending on the substrate temperature during deposition the pentacene films consist of varying fractions of bulk and thin-film phases, in which for higher substrate temperature the bulk-phase fraction dominates [33]. While the bulk phase shows an interlayer distance of 14.1 Å [28,29], the interlayer distance of the thin-film phase on KCl(001) is increased to 15.4 Å [32]. This difference is too small to draw a final conclusion based on SFM measurements, but our results hint at a thin-film-phase configuration. Since already at submonolayer coverage the molecules are arranged in this upright configuration, our results demonstrate that the molecule–substrate interaction is indeed weak compared to the intermolecular interaction. Figure 1c illustrates the upright ordering of the molecules. For comparison we have added a top-view sketch of the well-known bulk phase, showing the herringbone arrangement that the molecules assume to optimize the π-stacking (Figure 1d). The thin-film phase differs in the top-view only slightly from the bulk phase.

Figure 2 and Figure 3 display molecularly resolved images providing more details about the molecular configuration obtained in this study. Mainly two different types of patterns (I, II) are observed. During imaging at the same frequency shift, the images change repeatedly between these two patterns. Pattern I is characterized by a nearly square surface unit cell (Figure 2c). The molecular unit cell is roughly aligned with the [010] and [100] directions of the KCl substrate. The difference between the experimentally observed alignment and the expected one is consistent with thermal drift. In Figure 2c two possible molecular arrangements are displayed. For both arrangements the molecules have been associated with the dark features of the image, as is typical for inverted contrast, but an association with the bright features is also possible. The red model is obtained when each dark feature is associated with one molecule. The green model is the one expected from X-ray diffraction studies [32,33]. In STM and SFM measurements of upright-standing pentacene molecules (see, e.g., [17]) the contrast of the turned molecule in the center of the unit cell is often weaker. This could also be the case here such that no dark feature is observed in the center of the unit cell. In particular if one or several molecules are located on the tip apex and contribute to the imaging forces, the contrast could strongly depend on the relative orientation of tip and surface molecules.

For pattern II (Figure 3a) rather small features are observed compared to the size of the molecule (van der Waals dimensions for 98% electron density contours: 15.5 Å × 6.3 Å × 2.4 Å [22]). Consequently, if the structure derived from X-ray diffraction measurements is superimposed on the SFM image, the unit cell has a substructure. This could be caused by a multiple tip. For pattern II, we associate the molecules with the bright features of the contrast. The repeated changes between pattern I and II could then be explained by contrast inversion or a tip switch due to pick-up or drop-off of a molecule. In Figure 3b a change of the pattern occurs in the lower part of the scanned area. This change is not caused by a tip change, as the border

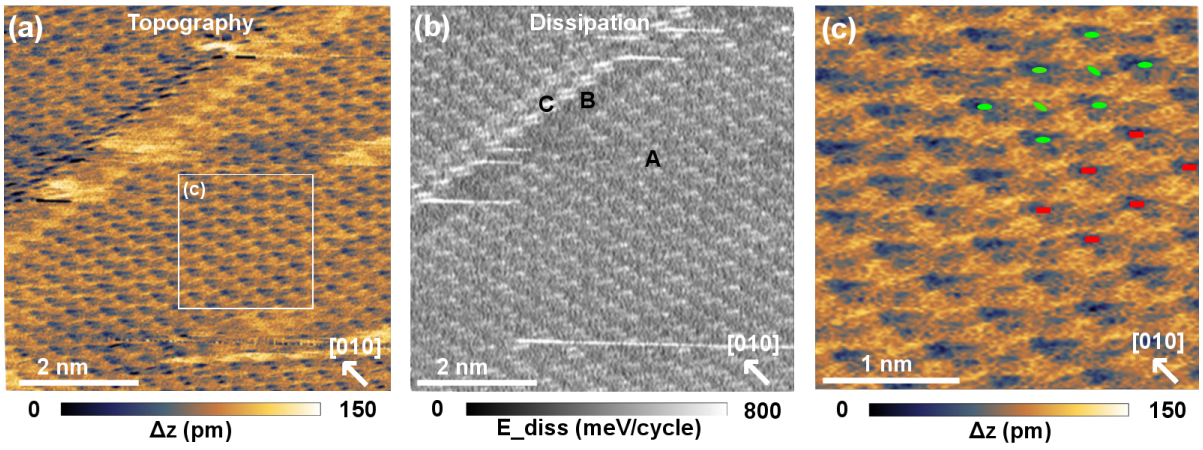

Figure 2: Pattern I. Imaged with an angle of 45°. (a) Topograph. (b) Simultaneously acquired dissipation signal. (c) Magnification of the section in (a) on which two possible molecular arrangements are displayed. Parameters: f_0 = 160.440 kHz, Δf = −1.541 Hz, A ≈ 125 nm, V_{bias} = −1.895 V.

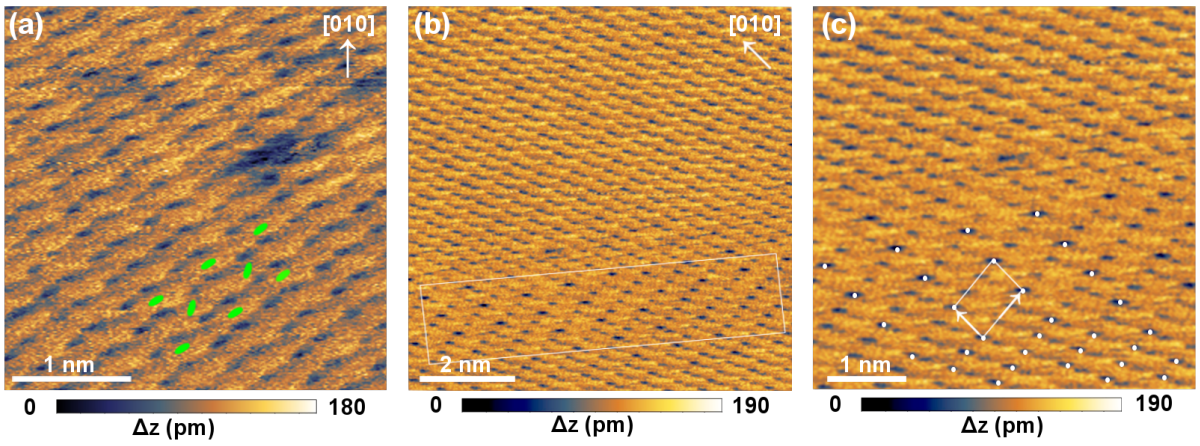

Figure 3: Pattern II. (a) Image displaying a defect. (b) Imaged with an angle of 45°. (c) Magnification of the contrast change in (b) with an illustration of the 3 × 1 superstructure. Parameters: f_0 = 160.440 kHz, Δf = −1.541 Hz, A ≈ 125 nm, V_{bias} = −1.895 V.

between the original and the modified pattern does not correspond to a line scan but occurs at an angle with respect to the fast-scan direction. In the modification of pattern II, marked by a rectangle, some of the dark features appear less pronounced while others appear more pronounced. In some parts, every third dark feature appears stronger than the other two, i.e., a 3 × 1 superstructure is formed (Figure 3c).

At least for pattern I an alignment along the substrate directions is observed, hinting at epitaxial growth. This is in agreement with the point-on-line epitaxy suggested for thicker pentacene films in the thin-film and bulk phases [32,33].

Additionally, two kinds of defects were observed. For pattern I, a line defect is observed that also follows the KCl [100] direction (Figure 2a and Figure 2b). On the upper side of the line defect the molecular pattern is displaced along the [100] direction compared to the lower side of the defect. The intrinsic distortions of the image make it difficult to estimate the amount of displacement in this direction. The image does not contradict the possibility that the pattern is displaced by a lattice vector of the substrate unit cell, which is much smaller than the molecular unit cell. In that case the line defect could release strain induced by the epitaxy of the molecules on the surface. Another possibility is that the line defect results from a twinned growth. The line defect also has a profound effect on the energy dissipation (Figure 2b). The dissipated energy per oscillation cycle can be estimated by $E_{diss} \approx E_0(A_{exc} - A_{exc,0})/A_{exc,0}$ with $E_0 = \pi k A^2/Q$ [36]. In this formula, $A_{exc,0}$ describes the excitation amplitude of the free cantilever and A_{exc} the excitation amplitude in the presence of the sample surface. A denotes the oscillation amplitude and Q the quality factor of the free cantilever. On the undisturbed part of the surface (marked with 'A' in Figure 2b) about 250 meV/cycle are additionally dissipated in each unit cell. At the line defect two areas can be distinguished. In one row of unit cells (area B) only the intrinsic dissipation of the cantilever is observed. Whereas, in another row (C) up to 760 meV are additionally dissipated per oscillation cycle. The increased energy dissipation could be due to extra uncompensated electrostatic charge that induces currents in the tip in each oscillation cycle. In this case, we would expect to see strong effects from this charge in the topographic image,which we do not observe. Another possibility is that in the first part of the defect (B) mobile molecules are clamped due to the locally occurring strain, thus resulting in a row of reduced energy dissipation. This would imply that the defect also contains rows of more loosely bound molecules (C), which cause enhanced energy dissipation compared to the undisturbed island. This line defect shows the true molecular resolution of pattern I.

For pattern II a point-like defect is displayed in Figure 3a. Here, a darker area is observed with the size of half a unit cell. We attribute this defect to a molecular vacancy caused by one missing molecule. This defect shows that also for pattern II true molecular resolution is obtained. The dissipation contrast in Figure 2b shows that the images were obtained at rather close tip–sample distances. At such small distances the positions of the molecules could be influenced reversibly by the interaction with the SFM tip. However, during the measurements also an irreversible modification of the sample took place. After the data shown in Figure 2 was acquired the molecular resolution was suddenly lost and a hole with a depth of the island was imaged in the area where the previous scans were performed (Figure 4). We exclude the possibility that one of the observed patterns was caused by an irreversible interaction with the scanning tip, because they repeatedly switched.

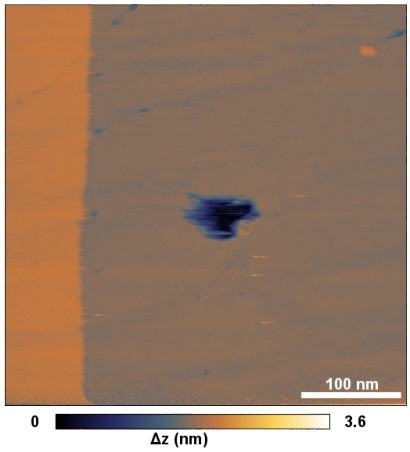

Figure 4: Large-area scan of the area where Figure 2 and Figure 3 were recorded with molecular resolution. f_0 = 160.440 kHz, Δf = −1.541 Hz, A ≈ 125 nm, V_{bias} = −1.895 V.

Conclusion

The arrangement of pentacene molecules in islands grown on KCl(001) at submonolayer coverage was investigated. It was found that the molecules form islands in an upright configuration. Molecularly resolved images of these islands showed two types of patterns that changed repeatedly. High resolution images revealed further characteristics of the molecular film, such as different defects, e.g., molecular vacancies and domain boundaries.

Acknowledgements

The authors thank the European Union for financial support through the ERC (ERC 2009-Stg 239838 NANOCONTACTS).

References

1. Rosei, F.; Schunack, M.; Naitoh, Y.; Jiang, P.; Gourdon, A.; Laegsgaard, E.; Stensgaard, I.; Joachim, C.; Besenbacher, F. *Progr. Surf. Sci.* **2003,** *71,* 95–146. doi:10.1016/S0079-6816(03)00004-2 Proceedings of the IXth Symposium on Surface Physics, Trest Castle 2002.
2. Kudernac, T.; Lei, S.; Elemans, J. A. A. W.; De Feyter, S. *Chem. Soc. Rev.* **2009,** *38,* 402–421. doi:10.1039/B708902N
3. Nony, L.; Gnecco, E.; Baratoff, A.; Alkauskas, A.; Bennewitz, R.; Pfeiffer, O.; Maier, S.; Wetzel, A.; Meyer, E.; Gerber, C. *Nano Lett.* **2004,** *4,* 2185–2189. doi:10.1021/nl048693v
4. Kunstmann, T.; Schlarb, A.; Fendrich, M.; Wagner, T.; Möller, R.; Hoffmann, R. *Phys. Rev. B* **2005,** *71,* 121403. doi:10.1103/PhysRevB.71.121403
5. Burke, S. A.; Mativetsky, J. M.; Hoffmann, R.; Grütter, P. *Phys. Rev. Lett.* **2005,** *94,* 096102. doi:10.1103/PhysRevLett.94.096102
6. Burke, S. A.; Ji, W.; Mativetsky, J. M.; Topple, J. M.; Fostner, S.; Gao, H.-J.; Guo, H.; Grütter, P. *Phys. Rev. Lett.* **2008,** *100,* 186104. doi:10.1103/PhysRevLett.100.186104
7. Dienel, T.; Loppacher, C.; Mannsfeld, S. C. B.; Forker, R.; Fritz, T. *Adv. Mater.* **2008,** *20,* 959–963. doi:10.1002/adma.200701684
8. Pawlak, R.; Nony, L.; Bocquet, F.; Oison, V.; Sassi, M.; Debierre, J.-M.; Loppacher, C.; Porte, L. *J. Phys. Chem. C* **2010,** *114,* 9290–9295. doi:10.1021/jp102044u
9. Such, B.; Trevethan, T.; Glatzel, T.; Kawai, S.; Zimmerli, L.; Meyer, E.; Shluger, A. L.; Amijs, C. H. M.; de Mendoza, P.; Echavarren, A. M. *ACS Nano* **2010,** *4,* 3429–3439. doi:10.1021/nn100424g
10. Hinaut, A.; Lekhal, K.; Aivazian, G.; Bataillé, S.; Gourdon, A.; Martrou, D.; Gauthier, S. *J. Phys. Chem. C* **2011,** *115,* 13338–13342. doi:10.1021/jp202873f
11. Körner, M.; Loske, F.; Einax, M.; Kühnle, A.; Reichling, M.; Maass, P. *Phys. Rev. Lett.* **2011,** *107,* 016101. doi:10.1103/PhysRevLett.107.016101
12. Dimitrakopoulos, C. D.; Purushothaman, S.; Kymissis, J.; Callegari, A.; Shaw, J. M. *Science* **1999,** *283,* 822–824. doi:10.1126/science.283.5403.822
13. Witte, G.; Wöll, C. *J. Mater. Res.* **2004,** *19,* 1889–1916. doi:10.1557/JMR.2004.0251
14. Ruiz, R.; Nickel, B.; Koch, N.; Feldman, L. C.; Haglund, R. F.; Kahn, A.; Scoles, G. *Phys. Rev. B* **2003,** *67,* 125406. doi:10.1103/PhysRevB.67.125406
15. Thayer, G. E.; Sadowski, J. T.; Meyer zu Heringdorf, F.; Sakurai, T.; Tromp, R. M. *Phys. Rev. Lett.* **2005,** *95,* 256106. doi:10.1103/PhysRevLett.95.256106
16. Mayer, A. C.; Kazimirov, A.; Malliaras, G. G. *Phys. Rev. Lett.* **2006,** *97,* 105503. doi:10.1103/PhysRevLett.97.105503
17. Zheng, Y.; Wee, A. T. S.; Chandrasekhar, N. *ACS Nano* **2010,** *4,* 2104–2108. doi:10.1021/nn9015218
18. Götzen, J.; Käfer, D.; Wöll, C.; Witte, G. *Phys. Rev. B* **2010,** *81,* 085440. doi:10.1103/PhysRevB.81.085440
19. Lukas, S.; Witte, G.; Wöll, C. *Phys. Rev. Lett.* **2001,** *88,* 028301. doi:10.1103/PhysRevLett.88.028301
20. Söhnchen, S.; Lukas, S.; Witte, G. *J. Chem. Phys.* **2004,** *121,* 525–534. doi:10.1063/1.1760076
21. France, C. B.; Schroeder, P. G.; Forsythe, J. C.; Parkinson, B. A. *Langmuir* **2003,** *19,* 1274–1281. doi:10.1021/la026221v
22. Käfer, D.; Ruppel, L.; Witte, G. *Phys. Rev. B* **2007,** *75,* 085309. doi:10.1103/PhysRevB.75.085309
23. Mete, E.; Demiroğlu, I.; Fatih Danışman, M.; Ellialtıoğlu, S. *J. Phys. Chem. C* **2010,** *114,* 2724–2729. doi:10.1021/jp910703n
24. Götzen, J.; Lukas, S.; Birkner, A.; Witte, G. *Surf. Sci.* **2011,** *605,* 577–581. doi:10.1016/j.susc.2010.12.022
25. Kawai, S.; Pawlak, R.; Glatzel, T.; Meyer, E. *Phys. Rev. B* **2011,** *84,* 085429. doi:10.1103/PhysRevB.84.085429
26. Dimitrakopoulos, C. D.; Malenfant, P. R. L. *Adv. Mater.* **2002,** *14,* 99–117. doi:10.1002/1521-4095(20020116)14:2<99::AID-ADMA99>3.0.CO;2-9
27. Yoshida, H.; Inaba, K.; Sato, N. *Appl. Phys. Lett.* **2007,** *90,* 181930. doi:10.1063/1.2736193
28. Campbell, R. B.; Robertson, J. M.; Trotter, J. *Acta Crystallogr.* **1962,** *15,* 289–290. doi:10.1107/S0365110X62000699
29. Siegrist, T.; Kloc, C.; Schön, J. H.; Batlogg, B.; Haddon, R. C.; Berg, S.; Thomas, G. A. *Angew. Chem., Int. Ed.* **2001,** *40,* 1732–1736. doi:10.1002/1521-3773(20010504)40:9<1732::AID-ANIE17320>3.0.CO;2-7
30. Wu, J. S.; Spence, J. C. H. *J. Appl. Crystallogr.* **2004,** *37,* 78–81. doi:10.1107/S0021889803025093

31. Kiyomura, T.; Nemoto, T.; Ogawa, T.; Minari, T.; Yoshida, K.; Kurata, H.; Isoda, S. *Jap. J. Appl. Phys.* **2006,** *45,* 401–404. doi:10.1143/JJAP.45.401
3rd International Conference on Molecular Electronics and Bioelectronics, Tokyo, JAPAN, MAR 03-04, 2005.
32. Kiyomura, T.; Nemoto, T.; Yoshida, K.; Minari, T.; Kurata, H.; Isoda, S. *Thin Solid Films* **2006,** *515,* 810–813. doi:10.1016/j.tsf.2005.12.228
33. Kakudate, T.; Yoshimoto, N.; Kawamura, K.; Saito, Y. *J. Cryst. Growth* **2007,** *306,* 27–32. doi:10.1016/j.jcrysgro.2007.02.044
34. Wisz, G.; Kuzma, M.; Virt, I.; Sagan, P.; Rudyj, I. *Appl. Surf. Sci.* **2011,** *257,* 5319–5323. doi:10.1016/j.apsusc.2010.12.018
35. Gross, L.; Mohn, F.; Moll, N.; Liljeroth, P.; Meyer, G. *Science* **2009,** *325,* 1110–1114. doi:10.1126/science.1176210
36. Anczykowski, B.; Gotsmann, B.; Fuchs, H.; Cleveland, J. P.; Elings, V. B. *Appl. Surf. Sci.* **1999,** *140,* 376–382. doi:10.1016/S0169-4332(98)00558-3

License and Terms

Beilstein Journal of Nanotechnology

Noncontact atomic force microscopy study of the spinel $MgAl_2O_4(111)$ surface

Morten K. Rasmussen, Kristoffer Meinander, Flemming Besenbacher and Jeppe V. Lauritsen*

Full Research Paper

Open Access

Address:
Interdisciplinary Nanoscience Center and Department of Physics and Astronomy, Aarhus University, Ny Munkegade, DK-8000 Aarhus C, Denmark

Email:
Jeppe V. Lauritsen* - jvang@inano.au.dk

* Corresponding author

Keywords:
aluminium oxide; metal oxide surfaces; noncontact atomic force microscopy (NC-AFM); polar surfaces; reconstructions; spinel

Beilstein J. Nanotechnol. **2012,** *3,* 192–197.
doi:10.3762/bjnano.3.21

Received: 22 November 2011
Accepted: 03 February 2012
Published: 06 March 2012

This article is part of the Thematic Series "Noncontact atomic force microscopy".

Guest Editor: U. D. Schwarz

Abstract

Based on high-resolution noncontact atomic force microscopy (NC-AFM) experiments we reveal a detailed structural model of the polar (111) surface of the insulating ternary metal oxide, $MgAl_2O_4$ (spinel). NC-AFM images reveal a $6\sqrt{3}\times6\sqrt{3}R30°$ superstructure on the surface consisting of patches with the original oxygen-terminated $MgAl_2O_4(111)$ surface interrupted by oxygen-deficient areas. These observations are in accordance with previous theoretical studies, which predict that the polarity of the surface can be compensated by removal of a certain fraction of oxygen atoms. However, instead of isolated O vacancies, it is observed that O is removed in a distinct pattern of line vacancies reflected by the underlying lattice structure. Consequently, by the creation of triangular patches in a $6\sqrt{3}\times6\sqrt{3}R30°$ superstructure, the polar-stabilization requirements are met.

Introduction

While the application of metal oxides in, e.g., catalysis, gas sensors, fuel cells, high-*k* dielectrics and corrosion protection has seen a very strong development, fundamental research on the surface properties of metal oxides has been a topic of growing interest [1]. However, in many interesting cases the metal oxide is electrically nonconducting, which severely complicates the use of almost all traditional surface-sensitive techniques relying on the scattering or emission of charged particles. As a consequence the basic surface characterization and in particular a direct atomic-scale characterization of the surface structure is largely missing for a range of important metal oxides. In recent years, the noncontact atomic force microscope (NC-AFM) has been established as a unique tool to provide atomic-resolution real-space images of all types of flat surfaces regardless of the conductivity of the material, including many of the important insulating metal oxides [2-4]. The

NC-AFM, applied to metal-oxide single-crystal surfaces under ultrahigh vacuum, thus allows the first detailed characterization of surface morphology down to the atomic scale of this important group of materials. In this work, a new surface-structure model of the $MgAl_2O_4(111)$ surface, based on experimental NC-AFM data obtained on this surface, prepared under well-controlled ultrahigh vacuum (UHV) conditions, is presented.

$MgAl_2O_4$ is a prototypical material with the so-called *spinel* structure, which defines a larger group of ionic materials with the AB_2X_4 stoichiometry [5]. For spinel, the repeat units perpendicular to any low-index surface normal consist of layers with alternating charge (see e.g., Figure 1a), and the surface terminations are therefore nominally polar and unstable in the truncated-bulk form [6-8]. The mechanisms that have been observed to lead to compensation of the surface dipole for such surfaces may strongly modify the surface relative to the truncated-bulk situation and are often divided into three groups: Change of the surface stoichiometry (reconstruction, terracing, etc.), adsorption of charge-compensating species from the residual gas (e.g., hydrogen), and electron redistribution between the top and bottom crystal faces. Depending on the material and the conditions under which the surface is kept, one or more of these stabilization mechanisms may be active, as previously observed, e.g., for ZnO [8-11]. It was recently shown that stabilization of the spinel $MgAl_2O_4(100)$ surface may be achieved by a combination of cation redistribution in the surface layers and adsorption of hydrogen [12]. LEED experiments on thin $Co_3O_4(111)$ films with the spinel structure [13,14] show evidence for an apparently unreconstructed (1×1) surface, the stability of which was proposed to be based on a Co^{2+}/Co^{3+} inversion process leading to charge compensation. In the present case of $MgAl_2O_4(111)$, no previous experimental studies are available concerning the surface structure. According to a theoretical study by Harding et al., and other theoretical studies [15-17], the oxygen-terminated $MgAl_2O_4(111)$ is evaluated to be in its lowest energy state with 42% of the oxygen atoms removed from the oxygen crystal plane to fulfill the stabilization requirements. Furthermore, calculations show that dissociative adsorption of water up to a 90% coverage is very favorable and leads to high stability [18,19]. The NC-AFM data presented in this work reveal the $MgAl_2O_4(111)$ surface to have a characteristic surface morphology consisting of triangular patches, the orientation and

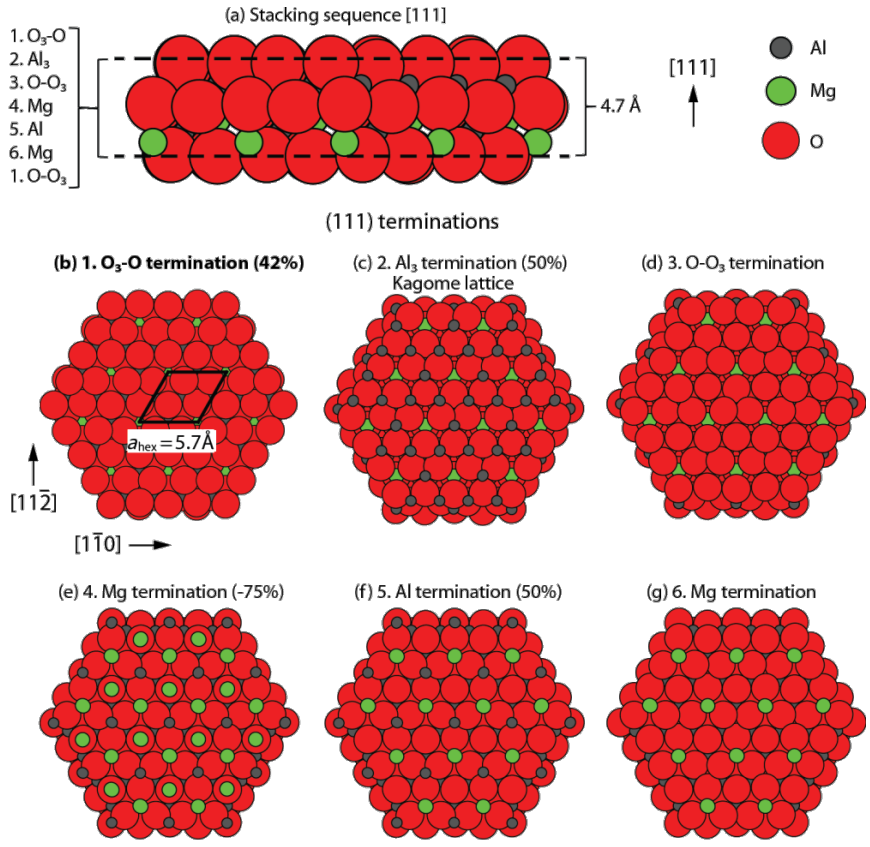

Figure 1: (a) Ball model of the $MgAl_2O_4$ stacking sequence in the [111] direction showing one repeat unit of 4.67 Å in height. (b–g) The hexagonal patches show six ball models, which illustrate the possible surfaces obtained from a bulk-truncation of the sequence in (a).

coverage of which are in agreement with the theoretical predictions for an oxygen-terminated surface with a certain percentage of the surface-layer atoms removed.

Results and Discussion

Figure 2a shows a large-scale NC-AFM image of the freshly prepared $MgAl_2O_4(111)$ sample revealing an almost perfectly flat surface. A few step edges are resolved on the surface, forming 60° angles, which reflects the hexagonal symmetry of surface atoms on the (111) surface. The bulk stacking sequence perpendicular to the surface in the [111] direction is somewhat complicated since it consists of 18 crystal layers in the form $(O_3O–Al_3–OO_3–Mg–Al–Mg)_3$. One of these three $O_3O–Al_3–OO_3–Mg–Al–Mg$ repeat units is illustrated in the side-view ball model in Figure 1a, indicating also the repeat-unit separation distance of $a·\sqrt{3}/3 = 4.67$ Å, where a = 8.08 Å [20]. Line scan 1 below Figure 2a shows the typical step-edge height measured at 4.7 ± 0.1 Å corresponding to the height of one $O_3O–Al_3–OO_3–Mg–Al–Mg$ repeat unit in the side-view ball model of Figure 1a. Because the measured step-edge height is always some multiple of 4.7 Å, it is assumed that the surface exposes only one type of termination. Figures 1b–g show top-view ball models of the six different possible (111) bulk-terminations obtained by truncating at each of the layers in the $O_3O–Al_3–OO_3–Mg–Al–Mg$ sequence. The six layers give rise to four types of surface termination: The surface can be terminated by either a hexagonally ordered oxygen plane (Figure 1b and Figure 1d), two different planes of Al^{3+} ions placed at octahedral sites (Figure 1c or Figure 1f), or a plane terminated by Mg^{2+} ions placed at tetrahedral sites (Figure 1e and Figure 1g). The distance between the O_3 and O crystal planes is ~0.16 Å, which is why these planes in practice are considered as one

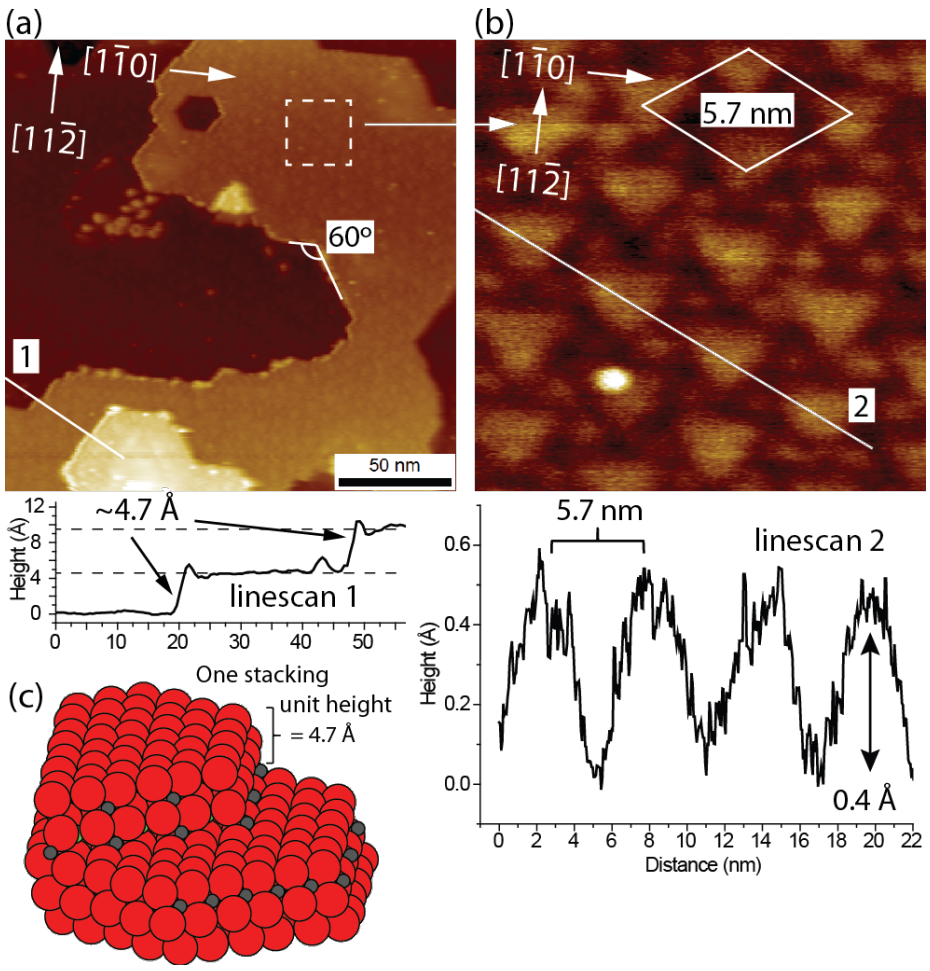

Figure 2: Experimental NC-AFM images recorded on the $MgAl_2O_4(111)$ surface prepared by sputtering and annealing in oxygen (1150 °C, $p(O_2) = 1 \times 10^{-7}$ mbar). (a) Large-scale NC-AFM image (200 × 200 nm^2) of the surface ($\Delta f_{set} = -15$ Hz, $U_{bias} = -8.5$ V, $A_{p-p} = 10$ nm) showing step edges forming 60° angles. The graph for line scan 1 reflects the corrugation of a step. The position of the line scan is indicated in the image. (b) High-resolution zoom-in on a terrace (20 × 20 nm^2), which shows a hexagonally ordered superstructure with a lattice parameter of 5.7 nm. The graph for line scan 2 shows the corrugation associated with the superstructure. The position of the line scan is indicated in the image. (c) Ball model of a single step edge on $MgAl_2O_4(111)$ terminated by Al atoms.

single O surface layer [15]. As also indicated on the oxygen-terminated surface in Figure 1b, the primitive surface unit cell in the hexagonal representation, a_{hex}, has a lattice constant of 5.72 Å. Considering that the crystal is prepared under an oxygen atmosphere we consider the surface terminated with an O_3–O layer as the most probable candidate from these six models (Figure 1b), in particular since this is also predicted to be the overall most stable (111) termination [15,16]. To achieve a completely stable nonpolar surface of this kind it is furthermore calculated that 42% of the surface O anions in the O_3 part of the O_3–O layer should be removed [15]. It was previously suggested that formation of a corrugated surface would contribute to the overall stabilization of a polar surface. The effect is explained by the nonstoichiometry involved in the formation of step edges. In the case of Zn-terminated ZnO(0001), a stabilization mechanism was proposed involving the formation of preferentially O-terminated edges and pits, which effectively lowers the excess amount of Zn on this polar surface and reduces the surface dipole [21,22]. To evaluate the effect of step edges in the present case for $MgAl_2O_4$(111), a ball model is constructed in Figure 2c, which illustrates the structure of single step edges arising for an oxygen-terminated surface. When a step edge is created and terminated by aluminium cations (grey balls) in this model, more oxygen atoms (red balls) than Al atoms are removed from the surface, which could contribute to the surface stabilization according to the electrostatic criteria. However, the step-edge density in the large-scale NC-AFM images is seen to be far too low for this to be the primary stabilizing effect, and therefore other types of surface reconstructions must be present.

Higher-resolution NC-AFM images indeed reveal that the $MgAl_2O_4$(111) surface exposes a characteristic superstructure shown in the zoom image in Figure 2b (zoom-in area marked on Figure 2a with a dashed white square). The superstructure is observed to be composed of large triangular patches arranged in hexagonal symmetry described by a 5.7 nm unit cell, with each of the large triangles surrounded by six smaller protrusions, which also appear to have a triangular outline. For comparison, the rhombic unit-cell vector of the unreconstructed (1×1) surface is ten times smaller, i.e., a_{hex} = 5.72 Å (Figure 1b). Large-scale NC-AFM images furthermore show that the unit-cell vectors defining the superstructure are rotated by 30° as compared to the well-defined directions of the step edge (Figures 2a and 2b), i.e., the superstructure is most likely rotated by 30° compared to the basic unit-cell vectors of the (111) surface. Line scan 2 in Figure 2b shows that the apparent depth associated with the dark regions surrounding the triangles is measured to be approximately 0.4 Å in NC-AFM images. This corrugation is below the minimum distance of ~1.2 Å between two consecutive crystal planes in the [111] direction, i.e., between the O_3–O and the Al_3 layer (Figure 1a). However, it is well known that the atomic-level NC-AFM contrast in topographic measurements between two areas with a different chemical composition may be affected by work-function differences [23] or the structure and composition of the tip [2]. Furthermore, the size of the NC-AFM tip apex may hinder the accurate measurement of the true lowest point in the narrow geometrical depression between the triangles, and from this perspective it is reasonable to consider the dark region to reflect so-called line vacancies in which O atoms have been desorbed from the topmost O_3–O layer.

Figure 3a shows a superstructure model superimposed on the NC-AFM image, which serves to illustrate the long-range hexagonal ordering of the two types of triangular patches. The experimentally observed superstructure, held together with the electrostatic stabilization criteria for the O_3–O-terminated $MgAl_2O_4$(111), can now be utilized to construct a tentative structural model of the $MgAl_2O_4$(111) surface termination. The structural model has to comply with the symmetry and the dimensions obtained from the NC-AFM data, i.e., a superstructure with a unit cell approximately ten times the size, and rotated by 30°, relative to the primitive hexagonal surface unit cell with lattice parameter a_{hex} = 5.72 Å. Furthermore, the model has to expose two types of triangular patches, and the number of oxygen atoms has to be decreased in order to comply with the electrostatic requirements. In principle, compensation of the surface polarity is achieved by the removal of 42% of the topmost O_3 layer only. However, selectively removing this fraction only from the O_3 part of the full O_3–O evidently does not match the experimentally observed superstructure. Instead we do not discriminate between O in the O_3–O layers, and therefore calculate that the total number of oxygen atoms in the O_3–O oxygen layer has to be reduced from 4 to 2.74. Before we proceed to the model, it is relevant to first inspect the subsurface Al_3 layer shown in Figure 3b, which is exposed when O is removed from the top layer. The underlying Al atoms constitute a so-called Kagomé lattice that, in this situation, may actually facilitate the creation of triangular shapes with a specific size and tentatively explain the experimentally observed structure. Considering that O needs to be removed in lines in order to comply with the observed structure, it is observed that Al has different densities along alternating lines on the Kagomé lattice, i.e., the density is a factor of two lower along the black line indicated in Figure 3b compared to the red line. Since undercoordinated Al is presumably associated with a high energy, we suggest that O is mainly removed along the low-density Al lines. Such circumstances clearly favor the formation of line vacancies, as compared to randomly distributed vacancies, which then, given the hexagonal surface crystal structure, drives the creation of triangular structures as observed in the experi-

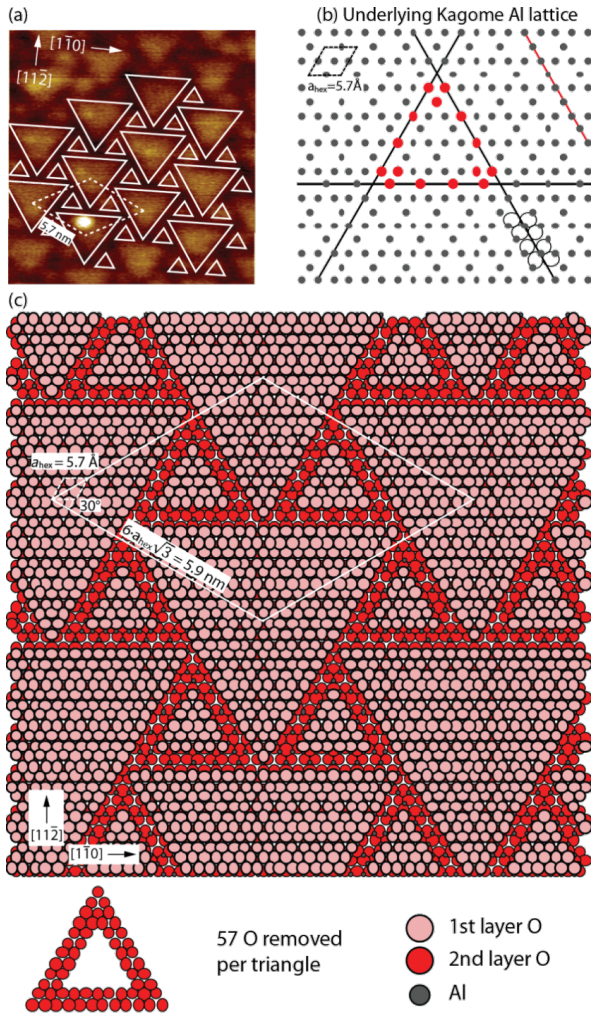

Figure 3: (a) Experimental NC-AFM image with the surface superstructure model superimposed. (b) Illustration of the subjacent aluminium lattice exposing a Kagomé pattern, which facilitates the formation of triangular patches. The O atoms are indicated along the black lines in order to illustrate the coordination along the lines. (Al: small grey, O: large, red). (c) Ball model illustrating the (6√3×6√3)R30° superstructure observed on the $MgAl_2O_4$(111) surface. The superstructure is created be the removal of oxygen atoms in triangular shapes.

ments. Starting from a fully covered O layer, the removal of oxygen atoms along the thin black line in Figure 3b, leads to a factor of two fewer aluminium atoms exposed as compared to removal of oxygen atoms along the thin red line. Figure 3c illustrates a structural model of the best fit to the experimentally observed pattern, constructed from the considerations above. The model is constructed by removing triangles consisting of double O rows coordinated only to the low-density Al rows in the subsurface layers as shown in the ball model below Figure 3c. All other configurations do not match either the size or symmetry of the observed superstructure, or lead to significant deviations in the amount of O removed from the surface compared to the optimum. The model in Figure 3c reflects a very large 6√3×6√3R30° superstructure with a unit cell parameter of $6\sqrt{3} \cdot a_{hex}$ = 5.9 nm, and the 30° orientation matches the experimentally observed structure. The amount of oxygen removed corresponds to 114 out of 432 per superstructure unit cell, leading to a total decrease in the initially O_4 surface layer to $O_{2.9}$, which is close to the theoretically predicted optimum amount of $O_{2.74}$ required to stabilize the surface by charge removal alone. Any remaining surface polarity can be explained by the compensation originating from the step edges (Figure 2c) or scattered O vacancies, which are not imaged in the NC-AFM images. It is noted that the criteria used above do not unambiguously determine the observed structure, and the detailed features, such as the specific size of the triangular features, may be influenced by other factors such as vacancy repulsion and edge energies, which are not readily explained by our data. It should be possible to image the surface in atomic detail with NC-AFM, and such future studies may be able to clarify the role of additional O vacancies and also shed light on surface hydroxy groups (OH), which have been observed to play a role in the stabilization of the $MgAl_2O_4$(100) surface [12].

Conclusion

The NC-AFM study presented in this work proposes a surface model for the polar $MgAl_2O_4$(111) surface. Under the assumption that the surface becomes terminated by an oxygen layer when synthesized in an oxygen atmosphere, a structural model is proposed that complies with both the electrostatic stabilization criterion for this polar surface, which requires the removal of ~42% of the surface oxygen, and fits with the size and triangular symmetry of the observed 6√3×6√3R30° superstructure. The preferred formation of the observed triangular shapes on an originally oxygen-terminated surface with hexagonal symmetry can be explained by the underlying Kagomé Al lattice, which is shown to facilitate the removal of oxygen in line vacancies with a triangular symmetry.

Experimental

The experiments were performed in ultrahigh vacuum (UHV) with a base pressure better than 1×10^{-10} mbar. The UHV system is equipped with a combined STM/AFM microscope, X-ray photoelectron spectroscopy (XPS) and means for sample preparation. The $MgAl_2O_4$ single crystal used for this NC-AFM study was purchased from the MTI Corporation with an EPI polished (111) facet. The crystal was first rinsed in a 1:1 mixture of nitric acid (65%) and water followed by annealing in a furnace at a temperature of 1000 °C for 4 h. After introduction to the vacuum chamber the samples underwent cycles of Ar^+ sputtering (5 min at 1 keV acceleration energy) followed by annealing (5 min at 1150 °C utilizing a 2 °C/s temperature up

and down ramp) in a 1×10^{-7} mbar O_2 atmosphere. After approximately 15 such cleaning cycles the crystal was sufficiently flat and clean for performing NC-AFM. We monitored the surface cleanliness by XPS using Mg Kα radiation (Phoibos 100 analyzer and XR 50 source, SPECS GmbH, Berlin, Germany). XPS spectra were recorded with the surface normal pointing in the direction of the analyzer and revealed the presence of only Mg, Al and O. XPS spectra were recorded regularly during the preparation, and the stoichiometry of the crystal was not observed to change as function of the number of preparation cycles.

For NC-AFM, silicon cantilevers from Nanoworld with a resonance frequency of 330 kHz and a force constant of 42 N/m were utilized. The constant-detuning mode was used for topographic imaging of the surface by fixing the detuning of the AFM cantilever at a specific setpoint (Δf_{set}) and recording the variation of the tip height (z) while raster scanning the surface. The surface potential, measured after annealing the crystal, was generally quite high, often in the range 4–8 V. Therefore, the voltage applied between the surface and the tip, U_{bias}, was monitored and adjusted regularly to minimize the electrostatic forces arising from the contact potential difference.

Acknowledgements

Financial support is gratefully acknowledged from Haldor Topsøe A/S and the European Research Council (ERC Grant no. 239834, “Oxidesynergy” (JVL)).

References

1. Heinrich, V. E.; Cox, P. A. *The Surface Science of Metal Oxides;* Cambridge University Press: Cambridge, U.K., 1994.
2. Lauritsen, J. V.; Reichling, M. *J. Phys.: Condens. Matter* **2010,** *22,* 263001. doi:10.1088/0953-8984/22/26/263001
3. Altman, E. I.; Schwarz, U. D. *Adv. Mater.* **2010,** *22,* 2854–2869. doi:10.1002/adma.200903927
4. Barth, C.; Foster, A. S.; Henry, C. R.; Shluger, A. L. *Adv. Mater.* **2011,** *23,* 477–501. doi:10.1002/adma.201002270
5. Sickafus, K. E.; Wills, J. M.; Grimes, N. W. *J. Am. Ceram. Soc.* **1999,** *82,* 3279–3292. doi:10.1111/j.1151-2916.1999.tb02241.x
6. Tasker, P. W. *J. Phys. C: Solid State Phys.* **1979,** *12,* 4977. doi:10.1088/0022-3719/12/22/036
7. Noguera, C. *J. Phys.: Condens. Matter* **2000,** *12,* R367–R410. doi:10.1088/0953-8984/12/31/201
8. Goniakowski, J.; Finocchi, F.; Noguera, C. *Rep. Prog. Phys.* **2008,** *71,* 016501. doi:10.1088/0034-4885/71/1/016501
9. Torbrügge, S.; Ostendorf, F.; Reichling, M. *J. Phys. Chem. C* **2009,** *113,* 4909–4914. doi:10.1021/jp804026v
10. Kresse, G.; Dulub, O.; Diebold, U. *Phys. Rev. B* **2003,** *68,* 245409. doi:10.1103/PhysRevB.68.245409
11. Lauritsen, J. V.; Porsgaard, S.; Rasmussen, M. K.; Jensen, M. C. R.; Bechstein, R.; Meinander, K.; Clausen, B. S.; Helveg, S.; Wahl, R.; Kresse, G.; Besenbacher, F. *ACS Nano* **2011,** *5,* 5987–5994. doi:10.1021/nn2017606
12. Rasmussen, M. K.; Foster, A. S.; Hinnemann, B.; Canova, F. F.; Helveg, S.; Meinander, K.; Martin, N. M.; Knudsen, J.; Vlad, A.; Lundgren, E.; Stierle, A.; Besenbacher, F.; Lauritsen, J. V. *Phys. Rev. Lett.* **2011,** *107,* 036102. doi:10.1103/PhysRevLett.107.036102
13. Vaz, C. A. F.; Prabhakaran, D.; Altman, E. I.; Henrich, V. E. *Phys. Rev. B* **2009,** *80,* 155457. doi:10.1103/PhysRevB.80.155457
14. Meyer, W.; Biedermann, K.; Gubo, M.; Hammer, L.; Heinz, K. *J. Phys.: Condens. Matter* **2008,** *20,* 265011. doi:10.1088/0953-8984/20/26/265011
15. Harding, J. H. *Surf. Sci.* **1999,** *422,* 87–94. doi:10.1016/S0039-6028(98)00884-X
16. Fang, C. M.; Parker, S. C.; de With, G. *J. Am. Ceram. Soc.* **2000,** *83,* 2082–2084. doi:10.1111/j.1151-2916.2000.tb01516.x
17. Davies, M. J.; Parker, S. C.; Watson, G. W. *J. Mater. Chem.* **1994,** *4,* 813–816. doi:10.1039/jm9940400813
18. Fang, C. M.; de With, G.; Parker, S. C. *J. Am. Ceram. Soc.* **2001,** *84,* 1553–1558. doi:10.1111/j.1151-2916.2001.tb00876.x
19. Fang, C. M.; Parker, S. C.; de With, G. *Key Eng. Mater.* **2001,** *206-213,* 543–546. doi:10.4028/www.scientific.net/KEM.206-213.543
20. Méducin, F.; Redfern, S. A. T.; Le Godec, Y.; Stone, H. J.; Tucker, M. G.; Dove, M. T.; Marshall, W. G. *Am. Mineral.* **2004,** *89,* 981–986.
21. Ostendorf, F.; Torbrügge, S.; Reichling, M. *Phys. Rev. B* **2008,** *77,* 041405. doi:10.1103/PhysRevB.77.041405
22. Dulub, O.; Diebold, U.; Kresse, G. *Phys. Rev. Lett.* **2003,** *90,* 016102. doi:10.1103/PhysRevLett.90.016102
23. Sadewasser, S.; Lux-Steiner, M. C. *Phys. Rev. Lett.* **2003,** *91,* 266101. doi:10.1103/PhysRevLett.91.266101

License and Terms

Beilstein Journal of Nanotechnology

Theoretical study of the frequency shift in bimodal FM-AFM by fractional calculus

Elena T. Herruzo and Ricardo Garcia*

Full Research Paper

Open Access

Address:
IMM-Instituto de Microelectrónica de Madrid (CSIC). C Isaac Newton 8, 28760 Madrid, Spain

Email:
Ricardo Garcia* - ricardo.garcia@imm.cnm.csic.es

* Corresponding author

Keywords:
AFM; atomic force microscopy; bimodal AFM; frequency shift; integral calculus applications

Beilstein J. Nanotechnol. **2012,** *3,* 198–206.
doi:10.3762/bjnano.3.22

Received: 19 December 2011
Accepted: 03 February 2012
Published: 07 March 2012

This article is part of the Thematic Series "Noncontact atomic force microscopy".

Guest Editor: U. D. Schwarz

Abstract

Bimodal atomic force microscopy is a force-microscopy method that requires the simultaneous excitation of two eigenmodes of the cantilever. This method enables the simultaneous recording of several material properties and, at the same time, it also increases the sensitivity of the microscope. Here we apply fractional calculus to express the frequency shift of the second eigenmode in terms of the fractional derivative of the interaction force. We show that this approximation is valid for situations in which the amplitude of the first mode is larger than the length of scale of the force, corresponding to the most common experimental case. We also show that this approximation is valid for very different types of tip–surface forces such as the Lennard-Jones and Derjaguin–Muller–Toporov forces.

Introduction

Since the invention of the atomic force microscope (AFM) [1], numerous AFM studies have been pursued in order to extract information from the sample properties in a quantitative way [2-16]. Both static (contact) [2-7] and dynamic [8-11,14-17] AFM methods have been applied. Static techniques such as nanoindentation [2], pulsed-force mode [3] and force modulation [4-6] are able to extract quantitative properties of the sample in a straightforward manner, but they are usually slow and invasive. Although these techniques allow control of the force applied to the sample, they are usually limited to forces above 1 nN, and such forces can damage the structure of soft samples.

On the other hand, AFM techniques based on dynamic AFM modes have the ability to make fast and noninvasive measurements. They are potentially faster because the quantitative measurements can be acquired simultaneously with the topography. In addition, the lateral forces applied to the sample can be smaller, which minimizes the lateral displacement of the molecules by the tip. Moreover, dynamic modes have already

demonstrated their ability to map compositional properties of the sample [11,18,19]. However, quantifying physical properties is hard, because a direct relationship between observables and forces is difficult to deduce.

Since the observable quantities in dynamic modes are averaged over many cycles of oscillation (amplitude and phase shift for amplitude modulation AFM (AM-AFM) [20,21], and frequency shift and dissipation for FM-AFM [22,23]), it is not straightforward to obtain an analytical relationship between observables and forces. It is known that in FM-AFM the frequency shift of the first mode can be directly related to the gradient of the force when the amplitude is much smaller than the typical length scale of the interaction. For larger amplitudes, the frequency shift is related to the virial of the force [24,25]. Sader and Jarvis have proposed an alternative interpretation of FM-AFM in terms of fractional calculus [26,27]. They showed that the frequency shift can be interpreted as a fractional differential operator, where the order of differentiation or integration is dictated by the difference between the amplitude of oscillation and the length scale of the interaction.

Successful approaches to reconstruct material properties in a quantitative way came along with the development of novel AFM techniques, such as scanning probe accelerometer microscopy (SPAM) [8,28], or by making use of higher harmonics of the oscillation in order to relate the force with the observable quantity through its transfer function [11]. In particular, the torsional-harmonic cantilevers introduced by Sahin et al. allowed the reconstruction of the effective elastic modulus of samples in air [14] and liquids [29-31].

Bimodal AFM [32,33] is a force-microscopy method that allows quantitative mapping of the sample properties (Figure 1). Bimodal AFM operates by exciting simultaneously the cantilever at its first and second flexural resonances. The technique provides an increase in the sensitivity toward force variations [15,18,19,33-36] with respect to conventional AFM. At the same time, it duplicates the number of information channels, through either the amplitude and phase shift of the second mode in bimodal AM-AFM, or the frequency shift Δf_2 and dissipation of the second mode in bimodal FM-AFM. Experimental measurements have shown the ability of bimodal AFM to measure a variety of interactions, from electrostatic to magnetic or mechanical, both in ultrahigh vacuum [36-38], air [33,34,39-41] and liquids [15,18,19]. Furthermore, it is compatible with both frequency-modulated [15,36-38] and amplitude-modulated AFM techniques [18,19,33,34,39-41]. Recently, Kawai et al. [36] and Aksoy and Atalar [42] found a relationship between Δf_2 and the average gradient of the force over one period of oscillation of the first mode.

Here, we propose a theoretical approach to determine the frequency shift in bimodal FM-AFM in terms of a fractional differential operator of the tip–surface interaction force. The frequency shift of the second mode is related to a quantity that is intermediate between the interaction force and the force gradient. This quantity is defined mathematically as the half-derivative of the interaction force. This approach does not make any assumptions on the force law, and it explains the advantages of bimodal FM-AFM with respect to conventional FM-AFM whenever the amplitudes of the first mode are larger that the characteristic length of scale of the interaction force.

Results and Discussion

Frequency shift of the second mode in bimodal AFM

The problem of a cantilever vibrating under bimodal excitation can be studied by means of the averaged quantities of the dissipated energy and the virial [43-45]. The virial of the n^{th} mode is defined as

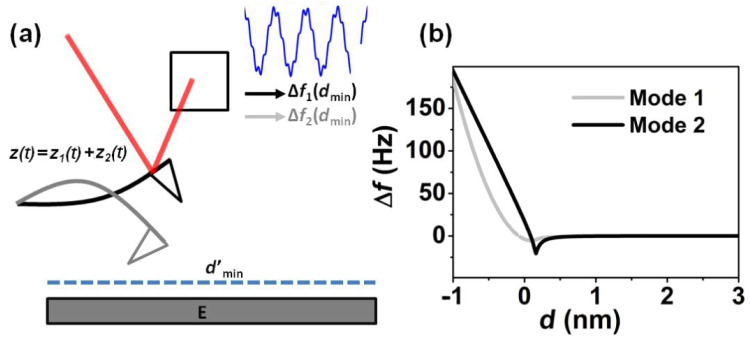

Figure 1: (a) Scheme of the first two eigenmodes of a cantilever and the tip deflection under bimodal excitation. In bimodal FM-AFM changes in the interaction force produce changes in the resonant frequency. The feedback loop keeps the resonant frequency of the 1^{st} mode constant by changing the minimum tip–surface distance. (b) Frequency shifts of the 1^{st} and 2^{nd} modes as a function of the tip–surface distance.

$$V_{ts}(n)=\frac{1}{T}\int_0^T F_{ts}(t)\,z_n(t)\,\mathrm{d}t \tag{1}$$

where t is the time and T is the period of the oscillation

The tip deflection in bimodal FM-AFM can be described as:

$$\begin{aligned} z(t) &= z_0+\sum_n A_n\cos(\omega_n t-\pi/2)\\ &\approx z_0+A_1\cos(\omega_1 t-\pi/2)+A_2\cos(\omega_2 t-\pi/2)\end{aligned} \tag{2}$$

where z_0 is the mean deflection, and A_n and ω_n are the amplitude and the frequency of the n^{th} mode.

By substituting Equation 2 into Equation 1 and replacing F_{ts} by its equivalent according to the Newton equation, an expression for the virial of the second mode that applies to bimodal FM-AFM is deduced [45]

$$V_{ts}(2)\approx -k_2A_2^2\frac{\Delta f_2}{f_2} \tag{3}$$

An additional approximation can be performed by considering that the free amplitude of the second mode A_2 is much lower than the free amplitude of the first mode ($A_2 << A_1$) [15,36,42]. In this case $z(t)$ can be expanded in powers of $A_2\cos(\omega_2 t-\pi/2)$, and the virial of the second mode is given by

$$V_{ts,2}\approx\frac{1}{4\pi}\int_{-\pi/\omega_1}^{\pi/\omega_1}F'_{ts}\left(z_c+A_1\cos\left(\omega_1 t-\frac{\pi}{2}\right)\right)A_2^2\omega_1\,\mathrm{d}t \tag{4}$$

where z_c is the average cantilever–sample separation.

By combining Equation 3 and Equation 4 we deduce a relationship between the second-mode parameters and the gradient of the force averaged over one cycle of the oscillation of the first mode.

$$\begin{aligned} -k_2\frac{\Delta f_2(d_{\min})}{f_2}\approx\frac{1}{4\pi}\int_{-\pi/\omega_1}^{\pi/\omega_1}F'_{ts}\big(d_{\min}+A_1\\ +A_1\cos(\omega_1 t-\pi/2)\big)\omega_1\,\mathrm{d}t\end{aligned} \tag{5}$$

where $f_n=\omega_n/2\pi$, and $d_{\min}$ is the minimum distance between tip and sample ($d_{\min}\approx z_c-A_1$).

Interpretation of the frequency shift in bimodal FM-AFM in terms of the half-derivative of the force

By defining a new variable $u=A_1\cos(\omega t-\pi/2)$, the frequency shift of the second mode (Equation 5) can be expressed as the convolution of the force gradient with the function $1\Big/\left(\pi\sqrt{A_1^2-u^2}\right)$, in the same way that the frequency shift of the first mode in conventional FM-AFM can be seen as the convolution of the force gradient with the semicircle $\frac{2A_1^2}{\pi}\sqrt{A_1^2-u^2}$ [24]:

$$\Delta f_2(d_{\min})\approx-\frac{f_2}{2\pi k_2}\int_{-A_1}^{A_1}F'_{ts}(d_{\min}+A_1+u)\frac{1}{\sqrt{A_1^2-u^2}}\,\mathrm{d}u \tag{6}$$

By using the definition of the Laplace transforms of the force $F(z)$ and its derivative $F'(z)$

$$F(z)=\int_0^\infty B(\lambda)\mathrm{e}^{-\lambda z}\,\mathrm{d}\lambda \tag{7}$$

$$F'(z)=\frac{\mathrm{d}}{\mathrm{d}z}\int_0^\infty B(\lambda)\mathrm{e}^{-\lambda z}\,\mathrm{d}\lambda \tag{8}$$

By substituting Equation 8 in Equation 6 we have

$$\Delta f_2(d_{\min})\approx-\frac{f_2}{2k_2}\frac{\mathrm{d}}{\mathrm{d}d_{\min}}\int_0^\infty B(\lambda)T'(\lambda A_1)\mathrm{e}^{-\lambda d_{\min}}\,\mathrm{d}\lambda \tag{9}$$

where

$$T'(x)=\int_{-1}^{1}\mathrm{e}^{-x(u+1)}\frac{1}{\sqrt{1-u^2}}\,\mathrm{d}u \tag{10}$$

$T'(x)$ can be expressed in terms of the modified Bessel function of the first kind of order zero $I_0(x)$ ($T'(x)=I_0(x)e^{-x}$) [46]. By comparing Equation 8 and Equation 9, it can be seen that Δf_2 is related to the gradient of the force through the derivative operator and a function $T'(\lambda)$. By analogy with the Sader and Jarvis method to express the frequency shift of the first mode in conventional AFM [27], the local power behavior of the function $T'(x)$ around any point $x=\bar{x}$ can be studied. By matching the value of $T'(x)$ and its first derivative to the expression $T'(x)\approx cx^d$, where c and d are local constants, we obtain an expression for the term d, which governs the power behavior of the function $T'(x)$, and for the term c

$$d = \bar{x}\left(-1+\frac{I_1(\bar{x})}{I_0(\bar{x})}\right) \tag{11}$$

$$c = \mathrm{e}^{\bar{x}}\bar{x}^{\bar{x}\left(1-\frac{I_1(\bar{x})}{I_0(\bar{x})}\right)}I_0(\bar{x}) \tag{12}$$

For $x \to 0$, we can see that $d_{\Delta f_2} \to 0$, which means that $T'(\bar{x}) \approx 1$. while for larger x, $d_{\Delta f_2} \to -\frac{1}{2}$, which means that $T'(\bar{x}) \approx \frac{1}{\sqrt{2\pi\bar{x}}}$. This implies that when $A_1 >> 1/\lambda$

$$T'(\lambda A_1) \approx \frac{1}{\sqrt{2\pi\lambda A_1}} \tag{13}$$

By introducing Equation 13 in Equation 9,

$$\Delta f_2(d_{\min}) \approx -\frac{f_2}{2k_2}\frac{1}{\sqrt{2\pi A_1}}\frac{\mathrm{d}}{\mathrm{d}d_{\min}} \cdot\int_0^\infty \frac{1}{\sqrt{\lambda}}B(\lambda)\mathrm{e}^{-\lambda d_{\min}}\,\mathrm{d}\lambda \tag{14}$$

By using the property of the Laplace transform [27]

$$L\left\{\lambda^{-\alpha}B(\lambda)\right\} = I_-^{\alpha}L\left\{B(\lambda)\right\} \tag{15}$$

a direct relationship between Δf_2 and the half-derivative of the force $D_-^{1/2}F(d_{\min})$ and, alternatively, to the half-integral of the force gradient $I_-^{1/2}F'(d_{\min})$ can be found

$$\Delta f_2(d_{\min}) = \frac{f_2}{2k_2}\frac{1}{\sqrt{2\pi A_1}}D_-^{1/2}F(d_{\min}) \tag{16}$$

$$\Delta f_2(d_{\min}) = -\frac{f_2}{2k_2}\frac{1}{\sqrt{2\pi A_1}}I_-^{1/2}F'(d_{\min}) \tag{17}$$

where

$$D_-^{1/2}F(z) = \frac{-1}{\Gamma(1/2)}\frac{\mathrm{d}}{\mathrm{d}z}\int_z^\infty \frac{F(t)}{\sqrt{t-z}}\mathrm{d}t \tag{18}$$

$$I_-^{1/2}F'(z) = \frac{1}{\Gamma(1/2)}\int_z^\infty \frac{F'(t)}{\sqrt{t-z}}\mathrm{d}t \tag{19}$$

and $\Gamma(n)$ is the Gamma function. The above fractional definitions correspond to the so-called right-sided forms of the fractional derivative and integrals [47]. Therefore the frequency shift of the second mode can be related to the half-derivative of the force, or, alternatively, it can be related to the half-integral of the force gradient whenever the amplitude of the first mode A_1 is larger than the typical length scale of the interaction force. This is the typical experimental situation in bimodal FM-AFM, in which large amplitudes of the first mode are used in order to make the imaging stable [36,37] and to increase the contrast in the bimodal channel [18,19].

Fractional derivatives have a wide range of applications [47,48]. For example, they have been used for describing anomalous-diffusion processes, for modeling the behavior of polymers and in viscoelastic-damping models. In general, there is a near-continuous transformation of a function into its derivative by means of fractional derivatives. To illustrate this, Figure 2 shows the behavior of a function, together with its derivative, half-derivative and half-integral. We observe that the half-derivative always lies between the function and its derivative, while the half-integral is displaced to the left with respect to the function, and lies between the function and its integral.

Figure 2 shows the function $(1/x^6 - 1/x^2)$, together with its derivative, its integral, its half-derivative and its half-integral. It is worth mentioning that the minimum and its x value for the half-derivative are situated between those of the derivative and the original function (Figure 2a). A similar situation happens with the half-integral in comparison with the function and its integral (Figure 2b).

Next, we demonstrate that the frequency shift in bimodal AFM is directly related to the half-derivative of the interaction force for two different tip–surface forces, namely Lennard-Jones forces and those described by the DMT model. We have compared the results obtained from Equation 6 with the results estimated from the half-derivative of the force (Equation 16) for a Lennard-Jones force and for the force appearing in the DMT model [49]. The force constant, resonant frequency and quality factor of the first and second flexural modes of the cantilever are, respectively, k_1 = 4 N/m, k_2 = 226.8 N/m, f_{01} = 103.784 kHz, f_{02} = 666.293 kHz, Q_1 = 200, Q_2 = 240. The ratio of the amplitudes A_1/A_2 = 1000 nm and the tip radius R = 3 nm.

The Lennard-Jones force for the interaction between two atoms is [50]

$$F_{LT}(d) = \varepsilon\sigma\left(\frac{\sigma^4}{d^6}-\frac{1}{d^2}\right) \tag{20}$$

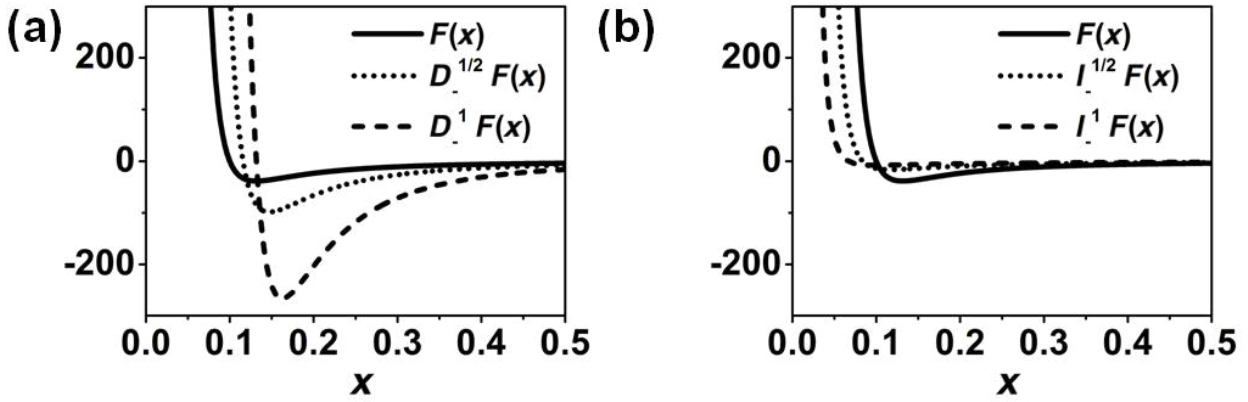

Figure 2: Fractional operators of $(0.1^4/x^6 - 1/x^2)$. (a) The function, half-derivative and derivative are plotted. (b) The function, half-integral and integral are plotted.

where ε is related to the depth of the energy potential and σ to the length scale of the interaction force.

For the force which appears in the DMT model [51]

$$F_{\mathrm{DMT}}(d)=\begin{cases}\dfrac{4E_{\mathrm{eff}}\sqrt{R}}{3}\left(d_0-d\right)^{3/2}-\dfrac{HR}{6d_0^2} & d<d_0\\ -\dfrac{HR}{6d_0^2} & d\geq d_0\end{cases} \tag{21}$$

where H is the Hamaker constant of the long-range van der Waals forces, d_0 is the equilibrium distance, R is the tip radius and E_{eff} is the effective Young's modulus, which is related to the Young's moduli E_t and E_s and Poisson coefficients ν_t and ν_s of the tip and sample by

$$\frac{1}{E_{\mathrm{eff}}}=\frac{1-\nu_t^2}{E_t}+\frac{1-\nu_s^2}{E_s} \tag{22}$$

Figure 3 shows the comparison between the frequency shift of the second mode found through Equation 6 compared to that found by using the numerical half-derivative of the force (Equation 16) for a Lennard-Jones force and for a DMT force. The agreement obtained between the numerical simulations and the results deduced from the half-derivative of the interaction force are remarkable (see insets). Because the dependencies of the force on the distance in the Lennard-Jones and DTM models are rather different, we infer that the approach deduced here is general and applies to any type of force that could be found in an AFM experiment.

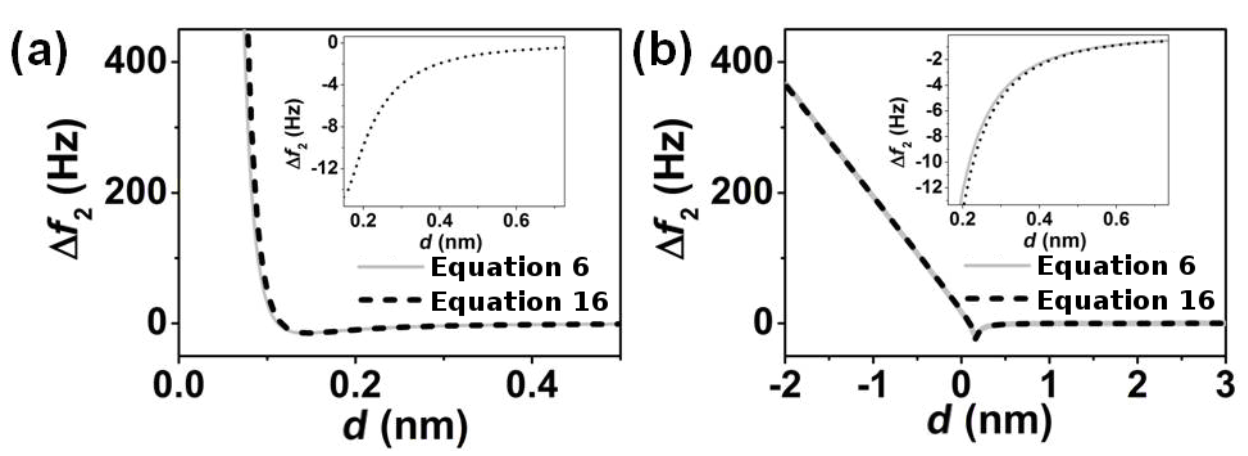

Figure 3: Comparison between the general expression (Equation 6) and the half-derivative (Equation 16) relationship to the frequency shift of the second mode in bimodal FM-AFM for two different forces. (a) Lennard-Jones force characterized by $\varepsilon = 0.5 \cdot 10^{-20}$ J and σ = 0.1 nm, and A_1 = 4 nm; (b) DMT force characterized by $H = 0.2 \cdot 10^{-20}$ J, E_{eff} = 300 MPa, and A_1 = 10 nm.

Interpretation of Δf_1 in bimodal FM-AFM in terms of the half-integral of the force

For the sake of completeness, we compare the results obtained by using the expressions relating the frequency shift of the first mode and the half-integral of the force as deduced by Sader and Jarvis [27]. Δf_1 can be seen as the convolution of the force with the function $\frac{2}{\pi A_1^2\sqrt{A_1^2-u^2}}$ [24]:

$$\Delta f_1\left(d_{\min}\right)\approx -\frac{f_1}{\pi k_1 A_1^2}\cdot\int_{-A_1}^{A_1} F_{ts}\left(d_{\min}+A_1+u\right)\frac{u}{\sqrt{A_1^2-u^2}}\,\mathrm{d}u \tag{23}$$

When the amplitude of the first mode is larger than the length scale of the interaction, the frequency shift of the first mode is related to the half-integral of the force:

$$\Delta f_1\left(d_{\min}\right)=\frac{f_1}{k_1}\frac{1}{\sqrt{2\pi A_1^3}}I_-^{1/2}F\left(d_{\min}\right) \tag{24}$$

Figure 4 shows the agreement obtained between the frequency shift of the first mode found through Equation 23 compared to that found by using the numerical half-integral of the force (Equation 24) for a Lennard-Jones force and for a DMT force. This agreement also supports the interpretation of the observable quantities in terms of fractional operators. In addition, it illustrates the differences of using bimodal AFM over conventional FM-AFM. When A_1 is much smaller than the length scale of the interaction, the corresponding observable is proportional to the derivative both in conventional FM-AFM and in bimodal FM-AFM. However, when A_1 is larger than the length scale of the interaction, Δf_1 is proportional to the half-integral of the force, while Δf_2 is proportional to the half-derivative of the force.

Dependence of the approximate expressions for Δf_1 and Δf_2 on A_1

To better appreciate the differences between the frequency shifts of the first and second modes, we represent their dependence on the amplitude of the first mode (Figure 5).

When the amplitude of the first mode is much smaller than the length scale of the force, the asymptotic limit of $d(x)$ and $c(x)$ (Equation 11 and Equation 12) for small x enables us to approximate $T'\left(\bar{x}\right)\approx 1$. By inserting this in Equation 9 we obtain

$$\Delta f_2\left(d_{\min}\right)=-\frac{f_2}{2k_2}F'\left(d_{\min}\right) \tag{25}$$

which corresponds to the experimental conditions of Naitoh et al. [35] in bimodal FM-AFM. This equation has the same dependence with the mode parameters and the force gradient as the one found for the frequency shift of the first mode in conventional FM-AFM in the limit of small amplitudes [24]

$$\Delta f_1\left(d_{\min}\right)=-\frac{f_1}{2k_1}F'\left(d_{\min}\right) \tag{26}$$

Figure 5a and Figure 5b show a comparison between the numerical results obtained from Equation 6 and the half-derivative (Equation 16) and derivative (Equation 25) for the frequency shift of the second mode approximations, which are valid in the

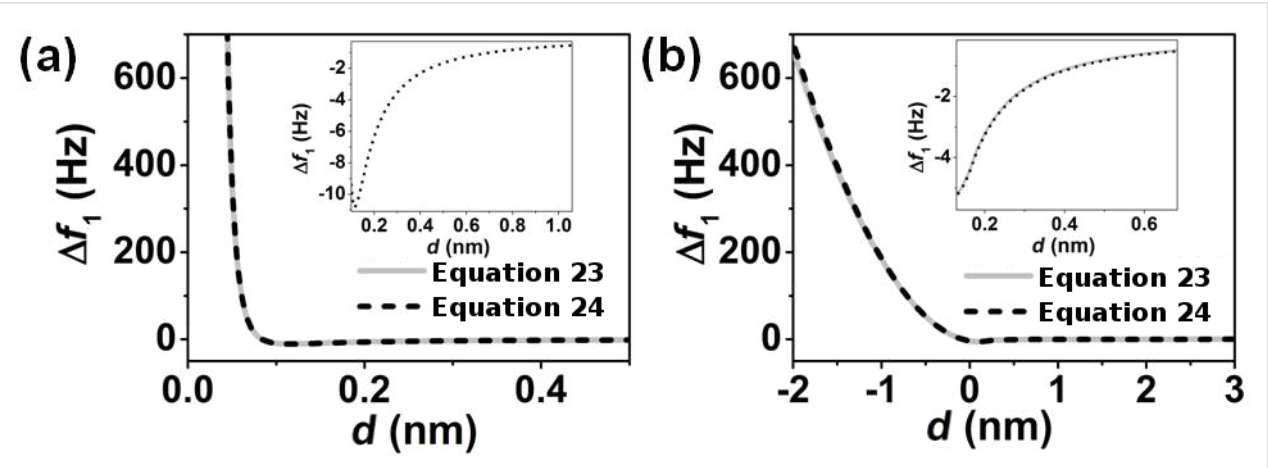

Figure 4: Comparison between the general expression (Equation 23) and the half-integral relationship (Equation 24) to the frequency shift of the first mode in bimodal FM-AFM for two different forces. (a) Lennard-Jones force characterized by $\varepsilon = 0.5\cdot 10^{-20}$ J and $\sigma = 0.1$ nm, and $A_1 = 4$ nm; (b) DMT force characterized by $H = 0.2\cdot 10^{-20}$ J, $E_{\text{eff}} = 300$ MPa, and $A_1 = 10$ nm.

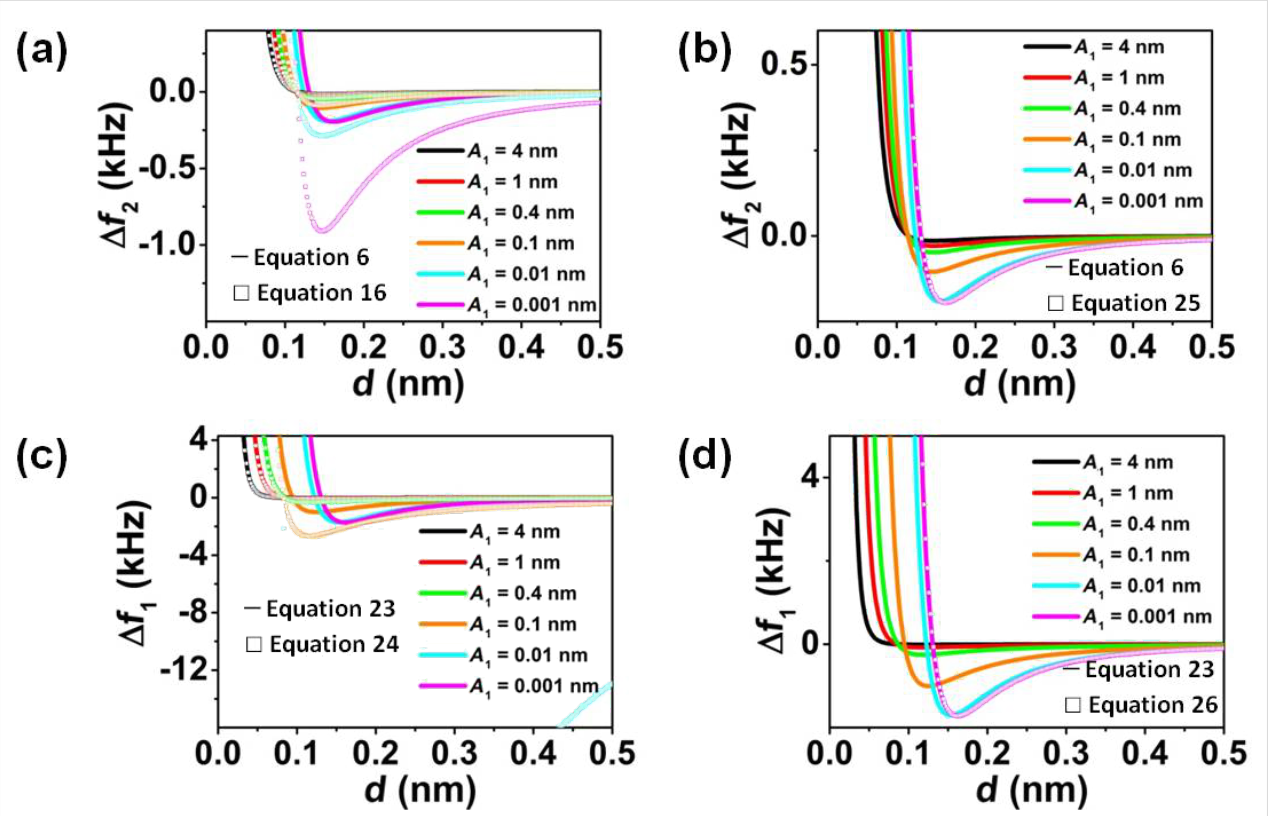

Figure 5: Comparison between the general expression for the frequency shift of the second mode in bimodal FM-AFM (Equation 6) and the (a) half-derivative relationship (Equation 16) and (b) derivative relationship (Equation 25). Comparison between the general expression for the frequency shift of the first mode in bimodal FM-AFM (Equation 23) and the (c) half-integral relationship (Equation 24) and (d) derivative relationship (Equation 26) for different A_1 and a Lennard-Jones force characterized by $\varepsilon = 0.5 \cdot 10^{-20}$ J and $\sigma = 0.1$ nm, $A_1/A_2 = 5000$.

large and small amplitude limits, respectively. For A_1 above 0.1 nm, the half-derivative approximation should be used, while for A_1 below 0.1 nm, the derivative approximation is a good choice. Figure 5c and Figure 5d show a comparison between the numerical results obtained from Equation 23 and the half-integral (Equation 24) and derivative (Equation 26) approximations for the frequency shift of the first mode, which are valid in the large and small amplitude limits. When A_1 is above 0.4 nm, the half-integral approximation can be used, while the derivative approximation is a good choice only when A_1 is smaller than 0.01 nm. There is a range between $A_1 = 0.01$ and $A_1 = 0.4$ nm, which depends on the typical length scale of the interaction, in which an approximation for intermediate amplitudes should be used.

Conclusion

We have deduced an expression that relates the frequency shifts in bimodal frequency modulation AFM with the half-derivative of the tip–surface force or, alternatively, with the half-integral of the force gradient. The approximations are valid for the common experimental situation in which the amplitude of the first mode is larger than the length scale of the interaction force. The approximations are also valid for two different types of forces, namely Lennard-Jones interactions and DMT contact-mechanics forces. We conclude that the fractional-calculus approach is well suited to describe bimodal frequency modulation AFM experiments, which are characterized by the presence of several forces with different distance dependencies.

Acknowledgements

This work was funded by the Spanish Ministry of Science (MICINN) (CSD2010-00024;MAT2009-08650), and the Comunidad de Madrid (S2009/MAT-1467)

References

1. Binnig, G.; Quate, C. F.; Gerber, C. *Phys. Rev. Lett.* **1986,** *56,* 930–933. doi:10.1103/PhysRevLett.56.930
2. Lee, C.; Wei, X.; Kysar, J. W.; Hone, J. *Science* **2008,** *321,* 385–388. doi:10.1126/science.1157996
3. Rosa-Zeiser, A.; Weilandt, E.; Hild, S.; Marti, O. *Meas. Sci. Technol.* **1997,** *8,* 1333. doi:10.1088/0957-0233/8/11/020
4. Maivald, P.; Butt, H. J.; Gould, S. A. C.; Prater, C. B.; Drake, B.; Gurley, J. A.; Elings, V. B.; Hansma, P. K. *Nanotechnology* **1991,** *2,* 103. doi:10.1088/0957-4484/2/2/004

5. Radmacher, M. *IEEE Eng. Med. Biol. Mag.* **1997,** *16,* 47–57. doi:10.1109/51.582176
6. O'Shea, S. J.; Welland, M. E.; Pethica, J. B. *Chem. Phys. Lett.* **1994,** *223,* 336–340. doi:10.1016/0009-2614(94)00458-7
7. Berquand, A.; Roduit, C.; Kasas, S.; Holloschi, A.; Ponce, L.; Hafner, M. *Microsc. Today* **2010,** *18,* 8–14. doi:10.1017/S1551929510000957
8. Legleiter, J.; Park, M.; Cusick, B.; Kowalewski, T. *Proc. Natl. Acad. Sci. U. S. A.* **2006,** *103,* 4813–4818. doi:10.1073/pnas.0505628103
9. Sader, J. E.; Uchihashi, T.; Higgins, M. J.; Farrell, A.; Nakayama, Y.; Jarvis, S. P. *Nanotechnology* **2005,** *16,* S94–S101. doi:10.1088/0957-4484/16/3/018
10. Hoogenboom, B. W.; Hug, H. J.; Pellmont, Y.; Martin, S.; Frederix, P. L. T. M.; Fotiadis, D.; Engel, A. *Appl. Phys. Lett.* **2006,** *88,* 193109. doi:10.1063/1.2202638
11. Stark, M.; Möller, C.; Müller, D. J.; Guckenberger, R. *Biophys. J.* **2001,** *80,* 3009–3018. doi:10.1016/S0006-3495(01)76266-2
12. Hutter, C.; Platz, D.; Tholén, E. A.; Hansson, T. H.; Haviland, D. B. *Phys. Rev. Lett.* **2010,** *104,* 050801. doi:10.1103/PhysRevLett.104.050801
13. Solares, S. D.; Chawla, G. *Meas. Sci. Technol.* **2010,** *21,* 125502. doi:10.1088/0957-0233/21/12/125502
14. Sahin, O.; Magonov, S.; Su, C.; Quate, C. F.; Solgaard, O. *Nat. Nanotechnol.* **2007,** *2,* 507–514. doi:10.1038/nnano.2007.226
15. Martinez-Martin, D.; Herruzo, E. T.; Dietz, C.; Gomez-Herrero, J.; Garcia, R. *Phys. Rev. Lett.* **2011,** *106,* 198101. doi:10.1103/PhysRevLett.106.198101
16. Raman, A.; Trigueros, S.; Cartagena, A.; Stevenson, A. P. Z.; Susilo, M.; Nauman, E.; Antoranz Contera, S. *Nat. Nanotechnol.* **2011,** *6,* 809–814. doi:10.1038/nnano.2011.186
17. Stark, R. W. *Mater. Today* **2010,** *13,* 24–32. doi:10.1016/S1369-7021(10)70162-0
18. Martínez, N. F.; Lozano, J. R.; Herruzo, E. T.; Garcia, F.; Richter, C.; Sulzbach, T.; Garcia, R. *Nanotechnology* **2008,** *19,* 384011. doi:10.1088/0957-4484/19/38/384011
19. Dietz, C.; Herruzo, E. T.; Lozano, J. R.; Garcia, R. *Nanotechnology* **2011,** *22,* 125708. doi:10.1088/0957-4484/22/12/125708
20. Martin, Y.; Williams, C. C.; Wickramasinghe, H. K. *J. Appl. Phys.* **1987,** *61,* 4723–4729. doi:10.1063/1.338807
21. García, R.; Pérez, R. *Surf. Sci. Rep.* **2002,** *47,* 197–301. doi:10.1016/S0167-5729(02)00077-8
22. Albrecht, T. R.; Grütter, P.; Horne, D.; Rugar, D. *J. Appl. Phys.* **1991,** *69,* 668–673. doi:10.1063/1.347347
23. Giessibl, F. J. *Rev. Mod. Phys.* **2003,** *75,* 949–983. doi:10.1103/RevModPhys.75.949
24. Giessibl, F. J. *Phys. Rev. B* **1997,** *56,* 16010–16015. doi:10.1103/PhysRevB.56.16010
25. Dürig, U. *Appl. Phys. Lett.* **1999,** *75,* 433–435. doi:10.1063/1.124399
26. Sader, J. E.; Jarvis, S. P. *Appl. Phys. Lett.* **2004,** *84,* 1801–1803. doi:10.1063/1.1667267
27. Sader, J. E.; Jarvis, S. P. *Phys. Rev. B* **2004,** *70,* 012303. doi:10.1103/PhysRevB.70.012303
28. Kumar, B.; Pifer, P. M.; Giovengo, A.; Legleiter, J. *J. Appl. Phys.* **2010,** *107,* 044508. doi:10.1063/1.3309330
29. Sahin, O. *Phys. Rev. B* **2008,** *77,* 115405. doi:10.1103/PhysRevB.77.115405
30. Sahin, O.; Erina, N. *Nanotechnology* **2008,** *19,* 445717. doi:10.1088/0957-4484/19/44/445717
31. Dong, M.; Husale, S.; Sahin, O. *Nat. Nanotechnol.* **2009,** *4,* 514–517. doi:10.1038/nnano.2009.156
32. Rodríguez, T. R.; García, R. *Appl. Phys. Lett.* **2004,** *84,* 449–451. doi:10.1063/1.1642273
33. Patil, S.; Martinez, N. F.; Lozano, J. R.; Garcia, R. *J. Mol. Recognit.* **2007,** *20,* 516–523. doi:10.1002/jmr.848
34. Li, J. W.; Cleveland, J. P.; Proksch, R. *Appl. Phys. Lett.* **2009,** *94,* 163118. doi:10.1063/1.3126521
35. Naitoh, Y.; Ma, Z.; Li, Y. J.; Kageshima, M.; Sugawara, Y. *J. Vac. Sci. Technol., B: Microelectron. Nanometer Struct.–Process., Meas., Phenom.* **2010,** *28,* 1210–1214. doi:10.1116/1.3503611
36. Kawai, S.; Glatzel, T.; Koch, S.; Such, B.; Baratoff, A.; Meyer, E. *Phys. Rev. Lett.* **2009,** *103,* 220801. doi:10.1103/PhysRevLett.103.220801
37. Kawai, S.; Glatzel, T.; Koch, S.; Such, B.; Baratoff, A.; Meyer, E. *Phys. Rev. B* **2010,** *81,* 085420. doi:10.1103/PhysRevB.81.085420
38. Kawai, S.; Pawlak, R.; Glatzel, T.; Meyer, E. *Phys. Rev. B* **2011,** *84,* 085429. doi:10.1103/PhysRevB.84.085429
39. Martinez, N. F.; Patil, S.; Lozano, J. R.; Garcia, R. *Appl. Phys. Lett.* **2006,** *89,* 153115. doi:10.1063/1.2360894
40. Proksch, R. *Appl. Phys. Lett.* **2006,** *89,* 113121. doi:10.1063/1.2345593
41. Dietz, C.; Zerson, M.; Riesch, C.; Gigler, A. M.; Stark, R. W.; Rehse, N.; Magerle, R. *Appl. Phys. Lett.* **2008,** *92,* 143107. doi:10.1063/1.2907500
42. Aksoy, M. D.; Atalar, A. *Phys. Rev. B* **2011,** *83,* 075416. doi:10.1103/PhysRevB.83.075416
43. San Paulo, A.; García, R. *Phys. Rev. B* **2002,** *66,* 041406. doi:10.1103/PhysRevB.66.041406
44. Lozano, J. R.; Garcia, R. *Phys. Rev. Lett.* **2008,** *100,* 076102. doi:10.1103/PhysRevLett.100.076102
45. Lozano, J. R.; Garcia, R. *Phys. Rev. B* **2009,** *79,* 014110. doi:10.1103/PhysRevB.79.014110
46. Abramowitz, M.; Stegun, A. *Handbook of Mathematical Functions;* Dover: New York, 1975.
47. Samko, S. G.; Kilbas, A. A.; Marichev, O. I. *Fractional Integrals and Derivatives: Theory and Applications;* CRC, 1993.
48. Oldham, K. B. *The fractional calculus: Theory, applications of differentiation, integration to arbitrary order;* Academic Press, Inc.: New York-London, 1974.
49. Derjaguin, B. V.; Muller, V. M.; Toporov, Yu. P. *J. Colloid Interface Sci.* **1975,** *53,* 314–326. doi:10.1016/0021-9797(75)90018-1
50. Israelachvili, J. N. *Intermolecular and Surface Forces,* 2nd ed.; Elsevier Academic Press: London, 2005.
51. García, R. *Amplitude Modulation AFM in Liquid;* Wiley-VCH: Weinheim, Germany, 2010.

Beilstein Journal of Nanotechnology

A measurement of the hysteresis loop in force-spectroscopy curves using a tuning-fork atomic force microscope

Manfred Lange*, Dennis van Vörden and Rolf Möller

Full Research Paper

Open Access

Address:
Faculty of Physics, University of Duisburg-Essen, Lotharstr.1-21
47048 Duisburg, Germany

Email:
Manfred Lange* - manfred.lange@uni-due.de

* Corresponding author

Keywords:
atomic force microscopy; energy dissipation; force spectroscopy; hysteresis loop; PTCDA/Ag/Si(111) √3 × √3

Beilstein J. Nanotechnol. **2012,** *3,* 207–212.
doi:10.3762/bjnano.3.23

Received: 22 November 2011
Accepted: 03 February 2012
Published: 08 March 2012

This article is part of the Thematic Series "Noncontact atomic force microscopy".

Guest Editor: U. D. Schwarz

Abstract

Measurements of the frequency shift versus distance in noncontact atomic force microscopy (NC-AFM) allow measurements of the force gradient between the oscillating tip and a surface (force-spectroscopy measurements). When nonconservative forces act between the tip apex and the surface the oscillation amplitude is damped. The dissipation is caused by bistabilities in the potential energy surface of the tip–sample system, and the process can be understood as a hysteresis of forces between approach and retraction of the tip. In this paper, we present the direct measurement of the whole hysteresis loop in force-spectroscopy curves at 77 K on the PTCDA/Ag/Si(111) √3 × √3 surface by means of a tuning-fork-based NC-AFM with an oscillation amplitude smaller than the distance range of the hysteresis loop. The hysteresis effect is caused by the making and breaking of a bond between PTCDA molecules on the surface and a PTCDA molecule at the tip. The corresponding energy loss was determined to be 0.57 eV by evaluation of the force–distance curves upon approach and retraction. Furthermore, a second dissipation process was identified through the damping of the oscillation while the molecule on the tip is in contact with the surface. This dissipation process occurs mainly during the retraction of the tip. It reaches a maximum value of about 0.22 eV/cycle.

Introduction

Noncontact atomic force microscopy (NC-AFM) is a powerful tool for the study of surface properties. The invention of the frequency-modulation mode (FM) [1] has made it possible to achieve true atomic resolution [2] with a NC-AFM. In this mode the distance between the sample and the tip is adjusted by maintaining the frequency shift of the cantilever at a constant value while scanning the sample. During operation the oscillation amplitude is kept constant by a second control loop. The amplitude control loop provides valuable information on nonconservative interactions between the tip apex and the

sample, which cause damping of the oscillation amplitude [3]. The excitation energy needed to keep the oscillation amplitude constant is directly related to the dissipation.

While the mechanisms of topographic imaging are well understood [4], the dissipation processes on the atomic scale need to be investigated. In general, dissipation can be understood as a hysteresis of forces between approach and retraction of the tip [5,6]. The hysteresis is caused by bistabilities in the potential energy surface of the tip–sample system. Experiments and calculations [7,8] show that dissipation on the atomic level originates from the adhesion or displacement of single atoms caused by strong interaction between the sample and the tip apex.

Simulations for an MgO tip and a MgO surface by L. N. Kantorovich and T. Trevethan [6] showed that the width of such a hysteresis, which may be observed experimentally, depends on the temperature. Due to thermal excitation the width reduces to 1 Å at 100 K and to 0.1 Å at room temperature. The development of NC-AFM instruments that operate at low temperatures and with small amplitudes should enable a direct evaluation of such a hysteresis by analysis of the differences between the force–distance curves during approach and retraction.

In this paper, we report the measurement of hysteresis in force-spectroscopy curves at 77 K with a home-built low-temperature tuning-fork-based AFM (LT-TF-AFM) [9]. When a conductive sample is used, scanning tunneling microscopy (STM) and FM-AFM measurements may be combined. The use of a tuning fork as a sensor allows an oscillation amplitude in the subnanometer regime to be used, due to its large spring constant of about 9000 N/m.

The force-spectroscopy measurements were performed on the organic molecule 3,4,9,10-perylene-tetracarboxylic-dianhydride (PTCDA) grown on a Ag/Si(111) √3 × √3 surface. PTCDA has been extensively studied as a candidate for organic devices [10-15] and its adsorption geometry and binding mechanism is well-known on several surfaces. Furthermore the electronic structure and growth of PTCDA on the Ag/Si(111) √3 × √3 surface is well understood [10,16,17]. In the submonolayer range the PTCDA molecules grow on the Ag/Si(111) √3 × √3 surface in three different phases, namely the herringbone, square and hexagonal phases.

Results and Discussion

Figure 1a shows an STM 250 nm × 250 nm overview scan of the PTCDA/Ag/Si(111) √3 × √3 surface after the deposition of ~0.3 ML PTCDA. The PTCDA molecules grow from step edges or between steps and form single- or double-layer islands. The PTCDA islands can be clearly distinguished from the Ag/Si(111) √3 × √3 surface by the simultaneously recorded frequency-shift (AFM) image (Figure 1b). The frequency shifts on the PTCDA islands and Ag/Si(111) √3 × √3 surface are about −1 Hz and −2 Hz, respectively. This means that for a given tunneling current the attractive forces are stronger on the Ag/Si(111) √3 × √3 surface than on the PTCDA islands.

Prior to the force-spectroscopy measurements the tungsten tip was prepared by making “soft contact” between the tip and a

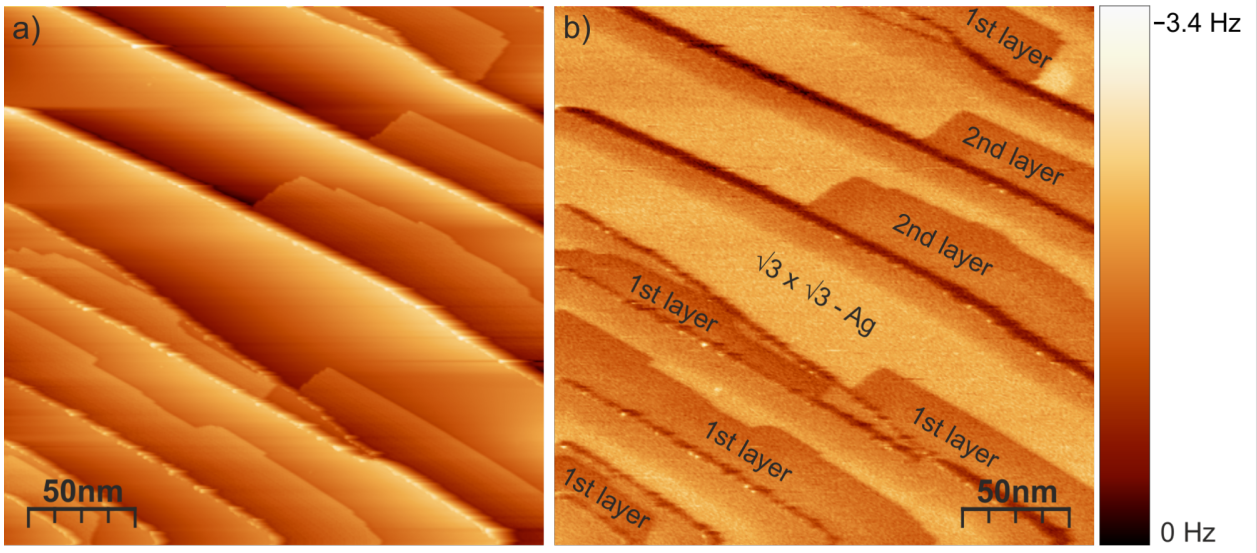

Figure 1: (a) STM image of the PTCDA/Ag/Si(111) √3 × √3 surface. Scan area: 250 nm × 250 nm, tunneling voltage U = 0.9 V, tunneling current I = 70 pA. (b) Simultaneously recorded frequency shift at an oscillation amplitude of 2.8 Å. The Ag/Si(111) √3 × √3 surface gives rise to a larger frequency shift than the PTCDA islands.

PTCDA island. Before and after the soft dipping process the area of contact was scanned to ensure that a PTCDA molecule was picked up with the tip apex. The force spectroscopy data presented in this paper are recorded on the double-layer PTCDA island displayed in Figure 2. The PTCDA molecules are arranged in a herringbone phase, as indicated by the drawing of the molecule.

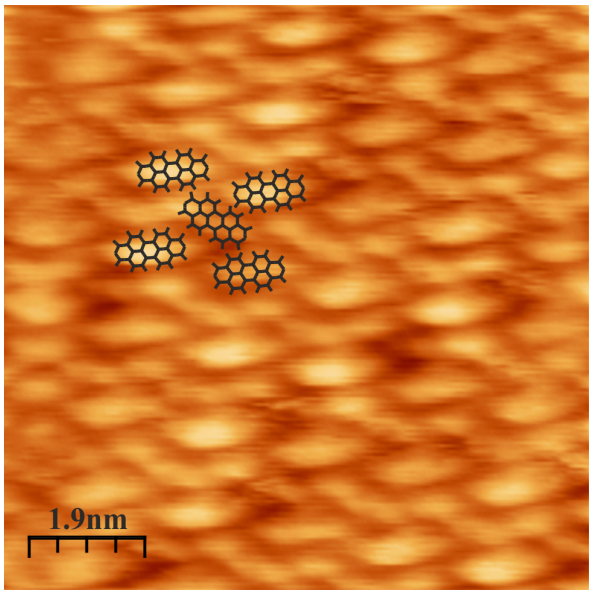

Figure 2: STM image of a double layer of PTCDA arranged in a herringbone phase. The structure is indicated by the schematic drawing of molecular lattice. Scan area: 9 nm × 9 nm; tunneling voltage U = 1 V; tunneling current I = 60 pA.

In order to compensate the electrostatic long-range forces, frequency-shift versus bias-voltage curves were recorded on the PTCDA herringbone island, revealing a contact potential difference of 0.1 V. By adjusting the bias voltage to this value the electrostatic long-range forces can be eliminated. The long-range van der Waals (vdW) interaction was determined by fitting the frequency-shift versus distance (df–z) data at large tip–sample separation by the function (2.8) given in [18]. The vdW fit was extrapolated and subtracted from the df–z curves, resulting in df–z curves determined by the pure short-range interaction (df_{SR}). Figure 3a shows the short-range df_{SR}–z curve measured on the PTCDA herringbone island with an amplitude of 2.8 Å. The black curve represents the approach of the tip towards the surface and the red curve the retraction. The df_{SR}–z curves reveal a hysteresis due to a change of the forces between the tip and sample. To ensure that the hysteresis loop was not induced by a permanent modification of the tip or sample, images of the surface were repeatedly taken before and after each measurement. Since the hysteresis was only observed after the tip had picked up a molecule we assume that it is induced by the PTCDA molecule on the tip apex. Most likely the molecule on the tip apex forms a bond with one or more molecules of the herringbone island when the tip comes very close to the surface. This bond is successively broken when the tip is retracted. The width of the hysteresis loop is about 3–4 Å, hence larger than the oscillation amplitude of the tuning fork. The width corresponds to a geometric change in the tip–sample configuration, which is probably caused by the lifting of the molecule. A schematic representation of the process is displayed in Figure 4.

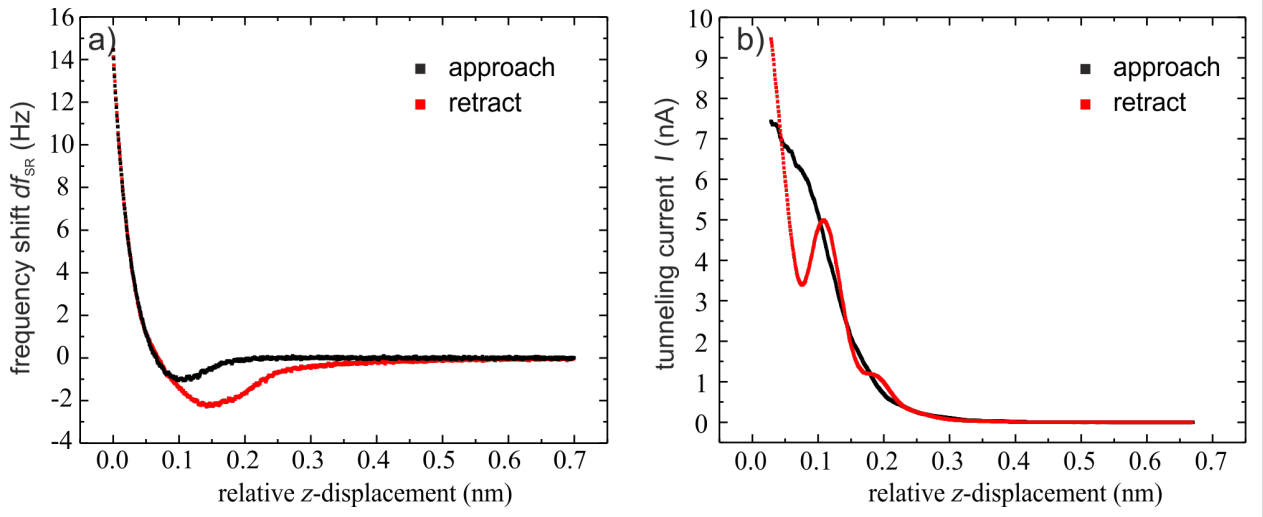

Figure 3: (a) Frequency-shift versus distance curve. The contribution from the long-range forces has been subtracted. The spectroscopy measurement was recorded with an oscillation amplitude of 2.8 Å and a bias voltage of 0.1 V to eliminate the electrostatic interaction. The black curves represent the approach of the tip to the surface, the red curves the retraction. (b) Simultaneously recorded tunneling current.

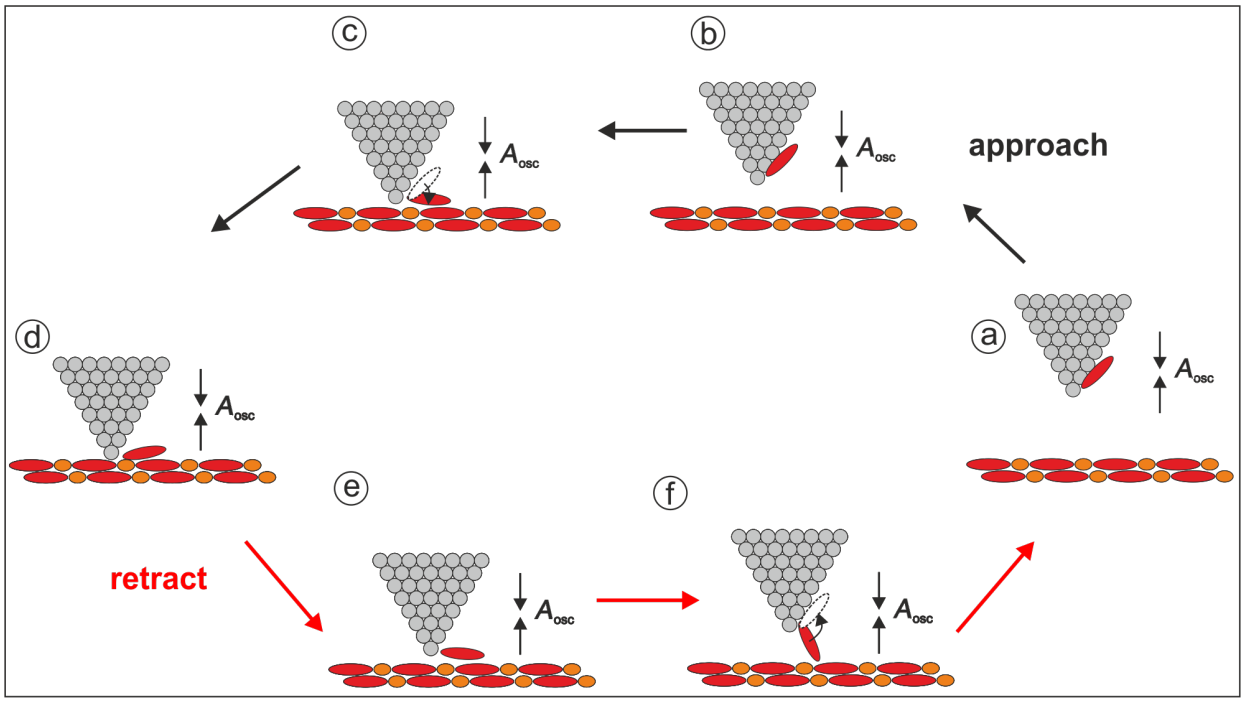

Figure 4: Scheme of the dissipation processes. The black arrows mark the different "snapshots" for the approach of the tip (upper part of the drawing), the red arrows for the retraction (lower part of the drawing). At points (c) and (f) the molecule at the tip abruptly flips to a new position thereby dissipating energy into short-lived vibronic excitations. This energy is given by the work done by the tip as can be seen from the hysteresis in the force distance curves. While the molecule is bridging the gap a second dissipation process occurs, which results in the damping of the oscillation of the tip.

The simultaneously measured tunneling current is shown in Figure 3b. It was calculated from the recorded time-averaged tunneling data by using the script of J. E. Sader and Y. Sugimoto [19]. Since it does not show a significant hysteresis, it may be concluded that the main contribution to the current does not flow through the molecule. Although there are minor kinks in the curve of the tunneling current when the tip approaches the surface, these cannot be uniquely attributed to bond formation by the PTCDA molecule. When the tip was retracted from the surface a significant dip in the tunneling current was found. By comparison to other measurements this may be attributed to the molecule between the tip and the surface.

A second dissipation process is observed through the damping of the oscillation of the tip. It occurs in every cycle of the oscillation, hence many thousands of times during the measurement of the force–distance curves. Figure 5a shows the dissipation signal (E_{diss}) for the approach (black dots) and the retraction (red dots) measured as the power needed to maintain a constant amplitude. As can be seen from the inset, the simultaneously measured oscillation amplitude varies by less than +/− 1%. During the approach of the tip this type of dissipation starts very close to the surface and becomes more prominent upon retraction, reaching a maximum value of 0.22 eV/cycle. It decreases with increasing distance and vanishes at a distance of 0.25 nm from the closest approach. Figure 5b displays the dissipation signal of the retraction together with the force–distance (F_{SR}–z) spectrum calculated from the df_{SR}–z data of Figure 3a by using the script by J. E. Sader and S. P. Jarvis [20]. The damping of the oscillation is observed within the distance range that corresponds to the hysteresis in the force–distance curves, i.e., where the forces for approach and retraction of the tip are different. As sketched in Figure 4, it is rather intuitive that this dissipation is associated with the motion of the molecule between the tip and the sample. It is interesting to compare the energy for this process to the energy associated with the making and breaking of the bond between the PTCDA molecule and the surface, which is given by the area of the hysteresis loop [5,6]. The dissipated energy of this process was determined to be approximately 0.57 eV, which is of the order of the energy of a chemical bond. In [21] the value of about 1 eV is given for the lifting off of the PTCDA molecule completely from the surface. Hence, the observed energy fits well for breaking the bond of a molecule that is partially bound to the surface. It is about two times larger than the maximal energy dissipated by the molecule during the oscillation of the tip.

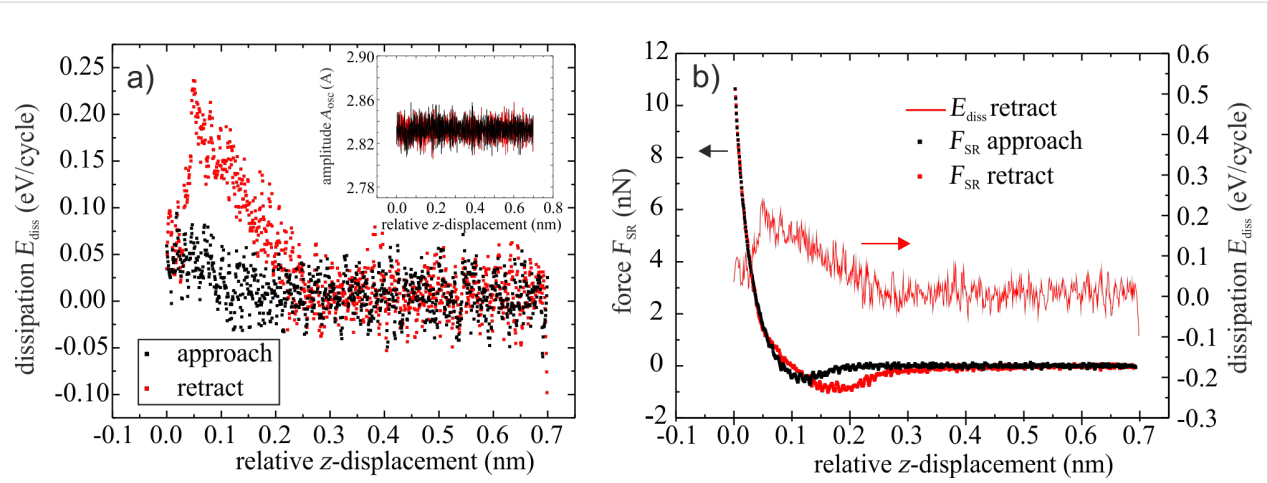

Figure 5: (a) Dissipation signal for approach (black dots) and retraction (red dots). The inset displays the simultaneously recorded oscillation amplitude. The maximum in the dissipation signal is found during the retraction. (b) Dissipation signal for the retraction together with the calculated force–distance curves.

Figure 4 illustrates a model to explain the two dissipation processes during the approach and retraction of the tip. The black arrows (upper path of the drawing) represent the approach corresponding to the black curve in Figure 5b. The red arrows in the drawing indicate the retraction and correspond to the red curves in Figure 5b. The bond formation between the PTCDA molecule at the tip and the molecules of the surface occurs in Figure 4c. Once the molecule is situated between the tip and the surface the oscillation of the tip is damped. During further approach of the tip towards the surface this dissipation increases. During the retraction of the tip the dissipation reaches a maximum before the bond is finally broken at much larger distance (Figure 4f). At that point the damping of the oscillation vanishes and there is no significant difference in the forces between the forward and backward directions. In contrast to the breaking of the bond of an individual atom, the binding of the molecule to the surface results from the superposition of many contributions and this binding can be successively torn apart, which may explain why no abrupt change is observed in the force–distance curve.

Conclusion

We have resolved the hysteresis loop in force-spectroscopy measurements induced by the bond formation and breakage between a PTCDA molecule at the tip of an NC-AFM probe and PTCDA molecules of the sample surface. The dissipated energy of this process is given by the area of the hysteresis loop and was determined to be 0.57 eV. While the molecule is situated between the tip and the surface the oscillation of the tip of the NC-AFM is damped. The dissipation energy of this process is 0.22 eV/cycle at maximum.

Experimental

The experiments were performed at 77 K under ultrahigh vacuum (UHV) conditions. Measurements were performed using a home-built LT-TF-AFM [9], which is able to operate both as an STM and as an FM-AFM. The tuning fork is used in the qPlus configuration [22]. The oscillation amplitude of the tuning fork can be chosen in the subnanometer regime due to its large spring constant of about 9000 N/m, preventing a jump to contact. This offers the advantage that in this regime the measurements are more sensitive to short-range forces and dissipation processes. The resonance frequency and quality factor of the tuning fork at 77 K temperature and under UHV conditions are about 28 kHz and 10000, respectively.

The tuning fork and tunneling signal are wired separately to avoid any crosstalk. Both signals are amplified by home-built current-to-voltage converters outside the vacuum system. For the detection and regulation of the tuning-fork oscillation a phase-locked-loop system supplied by Specs Zürich (Nanonis) is used. Scanning control and data acquisition are performed by the open-source software GXSM [23] combined with home-built electronics. For image processing the free software WSXM [24] is used.

Sample preparation was performed as follows. Si(111) was flash annealed at 1500 K by direct resistive heating. The sample was then cooled down slowly from 1200 K to 800 K to prepare the 7 × 7 reconstruction. Next, 1.0 ML of Ag was evaporated while the Si reconstruction was kept at 800 K. This results in a surface covered by the $\sqrt{3} \times \sqrt{3}$ reconstruction [25]. Finally, ~0.3 ML PTCDA was deposited while the sample was at room temperature.

Acknowledgements

Financial support from the Deutsche Forschungsgemeinschaft through SFB616 'Energy dissipation at surfaces' is gratefully acknowledged. The authors would like to thank D. Utzat for improving the electronics.

References

1. Albrecht, T. R.; Grütter, P.; Horne, D.; Rugar, D. *J. Appl. Phys.* **1991,** *69,* 668–673. doi:10.1063/1.347347
2. Giessibl, F. J. *Science* **1995,** *267,* 68–71. doi:10.1126/science.267.5194.68
3. Mortia, S.; Wiesendanger, R.; Meyer, E. *Noncontact Atomic Force Microscopy;* Springer: Berlin, 2002.
4. Giessibl, F. J. *Phys. Rev. B* **1997,** *56,* 16010–16015. doi:10.1103/PhysRevB.56.16010
5. Sasaki, N.; Tsukada, M. *Jpn. J. Appl. Phys., Part 2* **2000,** *39,* L1334–L1337. doi:10.1143/JJAP.39.L1334
6. Kantorovich, L. N.; Trevethan, T. *Phys. Rev. Lett.* **2004,** *93,* 236102. doi:10.1103/PhysRevLett.93.236102
7. Oyabu, N.; Pou, P.; Sugimoto, Y.; Jelinek, P.; Abe, M.; Morita, S.; Pérez, R.; Custance, Ó. *Phys. Rev. Lett.* **2006,** *96,* 106101. doi:10.1103/PhysRevLett.96.106101
8. Li, Y. J.; Nomura, H.; Ozaki, N.; Naitoh, Y.; Kageshima, M.; Sugawara, Y.; Hobbs, C.; Kantorovich, L. *Phys. Rev. Lett.* **2006,** *96,* 106104. doi:10.1103/PhysRevLett.96.106104
9. Wintjes, N.; Lange, M.; van Vörden, D.; Karacuban, H.; Utzat, D.; Möller, R. *J. Vac. Sci. Technol., B: Microelectron. Nanometer Struct.–Process., Meas., Phenom.* **2010,** *28,* C4E21. doi:10.1116/1.3374720
10. Swarbrick, J. C.; Ma, J.; Theobald, J. A.; Oxtoby, N. S.; O'Shea, J. N.; Champness, N. R.; Beton, P. H. *J. Phys. Chem. B* **2005,** *109,* 12167–12174. doi:10.1021/jp0508305
11. Fendrich, M.; Kunstmann, T. *Appl. Phys. Lett.* **2007,** *91,* 023101. doi:10.1063/1.2755879
12. Wagner, T.; Bannani, A.; Bobisch, C.; Karacuban, H.; Möller, R. *J. Phys.: Condens. Matter* **2007,** *19,* 056009. doi:10.1088/0953-8984/19/5/056009
13. Wagner, T.; Bannani, A.; Bobisch, C.; Karacuban, H.; Stöhr, M.; Gabriel, M.; Möller, R. *Org. Electron.* **2004,** *5,* 35–43. doi:10.1016/j.orgel.2003.12.001
14. Kilian, L.; Hauschild, A.; Temirov, R.; Soubatch, S.; Schöll, A.; Bendounan, A.; Reinert, F.; Lee, T.-L.; Tautz, F. S.; Sokolowski, M.; Umbach, E. *Phys. Rev. Lett.* **2008,** *100,* 136103. doi:10.1103/PhysRevLett.100.136103
15. Kunstmann, T.; Schlarb, A.; Fendrich, M.; Wagner, T.; Möller, R.; Hoffmann, R. *Phys. Rev. B* **2005,** *71,* 121403. doi:10.1103/PhysRevB.71.121403
16. Gustafsson, J. B.; Zhang, H. M.; Johansson, L. S. O. *Phys. Rev. B* **2007,** *75,* 155414. doi:10.1103/PhysRevB.75.155414
17. Zhang, H. M.; Gustafsson, J. B.; Johansson, L. S. O. *Chem. Phys. Lett.* **2010,** *485,* 69–76. doi:10.1016/j.cplett.2009.11.070
18. Guggisberg, M.; Bammerlin, M.; Loppacher, C.; Pfeiffer, O.; Abdurixit, A.; Barwich, V.; Bennewitz, R.; Baratoff, A.; Meyer, E.; Güntherodt, H.-J. *Phys. Rev. B* **2000,** *61,* 11151–11155. doi:10.1103/PhysRevB.61.11151
19. Sader, J. E.; Sugimoto, Y. *Appl. Phys. Lett.* **2010,** *97,* 043502. doi:10.1063/1.3464165
20. Sader, J. E.; Jarvis, S. P. *Appl. Phys. Lett.* **2004,** *84,* 1801–1803. doi:10.1063/1.1667267
21. Fournier, N.; Wagner, C.; Weiss, C.; Temirov, R.; Tautz, F. S. *Phys. Rev. B* **2011,** *84,* 035435. doi:10.1103/PhysRevB.84.035435
22. Giessibl, F. J. *Appl. Phys. Lett.* **1998,** *73,* 3956–3958. doi:10.1063/1.122948
23. Zahl, P.; Bierkandt, M.; Schröder, S.; Klust, A. *Rev. Sci. Instrum.* **2003,** *74,* 1222–1227. doi:10.1063/1.1540718
24. Horcas, I.; Fernández, R.; Gómez-Rodríguez, J. M.; Colchero, J.; Gómez-Herrero, J.; Baro, A. M. *Rev. Sci. Instrum.* **2007,** *78,* 013705. doi:10.1063/1.2432410
25. Wan, K. J.; Lin, X. F.; Nogami, J. *Phys. Rev. B* **1993,** *47,* 13700–13712. doi:10.1103/PhysRevB.47.13700

Beilstein Journal of Nanotechnology

An NC-AFM and KPFM study of the adsorption of a triphenylene derivative on KBr(001)

Antoine Hinaut, Adeline Pujol, Florian Chaumeton, David Martrou, André Gourdon and Sébastien Gauthier*

Full Research Paper

Open Access

Address:
CNRS, CEMES (Centre d'Elaboration des Matériaux et d'Etudes Structurales), BP 94347, 29 rue Jeanne Marvig, F-31055 Toulouse, France

Email:
Sébastien Gauthier* - gauthier@cemes.fr

* Corresponding author

Keywords:
atomic force microscopy; insulating surfaces; Kelvin force probe microscopy; molecular adsorption

Beilstein J. Nanotechnol. **2012,** *3,* 221–229.
doi:10.3762/bjnano.3.25

Received: 21 November 2011
Accepted: 15 February 2012
Published: 12 March 2012

This article is part of the Thematic Series "Noncontact atomic force microscopy".

Guest Editor: U. D. Schwarz

Abstract

The adsorption on KBr(001) of a specially designed molecule, consisting of a flat aromatic triphenylene core equipped with six flexible propyl chains ending with polar cyano groups, is investigated by using atomic force microscopy in the noncontact mode (NC-AFM) coupled to Kelvin probe force microscopy (KPFM) in ultrahigh vacuum at room temperature. Two types of monolayers are identified, one in which the molecules lie flat on the surface (MLh) and another in which they stand approximately upright (MLv). The Kelvin voltage on these two structures is negatively shifted relative to that of the clean KBr surface, revealing the presence of surface dipoles with a component pointing along the normal to the surface. These findings are interpreted with the help of numerical simulations. It is shown that the surface–molecule interaction is dominated by the electrostatic interaction of the cyano groups with the K^+ ions of the substrate. The molecule is strongly adsorbed in the MLh structure with an adsorption energy of 1.8 eV. In the MLv layer, the molecules form π-stacked rows aligned along the polar directions of the KBr surface. In these rows, the molecules are less strongly bound to the substrate, but the structure is stabilized by the strong intermolecular interaction due to π-stacking.

Introduction

The study of molecular adsorption on atomically clean, well-defined surfaces of bulk insulators is progressing rapidly due to the development of atomic force microscopy in the noncontact (or frequency modulation) mode [1-13]. A wide variety of structures, from 3-D islands to single molecules have been observed on different surfaces with an ever-increasing resolution, and there is still room for progress as shown by the impressive submolecular resolution that has been demonstrated

in recent works on the adsorption of pentacene [14] or decastarphene [15] molecules on Cu(111) and on a NaCl(001) bilayer on Cu(111). During the same period, Kelvin probe force microscopy (KPFM) has been combined with NC-AFM [16-19] to investigate metallic or semiconducting surfaces, as well as adsorbates [20,21] or thin insulating films on metals [18,22,23]. But its application to bulk insulating surfaces [24-26] is only beginning, and studies of molecular adsorption on these surfaces are still very scarce [6,8]. Coupling these two techniques is not only interesting for the characterization of the electrical properties of the adsorbates, but also for the extraction of topographic images that are free from distortion induced by electrostatic forces [27].

In the following, we present the first results of a coupled NC-AFM and KPFM study of the adsorption on KBr(001) of 2,3,6,7,10,11-hexa(cyanopropyloxy)triphenylene (HCPTP), presented in Figure 1. This molecule was designed to adsorb strongly on an alkali halide surface in the hope of blocking its diffusion at room temperature. It is equipped with six flexible propyl chains ending with dipolar CN groups. These groups were proven recently to behave as strong anchoring entities for a truxene derivative adsorbed on KBr(001) [10,11] due to their efficient electrostatic interaction with the K^+ ions of the surface.

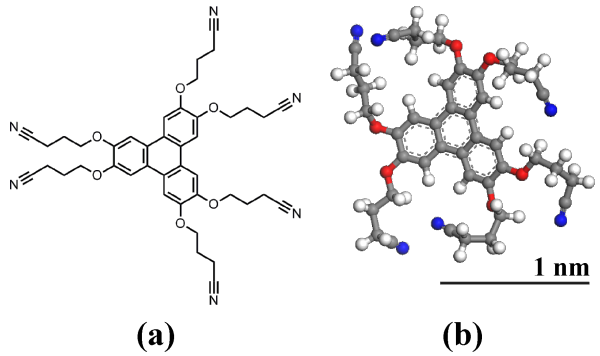

Figure 1: (a) Molecular scheme and (b) structure of HCPTP optimized in vacuum.

Results

Low coverage deposits

An image of the molecules at low coverage, deposited at room temperature on KBr(001), is shown in Figure 2. The white dots that appear on the step edge have a size that is compatible with single molecules, but the resolution is not high enough for a convincing identification. The dots on the terraces are more extended. Their diameter ranges from 3 to 5 nm whereas their height reaches 0.9 nm. We interpret them to be small molecular aggregates comprising a few to a few tens of molecules.

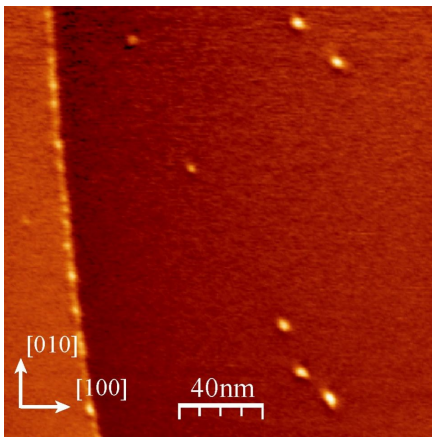

Figure 2: Constant-frequency-shift image of the KBr surface after the deposition of a small amount of molecules at room temperature. Imaging conditions: $\Delta f = -5$ Hz, oscillation amplitude $A = 2$ nm.

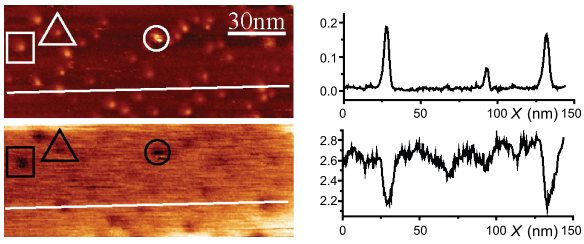

Figure 3: Upper image: topography and lower image: Kelvin map of a KBr terrace with a higher coverage. Imaging conditions: $\Delta f = -20$ Hz, $A = 2$ nm. The profiles correspond to the white lines drawn on the images.

A KBr terrace with a higher coverage is shown in Figure 3, with its simultaneously measured Kelvin voltage map. A negative shift of approximately 0.4 V appears on the largest aggregates relative to the mean KBr signal. According to the standard interpretation [28-30], the sign of this shift is indicative of the presence of permanent dipoles that have a component pointing outward from the surface, or of positive charges under the tip.

Higher coverage deposits

For higher coverage, the molecules were deposited at room temperature and the surface was studied at room temperature and after annealing at 80 °C and 150 °C. The complete study of the evolution of this system with temperature is not the purpose of this report. Here, for the sake of simplicity, we only discuss the results after annealing at 150 °C. Note that the types of structure we observed after the 150 °C annealing were already present at room temperature, differing essentially by the size of their domains. The images of a higher-coverage deposit, annealed at 150 °C during 30 min, presented in Figure 4, show that several structures coexist on the surface.

We first focus on the upper part of the images. It can be seen by comparing Figure 4a and Figure 4b that the line bordering the large triangular area on its right (arrows in Figure 4a and Figure 4b) has been displaced toward the right during the 13 h time lapse separating them. The enlargements of Figure 4c and Figure 4d show that the surface liberated by this process presents dots that are quite similar to the molecular aggregates of Figure 3. For this reason, we identify this region as the KBr substrate. The phenomenon observed in Figure 4 can then be attributed to a dewetting process of a molecular layer [4] corresponding to the domain labeled MLh in Figure 4a. Its height of 0.4 nm (profile in Figure 5a) is compatible with the height of a molecule lying flat on the substrate. Observation of such an evolution at room temperature on a system that has been annealed at 150 °C shows that it is kept far from equilibrium by the very slow kinetics of reorganization. The Kelvin maps of Figure 4e and Figure 4f show a very clear contrast between KBr and MLh (profile in Figure 5c). The Kelvin bias on MLh is shifted toward negative values relative to KBr, that is, in the same direction as for the aggregates discussed previously.

We now examine the third type of domain present in these images (labeled MLv), which displays dark lines oriented along a polar <110> direction (see also Figure 8). The profiles of Figure 5a and Figure 5b show that their height relative to the KBr surface amounts to approximately 1.6 nm. This value does

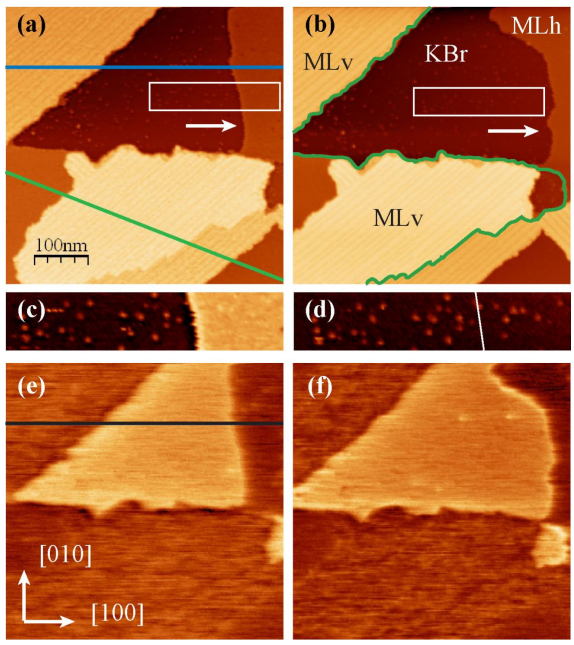

Figure 4: Images of a sample annealed at 150 °C after the deposition of the molecules at room temperature. (a) and (b): topographic images, (c) and (d): enlargement of the areas marked by a white rectangle on (a) and (b); (e) and (f): Kelvin maps obtained simultaneously with (a) and (b). (b), (d) and (f) were measured on the same area as (a), (c) and (e) after a time lapse of 13 h. Imaging conditions: $\Delta f = -20$ Hz, $A = 2$ nm. Two KBr monoatomic steps are outlined in green in (b).

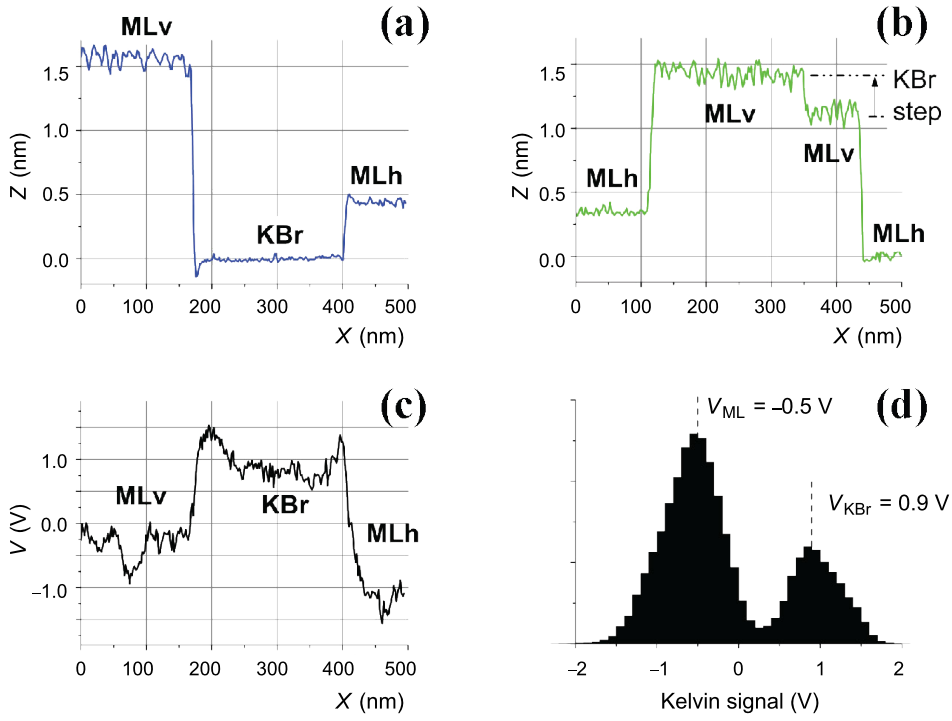

Figure 5: (a) and (b) are the profiles that correspond to the blue and green lines drawn in Figure 4a; (c) is the profile corresponding to the black line on Figure 4e, and (d) is the histogram of Figure 4e.

not vary from one layer to the other (note that the domain located in the lower part of Figure 4a and Figure 4b is crossed by a KBr monoatomic step, outlined in Figure 4b) and is comparable to the diameter of a molecule (see the scale in Figure 1). This observation indicates that these MLv domains comprise a layer of molecules standing approximately upright on the KBr surface. The mean distance between the dark lines is around 11 nm and the associated corrugation is between 0.1 and 0.2 nm. The Kelvin maps of Figure 4e and Figure 4f show that the Kelvin signal is also shifted toward negative values relative to KBr for the MLv domains, with a comparable mean Kelvin bias (histogram in Figure 5d). Nevertheless, the Kelvin map on the two types of structures has a different aspect, being more heterogeneous on the MLv domains. This heterogeneity is not clearly correlated to the topographic images.

Another example of images of a high-coverage deposit, annealed to 150 °C, is shown in Figure 6. Some well-resolved defects appear in the MLh domain in the upper-left area of the topographic image of Figure 6a (see the enlargement in Figure 6c). These defects are also visible in the Kelvin map of Figure 6b (enlarged in Figure 6d). They appear as clear dots, corresponding to a positive shift of the Kelvin voltage on the order of 0.8 V relative to the mean Kelvin voltage of the surrounding MLh domain. As expected the spatial resolution in the Kelvin map is lower than in the topography map due to the longer range of electrical forces relative to van der Waals forces.

The different domains that appear in Figure 6 have been labeled and the monoatomic KBr steps outlined in green. These attributions are based on the measurement of the height of the different structures and their Kelvin signature, as discussed previously. The steps have a remarkable shape, quite different from what is observed on the clean KBr surface, before adsorption, where they are mostly straight and aligned along the nonpolar KBr(001) directions. It is clearly seen that the step morphology is strongly coupled to the structure of the MLv domains. The steps tend to align along the same polar direction as the dark lines of the structure. These steps are highly unstable on the clean surface due to their high electrostatic energy. They can be stabilized only by charged species, in the present case by adsorption of the negatively charged N atoms of the CN groups. This observation also points to a massive KBr surface mass transfer during the annealing of the substrate due to molecular adsorption. The mechanisms at work during this transformation could be of the same nature as those discussed recently in the study of the restructuring of KBr(001) steps by truxene molecules [11]. Finally, we note that when the molecular structure crosses portions of steps that are not aligned in these directions, these dark lines are not visibly affected, indicating that this structure has a strong intrinsic cohesion.

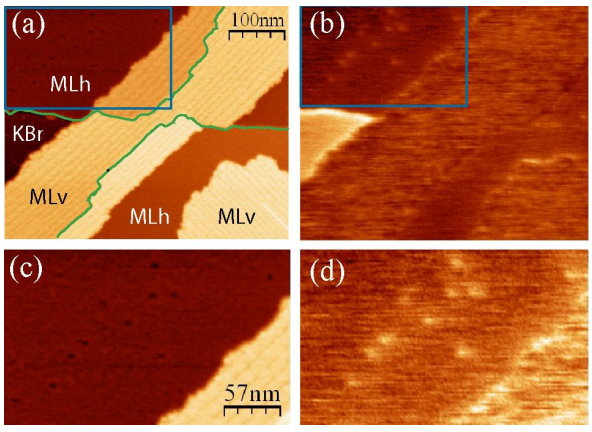

Figure 6: (a) Topographic and (b) Kelvin map of a high molecular coverage annealed to 150 °C; (c) and (d) are enlargements of the upper-left parts of (a) and (b) (blue rectangle). Δf = −20 Hz, A = 2 nm.

High-resolution images of MLh and MLv domains

Two high-resolution images obtained on the same MLh domain are shown in Figure 7. The molecular network can be described by a unit cell characterized by u (2.9 nm, −13° from [100]) and v (3.7 nm, +61° from [100]) (Figure 7b). Note that due to the different imaging conditions in Figure 7a and Figure 7b, the molecular layer appears as a network of black holes in (a) and white bumps in (b). Comparing the size of this unit cell with the size of the molecule (Figure 1) suggests that the basis of the network comprises two molecules.

The images on a MLv domain displayed in Figure 8 show that the dark lines that appear in the large-scale images of Figure 4 and Figure 6 are separated by thinner lines, delimiting rows with a width of ~2.3 nm, slightly larger than a single molecule. A modulation with a period of ~4 nm appears along the rows.

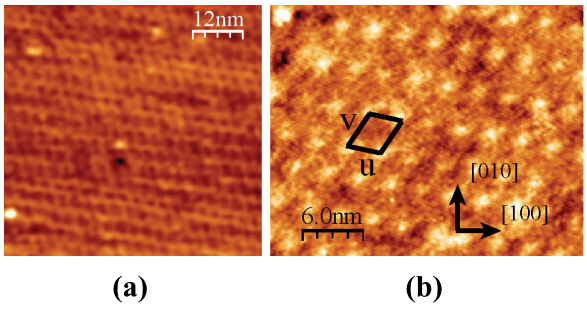

Figure 7: High resolution topographic images of an MLh domain. A = 2 nm. (a) Δf = −35 Hz, (b) Δf = −50 Hz. The unit cell is indicated in (b).

Because of the above-mentioned observation that the dark lines can cross a KBr atomic step without be perturbed, we tentatively interpret these observations as indicating that one row corresponds to a stack of molecules in relatively strong interaction. Note that, as remarked before, the Kelvin map (Figure 8b) is very heterogeneous, with values of the Kelvin voltage varying between −0.5 and +1.2 V. This dispersion is indicative of a certain degree of disorder as is also observable in the topography image of Figure 8a.

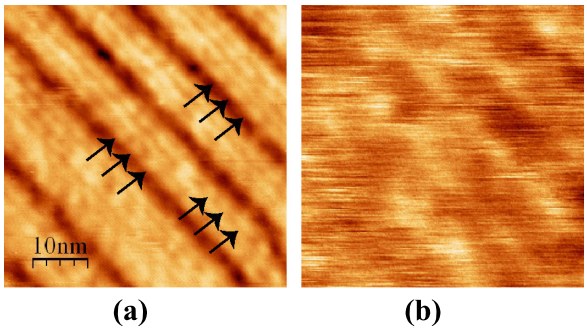

Figure 8: High resolution (a) topographic and (b) Kelvin image of an MLv domain. A = 2 nm, Δf = −20 Hz. The arrows in (a) point to the ~4 nm modulation.

Numerical simulations

To gain insight into the adsorption and dynamic properties of HCPTP on KBr(001), we performed numerical simulations, as described in the Methods section. The calculated lowest-energy adsorbed conformation of HCPTP on KBr(001) is displayed in Figure 9.

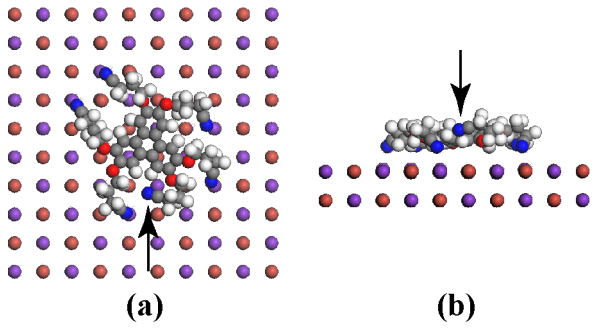

Figure 9: Lowest-energy adsorbed conformation of HCPTP adsorbed on KBr(001). (a) Top and (b) side view. K^+ ions are violet, N atoms are blue. The arrow in (b) points to the CN group that is not bound to a K^+ ion.

The molecule is bound to the surface by the electrostatic interaction between its CN groups and K^+ ions. The flexibility of the propyl chains allows the molecule to reach five K^+ ions. One of the chains cannot bind and its CN group stays at a larger distance from the surface (Figure 9b). The N atoms of the CN groups that bind the molecule are at a mean distance of 0.28 nm while the central aromatic core lies flat at a distance of 0.4 nm from the surface plane. The calculated adsorption energy of 1.8 eV is quite large. It includes not only the contribution of the five CN groups but also the interaction energy of the negatively charged oxygen atoms and the aromatic core with the surface, which can be roughly evaluated by calculating the adsorption energy of hexamethoxytriphenylene on KBr(001) under the same conditions. We obtain 0.8 eV, meaning that each CN group contributes approximately (1.8 − 0.8)/5 = 0.2 eV, in good agreement with the value obtained for the CN groups of the truxene derivative mentioned previously [10].

Molecular dynamics studies of the diffusion of a HCPTP molecule were performed with the same force field in the NVT ensemble with a Nose–Hoover thermostat. Simulations at 300 K show that the molecules diffuse by successive hopping of CN groups from one K^+ to another in a way that is similar to the "walking" of the truxene-derived molecule described recently [10]. To get an order of magnitude for the diffusion coefficient, we observe that the molecule travels approximately 1 nm in a time T = 2.5 ns. Thus, $D = \langle x^2\rangle/(4T) \approx 10^{-10}$ $m^2 \cdot s^{-1}$.

Discussion

Molecular structures

Figure 2 shows that step edges act as preferred adsorption sites for the molecules at low coverage. This is not surprising as the interaction of a CN group is expected to be enhanced due to the availability of adjacent K^+ sites on nonpolar steps, as shown for truxene molecules [11]. The origin of the molecular aggregates observed in Figure 2 and Figure 3 is less clear. As indicated previously a single molecule diffuses at room temperature despite its six CN anchoring groups. A lower estimate of the distance that a molecule would travel on a defect-free surface without interacting with another molecule during the deposition can be obtained in the following way: For a deposition molecular flux F, the mean time τ_F separating the arrival of two successive molecules in an area L^2 is $\tau_F = 1/(F \cdot L^2)$. During this time, a molecule travels a mean distance of $\langle L^2\rangle = 4D\tau_F$. Combining these relations, we get $(\langle L^2\rangle)^{1/2} \approx (4D/F)^{1/4} = 1$ µm (with $F = 3 \cdot 10^{14}$ molecules$\cdot m^{-2} \cdot s^{-1}$, corresponding to one MLh monolayer in 1000 s). This value is a lower estimate since landing in the same area is a necessary, but far from sufficient, condition for two molecules to meet. Considering that the mean distance between defects on KBr(001) is smaller than 1 µm, this estimation shows clearly that the nucleation is heterogeneous, i.e., dominated by the adsorption of the molecules on defects. Another observation, which points in the same direction, is that the aggregates have a height that is larger than the 0.4 nm of the MLh layer, i.e., they are 3-D. This transition to 3-D, which

happens neither for the MLh nor for the MLv, should be favored by a particular adsorption configuration of the molecules adsorbed on the defects responsible for the nucleation of the aggregates.

Note that the density of aggregates observed in Figure 2 and 3 is much higher than the density of defects that are observed on the clean KBr surface before adsorption. Associating each aggregate with one or several defects implies that the molecules are able either to create defects or to combine with preexisting defects, which are mobile at room temperature and consequently undetectable on the images of the clean surface. Investigating precisely the first stages of the growth of this system would answer these questions, but our present data set does not allow conclusions to be drawn. More extensive numerical simulations would also be necessary.

The measurement of a 0.4 nm height for the MLh monolayer and the high-resolution images of Figure 7 are indicative of a structure composed of molecules lying flat on the surface. The observation of the dewetting of this monolayer (Figure 4) shows that the molecules are mobile at the border of the layer. These observations suggest an adsorption geometry close to the calculated conformation in Figure 9. Indeed, considering the high value of the adsorption energy, one does not expect the lateral intermolecular interactions to be strong enough to significantly affect the adsorption conformation of the single molecule.

A tentative model of the MLh layer is shown in Figure 10. The unit cell vectors u and v have been chosen on the basis of the experimental values extracted from Figure 7b. They are given in terms of the conventional surface unit-cell vectors a and b by $u = 4a - b$ and $v = 2.5a + 4.5b$. Their modulus and angle are then given by u (2.7 nm, −14°/[100]) and v (3.4 nm, +61°/[100]) in good agreement with the experiment (Figure 7b). The molecular basis comprises two molecules that have been positioned on the surface in the lowest-energy conformation of Figure 9. Note that the molecules are separated enough to avoid van der Waals contact and should be only weakly interacting with each other, confirming our previous suggestion.

The images of Figure 4 do not show where the molecules of the dewetting MLh layer go. Nevertheless, the fact that the MLh layer was never observed to expand and that no other structures (such as double MLh layers) appeared during this phenomenon strongly suggests that they contribute to the growth of the MLv layer. This conclusion would imply that the MLv structure is more stable than the MLh structure. Considering the structure of the molecule, it is seen that only two CN groups can adsorb on K^+ ions when the molecule is nearly vertical, contributing approximately 0.4 eV to the adsorption energy. The stabilization of MLv relative to MLh should then result from the intermolecular interaction energy, which should exceed 1.8 − 0.4 = 1.4 eV. This is indeed the case. The interaction energy between two free HCPTP, calculated with the COMPASS force field when the triphenylene cores are in a π-stacking configuration, is on the order of 2.5 eV, well above this threshold. MLv is then more stable than MLh and the transition between these two structures is kinetically limited, as the dewetting transition observed in Figure 4 confirms.

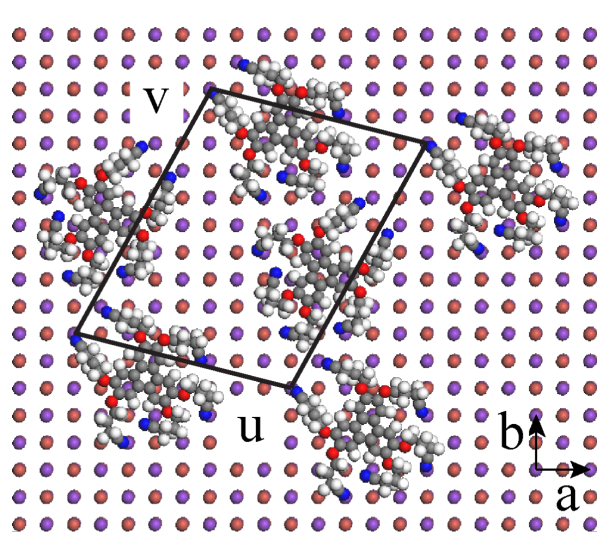

Figure 10: Tentative model of the MLh layer.

Interpretation of the observed Kelvin voltages

In the adsorption configuration shown in Figure 9, the molecule acquires a dipolar moment of 12 debyes pointing along the normal to the KBr surface. It is the interaction of the cyano groups with the K^+ ions that polarizes the molecule. According to the standard interpretation [28-30], such a dipole is expected to induce a negative shift of the Kelvin voltage. Consequently and considering that, as discussed previously, the adsorption conformation of the molecule in the MLh layer should not be significantly different from the single-molecule conformation, we interpret the negative shift of the Kelvin voltage observed on MLh relative to KBr as being due to the adsorption-induced polarization of HCPTP.

The Kelvin contrast on the aggregates is also negatively shifted relative to KBr, indicating that they exhibit either a dipole moment pointing along the KBr surface normal or a positive charge. The contrast on MLv is difficult to interpret without the help of a suitable model. A tentative explanation would be the following: The vertical molecule is adsorbed on two K^+ ions through two CN groups. This geometry leads to a high density of dipoles pointing along the KBr surface normal when the

molecules are stacked in rows. The upper part of the adsorbed molecules, far from this polarized interface, is disorganized, as revealed in particular in the Kelvin maps of this structure, and it is reasonable to assume that due to this randomness it contributes less to the Kelvin voltage. The tip feels dominantly the dipolar layer created by the adsorption of the CN groups on the K^+ ions. Note that a rapid evaluation gives a dipole density for the MLv that is twice that of MLh, but the precise orientation as well as the distance from the tip should be taken into account for a meaningful comparison of the Kelvin voltage on these two structures.

These considerations were aimed at explaining *the sign* of the shifts of the Kelvin voltage between the different structures. We now comment on *the magnitudes* of the Kelvin voltages that we observe. It has been suggested recently that the mean Kelvin voltage monitored on Kelvin maps can be related to the electrostatic nature of the tip (neutral, polar or charged) [31]. We observed occasionally abrupt variations of the Kelvin voltage (~100 mV), which signal evolutions of the tip structure, but these events were never accompanied by a significant change in the Kelvin contrast as reported in [31]. We conclude that our tips always had the same electrostatic behavior. We also measured slow drifts in the mean Kelvin voltage on a scale of a few volts around 0 V over a time scale of hours. For the three tips we used in these experiments (two Si uncoated tips and a Pt-coated tip) the Kelvin voltage difference between KBr and MLh/MLv was approximately constant at 1.4 ± 0.2 V. These relatively high values are in contrast to the values reported for studies of adsorbates on metals [20,21]. On these systems, the electric potential is fixed at the surface of the metal, at a microscopic distance from the tip. The situation is radically different on thick insulators, in which case the potential is imposed on the metallic plate that supports the sample, which is some millimeters away. Then, the potential drops in the insulator in a way that depends not only on the dielectric constant of the material and the tip–surface distance, but also on the tip radius. The effective potential applied to the surface structures is then largely smaller than the applied bias. This effect, which explains the high values we observe, renders a quantitative analysis of the Kelvin voltage more difficult on bulk insulators than on conducting substrates.

Conclusion

We have demonstrated that HCPTP forms two types of monolayer on KBr(001): MLh where the molecules are lying flat on the substrate and MLv where they stand upright. High-contrast, well-resolved Kelvin maps were obtained simultaneously with the topographic NC-AFM images. The precise structure of these two monolayers could not be determined from the images. But the measurement of their height on the electrostatic force-compensated topographic images, completed by numerical calculations of the adsorption conformation of the molecule leads to a consistent interpretation of the Kelvin maps in terms of adsorption-induced polarization of the molecule by the electrostatic interaction of the cyano groups with K^+ ions.

HCPTP was designed with its six CN groups to limit the diffusion of the molecule on the KBr(001) surface. What the present study demonstrates is that maximizing the adsorption energy does not necessarily imply a low diffusion coefficient. There is in fact no simple relation between adsorption and diffusion energy, especially for large molecules with numerous degrees of freedom [32]. Moreover, a high adsorption energy is likely to induce surface restructuring, as observed in the present case. While such processes could be useful to modify the surface at will, this is not always desirable. Clearly, more elaborate strategies are needed to progress toward our objective of immobilizing a molecule on a bulk insulating substrate at room temperature.

Methods

Experimental

Experiments were conducted in a commercial room-temperature (RT) ultrahigh vacuum STM/AFM (Omicron NanoTechnology GmbH, Taunusstein, Germany). The original optical beam-deflection system was improved by replacing the LED by a superluminescent laser diode (Superlum, Moscow, Russia) coupled to the system by an optical fiber. The control electronics were from Nanonis (SPECS, Zurich, Switzerland). The KBr crystal (~3 mm thick) was cleaved in air, quickly transferred to the UHV system and finally heated at 480 K for 1 h to remove the charges produced during the cleavage process. This preparation method produces an atomically well-ordered surface with (001) terraces separated by atomic steps, mainly oriented along the nonpolar <100> crystallographic directions of the surface. We characterized this surface by KPFM and found that charges are always present on the step edges, as reported in [25]. In contrast, only a few charged defects (less than 10 per μm^2) were observed on the terraces. Molecules were deposited from a heated boron nitride disk on which a few drops of the molecular solution were left to dry. QNCHR silicon cantilevers provided by NanoSensors (Neuchatel, Switzerland) were used, with no special preparation except a moderate heating (150 °C) in vacuum. The resonance frequencies were close to 290 kHz, with quality factors ranging from 40,000 to 45,000. An experiment was also performed with a Pt-coated tip (PtNCH), but the resolution obtained (in topography as well as in the Kelvin maps) was not satisfying. KPFM coupled to NC-AFM exists in two flavors [17], namely the frequency- and amplitude-modulation modes. In this work, we use the frequency-modulation mode. The voltage was modu-

lated at 1 kHz with an amplitude of 2 V. The images were obtained in the constant Δf mode with an oscillation amplitude of A = 2 nm and small values of Δf, corresponding to normalized frequency shifts [33] $\gamma = kA^{3/2}\Delta f/f_0 = 0.25$ fN·m$^{1/2}$ at most ($k \sim 40$ N·m^{-1}). Under these conditions the interaction of the tip with the surface is quite small and it is expected that only van der Waals and electrostatic forces contribute to the image. Note that at the Kelvin voltage, provided that no net surface charges are present, the topographic image becomes a pure van der Waals image. The measured height of the observed structures is then close to that given by the molecular models, facilitating the structural identification. Great care was taken to avoid any cross-talk between the different signal channels available in NC-AFM. Constant Δf images were recorded simultaneously with maps of the Kelvin voltage, the frequency shift, the amplitude and the excitation voltage. For all the images presented in this paper, the excitation voltage map was uniform, at a value close to its value in the absence of tip–surface interaction. The <100> nonpolar directions of the KBr(001) surface are oriented in the horizontal and vertical directions.

Molecular synthesis

2,3,6,7,10,11-Hexa(cyanopropyloxy)triphenylene (HCPTP) was prepared in 73% yield by reaction of 2,3,6,7,10,11-hexahydroxytriphenylene (HHTP) with 4-bromobutyronitrile in dry DMF in the presence of potassium carbonate. HHTP was obtained from 2,3,6,7,10,11-hexamethoxytriphenylene according to [34]. To a suspension of 4-bromobutyronitrile (636 mg, ca. 0.43 mL, 4.3 mmol) and dry potassium carbonate (3.2 g, 23.2 mmol) in dry DMF under argon was added HHTP (200 mg, 0.62 mmol). The mixture was then stirred under argon at RT for 55 h and then poured into water (150 mL) under stirring. Neutralization by H_2SO_4 (5 M) gave a beige precipitate, which was filtered and dried under vacuum. Recrystallization from ethyl acetate (300 mL) or by column chromatography (SiO_2, DCM–AcOEt, 8:2) and drying under vacuum at 40 °C for 7h gave HCPTP (319 mg, yield: 71%). R_f = 0.5 (TLC, DCM–AcOEt, 7:3); ^{1}H NMR (CD_2Cl_2, 300 MHz) δ 7.90 (s, 6H, arom), 4.36 (t, J = 5.7 Hz, 12H, CH_2O), 2.71 (t, J = 7 Hz, 12H, CH_2CN), 2.27 (m, 12H, NCCH$_2CH_2$) ppm; ^{13}C NMR (CD_2Cl_2, 75 MHz) δ 149.1, 124.4, 108.1, 67.8, 26.2, 14.9 ppm; MS m/z (DCI, NH_3): 728 $[M + H]^+$; Anal. calcd for $C_{42}H_{42}N_6O_6$: C, 69.4; H, 5.8; found: C, 69.2; H, 6.1.

Numerical simulation

The geometry of the molecule adsorbed on KBr(001) was optimized by using Materials Studio [35] with the COMPASS force field [36]. This force field is well adapted to the system that we consider here, because it has been parameterized by using condensed-phase properties in addition to ab initio and empirical data for isolated molecules [37,38]. It is well known from previous studies that the adsorption of organic molecules on this type of surface is dominated by van der Waals and electrostatic interactions, and that the charge transfer between the substrate and the molecule is negligible [39]. The KBr slab was composed of 6 × 6 × 3 unit cells. Two KBr layers were free to relax during the simulations.

Acknowledgements

We thank A. Shluger and C. Barth for useful discussions. This work was supported by the French National Agency (ANR) in the frame of its program in Nanosciences and Nanotechnologies (Nanosens project no. ANR-08-NANO-017) and by the European Commission within the project ARTIST (Contract no. 243421). The images of this article were processed with the WSxM software [40].

References

1. Pfeiffer, O.; Gnecco, E.; Zimmerli, L.; Maier, S.; Meyer, E.; Nony, L.; Bennewitz, R.; Diederich, F.; Fang, H.; Bonifazi, D. *J. Phys.: Conf. Ser.* **2005,** *19,* 166–174. doi:10.1088/1742-6596/19/1/027
2. Kunstmann, T.; Schlarb, A.; Fendrich, M.; Wagner, T.; Möller, R.; Hoffmann, R. *Phys. Rev. B* **2005,** *71,* 121403. doi:10.1103/PhysRevB.71.121403
3. Mativetsky, J. M.; Burke, S. A.; Fostner, S.; Grütter, P. *Small* **2007,** *3,* 818–821. doi:10.1002/smll.200600699
4. Burke, S. A.; Ji, W.; Mativetsky, J. M.; Topple, J. M.; Fostner, S.; Gao, H.-J.; Guo, H.; Grütter, P. *Phys. Rev. Lett.* **2008,** *100,* 186104. doi:10.1103/PhysRevLett.100.186104
5. Dienel, T.; Loppacher, C.; Mannsfeld, S. C. B.; Forker, R.; Fritz, T. *Adv. Mater.* **2008,** *20,* 959–963. doi:10.1002/adma.200701684
6. Burke, S. A.; LeDue, J. M.; Miyahara, Y.; Ji, W.; Topple, J. M.; Fostner, S.; Grütter, P. *Nanotechnology* **2009,** *20,* 264012. doi:10.1088/0957-4484/20/26/264012
7. Schütte, J.; Bechstein, R.; Rohlfing, M.; Reichling, M.; Kühnle, A. *Phys. Rev. B* **2009,** *80,* 205421. doi:10.1103/PhysRevB.80.205421
8. Glatzel, T.; Zimmerli, L.; Koch, S.; Kawai, S.; Meyer, E. *Appl. Phys. Lett.* **2009,** *94,* 063303. doi:10.1063/1.3080614
9. Pawlak, R.; Nony, L.; Bocquet, F.; Oison, V.; Sassi, M.; Debierre, J.-M.; Loppacher, C.; Porte, L. *J. Phys. Chem. C* **2010,** *114,* 9290–9295. doi:10.1021/jp102044u
10. Such, B.; Trevethan, T.; Glatzel, T.; Kawai, S.; Zimmerli, L.; Meyer, E.; Shluger, A. L.; Amijs, C. H. M.; de Mendoza, P.; Echavarren, A. M. *ACS Nano* **2010,** *4,* 3429–3439. doi:10.1021/nn100424g
11. Trevethan, T.; Such, B.; Glatzel, T.; Kawai, S.; Shluger, A. L.; Meyer, E.; de Mendoza, P.; Echavarren, A. M. *Small* **2011,** *7,* 1264–1270. doi:10.1002/smll.201001910
12. Hinaut, A.; Lekhal, K.; Aivazian, G.; Bataillé, S.; Gourdon, A.; Martrou, D.; Gauthier, S. *J. Phys. Chem. C* **2011,** *115,* 13338–13342. doi:10.1021/jp202873f
13. Kittelmann, M.; Rahe, P.; Nimmrich, M.; Hauke, C. M.; Gourdon, A.; Kühnle, A. *ACS Nano* **2011,** *5,* 8420–8425. doi:10.1021/nn2033192
14. Gross, L.; Mohn, F.; Moll, N.; Liljeroth, P.; Meyer, G. *Science (Washington, DC, U. S.)* **2009,** *325,* 1110–1114. doi:10.1126/science.1176210
15. Guillermet, O.; Gauthier, S.; Joachim, C.; de Mendoza, P.; Lauterbach, T.; Echavarren, A. *Chem. Phys. Lett.* **2011,** *511,* 482–485. doi:10.1016/j.cplett.2011.06.079

16. Kitamura, S.; Iwatsuki, M. *Appl. Phys. Lett.* **1998,** *72,* 3154–3156. doi:10.1063/1.121577
17. Glatzel, T.; Sadewasser, S.; Lux-Steiner, M. C. *Appl. Surf. Sci.* **2003,** *210,* 84–89. doi:10.1016/S0169-4332(02)01484-8
18. Zerweck, U.; Loppacher, C.; Otto, T.; Grafström, S.; Eng, L. M. *Phys. Rev. B* **2005,** *71,* 125424. doi:10.1103/PhysRevB.71.125424
19. Barth, C.; Foster, A. S.; Henry, C. R.; Shluger, A. L. *Adv. Mater.* **2011,** *23,* 477–501. doi:10.1002/adma.201002270
20. Zerweck, U.; Loppacher, C.; Otto, T.; Grafström, S.; Eng, L. M. *Nanotechnology* **2007,** *18,* 084006. doi:10.1088/0957-4484/18/8/084006
21. Nikiforov, M. P.; Zerweck, U.; Milde, P.; Loppacher, C.; Park, T.-H.; Uyeda, H. T.; Therien, M. J.; Eng, L.; Bonnell, D. *Nano Lett.* **2008,** *8,* 110–113. doi:10.1021/nl072175d
22. Zerweck, U.; Loppacher, C.; Eng, L. M. *Nanotechnology* **2006,** *17,* S107. doi:10.1088/0957-4484/17/7/S02
23. Léoni, T.; Guillermet, O.; Walch, H.; Langlais, V.; Scheuermann, A.; Bonvoisin, J.; Gauthier, S. *Phys. Rev. Lett.* **2011,** *106,* 216103. doi:10.1103/PhysRevLett.106.216103
24. Barth, C.; Henry, C. R. *Nanotechnology* **2006,** *17,* S155. doi:10.1088/0957-4484/17/7/S09
25. Barth, C.; Henry, C. R. *Phys. Rev. Lett.* **2007,** *98,* 136804. doi:10.1103/PhysRevLett.98.136804
26. Egberts, P.; Filleter, T.; Bennewitz, R. *Nanotechnology* **2009,** *20,* 264005. doi:10.1088/0957-4484/20/26/264005
27. Sadewasser, S.; Lux-Steiner, M. C. *Phys. Rev. Lett.* **2003,** *91,* 266101. doi:10.1103/PhysRevLett.91.266101
28. Terris, B. D.; Stern, J. E.; Rugar, D.; Mamin, H. J. *Phys. Rev. Lett.* **1989,** *63,* 2669–2672. doi:10.1103/PhysRevLett.63.2669
29. Stomp, R.; Miyahara, Y.; Schaer, S.; Sun, Q.; Guo, H.; Grütter, P.; Studenikin, S.; Poole, P.; Sachrajda, A. *Phys. Rev. Lett.* **2005,** *94,* 056802. doi:10.1103/PhysRevLett.94.056802
30. Azuma, Y.; Kanehara, M.; Teranishi, T.; Majima, Y. *Phys. Rev. Lett.* **2006,** *96,* 016108. doi:10.1103/PhysRevLett.96.016108
31. Barth, C.; Hynninen, T.; Bieletzki, M.; Henry, C. R.; Foster, A. S.; Esch, F.; Heiz, U. *New J. Phys.* **2010,** *12,* 093024. doi:10.1088/1367-2630/12/9/093024
32. Watkins, M.; Trevethan, T.; Sushko, M. L.; Shluger, A. L. *J. Phys. Chem. C* **2008,** *112,* 4226–4231. doi:10.1021/jp077680d
33. Giessibl, F. J. *Phys. Rev. B* **1997,** *56,* 16010. doi:10.1103/PhysRevB.56.16010
34. Krebs, F. C.; Schiødt, N. C.; Batsberg, W.; Bechgaard, K. *Synthesis* **1997,** *11,* 1285–1290. doi:10.1055/s-1997-3188
35. *Materials Studio,* v5.5.0.0; Accelrys Software, Inc.: San Diego, CA, USA, 2010.
36. COMPASS – Accelrys. http://accelrys.com/products/datasheets/compass.pdf (accessed Feb 3, 2012).
37. Sun, H. *J. Phys. Chem. B* **1998,** *102,* 7338–7364. doi:10.1021/jp980939v
38. Zhao, L.; Liu, L.; Sun, H. *J. Phys. Chem. C* **2007,** *111,* 10610–10617. doi:10.1021/jp071775y
39. Trevethan, T.; Shluger, A. L. *J. Phys. Chem. C* **2007,** *111,* 15375–15381. doi:10.1021/jp072857p
40. Horcas, I.; Fernández, R.; Gómez-Rodríguez, J. M.; Colchero, J.; Gómez-Herrero, J.; Baro, A. M. *Rev. Sci. Instrum.* **2007,** *78,* 013705. doi:10.1063/1.2432410

License and Terms

Beilstein Journal of Nanotechnology

Modeling noncontact atomic force microscopy resolution on corrugated surfaces

Kristen M. Burson[1,2], Mahito Yamamoto[1,2] and William G. Cullen[*1,2]

Full Research Paper

Open Access

Address:
[1]Materials Research Science and Engineering Center, Department of Physics, University of Maryland, College Park, Maryland 20742-4111, USA and [2]Center for Nanophysics and Advanced Materials, Department of Physics, University of Maryland, USA

Email:
William G. Cullen[*] - wcullen@physics.umd.edu

* Corresponding author

Keywords:
graphene; model; noncontact atomic force microscopy; SiO_2; van der Waals

Beilstein J. Nanotechnol. **2012,** *3,* 230–237.
doi:10.3762/bjnano.3.26

Received: 29 November 2011
Accepted: 16 February 2012
Published: 13 March 2012

This article is part of the Thematic Series "Noncontact atomic force microscopy".

Guest Editor: U. D. Schwarz

Abstract

Key developments in NC-AFM have generally involved atomically flat crystalline surfaces. However, many surfaces of technological interest are not atomically flat. We discuss the experimental difficulties in obtaining high-resolution images of rough surfaces, with amorphous SiO_2 as a specific case. We develop a quasi-1-D minimal model for noncontact atomic force microscopy, based on van der Waals interactions between a spherical tip and the surface, explicitly accounting for the corrugated substrate (modeled as a sinusoid). The model results show an attenuation of the topographic contours by ~30% for tip distances within 5 Å of the surface. Results also indicate a deviation from the Hamaker force law for a sphere interacting with a flat surface.

Introduction

Noncontact atomic force microscopy (NC-AFM) has brought considerable advancement to the atomic-scale study of surfaces, by allowing both atomic-resolution imaging and atomically resolved force spectroscopy. Generally, these advancements have been made on atomically flat crystalline surfaces. Yet, many surfaces of technological interest are neither crystalline nor atomically flat and this presents a challenge for the assessment of measurement resolution and the ultimate determination of the structures of interest. Problems of friction and adhesion serve as examples in which roughness is a determining factor, and a full understanding of the microscopic interactions requires adequately resolved measurements [1,2].

SiO_2 grown as a gate dielectric on Si wafers, for example, is amorphous and exhibits stochastic surface roughness. Precise measurement of this roughness by AFM has generated controversy following the widespread use of SiO_2 as a support for exfoliated graphene, which may be probed with UHV scanning tunneling microscopy (yielding full atomic resolution, as demonstrated by several groups) [3-7]. The controversy arises

when STM measurements of graphene/SiO_2 are compared with AFM measurements of the bare SiO_2 substrate, because AFM measurements of SiO_2 generally show a much smoother topography than is shown by STM of graphene/SiO_2. Motivated by the experimental difficulty in measuring SiO_2 surfaces, we propose a model to gain insight into this issue.

Here we present experimental findings on SiO_2 that have motivated the modeling of tip–surface interactions for the case of a corrugated surface. We discuss the issues that arise when the surface is corrugated on relatively small length scales (our best measurements on SiO_2 yield a correlation length of 8–10 nm). We develop a continuum model that explicitly accounts for a quasi-1-D substrate corrugation (modeled as a sinusoid) and obtain the response of a spherical tip to van der Waals (vdW) interactions. To our knowledge, it is the first model to directly incorporate the lateral variation of van der Waals forces due to surface corrugation and to attempt to quantify this in terms of contours of constant frequency shift. We discuss the first results of this model, specifically showing attenuation of the substrate corrugation in imaging. We also report a deviation from the generally assumed Hamaker force law for the interaction of a sphere with a flat surface ($F \sim A_H R/6z^2$).

SiO_2 resolution controversy

Graphene was brought to prominence by the pioneering work of Geim and Novoselov in developing a fabrication technique for graphene devices involving optical identification of exfoliated flakes on 300 nm thick SiO_2/Si [8]. As a result, much of the early scanning probe investigations were performed on SiO_2 and questions about the relationship between graphene device properties and substrate properties, including topography, remain prominent in the field of graphene research. The first investigations of SiO_2-supported graphene by means of scanning-probe methods appeared in 2007 [5,6]. These early investigations attributed the roughness of the graphene to the roughness of the underlying SiO_2. Previously, measurements of suspended graphene by TEM in diffraction mode suggested an "intrinsic" rippling in the graphene structure [9], which presumably originates from the same physics that describes the crumpling of soft membranes [10]. More recently, a study comparing scanning-probe measurements of the corrugation of single-layer graphene (by UHV STM) with that of SiO_2 (by ambient AFM) reported a significantly greater corrugation for the graphene than that observed for the SiO_2 [4]. These measurements were interpreted as an "intrinsic" rippling of the partially suspended graphene, presumably of the same origin as that observed by TEM for fully suspended graphene [9]. However, any significant "suspension" and intrinsic rippling of the graphene over SiO_2 is hard to reconcile with the energetics of substrate adhesion [11-13].

Our previous work [14] addressed the issue of intrinsic rippling in SiO_2-supported graphene by presenting high-resolution UHV NC-AFM measurements of the SiO_2, in which it was shown that there were more small-scale features present on the SiO_2 than previously measured. The corrugation of bare SiO_2 was shown to be slightly greater than the corrugation of the graphene over all relevant length scales and, thus, the graphene conforms to the substrate, consistent with the energetics of bending and adhesion. This study helped to resolve questions about the relationship between the substrate and the graphene topography for SiO_2. Specifically, the higher-resolution measurement of the substrate roughness allowed a quantitative analysis based on theories of membrane adhesion. It also brought to the fore the experimental difficulty of obtaining high-resolution AFM images on corrugated surfaces, given that many previous measurements of SiO_2 appear to be under-resolved. It is likely that further high-resolution SPM studies will provide breakthroughs in problems that are currently poorly understood, such as the unusually high adhesion energy of graphene to SiO_2 [15], and its anomalous frictional behavior [16]. Beyond graphene, the use of SiO_2 is commonplace as a substrate in electronic-device research (carbon-nanotube devices, organic electronics, etc.).

While one may readily obtain atomic resolution on certain flat surfaces, such as the well-studied (7 × 7) reconstruction of Si(111), obtaining this same level of resolution on rough surfaces presents an experimental challenge. Under suitable conditions, atomic resolution of amorphous surfaces has been achieved. For atomically resolved images of barium silicate glass, UHV contact-mode AFM with a relatively high loading force (25–50 nN) was utilized [17]. Quartz glass has also been measured with comparable resolution, leading to real-space images of the amorphous atomic structure [18]. Despite the atomic resolution obtained for quartz in [18], those measurements fail to account for the observed topography of SiO_2-supported graphene, due to apparent differences in surface structure between the carefully UHV-prepared quartz in that study and the SiO_2 substrates used for graphene. As with the barium silicate measurements, for high-resolution measurements of SiO_2, special conditions were necessary [18]. In order to obtain the high-resolution measurements of the SiO_2 presented in this paper, a supersharp tip, with a nominal radius of curvature of 2–5 nm, was crucial. Comparing the images obtained with these supersharp tips to those obtained with a metal-coated tip of nominal radius 30 nm, demonstrates the distinct improvement in resolution (Figure 1a and Figure 1b). Features with radius of curvature as small as 2.3 nm were observed in images with the supersharp tip (Figure 1a) [19]. Yet, under comparable experimental conditions, the (7 × 7) structure of Si(111) could be discerned with atomic resolution

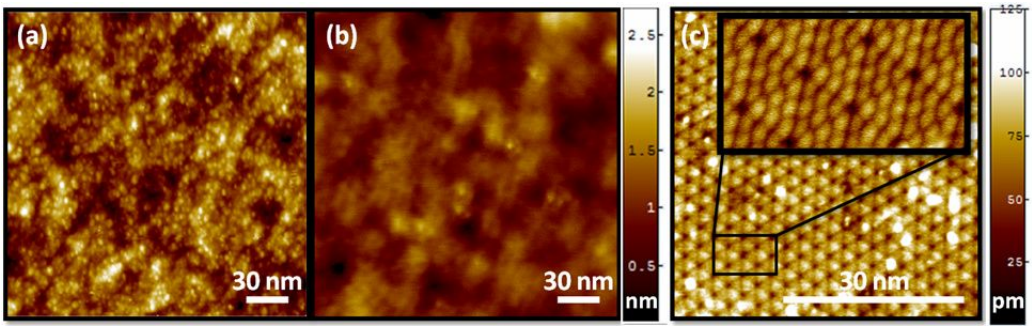

Figure 1: AFM resolution examples: (a) high resolution UHV NC-AFM image of SiO_2 displaying features with radius of curvature ~2.3 nm (R_{tip} nominally 2 nm, Δf = −20 Hz, A = 5.0 nm, image size = 200 nm × 200 nm) (b) under-resolved UHV NC-AFM image of SiO_2 with the same height scale as (a) (R_{tip} nominally 30 nm, Δf = −150 Hz, A = 1.0 nm, image size 200 nm × 200 nm) (c) UHV NC-AFM image of Si(111) with inset showing atomic resolution (R_{tip} nominally 7 nm, Δf = −40 Hz, A = 7.1 nm, image size 50 nm × 50 nm).

without the aid of a supersharp tip (Figure 1c). Atomic resolution on Si(111) depends on the short-range chemical forces and the bonding configuration of the tip apex atom [20-23], whereas long-range vdW interactions are a constant background force for AFM imaging of this and other flat surfaces. In contrast, for corrugated surfaces, the vdW interactions will vary laterally and thus play a greater role in determining the contour followed by the probe tip. These experimental observations highlight the difficulty in obtaining adequately resolved NC-AFM measurements on rough, amorphous surfaces and challenge the assumption that, for a given tip radius, the resolution on a rough surface will be comparable to the resolution on a flat surface. While it is the controversy over the resolution of the SiO_2 substrate that motivates our modeling of AFM resolution for corrugated surfaces, the vdW interaction model itself is more generally applicable to other corrugated surfaces.

Model of the corrugated-surface resolution

Here we briefly outline the analytic development of the model. Ultimately we wish to find the dependencies of the potential, force, frequency shift, etc., for the case of a spherical tip and a quasi-one-dimensional corrugated surface. The following sections develop the calculation on the assumption that interactions are pairwise additive, beginning with a Lennard-Jones interaction between two atoms [24]. The formalism here closely follows that of [11], in which a detailed analytical theory was developed to model the adhesion of graphene to a sinusoidally corrugated substrate.

This section is presented as follows:

1. Development of the basic formalism for carrying out numerical integration of a Lennard-Jones potential, for a "point atom" interacting with a semi-infinite substrate. By obtaining this "point atom" potential, one can then integrate over the tip volume to obtain the tip–surface potential. We first obtain results for a flat surface with boundary at $z = 0$, initially for the "point atom" and then for a spherical tip body. This allows a check of the numerical integration scheme by comparison with analytical results.
2. We then apply the method to a corrugated surface. As an intermediate result, we discuss the tip–surface potential and its z dependence since we find a different scaling from the sphere–plane result generally assumed.
3. Finally, to simulate NC-AFM imaging, we compute frequency shifts for the spherical-tip/corrugated-surface system.

We begin with the Lennard-Jones potential written as

$$w_{LJ}(r) = -\frac{C_1}{r^6} + \frac{C_2}{r^{12}}, \qquad (1)$$

which represents the interaction between a pair of atoms separated by a distance r. Following the Hamaker procedure, we assume that the total interaction energy (atom–surface or tip–surface) is obtained pairwise by integration of this potential.

1 Atom–surface potential

We first consider a "point atom" interacting with a flat, semi-infinite substrate with density ρ_S (number/volume). The integration may be written as

$$w_{a-s}(z) = \int_{-\infty}^{\infty} dx_s' \int_{-\infty}^{0} dz_s' \int_{-\infty}^{\infty} dy_s' w_{LJ}(r)\rho_s \,. \qquad (2)$$

As shown in [25], this has an analytic solution. For a general potential described by

$$w(r) = -\frac{C}{r^n}, \tag{3}$$

the substrate-integrated potential is

$$w_{a-s}(z) = -\frac{2\pi C\rho_s}{(n-2)(n-3)z^{n-3}}, \tag{4}$$

and this is valid for $n > 3$. Here z represents the distance from the "point atom" to the substrate surface. We use subsript "a–s" to denote that this is a potential for an "atom" interacting with the semi-infinite substrate.

For $n = 6$ (the usual attractive vdW form) this reduces to

$$w_{a-s}(z) = -\frac{\pi C\rho_s}{6z^3}. \tag{5}$$

Combining the attractive r^{-6} term and repulsive r^{-12} term, the result may be expressed as

$$w_{a-s}(z) = w_0\left[-\frac{3}{2}\left(\frac{h_0}{z}\right)^3 + \frac{1}{2}\left(\frac{h_0}{z}\right)^9\right] \tag{6}$$

with

$$w_0 = \frac{\pi C_1\rho_s}{9h_0^3}. \tag{7}$$

By inspection, it is apparent that Equation 6 represents a potential with depth w_0 at distance h_0 from the surface. Additionally, one sees that choosing (w_0, h_0) is equivalent to choosing (C_1, ρ_s), according to Equation 7. Thus, in our numerical implementation we choose values for w_0 and h_0. As a first check on our substrate by numerical integration, we compare the numerical integration of Equation 2 with the analytical result in Equation 6. In this case the interaction is parameterized as w_0 = 1.0 aJ and h_0 = 0.3 nm. The agreement is excellent, as shown in Figure 2.

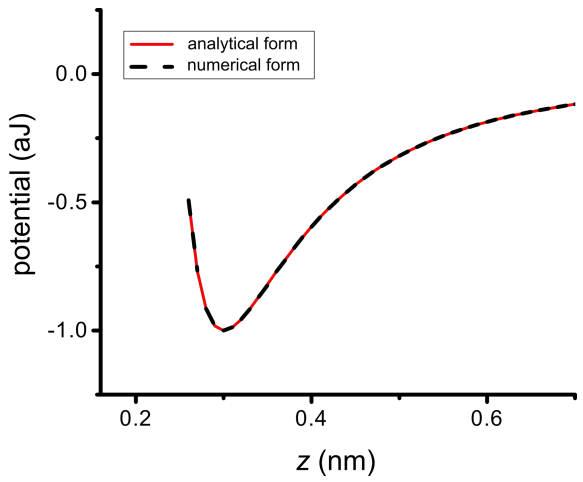

Figure 2: Verification of atom–substrate potential: Potential w_{a-s} versus z for numerical and analytical schemes for a "point atom" interacting with a flat surface. The near-perfect overlap of the curves demonstrates the fidelity of the numerical integration scheme.

2 Tip–surface potential

Once the atom–surface potential is obtained, the tip–surface potential is obtained in an analogous manner. It is computed as

$$W_{t-s}(z) = \int_{V_t} w_{a-s}(z_t)\rho_t dV_t, \tag{8}$$

where the uppercase W designates a potential between two extended objects. Here, ρ_t is the tip density (number/volume) and the integration is over the (spherical) tip volume. The z coordinate for $W_{t-s}(z)$ is the distance between the surface and the apex of the spherical tip (the point closest to surface), as depicted in Figure 3. Employing the NIntegrate function in Mathematica 8.0, the numerical integration of Equation 2 generates the atom–surface potential as a tabulated function of z, with scaling determined by (w_0, h_0). We then numerically integrate this tabulated function over the spherical tip volume, for varying tip–surface distance z, using an approach that incorporates the IDL routines INTERPOLATE and INT_3D. As a check on this numerical integration, we compare against the exact analytical result for a sphere attracted to a flat surface by

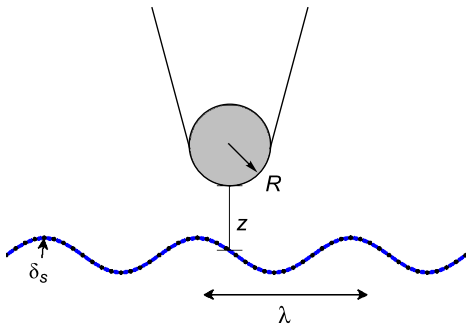

Figure 3: Schematic illustrating the model geometry: The surface is sinusoidally corrugated along the x direction only, with wavelength λ and amplitude δ_s. The surface corrugation is independent of y (quasi-1-D geometry). The tip is modeled as a sphere of radius R.

van der Waals forces. It is well-known that the sphere–plane Hamaker integration has the approximate solution [25]:

$$W_{t-s}(z) \approx -\frac{A_H R}{6z}, \quad (9)$$

in the limit $z << R$, where A_H is the Hamaker constant for the tip–surface material system, given by $A_H = C_1 \cdot \pi^2 \cdot \rho_s \cdot \rho_t$. Equation 9 is sometimes used for fitting the vdW background in NC-AFM experiments [26,27]. However, for the tip radii modeled here, the limiting approximation is not accurate enough to serve as a test for the tip integration scheme, and we use the following exact analytical expression:

$$W_{t-s}(z) = -\frac{A_H}{6}\frac{\{2R(z+R)+z(z+2R)[\ln z - \ln(z+2R)]\}}{z(z+2R)}, \quad (10)$$

In Figure 4, we plot $-W_{t-s}$ versus z to show that the numerical integration over the tip volume accurately reproduces the exact formula. Additionally, we plot the function z^{-1} to indicate the small-z limiting behavior. In all numerical calculations the full Lennard-Jones potential of Equation 6, including both the attractive and the repulsive terms, is utilized. While the analytical expression in Equation 10 is limited to the attractive interaction, the agreement in Figure 4 is excellent.

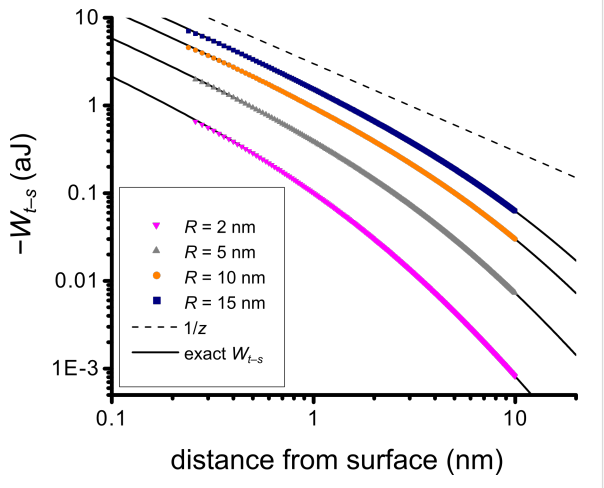

Figure 4: Hamaker force for flat surfaces: Relationship between tip potential and distance from the surface. Here the distance is taken relative to the surface position (distance from surface = $z(x) - z_s(x)$). The dashed line is a reference for the $1/z$ dependence expected from the Hamaker force law for the interaction between a flat surface and a sphere. The numerical results show excellent agreement with the exact potential (Equation 10).

Following these consistency checks on the numerical integrations with a flat substrate surface as a reference, we now extend the calculation to a corrugated surface. The treatment follows that of [11]; in analogy with Equation 2 the atom–substrate potential is written as

$$w_{a-s}(x,z) = \int_{-\infty}^{\infty} dx'_s \int_{-\infty}^{z_s(x)} dz'_s \int_{-\infty}^{\infty} dy'_s w_{LJ}(r)\rho_s, \quad (11)$$

with the essential difference being the upper integration limit on z. The upper integration limit in z is now the (sinusoidal) surface profile $z_s(x)$, given by $z_s(x) = \delta_s \cdot \sin(2\pi x/\lambda)$. Note that w_{a-s} is necessarily a function of x and z. The tip–surface potential is obtained in analogy with the calculation for the flat surface (Equation 8), and is also a function of x and z.

All computations are carried out with $\lambda = 10$ nm, $\delta_s = 0.5$ nm, $w_0 = 0.169$ aJ, and $h_0 = 0.3$ nm. The particular choice of amplitude and wavelength is based on our best measurements of SiO_2, which gave rms roughness ~0.38 nm and correlation length ~10 nm. The 10 nm period is divided into 16 intervals at which points the potential is calculated (shown as black dots on the sinusoidal surface in Figure 3). In the z direction, the grid is much finer, namely 0 to 40 nm in increments of 0.01 nm. The 40 nm range is necessary to incorporate realistic tip diameters, and to allow proper integration over the oscillation amplitude, as discussed below. Our scheme is motivated by simplicity; however, an adaptive grid scheme would be desirable to deal with the rapidly varying behavior of w_{a-s} near the surface and very smooth asymptotic behavior several nm from the surface.

The computation of the atom–surface potential $w_{a-s}(x,z)$ for the corrugated surface requires some careful discussion. In [11], analytical formulas were derived for the integration given in Equation 2. However, the formulae developed there ultimately make the approximation that $z >> \delta_s$, and consequently they do not work well at relatively small z (anomalies begin to appear even >1 nm from the surface contour). This is why a final numerical integration was adopted in our work to obtain $w_{a-s}(x,z)$. There appear to be inherent numerical difficulties in computing the integral for a sinusoidal surface, and we are currently limited in the closest distance to the surface for which we can compute w_{a-s}. For example, in the case of the flat substrate, our numerical integration routine allows computation of w_{a-s} to within 0.19 nm of the surface. In that case, the potential is in the highly repulsive regime with a value of about $+24.60 w_0$, where w_0 is the depth of the potential well at the minimum. The equivalent calculation for a corrugated surface with $\delta_s = 0.5$ nm and $\lambda = 10$ nm is generally limited to ~0.26 nm throughout most of the corrugation period (the potential cannot be computed closer than 0.26 nm to the surface). The limits on w_{a-s} carry over directly into limits on W_{t-s}, as we only integrate the tip potential where the integrand is defined. Thus within our continuum model with a perfectly rigid tip and substrate, we

cannot generally take the tip into the regime in which the *overall* interaction is repulsive. This is rather unsatisfactory at present, as it would be preferable to have well-defined numerical values (even if unrealistically large), and then let the limits of the model be decided on physical grounds, i.e., peak force or stress on the tip apex, etc.

3 Calculation of frequency shifts

Once the tip–surface interaction potential W_{t-s} is obtained, the interaction force F_{t-s} is found straightforwardly by differentiation with respect to z. We then compute the frequency shift using the following expression [28], which is exact to 1st order in classical perturbation theory:

$$\Delta f(x,z) = \frac{f_0^2}{kA}\int_0^{1/f_0} F_{t-s}[z + A\cos(\omega_0 t)]\cos(\omega_0 t)\mathrm{d}t \quad (12)$$

with spring constant k = 40 N/m and resonant frequency f_0 = 300 kHz. We then convert to the normalized frequency shift γ, which is defined as [20]

$$\gamma = \frac{kA^{3/2}}{f_0}\Delta f. \quad (13)$$

Results and Discussion

Using the model, we arrive at several key results. First, we find that the generally assumed Hamaker force law for the interaction between a spherical tip and a flat surface does not hold in the case of corrugated surfaces. Second, we find that the imaged structure is attenuated with respect to the surface geometry, even for small distances between the tip and the sample.

Deviation from the sphere–plane Hamaker force law

In the previous section, we discussed the Hamaker integration for a sphere interacting with a flat surface through van der Waals forces. The integration can be carried out without approximation to yield the exact formula; this exact formula is cumbersome and given by Equation 10. In the limit $z \ll R$, this formula simplifies greatly to $W_{t-s} \approx -A_H R/6z$, which is often used in describing tip–sample vdW forces. Applying the formalism developed for a sinusoidally corrugated surface, we find that the basic scaling with distance is fundamentally different when the surface is corrugated.

Figure 5 shows the relationship between W_{t-s} and the local height above the surface ($h = z(x) - z_s(x)$) for tip radii of 5 nm and 10 nm, at four high symmetry points on the corrugated surface (x = 0, x = λ/4, x= λ/2, and x = 3λ/4). We compare the curves derived from the corrugation model to the exact curves corresponding to a flat surface, and additionally show the reference curve $1/z$, which represents the small-z limiting behavior for the flat surface. We see that, unlike the flat case, the curves do not show a $1/z$ dependence in the limit of small tip–sample distances. Assuming a relationship of the form $1/z^{\beta}$ for W_{t-s} versus the tip–sample distance, we find β > 1. This means that the tip potential drops off more quickly with increasing distance than one would expect from application of the Hamaker force law for the relationship between a sphere and a plane. Additionally, the dependence of V_{tip} on the tip–sample distance varies with lateral position, showing the strongest distance dependence at the valley position (x = 3λ/4, blue curve) and the weakest distance dependence at the peak position (x = λ/4, red curve). For x = 0 and x = λ/2, the distance dependencies are equivalent, which is consistent with the observation that these two locations are mirror symmetric in geometry. For all lateral positions studied, a departure from the sphere–plane Hamaker force law results. The departure is most pronounced when the tip is in close proximity to the surface; as the distance from the surface increases the potential converges to the exact result for a flat surface. While the deviation from the sphere–plane Hamaker force law is not mapped throughout the corrugation (λ, δ) parameter space here, we expect that for a given tip radius the deviation will decrease with longer λ and smaller δ due to decreased interaction between the tip and the substrate side walls. This prediction is consistent with the flat surface case, which is restored in the limits λ → ∞ and δ → 0.

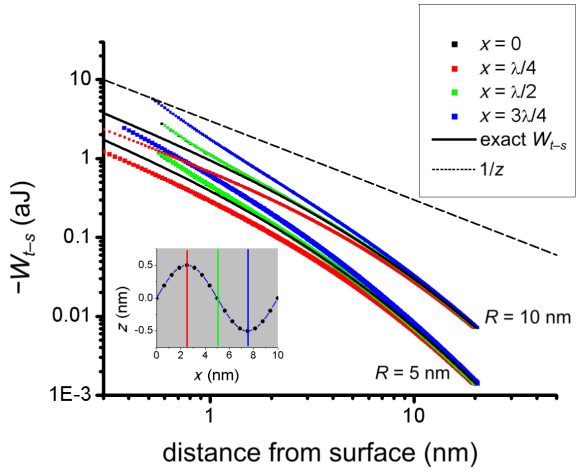

Figure 5: Hamaker force law for corrugated surfaces: Tip–sample distance dependence of tip potential for high-symmetry points (inset, x = 0, x = λ/4, x = λ/2, and x = 3 λ/4) for the two radii (R = 5 nm and R = 10 nm); for x = 0 and x = λ/2 the curves overlap. Lines for the exact analytical form (Equation 10) of the Hamaker relationship between a sphere and a plane are shown (black line) for comparison.

Attenuation of surface features

To determine the degree of attenuation of surface features for NC-AFM, contours of constant frequency shift were calculated (Figure 6) by using the method described in the previous section. Here, we present results for a tip with radius 5 nm. With increasing distance from the surface these contours show attenuation of the corrugation. As discussed in the previous section, the proximity to the surface is limited by our first numerical integration to obtain w_{a-s}. At our computational limit, the nearest contour that we can calculate corresponds to a normalized frequency shift of −0.72 nN·nm$^{1/2}$ (−22.8 fN·m$^{1/2}$), which is well into the range in which atomic-resolution images are normally obtained [20]. Most significantly, at this interaction level the contours are attenuated by ~30% (lower-most contour, purple curve in Figure 6). At −0.1 nN·nm$^{1/2}$ (upper-most contour, red curve in Figure 6) the model predicts over 50% attenuation compared to the surface corrugation. The attenuation of surface features can be understood intuitively by considering the vdW interaction of the tip and the corrugated sample surface. For flat surfaces, the vdW interaction provides a constant background and is most strongly concentrated at the tip apex, but for corrugated surfaces the vdW interactions over peak positions and valley positions are different and interactions with the side of the tip become more important. For the valley positions, the attractive force between the tip and the sides of the valley will lead to a stronger attraction than for the flat surface case and thus result in a higher z position for the same frequency shift. A similar physical argument can be made for the peak positions. In this case the downward slope means that neighboring atoms are farther away, the vdW interactions with these atoms is smaller compared with the flat case due to the increased distance, and as a result the same frequency shift will occur at a lower z position. The vdW interactions with neighboring atoms become more dominant at larger z distances (smaller frequency shifts), and therefore one can intuitively expect greater attenuation (lowering of peak positions and heightening of valley positions) based on these simple, physical vdW arguments. A similar argument was presented by Sun et. al in describing the attenuation in the graphene moiré structure on Ir(111) due to the vdW interaction between the tip and the underlying Ir(111) structure [29]. While attenuation is to be expected for increased distance between the tip and the sample, we emphasize that the degree of attenuation for a tip of 5 nm radius is significant even at small distances, with a normalized frequency shift that is relatively large. To obtain accurate experimental results with NC-AFM it is of critical importance to choose a frequency shift setpoint such that the distance between the tip and the surface is minimized, *especially* when seeking accurate topography of corrugated surfaces. The model used does not account for local bonding, electrostatic forces, or atomistic interactions beyond the inclusion of a pairwise vdW interaction, all of which affect the AFM resolution; nonetheless, even if these interactions were included, the varying vdW and resultant attenuation of features still presents a problem to resolution.

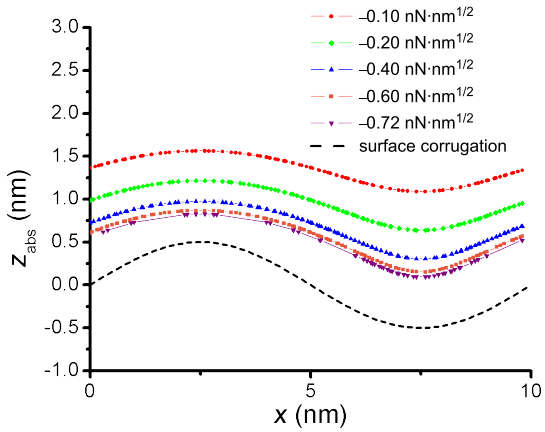

Figure 6: Contours of constant normalized frequency shift, γ, for a corrugated surface. Attenuation is observed as the distance from the surface increases. Here, z_{abs} gives an absolute position in the z direction, not a relative distance from the surface.

Conclusion

As is already well known in the field of atomic force microscopy, a sharp tip and close proximity to the surface is the key to obtaining accurate topographic images with high resolution. Here we have shown that, even more so than for flat surfaces, these factors are especially important for high-resolution imaging of rough surfaces, based only on the differences between vdW interactions. While the model results support the experimental difficulty of obtaining accurate images of rough surfaces, the model itself oversimplifies the multifaceted complexities of experimental AFM setups. More complex models, which include short-range bonding and electrostatic forces, more realistic tip geometries, and calculations for closer proximities between tip and sample, are needed for a more complete and quantitatively accurate understanding of the factors limiting the resolution of corrugated surfaces.

Experimental

All NC-AFM images were collected with a JEOL ultrahigh-vacuum atomic force microscope with a base pressure of 4×10^{-8} Pa. SiO_2 samples (Figure 1a and Figure 1b) were cleaved in air to the proper size then quickly transferred into the ultrahigh-vacuum JEOL AFM system (4500A, Nanonis controller). SiO_2 samples were baked at 130 °C for cleaning. In order to replicate the experimental substrate preparation often used for graphene exfoliation, no additional cleaning procedures were performed before imaging of the SiO_2. Si(111) samples (Figure 1c) were cleaned in UHV by the standard

procedure with repeated flashing at 1530 K, followed by slow cooling through the (1 × 1)-to-(7 × 7) phase transition [30]. NC-AFM measurements were performed with commercially available cantilevers; supersharp tips were used for the high-resolution SiO_2 measurements (Veeco TESP-SS with nominal radius of 2–5 nm), metal-coated Si for the under-resolved SiO_2 measurements (MikroMasch DPER15), and uncoated Si for the Si(111) measurements (Nanosensors Point Probe NCH with nominal radius 7 nm). All images are presented in raw form, with only a plane-fit background subtraction. Commercial software (SPIP) was used for the presentation of image data.

Acknowledgements

The authors acknowledge Prof. Peter Grutter and Prof. Santiago Solares for very insightful discussions. This work was supported by the University of Maryland NSF-MRSEC under Grant No. DMR 05-20471. MRSEC Shared Experimental Facilities were used in this work. Additional infrastructure support provided by the UMD NanoCenter and CNAM.

References

1. Luan, B.; Robbins, M. O. *Phys. Rev. E* **2006,** *74,* 026111. doi:10.1103/PhysRevE.74.026111
2. Zappone, B.; Rosenberg, K. J.; Israelachvili, J. *Tribol. Lett.* **2007,** *26,* 191. doi:10.1007/s11249-006-9172-y
3. Deshpande, A.; Bao, W.; Miao, F.; Lau, C. N.; LeRoy, B. J. *Phys. Rev. B* **2009,** *79,* 205411. doi:10.1103/PhysRevB.79.205411
4. Geringer, V.; Liebmann, M.; Echtermeyer, T.; Runte, S.; Schmidt, M.; Rückamp, R.; Lemme, M. C.; Morgenstern, M. *Phys. Rev. Lett.* **2009,** *102,* 076102. doi:10.1103/PhysRevLett.102.076102
5. Ishigami, M.; Chen, J. H.; Cullen, W. G.; Fuhrer, M. S.; Williams, E. D. *Nano Lett.* **2007,** *7,* 1643. doi:10.1021/nl070613a
6. Stolyarova, E.; Rim, K. T.; Ryu, S.; Maultzsch, J.; Kim, P.; Brus, L. E.; Heinz, T. F.; Hybertsen, M. S.; Flynn, G. W. *Proc. Natl. Acad. Sci. U. S. A.* **2007,** *104,* 9209. doi:10.1073/pnas.0703337104
7. Zhang, Y.; Brar, V. W.; Girit, C.; Zettl, A.; Crommie, M. F. *Nat. Phys.* **2009,** *5,* 722. doi:10.1038/nphys1365
8. Novoselov, K. S.; Geim, A. K.; Morozov, S. V.; Jiang, D.; Zhang, Y.; Dubonos, S. V.; Grigorieva, I. V.; Firsov, A. A. *Science* **2004,** *306,* 666. doi:10.1126/science.1102896
9. Meyer, J. C.; Geim, A. K.; Katsnelson, M. I.; Novoselov, K. S.; Booth, T. J.; Roth, S. *Nature* **2007,** *446,* 60. doi:10.1038/nature05545
10. Nelson, D. R.; Peliti, L. J. *J. Phys. (Paris)* **1987,** *48,* 1085. doi:10.1051/jphys:019870048070108500
11. Aitken, Z. H.; Huang, R. *J. Appl. Phys.* **2010,** *107,* 123531. doi:10.1063/1.3437642
12. Li, T.; Zhang, Z. *J. Phys. D: Appl. Phys.* **2010,** *43,* 075303. doi:10.1088/0022-3727/43/7/075303
13. Pierre-Louis, O. *Phys. Rev. E* **2008,** *78,* 021603. doi:10.1103/PhysRevE.78.021603
14. Cullen, W. G.; Yamamoto, M.; Burson, K. M.; Chen, J. H.; Jang, C.; Li, L.; Fuhrer, M. S.; Williams, E. D. *Phys. Rev. Lett.* **2010,** *105,* 215504. doi:10.1103/PhysRevLett.105.215504
15. Koenig, S. P.; Boddeti, N. G.; Dunn, M. L.; Bunch, J. S. *Nat. Nanotechnol.* **2011,** *6,* 543. doi:10.1038/nnano.2011.123
16. Lee, C.; Li, Q.; Kalb, W.; Liu, X.-Z.; Berger, H.; Carpick, R. W.; Hone, J. *Science* **2010,** *328,* 76. doi:10.1126/science.1184167
17. Raberg, W.; Wandelt, K. *Appl. Phys. A: Mater. Sci. Process.* **1998,** *66,* S1143. doi:10.1007/s003390051314
18. Raberg, W.; Ostadrahimi, A. H.; Kayser, T.; Wandelt, K. *J. Non-Cryst. Solids* **2005,** *351,* 1089. doi:10.1016/j.jnoncrysol.2005.01.022
19. Burson, K. M.; Yamamoto, M.; Cullen, W. G. High resolution microscopy of SiO2 and the structure of SiO2-supported graphene. In *Proceedings of the ASME 2011 International Design Engineering Technical Conferences & Computers and Information in Engineering Conference IDETC/CIE 2011,* Washington, DC, Aug 28–31, 2011; ASME: New York, 2012.
20. Giessibl, F. J. *Rev. Mod. Phys.* **2003,** *75,* 949. doi:10.1103/RevModPhys.75.949
21. Lantz, M. A.; Hug, H. J.; van Schendel, P. J. A.; Hoffmann, R.; Martin, S.; Baratoff, A.; Abdurixit, A.; Güntherodt, H.-J.; Gerber, C. *Phys. Rev. Lett.* **2000,** *84,* 2642. doi:10.1103/PhysRevLett.84.2642
22. Minobe, T.; Uchihashi, T.; Tsukamoto, T.; Shigeki, O.; Sugawara, Y.; Morita, S. *Appl. Surf. Sci.* **1999,** *140,* 298. doi:10.1016/S0169-4332(98)00544-3
23. Pérez, R.; Štich, I.; Payne, M. C.; Terakura, K. *Phys. Rev. B* **1998,** *58,* 10835. doi:10.1103/PhysRevB.58.10835
24. Hölscher, H.; Allers, W.; Schwarz, U. D.; Schwarz, A.; Wiesendanger, R. *Phys. Rev. B* **2000,** *62,* 6967. doi:10.1103/PhysRevB.62.6967
25. Israelachvili, J. N. *Intermolecular And Surface Forces,* 3rd ed.; Academic Press: Burlington, MA, 2011.
26. Hölscher, H.; Schwarz, A.; Allers, W.; Schwarz, U. D.; Wiesendanger, R. *Phys. Rev. B* **2000,** *61,* 12678. doi:10.1103/PhysRevB.61.12678
27. Lantz, M. A.; Hug, H. J.; Hoffmann, R.; van Schendel, P. J. A.; Kappenberger, P.; Martin, S.; Baratoff, A.; Güntherodt, H.-J. *Science* **2001,** *291,* 2580. doi:10.1126/science.1057824
28. Giessibl, F. J. *Appl. Phys. Lett.* **2001,** *78,* 123. doi:10.1063/1.1335546
29. Sun, Z.; Hämäläinen, S. K.; Sainio, J.; Lahtinen, J.; Vanmaekelbergh, D.; Liljeroth, P. *Phys. Rev. B* **2011,** *83,* 081415. doi:10.1103/PhysRevB.83.081415
30. Conrad, B. R.; Cullen, W. G.; Riddick, B. C.; Williams, E. D. *Surf. Sci.* **2009,** *603,* L27. doi:10.1016/j.susc.2008.12.020

License and Terms

Beilstein Journal of Nanotechnology

Analysis of force-deconvolution methods in frequency-modulation atomic force microscopy

Joachim Welker*, Esther Illek and Franz J. Giessibl

Full Research Paper

Open Access

Address:
Institute of Experimental and Applied Physics, Experimental Nanoscience, University of Regensburg, Universitaetsstrasse 31, 93053 Regensburg, Germany

Email:
Joachim Welker* - joachim.welker@physik.uni-regensburg.de

* Corresponding author

Keywords:
frequency-modulation atomic force microscopy; force deconvolution; numerical implementation

Beilstein J. Nanotechnol. **2012,** *3,* 238–248.
doi:10.3762/bjnano.3.27

Received: 30 November 2011
Accepted: 10 February 2012
Published: 14 March 2012

This article is part of the Thematic Series "Noncontact atomic force microscopy".

Guest Editor: U. D. Schwarz

Abstract

In frequency-modulation atomic force microscopy the direct observable is the frequency shift of an oscillating cantilever in a force field. This frequency shift is not a direct measure of the actual force, and thus, to obtain the force, deconvolution methods are necessary. Two prominent methods proposed by Sader and Jarvis (Sader–Jarvis method) and Giessibl (matrix method) are investigated with respect to the deconvolution quality. Both methods show a nontrivial dependence of the deconvolution quality on the oscillation amplitude. The matrix method exhibits spikelike features originating from a numerical artifact. By interpolation of the data, the spikelike features can be circumvented. The Sader–Jarvis method has a continuous amplitude dependence showing two minima and one maximum, which is an inherent property of the deconvolution algorithm. The optimal deconvolution depends on the ratio of the amplitude and the characteristic decay length of the force for the Sader–Jarvis method. However, the matrix method generally provides the higher deconvolution quality.

Introduction

The atomic force microscope (AFM) was invented 25 years ago as an offspring of the scanning tunneling microscope (STM), extending the imaging capabilities to insulators [1]. Nowadays the focus of development and investigation shifts from purely topographic imaging, in spite of this still being the main use of an AFM, to quantitative force measurements between single atoms or molecules in high-resolution, dynamic AFM modes. Examples are the measurement of the force needed to move an atom on surface [2] or the chemical identification of different adatom species [3]. Another trend is the three-dimensional force mapping [4,5] giving tomographic insight into the force field over atoms and molecules. However, all these remarkable results have to rely on inversion methods as the force is not directly measured in the dynamic modes of an AFM.

For high-resolution atomic force microscopy commonly the frequency-modulation (FM) technique is used [6]. In FM-AFM the direct observable is the frequency change of an oscillating cantilever due to the force field acting between the tip of the probe and the sample surface. The corresponding frequency shift is related to the actual force by a convolution [7]. Hence to obtain the force, deconvolution methods are necessary.

A number of inversion methods from frequency shift to force have been suggested. Iterative methods were proposed by Gotsmann [8] and Dürig [9]. The higher harmonics of the cantilever oscillation can be exploited to recover the force instantaneously [10]. Hölscher showed that a deconvolution is possible if the amplitude dependence of the frequency shift is known [11]. Predominantly, the direct deconvolution methods of the $\Delta f(z)$ dependency that were proposed by Sader and Jarvis [12] and Giessibl [13] are used. These methods were found to be the most robust [14]. Both methods start from the same equation for the convolution, but they have different approaches in solving it for the force.

In this paper we compare the Sader–Jarvis deconvolution method and Giessibl's matrix method. We use the analytical formulas of the Morse and Lennard-Jones model forces and the corresponding frequency shifts. The analytically calculated frequency shifts are deconvoluted back into a force and compared with the original model force.

In the first section we introduce the model forces and the corresponding frequency-shift curves. In the second section both deconvolution methods and their implementation for discrete data points are described. In the third section we present the results of the simulation showing a nontrivial amplitude dependence of the deconvolution quality and discuss the origin of the variations in deconvolution quality.

Forces and frequency shifts in FM-AFM

In FM-AFM the force is not directly proportional to the measured frequency shift, but instead to the average force gradient, as can be seen from a simple model. Let us assume an interaction potential between a tip and a sample denoted by $V_{ts}(z)$. Accordingly, the force is given by $F_{ts}(z) = -(\mathrm{d}V_{ts}(z)/\mathrm{d}z)$ and the force gradient by $k_{ts}(z) = -(\mathrm{d}F_{ts}(z)/\mathrm{d}z)$. If k_{ts} is constant over the range of one oscillation cycle, which is fulfilled, for example, for small amplitudes, the actual resonance frequency f can be calculated with an effective spring constant $k + k_{ts}$

$$f = \frac{1}{2\pi}\sqrt{\frac{k+k_{ts}}{m}}\,, \tag{1}$$

where m is the effective mass and k the spring constant of the cantilever. For $k_{ts} << k$ we can expand the square root in Equation 1 and calculate the frequency shift $\Delta f = f - f_0$

$$\Delta f = \frac{k_{ts}}{2k} f_0\,. \tag{2}$$

In general k_{ts} is not constant over the oscillation cycle, especially for larger amplitudes A. In this case the oscillation of the cantilever has to be taken into account. A derivation of the frequency shift caused by an arbitrary force F_{ts} is given, for example, in reference [15] based on the Hamilton–Jacobi formalism:

$$\Delta f(z_{ltp}) = \frac{f_0}{2k}\frac{2}{\pi A^2}\int_{-A}^{A} F_{ts}(z_{ltp}+A-q')\frac{q'}{\sqrt{A^2-q'^2}}\,\mathrm{d}q'\,, \tag{3}$$

where z_{ltp} is the lower turnaround point of the oscillation (see Figure 1a). Thus the frequency shift can be calculated by a

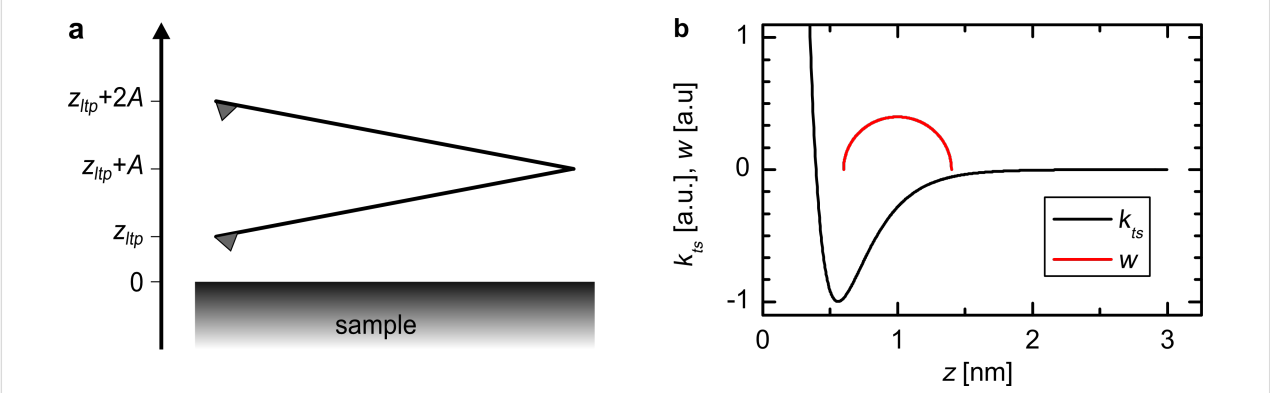

Figure 1: (a) Definition of the z-axis: The cantilever oscillates with a constant amplitude A. The lower turnaround point is denoted with z_{ltp} and the center of the oscillation is at $z_{ltp} + A$. (b) The frequency shift can be calculated as a convolution of the force gradient k_{ts} with a semicircular weight function w.

convolution of the force with an amplitude-dependent weight function. Integration by parts of Equation 3 leads to a more intuitive form:

$$\Delta f(z_{ltp}) = \frac{f_0}{2k}\frac{2}{\pi A^2}\int_{-A}^{A} k_{ts}(z_{ltp}+A-q')\sqrt{A^2-q'^2}\,\mathrm{d}q'. \quad (4)$$

This equation describes the frequency shift Δf as a convolution of the force gradient k_{ts} with a semicircular weight function with radius A (see Figure 1b). Equation 4 is equivalent to Equation 2 upon replacing k_{ts} with the average force gradient

$$\langle k_{ts}\rangle = \int_{-A}^{A} k_{ts}(q')\frac{2}{\pi A^2}\sqrt{A^2-q'^2}\,\mathrm{d}q'.$$

Equation 3 needs to be inverted in order to calculate the force for a given $\Delta f(z)$ curve. Additionally, it enables us to calculate the expected frequency shift for a given force law. In reference [16] analytical functions of $\Delta f(z)$ curves for power and exponential force laws were calculated. A common exponential force law is the force derived from the Morse potential used to describe the bonding between two atoms:

$$V_M(z) = -E_{bond}\left[2\,\mathrm{e}^{-\kappa(z-\sigma)} - \mathrm{e}^{-2\kappa(z-\sigma)}\right], \quad (5)$$

$$F_M(z) = -E_{bond}\,2\kappa\left[\mathrm{e}^{-\kappa(z-\sigma)} - \mathrm{e}^{-2\kappa(z-\sigma)}\right]. \quad (6)$$

Here E_{bond} is the bond energy, κ is the decay constant and σ is the equilibrium distance. The frequency shift that is derived from such a Morse force law is given by [16]:

$$\begin{aligned}\Delta f_M(z_{ltp}) = &-\frac{f_0}{kA}E_{bond}\\ &\cdot 2\kappa\Big\{\mathrm{e}^{-\kappa(z_{ltp}-\sigma)}\left[M_1^{0.5}(-2\kappa A) - M_2^{1.5}(-2\kappa A)\right] \quad (7)\\ &-\mathrm{e}^{-2\kappa(z_{ltp}-\sigma)}\left[M_1^{0.5}(-2\kappa A) - M_2^{1.5}(-2\kappa A)\right]\Big\}\end{aligned}$$

with $M_b^a(z)$ being the Kummer function (see section 13.2.1 in [17]).

Another potential commonly used to describe the interaction between two atoms is the Lennard-Jones potential. In contrast to the Morse potential, the Lennard-Jones potential is based on power functions and has only two parameters, that is, the equilibrium distance σ and the bond energy E_{bond}:

$$V_{LJ}(z) = -E_{bond}\left[2\left(\frac{\sigma}{z}\right)^6 - \left(\frac{\sigma}{z}\right)^{12}\right], \quad (8)$$

$$F_{LJ}(z) = -12\frac{E_{bond}}{\sigma}\left[\left(\frac{\sigma}{z}\right)^7 - \left(\frac{\sigma}{z}\right)^{13}\right]. \quad (9)$$

The Lennard-Jones force law leads to the frequency shift [16]:

$$\begin{aligned}\Delta f_{LJ}(z_{ltp}) = &-\frac{f_0}{kA}12\frac{E_{bond}}{\sigma}\\ &\cdot\Big\{\left(\frac{\sigma}{z_{ltp}}\right)^7\left[F_1^{7,0.5}\left(-\frac{2A}{z_{ltp}}\right) - F_2^{7,1.5}\left(-\frac{2A}{z_{ltp}}\right)\right] \quad (10)\\ &-\left(\frac{\sigma}{z_{ltp}}\right)^{13}\left[F_1^{13,0.5}\left(-\frac{2A}{z_{ltp}}\right) - F_2^{13,1.5}\left(-\frac{2A}{z_{ltp}}\right)\right]\Big\}\end{aligned}$$

with $F_c^{a,b}(z)$ being the hypergeometric function (see section 15.3.1 in [17]). In this work we use both the Morse and the Lennard-Jones force laws as model systems to judge the quality of the force-deconvolution methods.

Force-deconvolution methods for discrete data

Sader and Jarvis [12] proposed an analytical force-deconvolution method (hereinafter called the Sader–Jarvis method). The force $F_{ts}(z_{ltp})$ is expressed in terms of a Laplace transformation. In doing so, Equation 3 can formally be solved for F_{ts}. But to calculate the actual expression numerically, part of the Laplace transformed function needs to be approximated by a rational function. Using fractional calculus, Sader and Jarvis provide an equation to recover the force F_{ts} from a $\Delta f(z)$ in a closed analytical form:

$$\begin{aligned}F_{ts}(z_{ltp}) = \frac{2k}{f_0}\int_{z_{ltp}}^{\infty}\Bigg[&\left(1+\frac{\sqrt{A}}{8\sqrt{\pi(t-z_{ltp})}}\right)\Delta f(t)\\ &-\frac{A^{3/2}}{\sqrt{2(t-z_{ltp})}}\frac{\mathrm{d}\Delta f(t)}{\mathrm{d}t}\Bigg]\mathrm{d}t.\end{aligned} \quad (11)$$

Practically, the frequency shift is not given as an analytical function but in discrete data points $\Delta f_i = \Delta f(z_i)$, $i = 1,\ldots,N$. It is convenient to define z_1 as the point of closest approach and $z_{i+1} > z_i$, but the data points do not need to be equidistant. Upon implementation of Equation 11, both the derivation and the integration have to be calculated numerically. The derivation is

replaced by the difference quotient and the integral is calculated following, for example, the trapezoidal rule:

$$F_j = \frac{2k}{f_0}\left\{C(j) + \sum_{i=j+1}^{N-2}(z_{i+1}-z_i)\frac{g_{i+1}+g_i}{2}\right\}, \qquad (12)$$

where

$$C(j) = \Delta f_j(z_{j+1}-z_j) + 2\frac{\sqrt{A}}{8\sqrt{\pi}}\Delta f_j\sqrt{z_{j+1}-z_j} - 2\frac{A^{3/2}}{\sqrt{2}}\frac{\Delta f_{j+1}-\Delta f_j}{z_{j+1}-z_j}\sqrt{z_{j+1}-z_j} \qquad (13)$$

is a correction term. Sader introduced this term in his implementation of the force-deconvolution algorithm [18] to account for the divergence of the integrand in Equation 11 at $t = z_{ltp}$. The correction term is given by the integration over the interval $[z_j, z_j + 1]$ with $\Delta f(t)$ assumed to be constant. The numerical integration is conducted over the discretized integrand

$$g_k = \left(1 + \frac{\sqrt{A}}{8\sqrt{\pi(z_k - z_j)}}\right)\Delta f_k - \frac{A^{3/2}}{\sqrt{2(z_k - z_j)}}\frac{\Delta f_{k+1}-\Delta f_k}{z_{k+1}-z_k}. \qquad (14)$$

This implementation is of course only one possibility. There are, for example, other algorithms than the trapezoidal rule to perform the numerical integration in Equation 12. Choosing another integration algorithm, the correction term in Equation 13 may become unnecessary (see for example [19]). However, further below we will show that it is not the numerical integration that is the limiting factor in accuracy, but rather the used approximation.

Another method was proposed by Giessibl [13] (hereinafter called the matrix method). This method directly uses the discrete nature of the frequency shift versus distance data. The starting point is also the discretized Equation 3, but the data points $\Delta f_i = \Delta f(z_i)$, $i = 1,\ldots,N$ must be equidistant: $z_i = (i - 1)d + z_1$. Here, z_1 is the first z value with nonzero frequency shift coming from far away from the sample. Hence the z-axis is opposite to the one used in the Sader–Jarvis method. Equation 3 can be expressed as a matrix equation by appropriate substitution and index shifting:

$$\Delta f_i = \sum_{j=1}^{N} W_{ij} F_{ts,j}. \qquad (15)$$

The matrix elements W_{ij} are given by

$$W_{ij} = \begin{cases} \frac{f_0}{2k}\frac{2}{\pi A}\int_l^u \frac{\tau}{\sqrt{1-\tau^2}}\mathrm{d}\tau & \text{for } 0 \le i-j \le 2\alpha \\ 0 & \text{else}, \end{cases} \qquad (16)$$

where $\alpha = \mathrm{round}(A/d)$ is the ratio of the amplitude A and the step width d rounded to the nearest integer. The upper and lower boundaries of the integral are given by

$$u = \frac{1-2(i-j)}{2\alpha+1} \text{ and } l = \frac{1-2(i-j+1)}{2\alpha+1}. \qquad (17)$$

The integral in Equation 16 can be evaluated analytically resulting in $-\sqrt{1-\tau^2}\Big|_l^u$. In order to solve Equation 15 for F_{ts} the equation needs to be multiplied from the left with the inverse matrix $\mathbf{M} = \mathbf{W}^{-1}$ resulting in

$$\Delta F_{ts,j} = \sum_{i=1}^{N} M_{ji}\Delta f_i. \qquad (18)$$

Hence the deconvolution method does not need any approximation and only involves the calculation of the inverse matrix **M**.

It is a common argument that the implementation of the matrix method is more complicated than the Sader–Jarvis method and needs high-performance mathematical software tools [14]. The implementation of Equation 12 and Equation 18 used in this work was done in MATLAB [20], and the scripts are available in Supporting Information File 1. Both implementations are straightforward and work also with the freely available software GNU Octave [21] without modification. As both MATLAB and Octave have built-in optimized routines for matrix operations, the matrix method is slightly faster. This may change upon use of a different implementation or different software.

Comparison of the force-deconvolution methods

For comparison we consider two theoretical model systems, the Morse potential (Equation 5) and the Lennard-Jones potential (Equation 8). For these model systems we can derive the force laws $F_{ts}(z)$ (Equation 6, Equation 9) and the frequency-shift curves $\Delta f(z)$ (Equation 7, Equation 10) for an FM-AFM force sensor. The calculated frequency-shift curves are deconvoluted back to a force curve $F_{S/M}$ by using the Sader–Jarvis (S) and the matrix (M) method, respectively.

In order to compare the two deconvolution methods for different force laws, we need a measure for the deconvolution quality. In this work we use the coefficient of determination (CoD)

$$R^2 = 1 - \frac{\sum_{i=1}^{N}(F_{S/M,i} - F_{ts,i})^2}{\sum_{i=1}^{N}(F_{S/M,i} - \overline{F_{S/M}})^2} \tag{19}$$

as a measure of the similarity of the modeled force F_{ts} to the deconvoluted force $F_{S/M}$. The $\overline{F_{S/M}}$ denotes the average of the deconvoluted force and N is the number of data points. The CoD is widely used as a measure of the goodness of fit. Generally, $0 < R^2 \leq 1$ holds independently of the number of data points, and the order of magnitude of the force giving a CoD of 1 corresponds to a perfect match. In principle, a negative CoD can also occur, if the force model fits the deconvoluted force worse than just taking the average of the deconvoluted force. As the CoD does not give information about the shape of the deviation, the residuals

$$\Delta F_{S/M}(z) = F_{S/M}(z) - F_{ts}(z) \tag{20}$$

are calculated for selected amplitudes (see below). Both the CoD and the residuals as a measure of the deconvolution quality emphasize the errors at positions with very steep gradients. Therefore, a small shift of the deconvoluted forces, especially in the repulsive regime, leads to strong deviations. However, as the analysis shows, both measures provide a good insight into the deconvolution quality.

Two important parameters of the atomic interaction are the position and the value of the force minimum (maximum attractive force). Therefore, we also compare the deviation from the model values:

$$\Delta F_{min} = \min(F_{S/M}) - \min(F_{ts}) \quad \text{and} \tag{21}$$

$$\Delta z_{F_{min}} = z_{F_{min},S/M} - z_{F_{min},ts}\,. \tag{22}$$

To calculate the frequency shift we chose a tuning fork sensor in the qPlus design [13] with a spring constant of k = 1800 N/m and a resonance frequency of f_0 = 32768 Hz. This sensor can operate with very small amplitudes in the picometer range up to large amplitudes in the nanometer range [22]. The amplitude contributes to the deconvolution in a nontrivial way, whereas k and f_0 are just linear factors. Therefore, we investigated the amplitude dependence of the deconvolution for the Sader–Jarvis and the matrix method.

We took 500 logarithmically distributed amplitude values A in the range from 10 pm to 1 nm. For each amplitude the Morse and Lennard-Jones force and frequency-shift curves were calculated in a z range from 0.23 nm to 5 nm with 5000 data points. We assumed an equilibrium distance of σ = 0.235 nm and a bond energy of E_{bond} = 0.371 aJ, which were previously used to model a silicon–silicon interaction [15]. Additionally, for the Morse potential we assumed a decay constant of κ = 4.25 nm^{-1}. This leads to a maximum attractive force of F_{min} = −790 pN at z_{min} = 398 pm and F_{min} = −4.25 nN at z_{min} = 261 pm for the Morse and Lennard-Jones force laws, respectively.

Results

Results for a Morse force law

Figure 2 shows the amplitude dependence of the CoD R^2 of the Morse force law based on both the Sader–Jarvis and the matrix deconvolution method. Both methods reveal a nontrivial amplitude dependence of the deconvolution quality. Upon using the Sader–Jarvis method the CoD varies continuously reaching the smallest value at an amplitude of A = 137 pm and the largest at A = 352 pm. With the matrix method the CoD exhibits periodic spikelike features that grow in magnitude as the amplitude is decreased. For larger amplitudes A > 100 pm the CoD converges to 1. However, both deconvolution methods have a R^2 > 0.990 over the whole of the considered amplitude range. Thus in terms of the CoD both methods work very well.

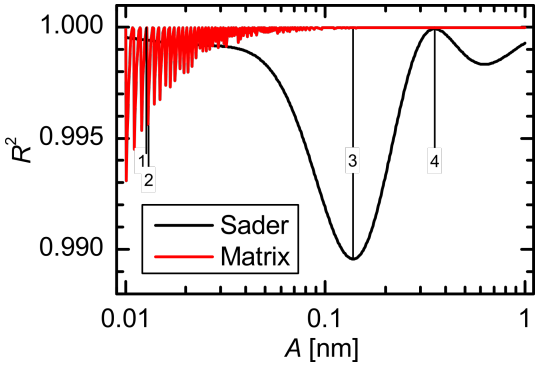

Figure 2: Amplitude dependence of the CoD for the Morse force law. The positions marked with 1, 2, 3, and 4 correspond to the amplitudes 12.8 pm, 12.9 pm, 137 pm and 352 pm, respectively.

In order to show that these small variations in the CoD represent measurable differences between deconvoluted force and the model force, the model and deconvoluted force curves $F_{S/M}(z)$ and the residuals $\Delta F_{S/M}(z)$ are plotted in Figure 3 for selected amplitudes marked in Figure 2. For tip–sample distances greater than 1.5 nm the deviation is below 1 pN. But in the interesting region around the force minimum and in the repulsive regime there are deviations up to 109 pN for both deconvolution methods.

A comparison of the residuals $\Delta F_{S/M}(z)$ for an amplitude of 12.8 pm (Figure 3a) and 12.9 pm (Figure 3b) reveals that in case of the matrix method even tiny differences in the oscillation amplitude can have a great effect on the quality of the deconvolution. This manifests as a drop in the CoD from 1 to 0.995. Similarly, strong deviations are present in the residuals for the Sader–Jarvis method. The Sader–Jarvis method leads to a CoD of $R^2 = 0.990$ at the lowest amplitude of $A = 137$ pm (see Figure 3c) and to $R^2 \approx 1$ at the highest amplitude of $A = 352$ pm (see Figure 3d). This rise in the CoD of 0.01 connotes a decrease in the maximum deviation from 109 pN to 13 pN in the residuals. The greatest deviation occurs in the region of the steep gradient to the left of the force minimum, which is caused by a small shift in the z values of the deconvoluted force. As can be seen from the force curves, the agreement in that range is still reasonably good.

The amplitude dependence of the force minimum $\Delta F_{min}(A)$ in Figure 4a has a similar shape to the amplitude dependence of the CoD in Figure 2. The deviations from the force minimum in the Sader–Jarvis method vary continuously, and the largest deviation at an amplitude of $A = 123$ pm almost coincides with the minimum of the CoD at $A = 137$ pm. The matrix method shows spikelike features similar to Figure 2 in the deviation of the force minimum that become greater with decreasing amplitude. However, for amplitudes exceeding 110 pm these deviations become smaller than 3 pN. Whereas the CoD is always above 0.990, the deviations of the force minimum are up to 53 pN corresponding to 7% of the actual value $F_{min} = -790$ pN for both deconvolution methods. For most of the considered amplitude range ΔF_{min} is positive for both methods. Therefore, the absolute value of the deconvoluted maximum attractive force is smaller than the actual maximum attractive force. The deviation in the position can only take an integer multiple of the step width d between the z values (see Figure 4b). For the Sader–Jarvis method deviations up to nine data points corresponding to $\Delta z_{Fmin} = 9$ pm occur. The matrix method is in this regard very accurate as there are only deviations of one data point at most.

Results for a Lennard-Jones force law

In Figure 5 the amplitude dependence of the CoD for the Lennard-Jones force law is shown. The amplitude dependence is again continuous for the Sader–Jarvis method, but the curve

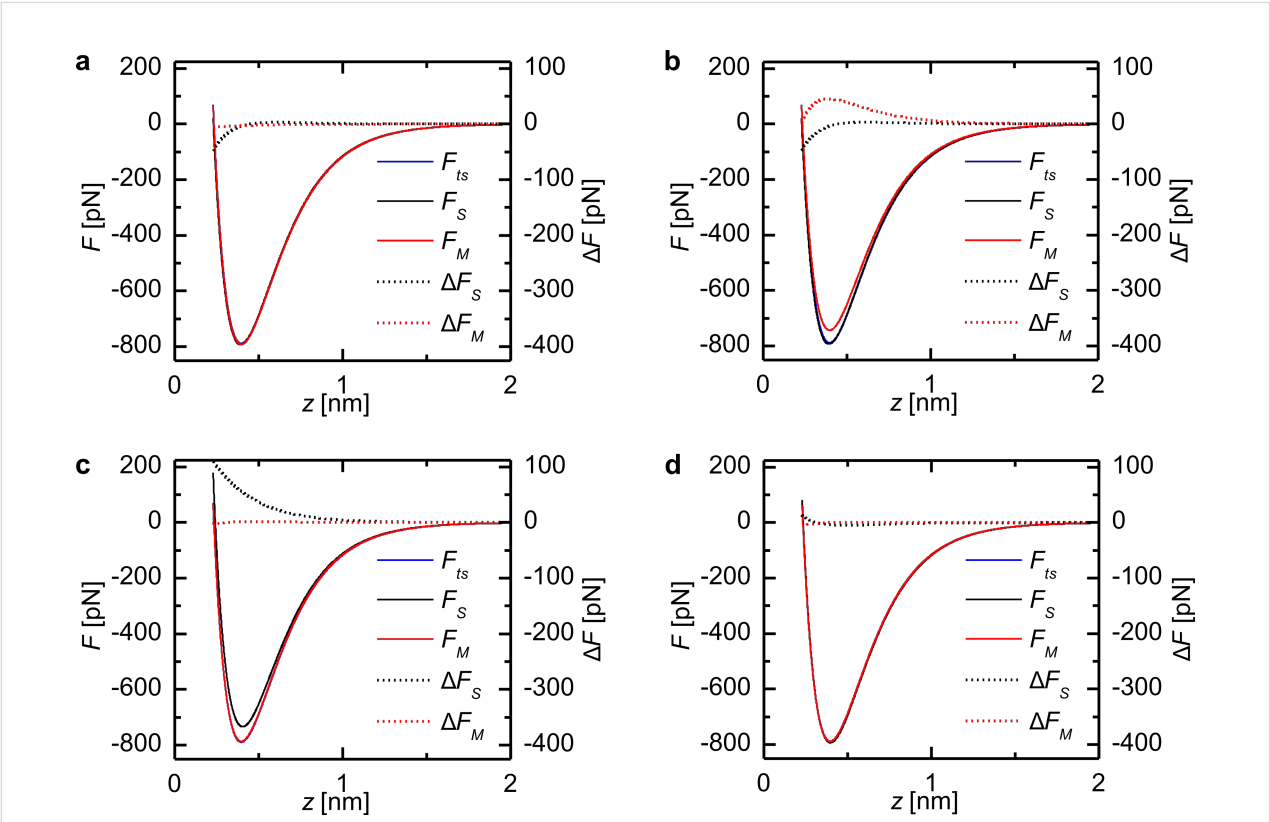

Figure 3: Model force $F_{ts}(z)$, deconvoluted force $F_{S/M}(z)$ and the residuals $\Delta F_{S/M}(z)$ for the Morse force law with selected oscillation amplitudes. (a) Amplitude 1 in Figure 2 (12.8 pm) with $R^2 \approx 1$ for the matrix method. (b) Amplitude 2 in Figure 2 (12.9 pm) with $R^2 = 0.995$ for the matrix method. (c) Amplitude 3 in Figure 2 (137 pm) with $R^2 = 0.990$ for the Sader–Jarvis method. (d) Amplitude 4 in Figure 2 (352 pm) with $R^2 \approx 1$ for both methods.

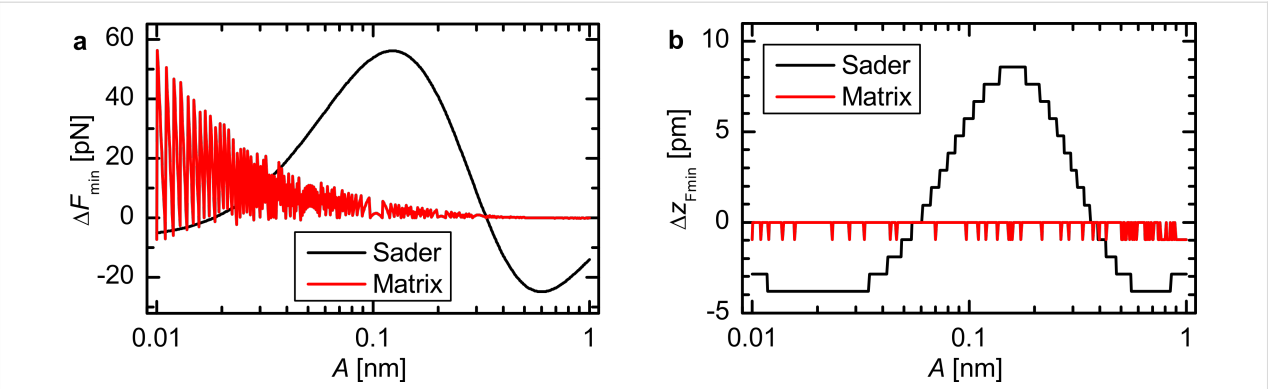

Figure 4: Amplitude dependence of the deviation in magnitude (a) and position (b) from the force minimum for the Morse force law. The steps in (b) are due to the discretization of the *z*-values.

is shifted to smaller amplitudes compared to the Morse force law in Figure 2. The Sader–Jarvis method exhibits minima at amplitudes of 23 pm and 122 pm and a maximum at 58 pm. The matrix method shows again the periodic spikelike features. Additionally, for larger amplitudes the CoD R^2 does not converge to 1. The deconvolution quality expressed by the CoD $R^2 \geq 0.993$ is also very high for the Lennard-Jones force law.

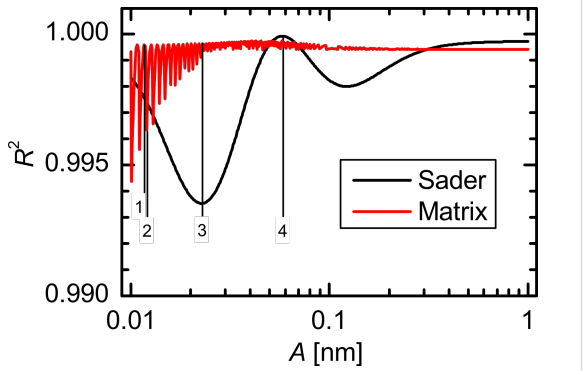

Figure 5: Amplitude dependence of the CoD for a Lennard-Jones force law. The positions marked with 1, 2, 3, and 4 correspond to the amplitudes 11.7 pm, 12.0 pm, 23 pm and 58.3 pm, respectively.

The deconvoluted force curves and the residuals of the Lennard-Jones force law shown in Figure 6 show significant deviations only for tip–sample distances below 0.55 nm. Comparing the residuals of the matrix method for an amplitude of 11.8 pm (Figure 6a) and 12.0 pm (Figure 6b) also shows a strong deviation of the deconvolution quality due to only a small increase in amplitude, as was observed for the Morse force law. At the first minimum of the CoD for the Sader–Jarvis method the maximum difference between the deconvoluted force and the model force is 460 pN (Figure 6c). For an amplitude of 58.3 pm (Figure 6d) the deviation for the Sader–Jarvis method is only 78 pN corresponding to a CoD of $R^2 \approx 1$.

For the Lennard-Jones force law the shape of the $\Delta F_{min}(A)$ curve (Figure 7a) is similar to the amplitude dependence of the CoD in Figure 5. Using the Sader–Jarvis method the largest deviation appears at an amplitude of 21 pm, approximately where the CoD has its first minimum. At this position, the deconvoluted force minimum is larger than the minimum of the model force. Therefore, the absolute value of the maximum attractive force is smaller than the correct value. At the second minimum of the CoD (A = 120 pm) the deviation is negative. For the matrix method most amplitudes result in a positive ΔF_{min} meaning that the absolute value of the maximum attractive force is underestimated. The deviations from the actual force minimum rise up to 293 pN for the matrix method and up to 259 pN for the Sader–Jarvis method, which is 7% and 6%, respectively, of the correct value F_{min} = −4.25 nN. The deviations of the position of the force minimum shown in Figure 7b are very small in the case of the Lennard-Jones force law compared to the Morse force law. There are no deviations for the matrix method and the Sader–Jarvis method shows only deviations of one data point at most.

Discussion

To determine the origin of the amplitude-dependent periodic spikes in the CoD for the matrix method, in Figure 8, we plot the CoD versus the ratio of amplitude and step width A/d for the Morse and the Lennard-Jones force law. The position of the best deconvolution quality strongly depends on the simulation parameters (force law, amplitude range). But a sharp drop of R^2 for $A/d \approx n + 0.5$ is seen for all parameters. Therefore, we suggest using only integer ratios of A/d as they are furthest away from the singularities.

At first glance the matrix method does not seem to be suitable for small amplitudes. But the drop in the CoD for small ratios A/d is not related to a shortcoming of the matrix method for small amplitudes but rather to a numerical artifact that is

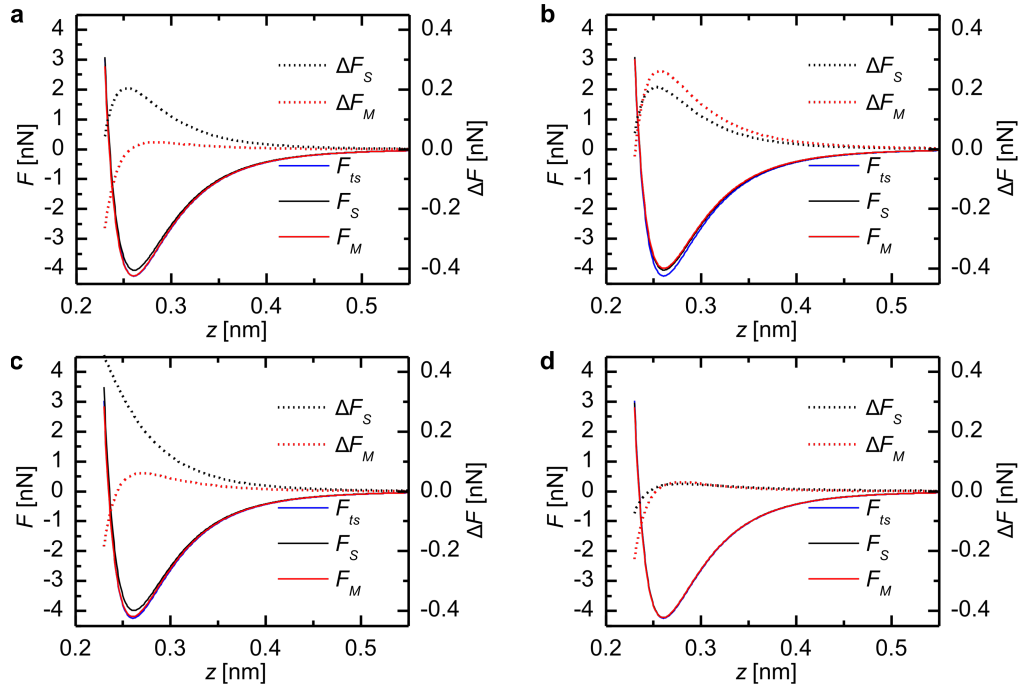

Figure 6: Model force $F_{ts}(z)$, deconvoluted force curves $F_{S/M}(z)$ and the residuals $\Delta F_{S/M}(z)$ for the Lennard-Jones force law with selected oscillation amplitude. (a) Amplitude 1 in Figure 5 (11.7 pm) with R^2 = 0.9996 for the matrix method. (b) Amplitude 2 in Figure 5 (12.0 pm) with R^2 = 0.996 for the matrix method. (c) Amplitude 3 in Figure 5 (23 pm) with R^2 = 0.994 for the Sader–Jarvis method. (d) Amplitude 4 in Figure 5 (58.3 pm) with $R^2 \approx 1$ for the Sader–Jarvis method.

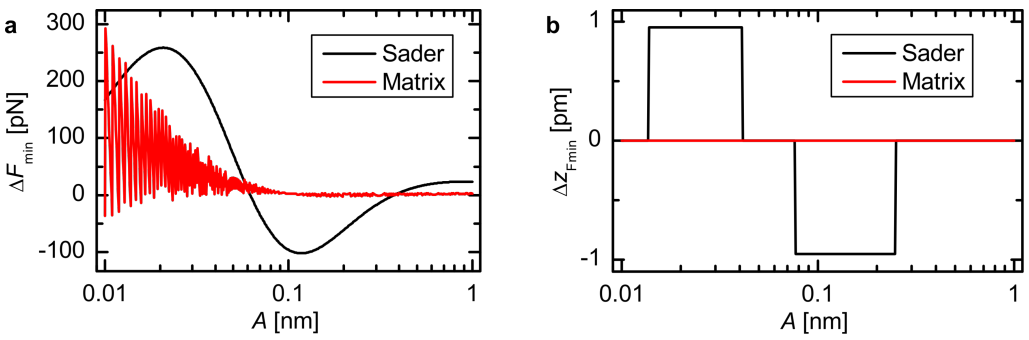

Figure 7: Amplitude dependence of the deviation in magnitude (a) and position (b) from the force minimum for the Lennard-Jones force law. The steps in (b) are due to the discretization of the *z*-values.

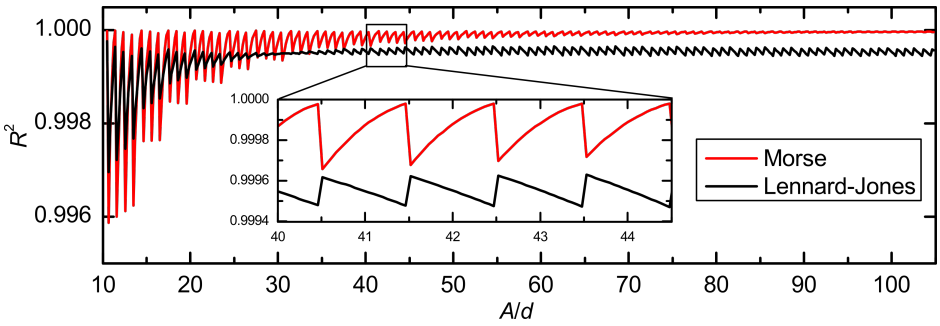

Figure 8: Dependence of the CoD on the ratio A/d of amplitude and step width for the Morse and the Lennard-Jones force law. The inset shows that the spikes are always at positions $A/d = n + 0.5$ for both force laws with an integer n.

emphasized by using too few data points for the deconvolution. This can be seen as the CoD always goes back to its optimum value even for low ratios of $A/d < 30$. If the data points are not given in an appropriate spacing, interpolation methods can be used. This additional data processing increases computational time and memory requirements for the deconvolution. In general it is advisable to use ratios $A/d > 50$ as the variation in R^2 becomes very small for greater ratios, whereas a very small ratio $A/d \leq 1$ can even result in a negative CoD.

For the Sader–Jarvis method the situation is different. The $R^2(A)$ curves show two distinct minima and one maximum at which the deconvolution quality is optimal. However, the positions of the minima and the maximum are not connected to the ratio A/d. Therefore, interpolation does not yield a better deconvolution performance.

In fact, the deconvolution quality depends on the ratio of the amplitude and the characteristic decay length of the force law. For a Morse force law the decay length is inversely proportional to the parameter κ. In Figure 9a the CoD is shown for Morse force laws with κ's from 2 nm^{-1} to 10 nm^{-1}. We can scale the amplitude axis for every individual CoD curve by κ, as is shown in Figure 9b. The minima and maxima of all curves coincide very well on the scaled axis. In the derivation of Equation 11 the function $T(x) = e^{-x}I_1(x)$, where $I_1(x)$ is the modified Bessel function of the first order [17], is approximated by [12]

$$T_{\text{appr}}(x) = \frac{x}{2}\left(1+\frac{1}{8}\sqrt{x}+\sqrt{\frac{\pi}{2}}x^{3/2}\right)^{-1}.$$

In Figure 9c the squared relative error of this approximation

$$SqRE = \left(\frac{T(x)-T_{\text{appr}}(x)}{T(x)}\right)^2 \qquad (23)$$

is shown. By comparison of Figure 9b and Figure 9c it is evident that the variation in the deconvolution quality is not a numerical artifact, but an inherent property of the deconvolution method due to this approximation. This approximation exhibits a maximum error of 5%, as already pointed out in [12,23]. This is in concordance with the results presented in this work yielding a maximum error of 7% in the force minimum.

Unfortunately, the optimal and the worst deconvolution lie very close together on the order of the characteristic decay length. For a Morse law the optimal deconvolution is attained for $A \approx 1.5\ \kappa^{-1}$ and the worst for $A \approx 0.59\ \kappa^{-1}$. The deconvolution quality rises again for larger amplitudes $A > 7\ \kappa^{-1}$. However, usually amplitudes in the order of the characteristic decay length of the force are desired to obtain the best signal-to-noise ratio [24]. Therefore, in a real experiment it is difficult to judge whether the Sader–Jarvis method will provide an optimal deconvolution.

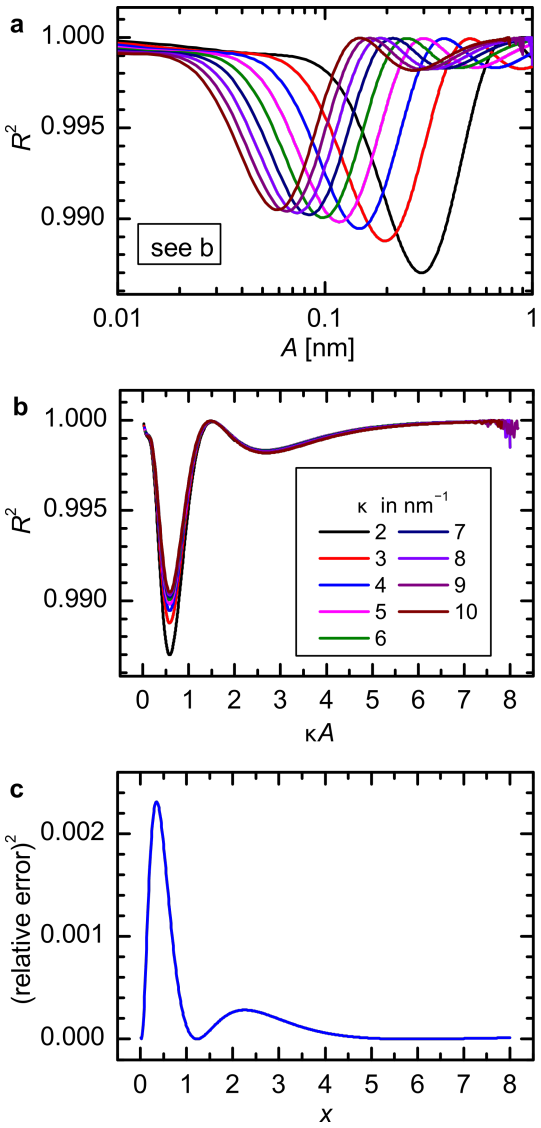

Figure 9: (a) Amplitude dependence of the CoD for Morse force law with different decay constants κ (see legend in (b)). (b) The same data shown in (a) but with a scaled abscissa κ*A*. The minima and maxima coincide on the scaled axis. (c) square of the relative error *SqRE* of the approximation of the function *T*(*x*).

Besides the deconvolution algorithm, there are other uncertainties in the experimental parameters that have a direct effect on the correctness of the force deconvolution: The stiffness k, the amplitude A (sensor sensitivity) and the tip–sample distance z (z-piezo sensitivity). The uncertainties of these parameters are

in the range of a few percent. Another important prerequisite to the experimental data is that the frequency shift curves extend far enough from the surface, so that $\Delta f(z)$ and its derivative $d\Delta f(z)/dz$ go to zero, because of the finite number of data points used for the deconvolution.

Conclusion

We have shown how the deconvolution methods proposed by Sader and Jarvis and Giessibl can be implemented for discrete data points. The analysis of the deconvolution methods has shown that both methods work fine when we are considering the coefficient of determination. However, in certain cases there are significant differences in the deconvolution quality with respect to the amplitude dependence. The deviation from the force minimum was found to be 7% for both methods in the worst case. The matrix method is very sensitive to the ratio A/d of the amplitude A and the step width d of the $\Delta f(z_i)$. The deconvolution can always be optimized by using this method either by taking an integer value of A/d or by interpolating the data to an integer or very large ratio. The deviations with the Sader–Jarvis method do not originate from the discrete nature of the data points. Therefore, interpolation does not increase the deconvolution quality. The quality is related to the ratio of the amplitude and the characteristic decay length of the force due to the approximation used. For a Morse force law with a decay constant κ it was found that optimal deconvolution is reached for $\kappa A = 1.5$. Generally, the matrix method provides the higher deconvolution quality, as the data, if necessary, can always be interpolated to equidistant points with a high integer ratio A/d. If additional data processing is not desired and the data is given in a low or unsuitable ratio A/d, the Sader–Jarvis method provides a good alternative.

Supporting Information

Supporting Information File 1

Implementation of the Sader–Jarvis and the matrix force deconvolution algorithm in MATLAB [20].
[http://www.beilstein-journals.org/bjnano/content/supplementary/2190-4286-3-27-S1.zip]

Acknowledgements

We acknowledge Alfred. J. Weymouth, Matthias Emmrich and Thomas Hofmann for help and discussion.

References

1. Binnig, G.; Quate, C. F.; Gerber, C. *Phys. Rev. Lett.* **1986,** *56,* 930–933. doi:10.1103/PhysRevLett.56.930
2. Ternes, M.; Lutz, C. P.; Hirjibehedin, C. F.; Giessibl, F. J.; Heinrich, A. J. *Science* **2008,** *319,* 1066–1069. doi:10.1126/science.1150288
3. Sugimoto, Y.; Pou, P.; Abe, M.; Jelinek, P.; Pérez, R.; Morita, S.; Custance, O. *Nature* **2007,** *446,* 64–67. doi:10.1038/nature05530
4. Hölscher, H.; Langkat, S. M.; Schwarz, A.; Wiesendanger, R. *Appl. Phys. Lett.* **2002,** *81,* 4428. doi:10.1063/1.1525056
5. Albers, B.; Schwendemann, T.; Baykara, M.; Pilet, N.; Liebmann, M.; Altman, E.; Schwarz, U. *Nanotechnology* **2009,** *20,* 264002. doi:10.1088/0957-4484/20/26/264002
6. Albrecht, T.; Grütter, P.; Horne, D.; Rugar, D. *J. Appl. Phys.* **1991,** *69,* 668–673. doi:10.1063/1.347347
7. Giessibl, F. J. *Rev. Mod. Phys.* **2003,** *75,* 949–983. doi:10.1103/RevModPhys.75.949
8. Gotsmann, B.; Anczykowski, B.; Seidel, C.; Fuchs, H. *Appl. Surf. Sci.* **1999,** *140,* 314–319. doi:10.1016/S0169-4332(98)00547-9
9. Dürig, U. *Appl. Phys. Lett.* **2000,** *76,* 1203–1205. doi:10.1063/1.125983
10. Dürig, U. *New J. Phys.* **2000,** *2,* 5. doi:10.1088/1367-2630/2/1/005
11. Hölscher, H.; Allers, W.; Schwarz, U. D.; Schwarz, A.; Wiesendanger, R. *Phys. Rev. Lett.* **1999,** *83,* 4780–4783. doi:10.1103/PhysRevLett.83.4780
12. Sader, J. E.; Jarvis, S. P. *Appl. Phys. Lett.* **2004,** *84,* 1801–1803. doi:10.1063/1.1667267
13. Giessibl, F. J. *Appl. Phys. Lett.* **2001,** *78,* 123–125. doi:10.1063/1.1335546
14. Custance, O.; Oyabu, N.; Sugimoto, Y. Force Spectroscopy on Semiconductor Surfaces. In *Noncontact atomic force microscopy;* Morita, S.; Giessibl, F. J.; Wiesendanger, R., Eds.; Nanoscience and Technology, Vol. 2; Springer-Verlag: Berlin, 2009; pp 31–68. doi:10.1007/978-3-642-01495-6_3
15. Giessibl, F. J. *Phys. Rev. B* **1997,** *56,* 16010–16015. doi:10.1103/PhysRevB.56.16010
16. Giessibl, F. J.; Bielefeldt, H. *Phys. Rev. B* **2000,** *61,* 9968–9971. doi:10.1103/PhysRevB.61.9968
17. Abramowitz, M.; Stegun, I. A. *Handbook of Mathematical Functions,* 10th ed.; U.S. Department of Commerce: Washington D.C., 1972.
18. Frequency modulation dynamic force spectroscopy – Determination of Force and Energy vs Separation from Frequency vs Separation Data. http://www.ampc.ms.unimelb.edu.au/afm/bibliography.html (accessed May 31, 2011).
19. Press, W. *Numerical recipes: the art of scientific computing;* Cambridge University Press: Cambridge, 2007.
20. *MATLAB,* R2010b; The MathWorks, Inc: Ismaning, Germany, 2010.
21. Octave. http://www.gnu.org/software/octave/ (accessed May 31, 2011).
22. Schneiderbauer, M.; Wastl, D.; Giessibl, F. J. *Beilstein J. Nanotechnol.* **2012,** *3,* 174–178. doi:10.3762/bjnano.3.18
23. Sader, J.; Uchihashi, T.; Higgins, M.; Farrell, A.; Nakayama, Y.; Jarvis, S. *Nanotechnology* **2005,** *16,* S94. doi:10.1088/0957-4484/16/3/018
24. Giessibl, F. J.; Bielefeldt, H.; Hembacher, S.; Mannhart, J. *Appl. Surf. Sci.* **1999,** *140,* 352–357. doi:10.1016/S0169-4332(98)00553-4

Beilstein Journal of Nanotechnology

Simultaneous current, force and dissipation measurements on the Si(111) 7×7 surface with an optimized qPlus AFM/STM technique

Zsolt Majzik*[1], Martin Setvín[1], Andreas Bettac*[2], Albrecht Feltz[2], Vladimír Cháb[1] and Pavel Jelínek[1]

Full Research Paper

Open Access

Address:
[1]Institute of Physics, Academy of Sciences of the Czech Republic, Cukrovarnicka 10, 162 53, Prague, Czech Republic and [2]Omicron NanoTechnology GmbH, Limburger Strasse 75, D-65232 Taunusstein, Germany

Email:
Zsolt Majzik* - majzik@fzu.cz; Andreas Bettac* - a.bettac@omicron.de

* Corresponding author

Keywords:
AFM; cross-talk; current; dissipation; force; qPlus; STM; tuning fork

Beilstein J. Nanotechnol. **2012,** *3,* 249–259.
doi:10.3762/bjnano.3.28

Received: 30 November 2011
Accepted: 15 February 2012
Published: 15 March 2012

This article is part of the Thematic Series "Noncontact atomic force microscopy".

Guest Editor: U. D. Schwarz

Abstract

We present the results of simultaneous scanning-tunneling and frequency-modulated dynamic atomic force microscopy measurements with a qPlus setup. The qPlus sensor is a purely electrical sensor based on a quartz tuning fork. If both the tunneling current and the force signal are to be measured at the tip, a cross-talk of the tunneling current with the force signal can easily occur. The origin and general features of the capacitive cross-talk will be discussed in detail in this contribution. Furthermore, we describe an experimental setup that improves the level of decoupling between the tunneling-current and the deflection signal. The efficiency of this experimental setup is demonstrated through topography and site-specific force/tunneling-spectroscopy measurements on the Si(111) 7×7 surface. The results show an excellent agreement with previously reported data measured by optical interferometric deflection.

Introduction

The invention of scanning probe techniques, in particular scanning tunneling microscopy (STM) [1] and atomic force microscopy (AFM) [2], had a tremendous impact on our understanding of the physical, chemical and material properties of surfaces and nanostructures at the atomic scale. STM is based on the detection of the tunneling current between a probe and a sample, and it turned quickly into a standard technique widely used to characterize conductive surfaces and to modify objects at the atomic scale. Unfortunately, the requirement of conductive samples strongly prevents the STM technique from potential applications on nonconductive surfaces, e.g., technologically important oxide materials.

This serious limitation was overcome by the introduction of AFM, which detects forces acting between the tip and the sample. Atomic-scale imaging was achieved later on for both conductors and insulators [3] by means of the so-called static mode. The main drawback of static-mode AFM is the presence of a strong tip–sample interaction, which makes scanning destructive for both the tip and sample, and reliable interpretation of the atomic contrast becomes very difficult. The next milestone in AFM history was the introduction of the frequency-modulation (FM)-AFM technique by Albrecht and co-workers [4]. By applying this method Giessibl demonstrated the possibility of achieving true atomic resolution on the prototypical Si(111) 7×7 surface [5]. Among others, this seminal work initiated a fast progression of the FM-AFM technique over the past decade [6,7].

At the beginning, mainly silicon-based cantilevers oscillating with large amplitudes (tens of nanometers) were used, because they possess the important oscillation stability [8-10]. The key factor to achieve atomic resolution is the proper choice of several parameters, for example, the spring constant and the oscillation amplitude (see Table I in [11]). Theoretically, the optimal signal-to-noise ratio (SNR) is achieved at a value of the oscillation amplitude that is comparable with the characteristic decay length (κ_F) of the forces responsible for imaging. Thus, the optimal oscillation amplitude should be on the order of a few angstroms or even less. Furthermore, an additional benefit of a small oscillation amplitude is the reduction of the sensitivity to contributions from long-range forces. Also large-amplitude operation significantly decreases the measured value of the time-averaged current and subsequently reduces the sensitivity in detection of the tunneling current. Therefore the application of small amplitudes in simultaneous AFM/STM experiments seems to be a natural choice.

Consequently, a new kind of sensor was introduced, based on a quartz resonator, into the field of FM-AFM. So far, the most popular and reasonable way to reach the desired small amplitudes is to replace the microfabricated (Si) cantilevers by stiff, piezoelectric quartz tuning forks similar to those used as frequency references in watches. The configuration when one of the prongs is attached to a solid substrate and the free prong acts as a cantilever with the capability of self-sensing, is called qPlus, named by Giessibl [12]. One of the largest benefits of this design is that it has nearly the optimal stiffness for the operation of FM-AFM at low amplitudes while keeping the force sensitivity high enough [13]. Not surprisingly, the qPlus design presented high potential for outstanding atomic-scale imaging from its early stages [14]. In addition, the parts of the qPlus sensor are large enough for assembly of the sensor simply by hand. Let us note that using a length-extensional resonator is another interesting alternative to the qPlus configuration [15,16]. The comparison of their performance is still an open issue in the community [13].

Probably the first measurement of forces acting between the tip and the sample during STM scanning was performed by Dürig et al. [17] already in 1986. Further attempts to perform simultaneous STM and AFM measurements by FM-AFM [18-20] appeared almost a decade ago. Recently, there has been an increasing number of successful simultaneous AFM/STM measurements with coated Si-cantilevers [21-24], qPlus sensors [25-28] and length-extensional quartz resonators [16,29]. The possibility of measuring the interaction forces simultaneously with the flow of electrons between the tip and the sample opens a new horizon in the understanding of elemental processes of the electron transport on surfaces [30] and in clarifying the relationship between the short-range force and the tunneling current in metal contacts [31,32].

Unfortunately, in the case of quartz-based sensors with self-sensing, the presence of the tunneling current may introduce an undesired interference (cross-talk) between the current and the deflection channel. Therefore special attention has to be paid to minimize the impact of this phenomena to a negligible level. Albers et al. [33] already mentioned a kind of coupling of the tunneling current and used, as a solution, a separate wire for the current measurement.

In this paper, we investigated the origin of the coupling between the deflection and the tunneling-current channel. As a result, we show that the cross-talk is a result of the speed limit of the current-to-voltage converter used for detection of the tunneling current and the stray capacitance between the internal connections of the microscope. Based on our findings, we made some modifications of the sensor design and of the internal wiring too. Simultaneous STM/AFM measurements on the Si(111) 7×7 surface with the modified setup were carried out to prove that the cross-talk has no significant impact on the measured quantities. Simultaneously measured force, tunneling current and dissipation are compared to theoretical predictions [34] and with measurements of the optical interferometric deflection [21].

Experimental

General description

The measurements were performed at room temperature with an Omicron VT XA qPlus AFM/STM system operating at a base pressure below 1×10^{-10} mbar. In this experimental setup, the tunneling current is acquired with an in vacuo preamplifier floating at the potential of the bias voltage and the sample holder is grounded. NanoSurf EasyPLL is used for the FM

demodulation and the Omicron MATRIX control system for the data acquisition. The qPlus sensors were built from commercially available tuning forks from Micro Crystal, originally packed in the SMD package MS1V-T1K. The original tuning fork was shortened in order to reach higher sensitivity (charge produced by deflection) [35], which allows us to reach lower amplitudes. The interaction force between the tip and surface atoms was calculated from the measured frequency-shift data by means of the Sader formula [36]. The tunneling current I_t was calculated from the time-averaged tunneling current $<I_t>$ by using a similar approach [37].

Cross-talk between the deflection and the tunneling-current channel

The aim of this section is to discuss the basics of the so-called cross-talk phenomenon, in which interference between the current and deflection channels leads to undesired modulation of the tuning-fork motion. First, we will demonstrate how the modulation of the tunneling-current signal due to dynamic motion of the probe may affect the functionality of the current-to-voltage converter. In particular, we will discuss conditions under which the virtual ground is no longer constant. Combination of the oscillating ground potential with the presence of a stray capacitance between the wires connecting the electrodes to operational amplifiers may induce a current between the channels. This current leads to artificial modulation of the detection channel resulting in the so-called cross-talk phenomena. We will show, that the cross-talk is controlled by three parameters: (i) The resonant frequency f_0 of the fork; (ii) the stray capacitance C_c and (iii) the maximum amplitude of the modulation V_g^{max} of the virtual ground potential. The last parameter is a function of the oscillation amplitude A and the characteristic decay length of the tunneling current κ_I and depends on the characteristics (mainly on the slew rate) of the preamplifier.

In FM-AFM mode, the sensor oscillates with the resonant frequency f_0. Upon a decrease of the tip–sample distance the value of f_0 is changed by Δf due to forces acting between the probe and the sample. If the tip and the sample are conductive, a tunneling current I_t can be detected. The impact of the modulation of the tip–sample distance on the tunneling current is shown in Figure 1. Since the tunneling current depends exponentially on the tip–surface separation z as $I_t(z)=I_0e^{-2\kappa z}$, the harmonic modulation produces sharp peaks in the current signal (Figure 1B). As a consequence, the frequency spectrum of the tunneling current shows higher harmonics of the modulation signal (Figure 1C).

The tunneling current I_t is converted to a voltage signal V_{out} with the current-to-voltage converter (IVC). The circuit diagram of an IVC is presented in Figure 2, where R_f is the feedback

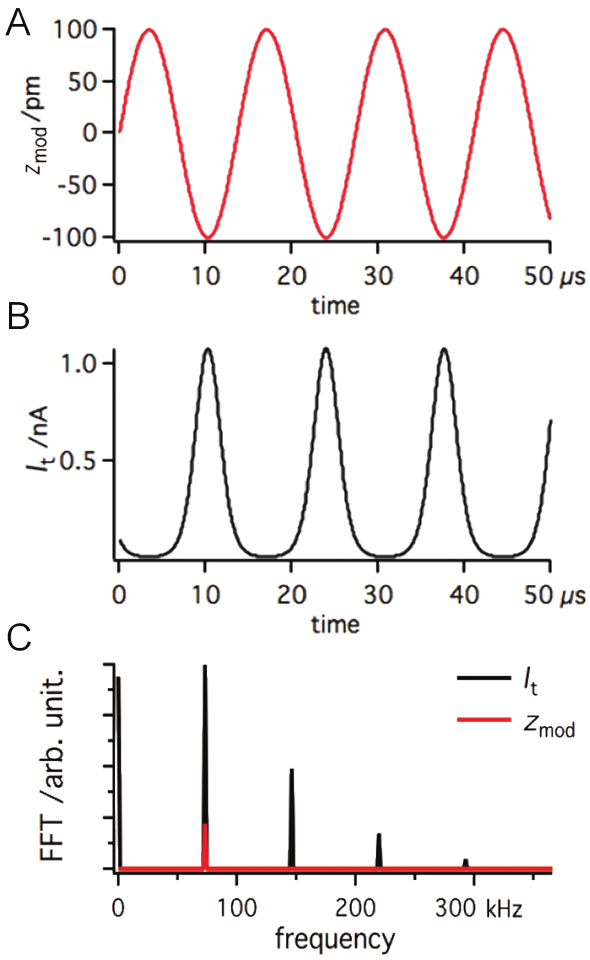

Figure 1: The effect of z modulation (A) on the tunneling current (B). a_{mod} = 0.1 nm and f_0 = 73180 Hz; I_t calculated by using $I_t(z) = I_0e^{-2\kappa z}$ where κ_I = 11.9 nm^{-1} and I_0 = 0.1 nA. In order to see better, the frequency distribution FFT is also shown (C).

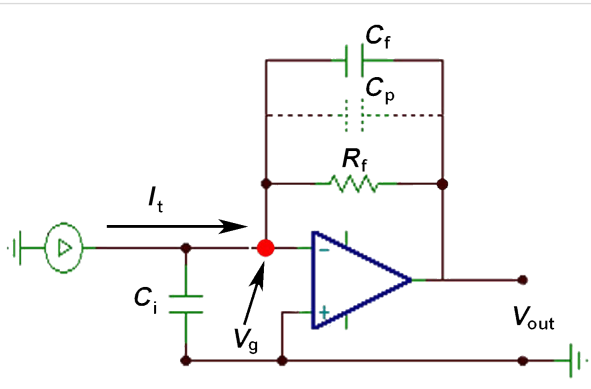

Figure 2: Circuit diagram of a current-to-voltage converter (IVC) where R_f is the feedback resistance with the parallel capacitance C_f. C_i is the input capacitance (in addition to the one of the amplifier). C_p represents the parasitic capacitance of the feedback resistor. The input of the operational amplifier floats at the virtual ground potential (V_g).

resistor with the parallel capacitance C_f and C_i represents the input capacitance caused by cabling. The current passing through the feedback resistor R_f induces a voltage drop that is equal to the value of $R_f I_t$. Due to the potential difference between the input terminals, the operational amplifier (OPA) will change its output voltage V_{out}, compensating the voltage drop to ensure zero potential-difference between the input terminals. Because the inverting input is kept at the ground potential this terminal is called the virtual ground. The output voltage correlated with the tunneling current is $V_{out} = -R_f I_t$.

When working with small values of the tunneling current (on the order of nA) the feedback resistance R_f must be high enough to achieve a reasonable value for the output voltage. However there is a side effect to high-gain operation. The frequency response is strongly reduced as the gain is inversely proportional to the bandwidth. In such a regime, the feedback capacitor C_f plays an important role in the circuit reducing the gain at high frequencies (i.e., eliminates instabilities and prevents self-oscillations). In a real circuit, the parasitic capacitance C_p across the large-feedback resistor R_f (≈100 MΩ) is in the range of a picofarad, which fully covers the function of the feedback capacitor C_f. Therefore, we will consider only the parasitic capacitance C_p in the rest of the discussion.

For circuit analyses we performed numerical simulations with the SPICE-based analog simulation program TINA-TI [38]. The frequency response of the IVC is shown in Figure 3A. For calculations we used the macro model of Op111 with parameters R_f = 100 MΩ, C_p = 1 pF and C_i = 10 pF. The parameter C_i corresponds to the capacitance of the ≈10–15 cm long coaxial cable (depending on the exact type of the cable) making the connection between the tip and the input of the OPA [39].

As already mentioned, the voltage drop will appear on the inverting input of the OPA. The OPA will counteract by producing the same voltage on the output, but with opposite sign to keep the differential voltage at zero between the input terminals. As it can be seen from Figure 3A the output voltage V_{out} varies with the frequency. In terms of currents, the output voltage can be better expressed as $-R_f I_t/(1 + 2\pi f R_f C_p)$ [40]. At small frequencies, the term $2\pi f R_f C_p$ is negligible and the original expression for the output voltage $V_{out} = -R_f I_t$ is recovered. For the frequencies higher than the first frequency pole $f_1 = 1/(2\pi R_f C_p)$ (in our case f_1 = 1.6 kHz) the amplifier gain drops −20 dB/decade, being proportional to $1/f$. In this regime, the amplifier behaves as an integrator circuit and the value of C_p becomes dominant. The voltage at the capacitor is equal to the charge q on the capacitor divided by its capacitance, therefore $V_{out} = q/C_p$. Because the output voltage V_{out} is proportional to the charge, it is also called a charge amplifier. The charge

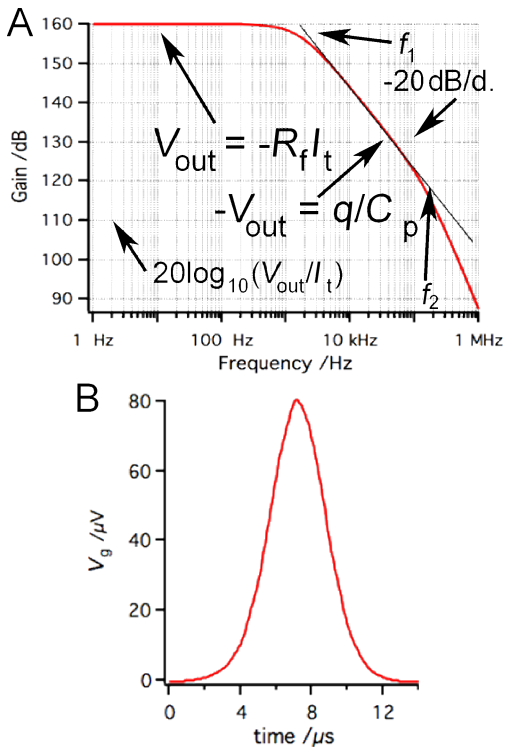

Figure 3: (A) Frequency response of the IVC presented in Figure 2. The following parameters were used to simulate R_f = 100 MΩ, C_p = 1 pF and C_i = 10 pF. (B) The effect of the tunneling current presented in Figure 1 on the virtual ground.

amplification breaks at the second pole in the frequency response (f_2) which is around 110 kHz in this particular example setup.

The optimal function of the IVC is guaranteed as long as the value of the virtual ground potential V_g is held at the ground potential. V_g is kept constant by varying the output voltage V_{out}. The slew rate of the OPA determines the maximum speed at which the output voltage can change. For sinusoidal changes given by $V_{out} = V_{out}^{peak} \sin(2\pi f t)$, the slew rate must exceed

$$\frac{dV_{out}}{dt} = 2\pi f \cdot V_{out}^{peak} \cos(2\pi f t), \quad (1)$$

with the maximum value at $t = 0$:

$$\left(\frac{dV_{out}}{dt}\right)_{max} = 2\pi f \cdot V_{out}^{peak}. \quad (2)$$

For the resonant frequency of the tuning fork (73180 Hz) and the output voltage of 1 V, the maximum speed (dV_{out}/dt) is

0.46 V/µs. The maximum slew rate of Op111 is 2 V/µs which means that optimal operation of the IVC is ensured for output amplitudes <4.3 V at the given frequency. As was already shown in Figure 1, the tunneling current during dynamic AFM measurements contains much higher frequency components than the resonant frequency of the tuning fork. Therefore the OPA may not be able to keep the virtual ground (gap voltage) constant with high precision, due to the speed limit of the amplifier. When data from Figure 1 are used for simulation of the circuit function, V_g shows oscillations with peak amplitudes $V_g^{peak} \approx 80$ µV.

The modulated potential in the current channel may interfere with the input signal of the deflection channel. The coupling of the channels is driven by the stray capacitance C_s (Figure 4). To demonstrate how the crosstalk affects the deflection signal, we analyzed the configuration shown in Figure 4. To simplify the electric circuit, identical amplifiers were used in both channels (Figure 2). For the given resonant frequency f_0 = 73180 Hz the amplifier operates in the charge amplifier regime (Figure 2). To simulate the output from the deflection channel close to our experimental conditions, 3 µC/m sensitivity was used for the sensor [13]. The transmitted signals, shown in Figure 1, were used as input values of the amplifiers in our simulation. Using 100 pm deflection amplitude with a capacitance C_p of 1 pF we obtain an output voltage of approx. 300 µV.

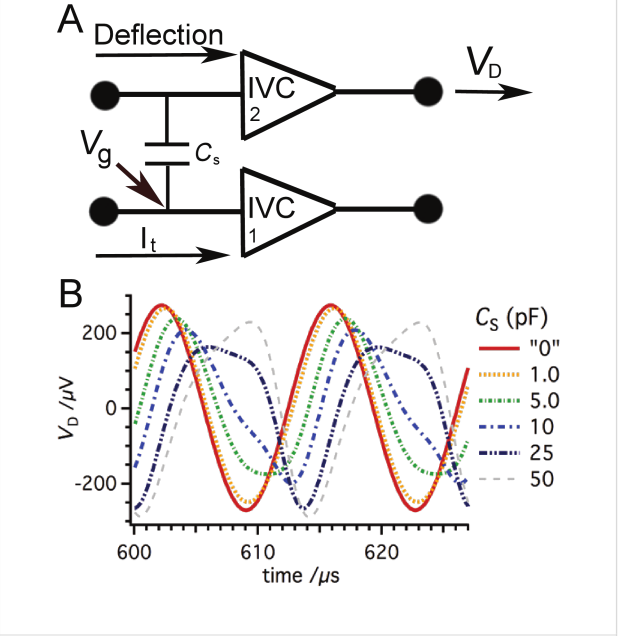

Figure 4: (A) The coupling between the deflection and the tunneling current channel is established by the stray capacitance C_s. To show the effect of the cross talk, signals shown in Figure 1 were used as input values for the amplifiers. (B) The signal in the deflection channel is altered significantly at the output V_D for C_s values exceeding 1 pF.

If the input terminal of the amplifier in the deflection channel is held at the ground potential, the current I_{C_s} due to the stray capacitance between the channels can be expressed as

$$I_{C_s} = C_s \cdot (\mathrm{d}V_g / \mathrm{d}t) . \quad (3)$$

Hence the maximum current $I_{C_s}^{max}$ is defined (using Equation 2 for V_g instead of V_{out}) as

$$I_{C_s}^{max} = 2\pi f C_s V_g^{max} , \quad (4)$$

where V_g^{max} can be estimated by circuit simulations. From Equation 4 we immediately see that the maximum current $I_{C_s}^{max}$ (or in other words the degree of the cross-talk) depends on the value C_s as well as on the resonance frequency f_0 and the maximum amplitude of the ground potential oscillation V_g^{max}. The magnitude of V_g^{max} depends also on the frequency f_0, the oscillation amplitude A and the characteristic decay length of the tunneling current κ_I. Therefore the crosstalk can be enhanced when the sensor is operated at high frequencies. Figure 4 shows that the signal in the deflection channel appears significantly altered at the output, V_D, for C_s values exceeding 1 pF. In the case of a stray capacitance of 5 pF the crosstalk causes a decrease of the initial value of V_D from 273 µV to 250 µV with a 6.8° phase shift. Note here, that by inverting the sign of the bias voltage the result will be different and even larger oscillation signals can be detected.

Together with C_s, the crosstalk depends also on the speed of the amplifier response. It was shown that the virtual ground is modulated when the amplifier response is too slow. The same analysis was carried out with Op637 instead of Op111. The Op637 has a much higher slew rate (≈50 times). The results show that the modulation of the virtual ground is reduced by a factor of 40 (Figure 5A). As a consequence, the crosstalk appears at much higher values of C_s (Figure 5B).

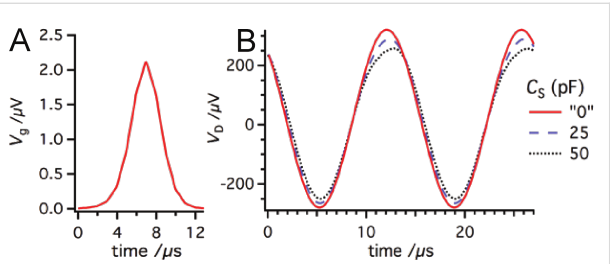

Figure 5: (A) If the slow Op111 is replaced by a faster OPA, Op637, the modulation of the virtual ground V_g^{peak} can be significantly reduced (by a factor of 40). (B) Consequently, the signal in the deflection channel is altered at much higher C_s values.

In conclusion, we showed that the crosstalk between the current channel and the deflection depends mainly on two parameters: (i) The stray capacitance C_s between the channels; (ii) the resonance frequency f of the sensor. The cross-talk alters the detected oscillation amplitude and its phase. The amplitude regulator tends to suppress the artificial oscillation amplitude leading to the appearance of a "dissipation" signal. This can take both positive and negative values. Finally, special attention has to be paid when the tuning fork is used at higher harmonics or higher flexural modes, because the harmonic modulation of the tunneling current can appear in the deflection signal due to the coupling between the channels.

The prevention of the cross-talk phenomena

In a joint project with Omicron Nanotechnology, we evaluated the crosstalk in the qPlus sensor. We suggested several improvements in order to keep the capacitive couplings as low as possible. First, we modified the construction of the sensor. Originally, one of the electrodes of the tuning fork was connected to the deflection amplifier and the second electrode was used for detection of the tunneling current. The tip was glued directly to the electrode. This arrangement of electrodes can lead to self excitations by the AC component of the virtual ground potential at the I_t detection path. The capacitance between the electrodes of the tuning fork acts as a coupling capacitor.

In the new sensor design, the tip is connected with a separate wire (0.25 µm gold) to the OPA for the current channel. The measurement of the tunneling current by means of a separate wire was also reported by other groups [33,41,42]. The electrode originally used for detection of the tunneling current is grounded to create a shielding electrode (Figure 6). The gold wire and the tip on the active prong have to be electrically isolated from the quartz of the prong to avoid self-oscillations of the sensor.

We found that the original ceramic support of the tuning fork with printed wiring increases the capacitance between the tunneling current and the deflection channels. We replaced the ceramics with a metal plate connected to the ground potential. The electrodes of the tuning fork and the tip itself are directly connected to the connector pins. The metal plate now works as an extra shielding between the pins used to connect the current and deflection channels. The modified wiring on the ceramic support, with grounded metal plates on both sides, shows similar electrical properties to those expected for a fully metallic support. Beside the modifications in the sensor design, we replaced the internal coaxial cable making connection between the tip and the tunneling-current amplifier with a double-shielded one, and also the sensor reception stage was

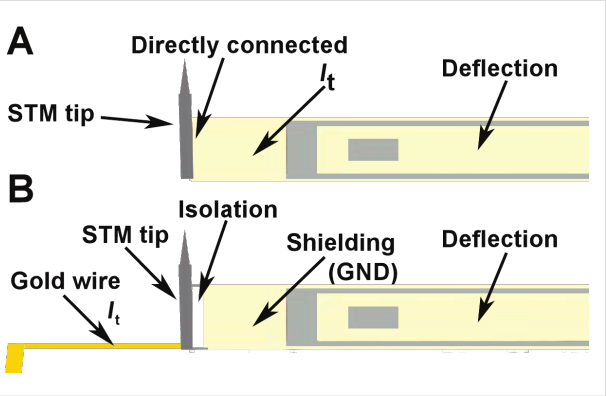

Figure 6: (A) Original connections in which one of the electrodes of the tuning fork was connected to the deflection amplifier and the second electrode was used for detection of the tunneling current. (B) To reduce the capacitance between the channels and eliminate any possibility of self-excitation, the tip is connected by a separated gold wire to the IVC and the electrode originally used for the tunneling current is now grounded. The wire and the tip is electrically isolated from the rest of the fork.

altered to reduce the stray capacitance even further. Moreover, as was already mentioned, the sensitivity of the sensor can be increased by shortening the tuning fork. The higher deflection signal reduces the impact of the cross-talk at a given amplitude compared to sensors having the original length, and lower amplitudes can be reached. Let us note that collecting the tunneling current on the sample side with carefully designed internal wiring can be an alternative option for several microscopes.

Results and Discussion

Force and tunneling current

We performed simultaneous STM/AFM measurements on the Si(111) 7×7 surface using our modified sensor. The measurements were performed in the constant frequency shift mode at room temperature. To compensate for long-range electrostatic forces, the bias voltage was adjusted to the minimum of the Kelvin parabola (generally about +0.4 V). Figure 7 shows a set of images of the average tunneling current $\langle I_t \rangle$ and topography at a constant frequency shift (z) for decreasing tip–sample separation. While we were unable to observe any atomic contrast in the topography signal at Δf setpoints above about −35 Hz (Figure 7A and Figure 7B), the atomic contrast in $\langle I_t \rangle$ was already achieved. Upon approach of the tip further towards the sample, the onset of the short-range chemical force F_{SR} is reached and the atomic contrast in the z map appears. When the setpoint Δf is tuned to more negative values, the atomic corrugation induced by the chemical interaction [43] between the tip apex and the adatoms becomes larger.

In addition, we performed site-specific point spectroscopy [44,45] above Si adatoms. Note that the spectroscopy curves

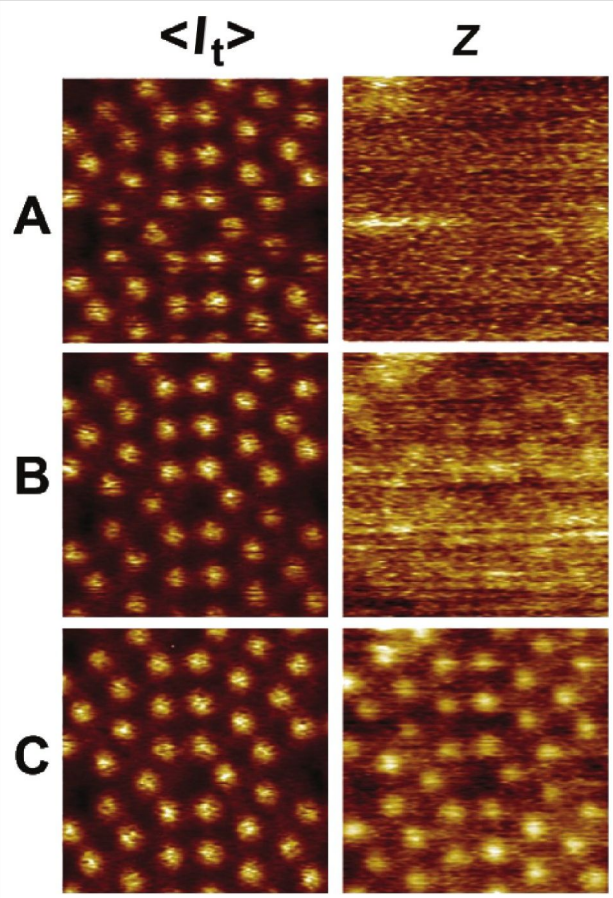

Figure 7: A set of constant-frequency-shift maps (z) and simultaneously recorded average-tunneling-current maps (<I_t>). The frequency-shift setpoints for topographic imaging are (A) −35 Hz, (B) −40 Hz and (C) −45 Hz.

shown in Figure 8A were obtained with a slightly different tip than the maps in Figure 7. To obtain the bare short-range force above an adatom, we subtracted the long-range component of the force measured above the corner hole site. The dependence of the short-range chemical force and the tunneling current on the tip–sample distance is plotted in Figure 8A.

For this particular tip, the short-range force maximum reached 1.5 nN. Both the tunneling current and the short-range force show an exponential dependence, $A(z) = A_0 e^{-2\kappa z}$ where A stands for I_t or F_{SR}, on the tip–sample distance z at large distances (for $z > 0.24$ nm for I_t). We also estimated the characteristic decay lengths of the tunneling current $\kappa_I = 11.9$ nm^{-1} and the short-range force $\kappa_F = 6.3$ nm^{-1}. Comparing the characteristic decay lengths $\kappa_I \approx 1.89 \times \kappa_F$, we immediately find that the tunneling current is proportional to the square of the short-range force ($I_t = F_{SR}^2$). Note that this relation corresponds to the interaction between two localized states degenerate in energy, as was recently predicted theoretically (see a related discussion in [34]).

For distances z smaller than 0.24 nm, the tunneling current is no longer an exponential function of the distance z. It drops significantly due to the substantial modification of the atomic and electronic structure of the surface dangling-bond state [46]. The drop occurs close to the setpoint, at which the short-range force reaches the maxima. Our spectroscopic data agree very well with similar measurements by means of the beam-deflection method [21].

Additionally, we repeated the spectroscopy measurement with the same sensor but with a different tip apex. The tip change was induced by applying a combination of z pulses and voltage pulses. The obtained data show (Figure 8B) a significant reduction of the force maximum of the short-range force $F_{SR} \approx 0.8$ nN. In the weak-interaction regime (here $z > 0.07$ nm), the exponential dependence is presented. However, the character-

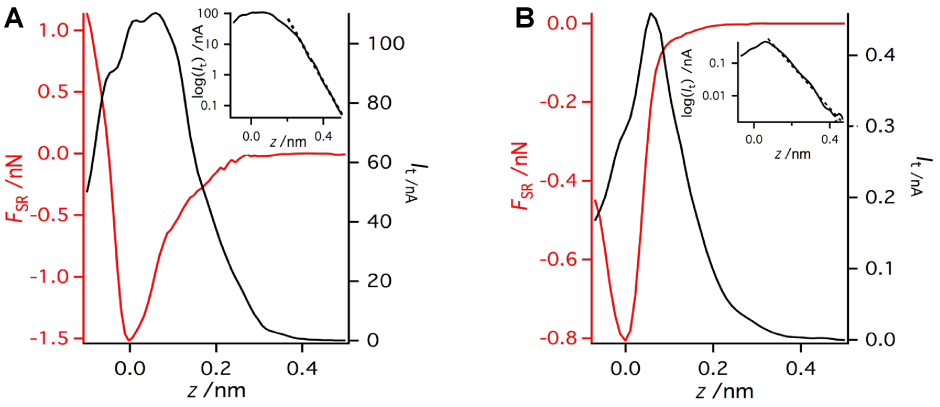

Figure 8: Two typically observed profiles of the dependence of the short-range interaction force (F_{SR}) and the tunneling current (I_t) on the tip–sample separation (z) with a logarithmic plot of I_t in the inset. The first tip termination (A) presents a much stronger attractive short-range interaction than the second (B), and in addition the tunneling current is much smaller in case (B). The acquisition parameters are $f_0 = 73180$ Hz, $a = 0.215$ nm, $k = 3750$ N/m, and $V_{bias} = 0.4$ V.

istic decay length of the tunneling current κ_I = 7.6 nm^{-1} decreases while the decay length of the short-range force increased to κ_F = 6.9 nm^{-1}. The ratio between the characteristic decay lengths is now $\kappa_I \approx 1.10 \times \kappa_F$. Therefore, in this particular case the tunneling current I_t is closely proportional to the chemical force F_{SR}, as has been observed experimentally [32] and predicted theoretically [32,34].

Dissipation signal

The appearance of the dissipation signal and its origin in the FM-AFM experiment has received a lot of both experimental [18,47,48] and theoretical [49-52] attention in recent years. However, a general understanding of the dissipation mechanism is still lacking. Beside the electronic-structure effects [53,54] and adhesion hysteresis at the atomic scale [49,51], there is also a so called "apparent dissipation". Recently Labuda et al. [55] showed that the apparent damping can be attributed to the transfer function of the piezo-acoustic excitation system. Therefore the dissipation signal needs to be carefully analyzed because it is one of the best indicators of the instrumental artifacts. As discussed in the previous section, the cross-talk is accompanied by the presence of a distinct dissipation signal.

Furthermore, the simultaneous measurement of the tunneling current and the frequency shift introduces additional complexity to the origin of the dissipation signal. Recently, Weymouth et al. reported a so called "phantom force" phenomenon [30], in which an additional force arises due to a limited electron transport of injected charge in samples with low conductance. However, not much is known currently about its impact on the dissipation signal.

In this section we analyze the effect of the tunneling current on the dissipation signal. This can be achieved by directly comparing the dissipation and tunneling current above the corner hole and adatom. As clearly shown in Figure 9 the dissipation signals are very similar, despite the strong difference in the magnitude of the tunneling current. Hence it can be concluded that the tunneling current does not directly affect (due to any kind of the cross-talk) the amplitude regulation in our modified experimental setup. One could also note that at room temperature the tunneling current does not give rise to any nonconservative forces in the case of the Si(111) 7×7 substrate.

In order to analyze the long-range dissipation in Figure 9, the relationship between the frequency shift and dissipation was investigated for both tip terminations presented in the previous subsection (reactive "tip A" and less reactive "tip B"). Comparing the frequency shift during the z approach for both tips, we can see that the the long-range forces are more dominant for "tip A".

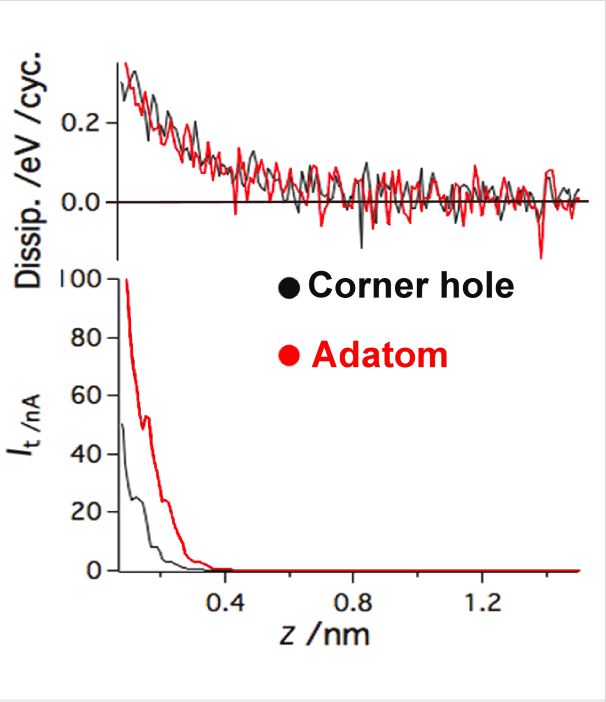

Figure 9: Analyses of the impact of the tunneling current on dissipation. It can be clearly seen that the tunneling current does not affect the dissipation, either directly (by cross-talk) or indirectly by induced nonconservative forces

Interestingly we found that the long-range dissipation signal is correlated with the frequency shifts. In order to see the relationship between the frequency shift and the dissipation signal better, we plot the dissipation as a function of Δf for data measured above the adatoms (see insets in Figure 10). In both cases, the long-range parts show a linear relationship. Furthermore, the slopes are nearly identical in both cases (4.0 ± 0.3) × 10^{-3} eV/Hz for "tip A" and (3.7 ± 0.6) × 10^{-3} eV/Hz for "tip B". The proportional relationship is broken at −76 Hz in the case of "tip A" and −20 Hz in the case of "tip B". The linear dependence between dissipation and Δf suggests that the origin of the dissipation here is more instrumental (apparent) than related to the tip–sample interaction.

The apparent dissipation presented in our data can be explained by means of the effect of the piezo-transducer transfer function reported recently [55]. This idea is supported by the fact that the relationship between the frequency shift and the apparent dissipation in Figure 10 shows the same quantitative characteristics for both data sets. However, other tuning forks (operating at different eigenfrequencies) show different apparent dissipation or even no apparent dissipation at all.

Using the linear dependence of the apparent dissipation signal on Δf, we can define a simple correction function independent of the surface site. Using the correction function, we can

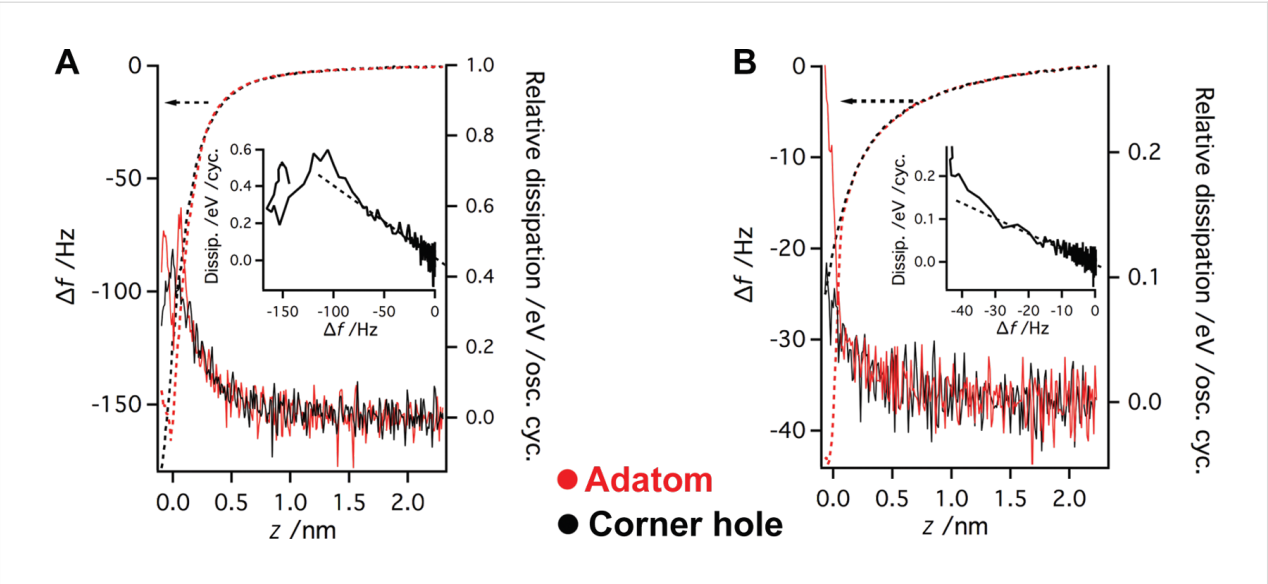

Figure 10: Relationship between the frequency shift and the dissipation for the reactive tip termination (A) and also for the less reactive one (B). Dissipation is plotted with a continuous line and the frequency shift with a dashed line. The corner hole data is marked with black and the adatom with red. In the insets the dissipation is plotted as a function of the frequency shift for the adatom data.

subtract the apparent dissipation signal from the data set. The bare short-range dissipation signal is plotted in Figure 11 together with the short-range interaction for better comparison. The same correction function was applied for damping measured above the corner hole as well. The dissipation signal becomes flat after the correction at large distances. A minor increase of the dissipation signal appears upon the onset of the chemical force above the adatom site. Therefore, we can attribute the origin of the dissipation signal to the adhesion hysteresis [49].

Conclusion

We presented a modification of an Omicron qPlus VT system, designed to avoid crosstalk between the deflection and the tunneling-current channels. In the new design of the sensor, the current-to-voltage converter of the STM is connected directly to the tip with a gold wire. Beside separating the tunneling-current signal, it was necessary to replace the original ceramic support by a metal one in order to reduce the capacitive coupling between the channels. The site-specific force/tunneling-current measurements on the Si(111) 7×7 surface show excellent agreement with the published results obtained with an optical beam-deflection system. The sudden decrease of the tunneling current [46] caused by the formation of a covalent bond between the tip and the sample was clearly repeated, as in the previous work. Analysis of the dissipation signal shows that the tunneling current does not induce artificial damping up to 100 nA at room temperature. The dissipation detected by the amplitude regulator is the result of mainly two contributions. The first one, which has a long-range characteristic, is related to the instrumentation and can be subtracted. The second one appears only above the adatom site after the tip approach exceeds the position of the maximum of the short-range attractive force. We attribute the second contribution to the adhesion hysteresis [49].

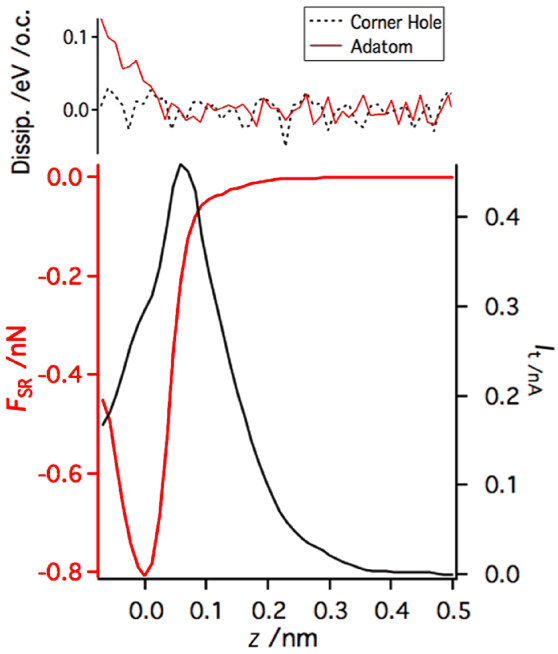

Figure 11: Corrected dissipation for damping measured above the adatom and above the corner hole. The corner hole shows only nondissipative interactions. The adatom starts to show dissipation when the *z* approach reaches and exceeds the force maximum.

Acknowledgements

This work has been supported by the GAAV grants No. M100100904 and No. IAA100100905 and the GAČR projects No. 204/10/0952, No. 202/09/H041 and Ministry of Education No. ME 10076. The authors give thanks to Franz J. Giessibl and all of his group, especially to Maximilian Schneiderbauer, for all the help and valuable discussions. Finally, we thank Martin Švec for all his support during our experiment.

References

1. Binnig, G.; Rohrer, H.; Gerber, C.; Weibel, E. *Phys. Rev. Lett.* **1982,** *49,* 57. doi:10.1103/PhysRevLett.49.57
2. Binnig, G.; Quate, C.; Gerber, C. *Phys. Rev. Lett.* **1986,** *56,* 930. doi:10.1103/PhysRevLett.56.930
3. Binnig, G.; Gerber, C.; Stoll, E.; Albrecht, T.; Quate, C. *Surf. Sci.* **1987,** *189-190,* 1. doi:10.1016/S0039-6028(87)80407-7
4. Albrecht, T.; Grütter, P.; Horne, D.; Rugar, D. *J. Appl. Phys.* **1991,** *69,* 668. doi:10.1063/1.347347
5. Giessibl, F. J. *Science* **1995,** *267,* 68. doi:10.1126/science.267.5194.68
6. Morita, S.; Wiesendanger, R.; Meyer, E. In *Noncontact Atomic Force Microscopy;* Avouris, P.; von Klitzing, K.; Sakaki, H.; Wiesendanger, R., Eds.; Nanoscience and Technology; Springer: Berlin, Heidelberg, 2002.
7. Morita, S.; Giessibl, F. J.; Wiesendanger, R. In *Noncontact Atomic Force Microscopy;* Avouris, P.; von Klitzing, K.; Sakaki, H.; Wiesendanger, R., Eds.; Nanoscience and Technology, Vol. 2; Springer: Berlin, Heidelberg, 2009.
8. Giessibl, F. J.; Bielefeldt, H.; Hembacher, S.; Mannhart, J. *Appl. Surf. Sci.* **1999,** *140,* 352. doi:10.1016/S0169-4332(98)00553-4
9. Garcia, R.; Perez, R. *Surf. Sci. Rep.* **2002,** *47,* 197. doi:10.1016/S0167-5729(02)00077-8
10. Giessibl, F. J.; Hembacher, S.; Herz, M.; Schiller, Ch.; Mannhart, J. *Nanotechnology* **2004,** *15,* S79. doi:10.1088/0957-4484/15/2/017
11. Giessibl, F. J. *Rev. Mod. Phys.* **2003,** *75,* 949. doi:10.1103/RevModPhys.75.949
12. Giessibl, F. J. *Appl. Phys. Lett.* **1999,** *74,* 4070. doi:10.1063/1.123265
13. Giessibl, F.; Pielmeier, F.; Eguchi, T.; An, T.; Hasegawa, Y. *Phys. Rev. B* **2011,** *84,* 125409. doi:10.1103/PhysRevB.84.125409
14. Giessibl, F. J. *Appl. Phys. Lett.* **2000,** *76,* 1470. doi:10.1063/1.126067
15. An, T.; Eguchi, T.; Akiyama, K.; Hasegawa, Y. *Appl. Phys. Lett.* **2005,** *87,* 133114. doi:10.1063/1.2061850
16. An, T.; Nishio, T.; Eguchi, T.; Ono, M.; Nomura, A.; Akiyama, K.; Hasegawa, Y. *Rev. Sci. Instrum.* **2008,** *79,* 033703. doi:10.1063/1.2830937
17. Dürig, U.; Gimzewski, J. K.; Pohl, D. W. *Phys. Rev. Lett.* **1986,** *57,* 2403. doi:10.1103/PhysRevLett.57.2403
18. Loppacher, Ch.; Bammerlin, M.; Guggisberg, M.; Schär, S.; Bennewitz, R.; Baratoff, A.; Meyer, E.; Güntherodt, H.-J. *Phys. Rev. B* **2000,** *62,* 16944. doi:10.1103/PhysRevB.62.16944
19. Schirmeisen, A.; Cross, G.; Stalder, A.; Grütter, P.; Dürig, U. *New J. Phys.* **2000,** *2,* 29. doi:10.1088/1367-2630/2/1/329
20. Hembacher, S.; Giessibl, F. J.; Mannhart, J.; Quate, C. F. *Proc. Natl. Acad. Sci. U. S. A.* **2003,** *100,* 12539. doi:10.1073/pnas.2134173100
21. Sawada, D.; Sugimoto, Y.; Morita, K.-i.; Abe, M.; Morita, S. *Appl. Phys. Lett.* **2009,** *94,* 173117. doi:10.1063/1.3127503
22. Sugimoto, Y.; Yi, I.; Morita, K.-i.; Abe, M.; Morita, S. *Appl. Phys. Lett.* **2010,** *96,* 263114. doi:10.1063/1.3457997
23. Sugimoto, Y.; Nakajima, Y.; Sawada, D.; Morita, K.-i.; Abe, M.; Morita, S. *Phys. Rev. B* **2010,** *81,* 245322. doi:10.1103/PhysRevB.81.245322
24. Sun, Y.; Mortensen, H.; Schär, S.; Lucier, A.-S.; Miyahara, Y.; Grütter, P.; Hofer, W. *Phys. Rev. B* **2005,** *71,* 193407. doi:10.1103/PhysRevB.71.193407
25. Ternes, M.; Lutz, C. P.; Hirjibehedin, C. F.; Giessibl, F. J.; Heinrich, A. J. *Science* **2008,** *319,* 1066. doi:10.1126/science.1150288
26. König, T.; Simon, G. H.; Rust, H.-P.; Heyde, M. *Appl. Phys. Lett.* **2009,** *95,* 083116. doi:10.1063/1.3189282
27. Fournier, N.; Wagner, C.; Weiss, C.; Temirov, R.; Tautz, F. S. *Phys. Rev. B* **2011,** *84,* 035435. doi:10.1103/PhysRevB.84.035435
28. Sun, Z.; Boneschanscher, M. P.; Swart, I.; Vanmaekelbergh, D.; Liljeroth, P. *Phys. Rev. Lett.* **2011,** *106,* 046104. doi:10.1103/PhysRevLett.106.046104
29. Torbrügge, S.; Schaff, S. T. O.; Rychen, J. *J. Vac. Sci. Technol., B: Microelectron. Nanometer Struct.–Process., M eas., Phenom.* **2010,** *28,* C4E12. doi:10.1116/1.3430544
30. Weymouth, A. J.; Wutscher, T.; Welker, J.; Hofmann, T.; Giessibl, F. J. *Phys. Rev. Lett.* **2011,** *106,* 226801. doi:10.1103/PhysRevLett.106.226801
31. Rubio-Bollinger, G.; Joyez, P.; Agraït, N. *Phys. Rev. Lett.* **2004,** *93,* 116803. doi:10.1103/PhysRevLett.93.116803
32. Ternes, M.; González, C.; Lutz, C. P.; Hapala, P.; Giessibl, F. J.; Jelínek, P.; Heinrich, A. J. *Phys. Rev. Lett.* **2011,** *106,* 016802. doi:10.1103/PhysRevLett.106.016802
33. Albers, B. J.; Liebmann, M.; Schwendemann, T. C.; Baykara, M. Z.; Heyde, M.; Salmeron, M.; Altman, E. I.; Schwarz, U. D. *Rev. Sci. Instrum.* **2008,** *79,* 033704. doi:10.1063/1.2842631
34. Jelínek, P.; Ondráček, M.; Flores, F. *J. Phys.: Condens. Matter* **2012,** *24,* 084001. doi:10.1088/0953-8984/24/8/084001
35. Wutscher, E.; Giessibl, F. J. *Rev. Sci. Instrum.* **2011,** *82,* 093703. doi:10.1063/1.3633950
36. Sader, J. E.; Jarvis, S. P. *Appl. Phys. Lett.* **2004,** *84,* 1801. doi:10.1063/1.1667267
37. Sader, J. E.; Sugimoto, Y. *Appl. Phys. Lett.* **2010,** *97,* 043502. doi:10.1063/1.3464165
38. SPICE-Based Analog Simulation Program - TINA-TI. http://www.ti.com/tool/tina-ti (accessed Feb 13, 2012).
39. General Cable - Electronics Catalog. http://catalog.proemags.com/publication/cd728f6b#/cd728f6b/1 (accessed Feb 13, 2012).
40. Hayes, T.; Horowitz, P. *Student Manual for The Art of Electronics;* Cambridge University Press: Cambridge, New York, 1989.
41. Gross, L.; Mohn, F.; Moll, N.; Liljeroth, P.; Meyer, G. *Science* **2009,** *325,* 1110. doi:10.1126/science.1176210
42. Heyde, M.; Sterrer, M.; Rust, H.-P.; Freund, H.-J. *Appl. Phys. Lett.* **2005,** *87,* 083104. doi:10.1063/1.2012523
43. Pérez, R.; Štich, I.; Payne, M. C.; Terakura, K. *Phys. Rev. B* **1998,** *58,* 10835. doi:10.1103/PhysRevB.58.10835
44. Lantz, M.; Hug, H. J.; Hoffmann, R.; van Schendel, P. J. A.; Kappenberger, P.; Martin, S.; Baratoff, A.; Güntherodt, H.-J. *Science* **2001,** *291,* 2580. doi:10.1126/science.1057824
45. Sugimoto, Y.; Pou, P.; Custance, Ó.; Jelínek, P.; Morita, S.; Pérez, R.; Abe, M. *Phys. Rev. B* **2006,** *73,* 205329. doi:10.1103/PhysRevB.73.205329
46. Jelínek, P.; Švec, M.; Pou, P.; Perez, R.; Cháb, V. *Phys. Rev. Lett.* **2008,** *101,* 176101. doi:10.1103/PhysRevLett.101.176101

47. Hoffmann, R.; Lantz, M. A.; Hug, H. J.; van Schendel, P. J. A.; Kappenberger, P.; Martin, S.; Baratoff, A.; Güntherodt, H.-J. *Phys. Rev. B* **2003,** *67,* 085402. doi:10.1103/PhysRevB.67.085402
48. Garcia, R.; Gómez, C. J.; Martinez, N. F.; Patil, S.; Dietz, C.; Magerle, R. *Phys. Rev. Lett.* **2006,** *97,* 016103. doi:10.1103/PhysRevLett.97.016103
49. Kantorovich, L. N.; Trevethan, T. *Phys. Rev. Lett.* **2003,** *93,* 236102. doi:10.1103/PhysRevLett.93.236102
50. Ghasemi, S. A.; Goedecker, S.; Baratoff, A.; Lenosky, T.; Meyer, E.; Hug, H. J. *Phys. Rev. Lett.* **2008,** *100,* 236106. doi:10.1103/PhysRevLett.100.236106
51. Oyabu, N.; Pou, P.; Sugimoto, Y.; Jelínek, P.; Abe, M.; Morita, S.; Pérez, R.; Custance, Ó. *Phys. Rev. Lett.* **2006,** *96,* 106101. doi:10.1103/PhysRevLett.96.106101
52. Kamiński, W.; Pérez, R. *Tribol. Lett.* **2010,** *39,* 295. doi:10.1007/s11249-010-9662-9
53. Cockins, L.; Miyahara, Y.; Bennett, S. D.; Clerk, A. A.; Studenikin, S.; Poole, P.; Sachrajda, A.; Grutter, P. *Proc. Natl. Acad. Sci. U. S. A.* **2010,** *107,* 9496. doi:10.1073/pnas.0912716107
54. Kisiel, M.; Gnecco, E.; Gysin, U.; Marot, L.; Rast, S.; Meyer, E. *Nat. Mater.* **2011,** *10,* 119. doi:10.1038/nmat2936
55. Labuda, A.; Miyahara, Y.; Cockins, L.; Grütter, P. H. *Phys. Rev. B* **2011,** *84,* 125433. doi:10.1103/PhysRevB.84.125433.

License and Terms

Beilstein Journal of Nanotechnology

Pulse-response measurement of frequency-resolved water dynamics on a hydrophilic surface using a Q-damped atomic force microscopy cantilever

Masami Kageshima

Full Research Paper

Open Access

Address:
Department of Physics, Tokyo Gakugei University, 4-1-1 Nukui-kita-machi, Koganei, Tokyo 184-8501, Japan

Email:
Masami Kageshima - masami@u-gakugei.ac.jp

Keywords:
atomic force microscopy; hydration; pulse-response; quality-factor control; viscoelasticity

Beilstein J. Nanotechnol. **2012,** *3,* 260–266.
doi:10.3762/bjnano.3.29

Received: 22 November 2011
Accepted: 03 February 2012
Published: 19 March 2012

This article is part of the Thematic Series "Noncontact atomic force microscopy".

Guest Editor: U. D. Schwarz

Abstract

The frequency-resolved viscoelasticity of a hydration layer on a mica surface was studied by pulse-response measurement of a magnetically driven atomic force microscopy cantilever. Resonant ringing of the cantilever due to its 1st and 2nd resonance modes was suppressed by means of the Q-control technique. The Fourier–Laplace transform of the deflection signal of the cantilever gave the frequency-resolved complex compliance of the cantilever–sample system. The significant viscoelasticity spectrum of the hydration layer was successfully derived in a frequency range below 100 kHz by comparison of data obtained at a distance of 300 nm from the substrate with those taken in the proximity of the substrate. A positive value of the real part of the stiffness was determined and is attributed to the reported solidification of the hydration layers.

Introduction

Liquid solvation is a phenomenon common to a large variety of liquid–solid interfaces [1]. In particular, water solvation, or hydration, on hydrophilic surfaces has drawn interest because of its relevance to biological phenomena on the molecular scale. The dynamical properties of hydrated water have been reported to largely differ from those of bulk water based on the analysis of results from various macroscopic experimental approaches [2-4]. Among the new experimental methods developed in the last few decades, atomic force microscopy (AFM), which was originally invented as an imaging method, has also manifested its potential as a site-specific profiling tool of force interaction. Utilizing the high spatial resolution of AFM, various intriguing properties of liquid solvation [5-19], especially hydration [8,9,11-15,18,19], have been newly revealed. It should be noted that, in addition to its high spatial resolution, AFM possesses a distinguished aptitude for dynamical measurements, which is

mainly due to the cantilever sensor having the character of a well-defined oscillator. Measurement of the complex response function to oscillatory stress of the sample under study, i.e., the viscoelasticity, is a common approach for studying the dynamical properties of matter, especially so-called soft matter.

It is remarkable that the time-scales of hydration dynamics reported, based on AFM [11,13,15,19] and other mechanical measurements [20,21], differ by orders of magnitude from even those reported from conventional macroscopic hydration measurements, and thus are enormously longer than the bulk value of about 8 ps derived from dielectric relaxation measurements. Here it should be noted that the dielectric measurements detect rotational relaxation of the molecules and therefore should not necessarily coincide with mechanical measurements, such as AFM, in which the translational motion of molecules is considered to play a role. Microscopic viscoelasticity measurements using the AFM hold the potential to approach water hydration from an aspect that has been little explored. At the moment viscoelasticity measurements of hydrated water using the AFM have mostly been carried out only at a single frequency. As a matter of course, interest is oriented toward the mapping of the frequency-resolved viscoelasticity spectrum. The number of reports of the frequency-resolved viscoelasticity analysis of soft matter using the AFM is quite limited [22-25].

Using the method of exciting the AFM cantilever with a well-characterized magnetic force [26,27], attempts have been made to measure the frequency-resolved viscoelasticity spectrum of soft-matter systems. The most straightforward approach is a frequency-domain measurement, in which an oscillatory stress is applied to the cantilever interacting with the sample while its frequency is swept, and the viscoelasticity of the sample is derived from the transfer function of the cantilever response. This was applied to a single polymer chain tethered between the probe and the substrate [24]. Another approach contrasting with the frequency-domain measurement is a time-domain measurement in which the time-dependent response to a stress pulse or step is analyzed [28]. Implementation of a simple step-response measurement based on AFM was exemplified previously [25]. In this measurement a step stress is applied to the cantilever and the response signal $u(t)$ is converted to the corresponding frequency response function, i.e., a complex compliance $\hat{J}(\omega) = J'(\omega) - iJ''(\omega)$, by Fourier–Laplace transformation as,

$$\begin{pmatrix} J'(\omega) \\ J''(\omega) \end{pmatrix} = \int_0^\infty \frac{\mathrm{d}u(t)}{\mathrm{d}t} \begin{pmatrix} \cos\omega t \\ \sin\omega t \end{pmatrix} \mathrm{d}t. \qquad (1)$$

Actually, the time differentiation of $u(t)$ required prior to Fourier–Laplace transformation is disadvantageous with respect to the signal-to-noise ratio. In the previous report of the step-response measurement the inferior signal-to-noise ratio of the signal hindered detailed analysis. In the present report a pulse-response measurement in which differentiation of the response signal can be dispensed with is described. The viscoelastic response of water in the proximity of hydrophilic mica surface is extracted as a frequency spectrum.

Results and Discussion

The experimental setup for the magnetic control of the cantilever is essentially similar to the one reported previously [25] and is briefly described below. Since in the present approach the viscoelastic response of the composite system of the cantilever and sample is measured, if the response of the cantilever is too strong it can screen the contribution of the sample. In order to suppress the resonant response of the cantilever the technique of quality-factor-control (Q-control) [29] is employed. The device for magnetic driving of the cantilever consists of two sections; a Q-control circuit for suppression of resonant ringing and a wide-band electromagnet driver, as shown in Figure 1. The Q-control section has an op-amp differentiator, for conversion of the cantilever deflection into velocity, and an amplifier. Although it is ideal to suppress multiple resonance modes independently, the implementation is not realistic; independent setting of feedback gains requires filters in the circuit, which would inevitably perturb its phase response. It is much more practical to cover multiple resonance modes with a single differentiator having a fairly large bandwidth. Since the gain of a differentiator is proportional to the frequency, a cutoff frequency $f_c = (2\pi R_i C_i)^{-1}$ is set to ca. 80 kHz. Figure 2 shows the gain and phase of the Q-control section measured with its pulse input shunted to the ground and the amplifier gain set to the typical operational condition. It is well known that an ideal differentiator has a gain proportional to the frequency and a phase at 90 degrees to that of the input. In Figure 2, the differentiated signal can be detected above the noise at around 1 kHz and the phase reaches 90 degrees at around 4 kHz. The influence of the cutoff, however, soon starts to make it deviate from 90 degrees as the frequency increases. Since a phase error of 45 degrees is often used as a standard for secure feedback, the operation range of this Q-control circuit is evaluated to be from 1.2 to 60 kHz, over which also the gain is almost linear with the frequency. As an inevitable result of using the differentiator, the gain of the Q-control feedback increases with the frequency. This is, however, advantageous in compensating the increase in effective stiffness with mode number [30]. The subsequent electromagnet-driver section is a constant-current amplifier that detects the load current through a resistor inserted in series with the load and keeps it proportional to the input voltage signal with the help of a wideband amplifier inserted in the feedback loop.

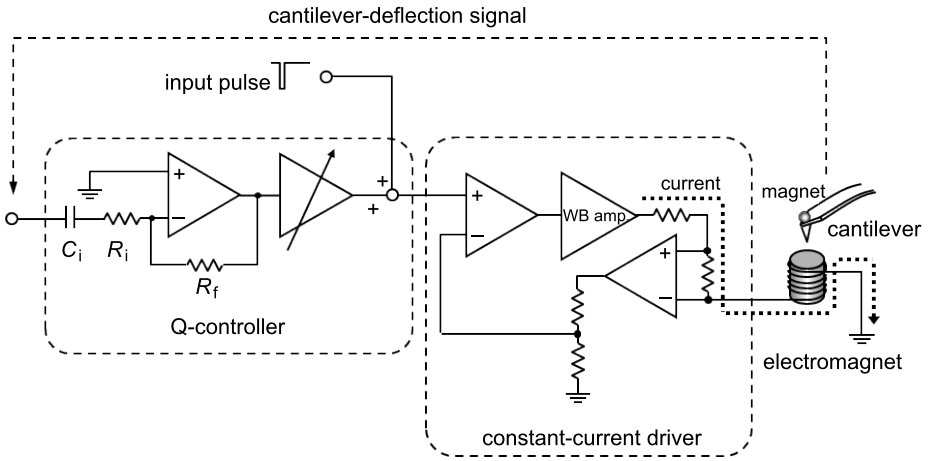

Figure 1: Schematic diagram of cantilever regulation by means of magnetic force. The system consists of a Q-control circuit with a differentiator and a wide-band constant-current driver.

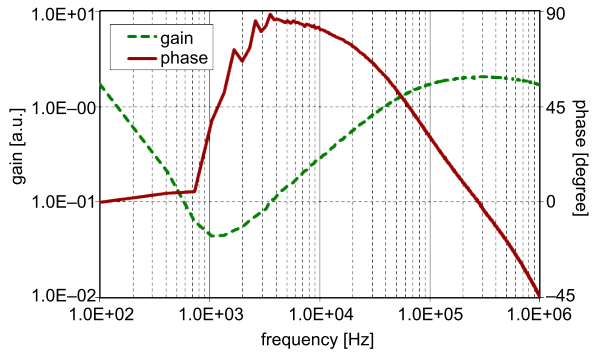

Figure 2: Transfer function of the differentiator in the Q-control circuit with a cutoff frequency of about 80 kHz. The solid and broken lines indicate phase and gain, respectively.

The net bandwidth of the constant-current driver and the electromagnet is larger than 1 MHz [24,25], which is sufficient for the present measurement.

The measurement was carried out with a 0.03 N/m silicon nitride cantilever integrated with a probe tip. The tip surface was cleaned by UV irradiation in air prior to the installation. After the tip was brought into contact with a freshly cleaved mica substrate, the sample stage of the AFM apparatus was readjusted to give an appropriate tip–substrate separation. For the reduction of noise, the wave data were averaged 256 times. Prior to the measurement a 500 Hz square wave with a duty cycle of 50% was applied to the driving circuit for Q-control gain adjustment. Figure 3a shows the input wave, the current in the electromagnet, and the cantilever deflection recorded with a Q-control gain of zero at a tip–substrate separation of ca. 700 nm. The cantilever deflection shows undulation due to the 1st mode resonance and also a spikelike shoulder due to the 2nd mode. With the Q-controller gain adjusted, the feedback action is superimposed on the current and the ringing features in the deflection signal disappear as shown in Figure 3b. Although the profile of the actual coil current is no longer identical to the input signal due to the Q-control feedback as shown in

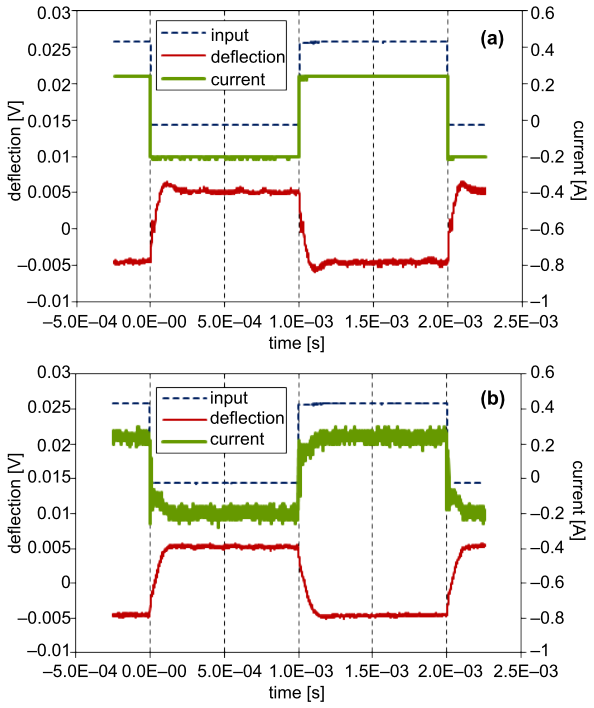

Figure 3: Effect of Q-control on the step-response of the cantilever recorded at about 700 nm from a mica substrate in water with zero Q-control gain (a) and with the optimum gain (b). The fine broken, thick solid, and fine solid lines indicate the input-voltage signal, current in the electromagnet, and cantilever deflection, respectively. The cantilever swing amplitude corresponds to about 4 nm.

Figure 3b, a simple consideration of the transfer function reveals that the situation is effectively identical to the case of driving a virtual, resonance-free cantilever with the input waveform [25]. The Q-control gain was fixed to this value throughout the measurement. Figure 4 shows a comparison of the power spectrum density (PSD) of thermal noise in the cantilever-deflection signal before and after Q-control gain optimization. The peaks in the noise density at the 1st and 2nd resonance modes are suppressed, whereas the peaks at the 3rd and 4th modes are enhanced as a result of the above-mentioned cutoff frequency, although this is not harmful for the measurement.

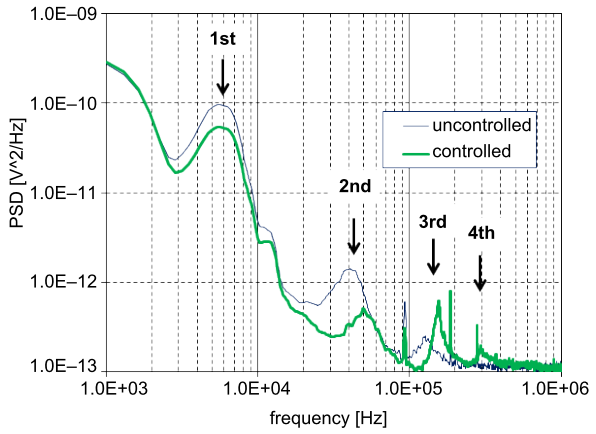

Figure 4: Comparison of the power spectrum density (PSD) of thermal noise in the cantilever-deflection signal before (fine line) and after (thick line) Q-control gain optimization. The peaks in the noise density at the 1st and 2nd resonance modes are suppressed whereas the peaks at the 3rd and 4th modes are enhanced due to the cutoff frequency of 80 kHz.

It is crucial to accurately regulate the tip–substrate distance for a reliable measurement. In the case of the present pulse-response measurement, however, an appropriate signal for feedback regulation is not present. As a compromise, prior to the pulse-response measurement the above mentioned 500 Hz square wave was applied to the driver and the tip–substrate distance was regulated with the amplitude of the 500 Hz component of the cantilever deflection being detected with a lock-in amplifier. By setting the feedback reference to 90% of the full amplitude, the cantilever proved to remain stably at about 1 nm from the substrate. After the distance was stabilized the feedback loop was held and the duty cycle of the input signal was immediately changed to 99.5% so that a square pulse with a duration of 10 μs was applied to the driver circuit. Since a soft cantilever with a nominal spring constant of 0.03 N/m was used, once it drifted into contact with the substrate during data acquisition, it could hardly be separated unless the sample stage was moved. Thus, such data could be readily discriminated after the acquisition and be excluded from analysis.

Figure 5a shows the input pulse signal, the current, and the cantilever deflection at a tip–substrate gap of ca. 300 nm, and Figure 5b the same signals with the tip brought close to the point of contact. Since the feedback of the sample stage is temporarily held during the pulse measurement, the accurate value of the tip–substrate gap is not known for the data shown in Figure 5b. The cantilever deflection signal swings by 2.5 mV, which corresponds to a downward deflection of about 1 nm, and then relaxes to the rest position in both Figure 5a and Figure 5b. Although these two response waveforms seem alike at a glance, a closer look reveals that the one recorded in proximity to the substrate decays faster. The waveform segments corresponding to a time section of 0 to 0.3 ms in Figure 5a and Figure 5b were extracted for analysis.

Figure 6 shows complex compliances

$$\hat{J}_1(\omega) = J_1'(\omega) - iJ_1''(\omega)$$

and

$$\hat{J}_2(\omega) = J_2'(\omega) - iJ_2''(\omega)$$

derived by Fourier–Laplace transformation of the response waveforms shown in Figure 5a and Figure 5b, respectively. One common and pronounced feature in these compliances is a peak at about 3 kHz in the imaginary parts and the corresponding drop in the real parts. These features are typical of a relaxation determined by a single pair of simple elastic and viscous elements, and is immediately attributed to the cantilever response. For further analysis the compliances $\hat{J}_1(\omega)$ and $\hat{J}_2(\omega)$ were inverted to complex elasticities

$$\hat{K}_1(\omega) = K_1'(\omega) + iK_1''(\omega)$$

and

$$\hat{K}_2(\omega) = K_2'(\omega) + iK_2''(\omega)$$

as,

$$K_i'(\omega) = \frac{J_i'(\omega)}{J_i'(\omega)^2 + J_i''(\omega)^2}, \qquad K_i''(\omega) = \frac{J_i''(\omega)}{J_i'(\omega)^2 + J_i''(\omega)^2}, \tag{2}$$

where i = 1,2, as shown in Figure 7a. Since elasticities of parallel mechanical elements are additive, the stiffness of the hydrated water interacting with the probe

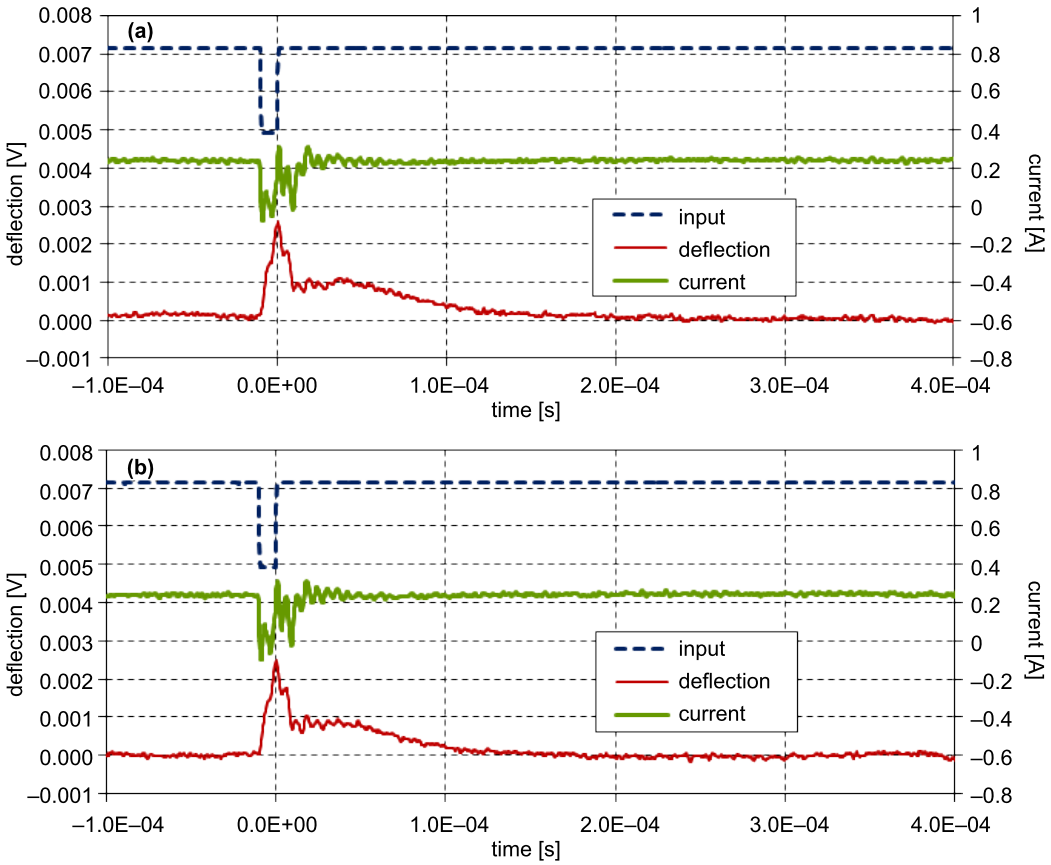

Figure 5: Comparison of pulse responses recorded at 300 nm from the substrate (a) and in close proximity (b). The fine broken, thick solid, and fine solid lines indicate the input-voltage signal, current in the electromagnet, and cantilever deflection, respectively. The cantilever swings toward the substrate with an amplitude of about 1 nm.

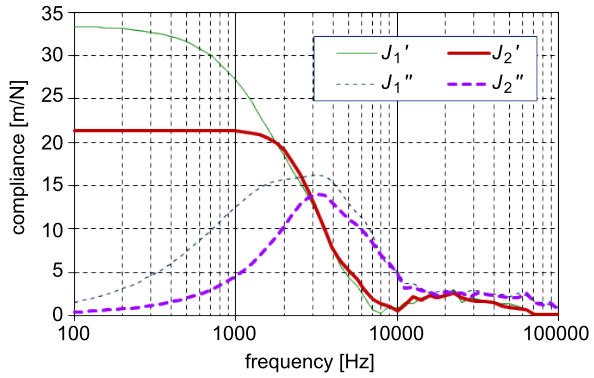

Figure 6: Complex compliance of cantilever–water system calculated by Fourier–Laplace transformation of the response signals in Figure 5(a) and Figure 5(b). The solid and broken lines indicate the real and imaginary parts, respectively, and the fine and thick lines the data at 300 nm and in close proximity, respectively.

$\hat{K}(\omega) = \Delta K'(\omega) + i\Delta K''(\omega) = \hat{K}_2(\omega) - \hat{K}_1(\omega)$ can be derived as shown in Figure 7b. The above mentioned response of the cantilever is well suppressed by subtraction, with the exception of a slight subtraction error, especially evident as a negative value of $\Delta K''(\omega)$ around 1 kHz. Since the original response signal in Figure 5 decays in about 0.3 ms, the elasticity data below 3 kHz is not so informative. Probing a frequency regime below this would require a cantilever having a longer relaxation time in water. Therefore the positive constant value of $\Delta K'(\omega)$ in the low-frequency regime in Figure 7b is not realistic. This is obvious also from the fact that a fluid cannot maintain finite stiffness down to zero frequency unless it is completely solidified. However, this positive value is maintained in the higher frequency regime, and this stiffening accounts for the observed shortening of the relaxation time. On the other hand, $\Delta K''(\omega)$ seems to start increasing above 10 kHz, although it substantially perturbed by noise. Similar behaviors of $\Delta K'(\omega)$ and $\Delta K''(\omega)$ were observed in a different data acquired in the same experimental run, apart from a irreproducible singularity around 6 kHz attributed to the influence of the residual 1st mode resonance of the cantilever. A constant value of $\Delta K'(\omega)$ hints at a system having only a single relaxation time. Then, however, it should show a simple linear increase in $\Delta K''(\omega)$, which seems contrary to the data in

Figure 7b. It is probable that the apparent onset in $\Delta K''(\omega)$ at 10 kHz is actually the point at which the signal reaches a measurable level. For a decisive conclusion a more refined measurement is indispensable.

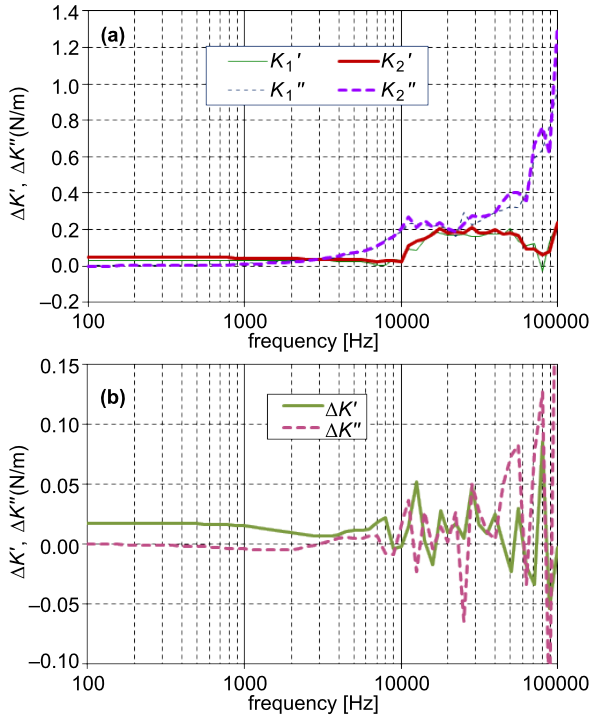

Figure 7: Derivation of the viscoelasticity of hydrated water. The compliance data shown in Figure 6 are inverted to give the elasticity (a). Solid and broken lines indicate the real and imaginary parts, respectively, and fine and thick lines the data at 300 nm and in close proximity, respectively. Subtraction of the two data sets gives the real (solid line) and imaginary (broken line) parts of the viscoelasticity (b).

In the previous report on step-response measurement, the response signal in the cantilever deflection exhibited a substantially longer decay time in the proximity of a mica substrate in water [25]. In the present experiment the result seems quite the contrary, that is, the decay time seems to be rather shortened by hydration, as shown in Figure 5. Although the properties probed by the step-response and pulse-response measurements are basically similar for an elastic sample, these two methods may lead to different outcomes for quasi-fluid samples. A quasi-fluid sample loaded with a step stress continues to relax until it reaches a new equilibrium state. This effect leads to a lateral flow of the fluid and is detected as a long decay time of the cantilever position and hence a large apparent drag coefficient [31]. This lateral flow is considered to cause coupling between the longitudinal response of the hydration layer and its shear property, and thus complicates the data analysis [19]. In the case of the pulse-response measurement, the effect of such a flow is expected to be weaker.

In the present measurement the feedback loop for regulation of the tip–sample gap must be suspended during the period of data acquisition. There is no insurance against fluctuation of the true tip–sample distance due to thermal or mechanical drift, although it was confirmed after data acquisition that the tip had not drifted into contact with the substrate. For further progress it is necessary to combine the present method with operation modes having resolution along the substrate-normal direction, such as the force-profile measurement. It should also be noted that the properties of solvation layers are strongly dependent on the number of layers. In order for the probe not to destroy the layer with the pulse motion, the S/N ratio must be improved such that a pulse with smaller amplitude is sufficient. Since hydration on mica is considered to become distinguished when the film thickness is reduced to several molecular layers, i.e., less than 1 nm, an improved measurement with a smaller pulse magnitude is expected to reveal more detail on the properties of the hydration.

Acknowledgements

The author expresses his gratitude for support from Grant-in-Aid for Scientific Research (20360019).

References

1. Israelachvili, J. N. *Intermolecular and Surface Forces,* 2nd ed.; Academic Press: London, U.K., 1992. And references therein.
2. Nandi, N.; Bagchi, B. *J. Phys. Chem. B* **1997,** *101,* 10954. doi:10.1021/jp971879g
3. Mashimo, S.; Kuwabara, S.; Yagihara, S.; Higasi, K. *J. Phys. Chem.* **1987,** *91,* 6337. doi:10.1021/j100309a005
4. Kabir, S. R.; Yokoyama, K.; Mihashi, K.; Kodama, T.; Suzuki, M. *Biophys. J.* **2003,** *85,* 3154. doi:10.1016/S0006-3495(03)74733-X
5. O'Shea, S. J.; Welland, M. E.; Rayment, T. *Appl. Phys. Lett.* **1992,** *60,* 2356. doi:10.1063/1.107024
6. O'Shea, S. J.; Welland, M. E.; Pethica, J. B. *Chem. Phys. Lett.* **1994,** *223,* 336. doi:10.1016/0009-2614(94)00458-7
7. Cleveland, J. P.; Schäffer, T. E.; Hansma, P. K. *Phys. Rev. B* **1995,** *52,* R8692. doi:10.1103/PhysRevB.52.R8692
8. Jarvis, S. P.; Uchihashi, T.; Ishida, T.; Tokumoto, H.; Nakayama, Y. *J. Phys. Chem. B* **2000,** *104,* 6091. doi:10.1021/jp001616d
9. Antognozzi, M.; Humphris, A. D. L.; Miles, M. J. *Appl. Phys. Lett.* **2001,** *78,* 300. doi:10.1063/1.1339997
10. Lim, R.; O'Shea, S. J. *Phys. Rev. Lett.* **2002,** *88,* 246101. doi:10.1103/PhysRevLett.88.246101
11. Jeffery, S.; Hoffmann, P. M.; Pethica, J. B.; Ramanujan, C.; Özer, H. Ö.; Oral, A. *Phys. Rev. B* **2004,** *70,* 054114. doi:10.1103/PhysRevB.70.054114
12. Uchihashi, T.; Higgins, M.; Nakayama, Y.; Sader, J. E.; Jarvis, S. P. *Nanotechnology* **2005,** *16,* S49. doi:10.1088/0957-4484/16/3/009
13. Maali, A.; Cohen-Bouhacina, T.; Couturier, G.; Aimé, J.-P. *Phys. Rev. Lett.* **2006,** *96,* 086105. doi:10.1103/PhysRevLett.96.086105
14. Fukuma, T.; Higgins, M. J.; Jarvis, S. P. *Phys. Rev. Lett.* **2007,** *98,* 106101. doi:10.1103/PhysRevLett.98.106101

15. Li, T.-D.; Riedo, E. *Phys. Rev. Lett.* **2008,** *100,* 106102. doi:10.1103/PhysRevLett.100.106102
16. de Beer, S.; van den Ende, D.; Mugele, F. *Appl. Phys. Lett.* **2008,** *93,* 253106. doi:10.1063/1.3050532
17. Lim, L. T. W.; Wee, A. T. S.; O'Shea, S. J. *J. Chem. Phys.* **2009,** *130,* 134703. doi:10.1063/1.3096967
18. Fukuma, T.; Ueda, Y.; Yoshioka, S.; Asakawa, H. *Phys. Rev. Lett.* **2010,** *104,* 016101. doi:10.1103/PhysRevLett.104.016101
19. Khan, S. H.; Matei, G.; Patil, S.; Hoffmann, P. M. *Phys. Rev. Lett.* **2010,** *105,* 106101. doi:10.1103/PhysRevLett.105.106101
20. Zhu, Y.; Granick, S. *Phys. Rev. Lett.* **2001,** *87,* 096104. doi:10.1103/PhysRevLett.87.096104
21. Sakuma, H.; Otsuki, K.; Kurihara, K. *Phys. Rev. Lett.* **2006,** *96,* 046104. doi:10.1103/PhysRevLett.96.046104
22. Beumouna, F.; Johannsmann, D. *Eur. Phys. J. E* **2002,** *9,* 435. doi:10.1140/epje/i2002-10096-x
23. Hiratsuka, S.; Mizutani, Y.; Tsuchiya, M.; Kawahara, K.; Tokumoto, H.; Okajima, T. *Ultramicroscopy* **2009,** *109,* 937. doi:10.1016/j.ultramic.2009.03.008
24. Kageshima, M.; Chikamoto, T.; Ogawa, T.; Hirata, Y.; Inoue, T.; Naitoh, Y.; Li, Y. J.; Sugawara, Y. *Rev. Sci. Instrum.* **2009,** *80,* 023705. doi:10.1063/1.3080557
25. Ogawa, T.; Kurachi, S.; Kageshima, M.; Naitoh, Y.; Li, Y. J.; Sugawara, Y. *Ultramicroscopy* **2010,** *110,* 612. doi:10.1016/j.ultramic.2010.02.020
26. Jarvis, S. P.; Oral, A.; Weihs, T. P.; Pethica, J. B. *Rev. Sci. Instrum.* **1993,** *64,* 3515. doi:10.1063/1.1144276
27. Florin, E.-L.; Radmacher, M.; Fleck, B.; Gaub, H. E. *Rev. Sci. Instrum.* **1994,** *65,* 639. doi:10.1063/1.1145130
28. Kubo, R.; Toda, M.; Hashitsume, N. *Statistical Physics II: Nonequilibrium Statistical Mechanics;* Springer-Verlag: Berlin, Germany, 1985.
Example of a time-domain measurement in which a time-dependent response to a stress pulse or step is analyzed.
29. Mertz, J.; Marti, O.; Mlynek, J. *Appl. Phys. Lett.* **1993,** *62,* 2344. doi:10.1063/1.109413
30. Melcher, J.; Hu, S.; Raman, A. *Appl. Phys. Lett.* **2007,** *91,* 053101. doi:10.1063/1.2767173
31. Roters, A.; Johannsmann, D. *J. Phys.: Condens. Matter* **1996,** *8,* 7561. doi:10.1088/0953-8984/8/41/006

License and Terms

Beilstein Journal of Nanotechnology

Junction formation of Cu_3BiS_3 investigated by Kelvin probe force microscopy and surface photovoltage measurements

Fredy Mesa[1,2], William Chamorro[3], William Vallejo[3], Robert Baier[4], Thomas Dittrich[4], Alexander Grimm[4], Martha C. Lux-Steiner[4] and Sascha Sadewasser[*4,5]

Full Research Paper

Open Access

Address:
[1]Universidad Nacional de Colombia, Departamento de Física, Cra. 30 No 45-03, Bogotá, Colombia, [2]Universidad Libre, Departamento de Ciencias Básicas, Cra. 70 No 53-40, Bogotá, Colombia, [3]Universidad Nacional de Colombia, Departamento de Química, Cra. 30 No 45-03, Bogotá, Colombia, [4]Helmholtz-Zentrum für Materialien und Energie, Hahn-Meitner-Platz 1, 14109 Berlin, Germany and [5]International Iberian Nanotechnology Laboratory, Avda. Mestre José Veiga s/n, 4715-330 Braga, Portugal

Email:
Sascha Sadewasser[*] - sascha.sadewasser@inl.int

* Corresponding author

Keywords:
buffer layer; Cu_3BiS_3; Kelvin probe force microscopy; solar cells

Beilstein J. Nanotechnol. **2012,** *3,* 277–284.
doi:10.3762/bjnano.3.31

Received: 02 December 2011
Accepted: 21 February 2012
Published: 23 March 2012

This article is part of the Thematic Series "Noncontact atomic force microscopy".

Guest Editor: U. D. Schwarz

Abstract

Recently, the compound semiconductor Cu_3BiS_3 has been demonstrated to have a band gap of ~1.4 eV, well suited for photovoltaic energy harvesting. The preparation of polycrystalline thin films was successfully realized and now the junction formation to the n-type window needs to be developed. We present an investigation of the Cu_3BiS_3 absorber layer and the junction formation with CdS, ZnS and In_2S_3 buffer layers. Kelvin probe force microscopy shows the granular structure of the buffer layers with small grains of 20–100 nm, and a considerably smaller work-function distribution for In_2S_3 compared to that of CdS and ZnS. For In_2S_3 and CdS buffer layers the KPFM experiments indicate negatively charged Cu_3BiS_3 grain boundaries resulting from the deposition of the buffer layer. Macroscopic measurements of the surface photovoltage at variable excitation wavelength indicate the influence of defect states below the band gap on charge separation and a surface-defect passivation by the In_2S_3 buffer layer. Our findings indicate that Cu_3BiS_3 may become an interesting absorber material for thin-film solar cells; however, for photovoltaic application the band bending at the charge-selective contact has to be increased.

Introduction

Thin-film solar cells based on absorbers made from $Cu(In,Ga)Se_2$ [1] or CdTe [2] reach the highest efficiencies currently available. Both semiconductors are interesting for the application in solar cells because of their excellent absorption properties due to the direct band gap. With the current efforts towards a large-scale fabrication of such solar cells, problems

may occur due to the limited availability of some of the constituents, such as In, Se, Cd or Te, and the respective toxicity of some of these elements. Therefore, current research efforts are exploring alternative, nonconventional, highly absorbing semiconductors to be used in thin-film solar cells. As one possible alternative, it was demonstrated recently that thin films of Cu_3BiS_3 can be prepared in a combination of chemical bath deposition and a sputtering process [3,4]. The band gap of these Cu_3BiS_3 thin films was shown to be ~1.4 eV [3], which makes them an excellent candidate for application in solar cells. It was also shown that thin films prepared by a coevaporation process present good structural and optical properties [5,6]. Recently, the potential of the Cu_3BiS_3/In_2S_3 heterojunction was investigated by surface photovoltage (SPV) and Hall-effect measurements, showing a passivation of surface defect states in the Cu_3BiS_3 by the In_2S_3 buffer layer and the formation of a photovoltaic active interface with a SPV of ~130 mV [7].

It is well known from the $Cu(In,Ga)Se_2$ solar cells that a buffer layer is required between the n-ZnO window and the p-type absorber layer to reach high efficiency values [8]. Traditionally, CdS deposited by chemical bath deposition (CBD) has been used as a buffer layer to reach the highest efficiency figures. However, in recent years intensive research has been performed to avoid the toxic Cd-compound and implement a Cd-free buffer layer [9]. Successfully implemented materials include In_2S_3, ZnS, and $Zn_{1-x}Mg_xO$, deposited by a variety of techniques, such as chemical bath deposition, atomic layer deposition, ion layer gas reaction (ILGAR) deposition, evaporation, and spray deposition [9].

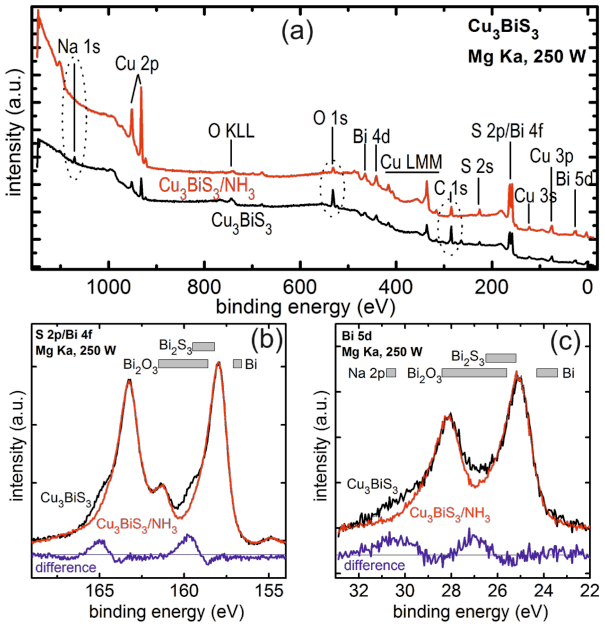

Figure 1: XPS measurements on Cu_3BiS_3 and Cu_3BiS_3 etched in NH_3. (a) Overview spectrum showing that Na, oxides, and C contamination are effectively reduced by the NH_3 etch. (b) Detailed spectrum of the S 2p and Bi 4f peaks showing the presence of Bi_2O_3 in the as-prepared Cu_3BiS_3 layer and its removal by the NH_3 etch. (c) Detailed spectrum of the Bi 5d and Na 2p peak showing the presence of Bi_2O_3 and Na and their effective removal by the NH_3 etch. The blue spectra represent the difference spectra between the as-prepared and the NH_3-etched Cu_3BiS_3 samples.

One interesting aspect of the above mentioned solar cell materials CdTe and $Cu(In,Ga)Se_2$ is their high efficiency despite the abundance of grain boundaries (GBs). Scanning probe microscopy experiments have provided significant insight into the physics of grain boundaries on these materials [10]. Specifically, recent experiments provided evidence for the benign properties of the GBs [11,12], in agreement with previous theoretical work [13,14]. Also the influence of the buffer layer on the grain boundaries was addressed, providing evidence for a diffusion of sulfur from the CdS buffer layer into the grain boundaries of the $Cu(In,Ga)Se_2$ absorber film [15,16].

In this work we present a comparative analysis of the nanoscale optoelectronic properties of Cu_3BiS_3 thin films and different buffer layers, investigated by KPFM, locally resolved SPV measurements, and macroscopic spectral SPV measurements.

Results and Discussion

Chemical surface analysis by X-ray photoelectron spectroscopy (XPS)

For the validity and interpretation of surface-sensitive KPFM measurements, it is important to know the state of the surface of the examined sample. Surface oxidation can modify the work function of the sample and complicate data analysis. To clean the surface of Cu_3BiS_3 samples, we used an NH_3 treatment prior to introduction into the ultrahigh-vacuum (UHV) system of the KPFM. To investigate the effect of this treatment, we analyzed samples exposed to the same NH_3 treatment by XPS. Figure 1a shows an overview XPS spectrum of the as-prepared (lower curve) and NH_3-etched (upper curve) Cu_3BiS_3 samples. The expected peaks of Cu, Bi and S are clearly visible. Additionally, the as-prepared Cu_3BiS_3 sample also shows signals of Na, C and O. Na presumably diffused out of the glass substrate, while C and O are a result of storage in air. The NH_3 etch effectively removes the Na from the surface, while the peak heights of the C and O peaks are significantly reduced. More details about the chemical form in which oxygen is present can be inferred from the detail spectra shown in Figure 1b and Figure 1c. The as-prepared Cu_3BiS_3 sample shows clearly asymmetric peak shapes due to the presence of Bi_2O_3. It is also clear that the NH_3 etch removes these oxide peaks to a large extent. This can be well seen by comparison of the difference

spectra (blue line) with the expected range of the Bi_2O_3 peaks (gray boxes) [17]. The presence of an additional Bi_2S_3 phase cannot be completely excluded from the present measurements. However, the presence of elemental Bi can almost certainly be excluded. The analysis of the S 2s peak (not shown) additionally confirms the removal of sulfate phases by the NH_3 treatment. Therefore, we can unambiguously confirm that the etched surface is in a state nearly free of oxides, which resembles the state of the Cu_3BiS_3 surface onto which the buffer layers from the chemical bath will be deposited.

Surface characterization by Kelvin probe force microscopy (KPFM)

In order to comparatively characterize the growth and electronic properties of the different buffers, we performed KPFM measurements on the Cu_3BiS_3 samples with all three buffer layers, and as a reference also on the pure Cu_3BiS_3 surface after NH_3 etching. Figure 2 shows the results on all surfaces, in which the topography is shown in the upper row, the derivative of the topography in the second row, and the work-function image in the third row; a histogram displaying the work-func-

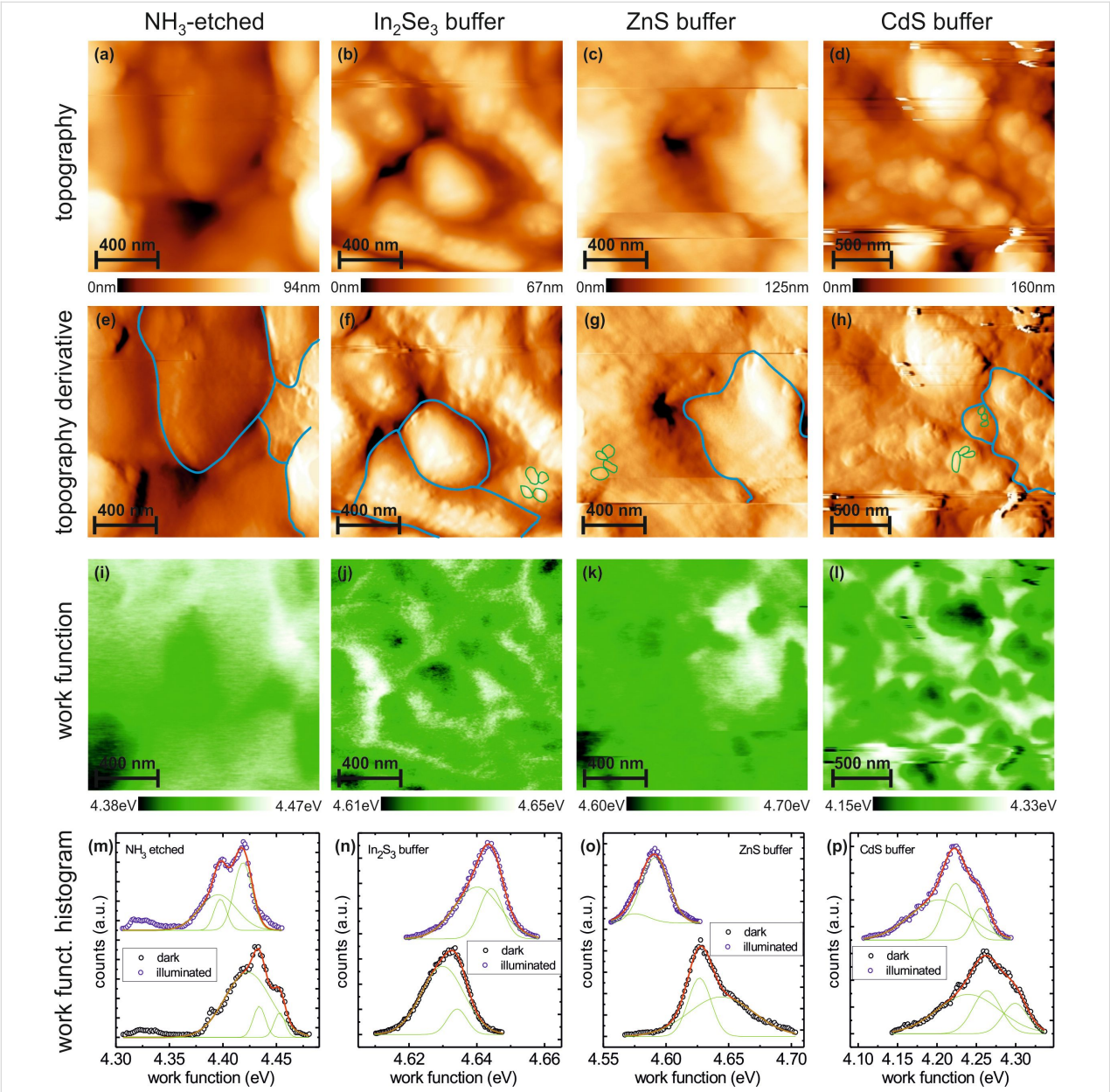

Figure 2: KPFM measurements of the (from left to right) NH_3-etched Cu_3BiS_3, and Cu_3BiS_3 with the In_2S_3, ZnS and CdS buffer layers. The rows show, from top to bottom, the topography image, the derivative image of the topography, and the simultaneously recorded work-function image in the dark. The bottom row shows histograms of the work-function images in the dark (lower curve) and under illumination (upper curve) with respective Gaussian fits to describe the work function distributions.

tion distribution in the dark and under illuminated conditions (red laser, λ = 675 nm, 70 mW/cm^2) is shown in the bottom row. The columns show the surfaces of the NH_3-treated Cu_3BiS_3, and the Cu_3BiS_3 with the In_2S_3, ZnS and CdS buffer layers, from left to right, respectively.

A wealth of information can be extracted from these KPFM images. The topography of all samples shows a granular structure with a grain size on the order of 300 to 600 nm, which corresponds to grains of the Cu_3BiS_3 film. The finer details of the topographic structure are more easily visible in the dz/dx-derivative images presented in the second row of Figure 2. Here a clear difference between the etched Cu_3BiS_3 sample and the samples with a deposited buffer layer is seen. The derivative image of the Cu_3BiS_3 sample shows smooth grain surfaces, whereas the corresponding images of the deposited buffer layers show small grains (exemplarily indicated by green lines) on top of the large grains of the Cu_3BiS_3 film (exemplarily indicated by blue lines). These smaller grains exhibit sizes on the order of 20 to 100 nm and can be attributed to the nanocrystalline nature of the deposited buffer layers.

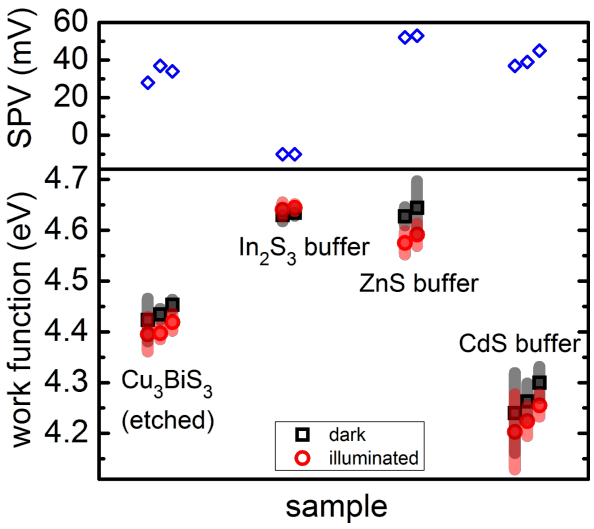

Figure 3: Overview of the measured work-function values and their distribution for all samples investigated. Black squares indicate values for measurements in the dark and red circles for measurements under illumination. The spread of the work function is indicated by the gray and light red bars around the data points.

The work-function images in the third row of Figure 2 provide additional information about the buffer layers and the Cu_3BiS_3 film. The presented images represent the raw data, shifted only by the constant work function of the tip. Due to the rough surface topography, sporadic tip changes could not be avoided (visible as the horizontal streaks). However, since the measured work function does not change abruptly at these tip changes, we can exclude a significant modification of the tip. The spread of the work-function distribution is therefore analyzed in the form of a work-function histogram, represented in the bottom row of Figure 2. The lower histogram represents the work-function measurement under dark conditions, while the upper histogram is measured for an illuminated sample.

The histograms can be fitted very well by two or three Gaussian distributions, where the center of each Gaussian distribution gives the most frequent value of the work function and the standard deviation σ gives a measure of the spread of the values. We would like to point out, that this spread is not to be confused with an error of measurement. It is a real distribution of work function values on the measured surface. The information thus extracted from the histograms is represented in a condensed form in Figure 3, showing for the different samples (on the x-axis) the center of the work function and the spread of the work function values. The values for each Gaussian curve are slightly offset for better visibility.

From Figure 3, it is clearly visible that the spreads of the work-function values for the etched Cu_3BiS_3 film and for the ZnS and CdS buffers on Cu_3BiS_3 are similar, in the range of 10 to 80 meV. In contrast to this, the spread of the Gaussian distribution for the sample with the In_2S_3 buffer is much smaller, only 6–13 meV. These results are in agreement with our previous measurements [7], from which we drew conclusions toward an effective passivation of the Cu_3BiS_3 surface by the In_2S_3 buffer layer.

Defining the surface photovoltage as the difference in work function between the dark and the illuminated state (SPV = $\Phi_{dark} - \Phi_{light}$), we can compare the SPV between the different samples. This is shown in the upper panel of Figure 3. While the etched Cu_3BiS_3 surface and the CdS and ZnS buffer layers exhibit a positive SPV, only the In_2S_3 buffer layer exhibits a negative SPV. This corresponds to charge separation due to band bending at the internal Cu_3BiS_3/In_2S_3 interface when considering a p-type Cu_3BiS_3 and an n-type buffer layer. The positive SPV for the other buffer layers can be interpreted as a separation of holes towards the surface and consequently a reduction of upward band bending. More insight into the effects of the In_2S_3 buffer layer was obtained by a detailed investigation of this surface by macroscopic spectrally resolved SPV (see next section).

A special strength of KPFM is the possibility to obtain locally resolved work-function information, as displayed in Figure 2. Special attention can be devoted to the electronic structure of grain boundaries in these polycrystalline materials. For the NH_3-etched Cu_3BiS_3 sample, only a weak correspondence can

be observed between the topography (Figure 2a) and the work function (Figure 2i), indicating that the charge state at the grain boundaries is similar to that of the grain surface. On the In_2S_3 and CdS buffer layers, the situation is significantly different. The work function images in Figure 2j and Figure 2l show an increased work function at the position of the grain boundaries of the Cu_3BiS_3 film. From the comparison with the small granular structure observed from the images of the topography derivative, it is evident that the increased work function coincides with the grain boundaries of the underlying Cu_3BiS_3 film and not the In_2S_3 or CdS buffer layer. The more positive work function indicates negatively charged grain boundaries in the Cu_3BiS_3 film, in contrast to the NH_3-etched film. The change in work function amounts to 10–20 meV for the In_2S_3 buffer layer and to 60–150 meV for the CdS buffer layer. The size of this upward band bending is in a similar range to the band bending observed for Cu(In,Ga)Se_2 solar-cell absorbers [18]. In contrast to the In_2S_3 and CdS buffer layers, the ZnS buffer layer does not exhibit any significant contrast at the grain boundaries.

Characterization using spectral surface photovoltage (SPV)

Figure 4 shows the in-phase (also called *x*-signal) and 90°-phase-shifted (also called *y*-signal) photovoltage (PV) spectra of Cu_3BiS_3 (a) and Cu_3BiS_3/In_2S_3 (b) samples. The *x*-signal begins at photon energies significantly below the optical band gap of Cu_3BiS_3. For Cu_3BiS_3 the in-phase PV signal is initially positive and increases to about 13 µV with increasing photon energy. Before a strong increase of the signal up to 114 µV at photon energies around 1.24 eV, several sign changes are observed at about 0.79, 0.87, 0.91 and 0.99 eV and respective transitions in between. The *y*-signal shows similar characteristic transitions but without changes of sign.

For the Cu_3BiS_3/In_2S_3 sample the *x*- and *y*-signals exhibit negative and positive signs, respectively, and the signs do not change over the whole spectrum, in contrast to the Cu_3BiS_3 sample. The *x*- and *y*-signals begin at photon energies between 0.9 and 1.0 eV and reach maxima of −0.65 and 0.24 mV at 1.32 and 1.20 eV, respectively. The present case of a negative sign of the *x*-signal together with a positive sign of the *y*-signal can be interpreted as photogenerated electrons being preferentially separated towards the internal interface [19].

Several peaks or changes of the sign in the SPV spectra disappeared after the deposition of In_2S_3 on Cu_3BiS_3. This can be interpreted as the disappearance of surface defect states from which separation of photoexcited charge carriers is possible, i.e., chemical reactions at the Cu_3BiS_3/In_2S_3 interface lead to the passivation of surface-defect states in the band gap of Cu_3BiS_3.

Often it is useful to analyze the amplitude and phase angle instead of the *x*- and *y*-signals; the amplitude is defined as the square root of the sum of the squared *x*- and *y*-signals, and the cotangent of the phase angle is the ratio of the *x*- and *y*-signals.

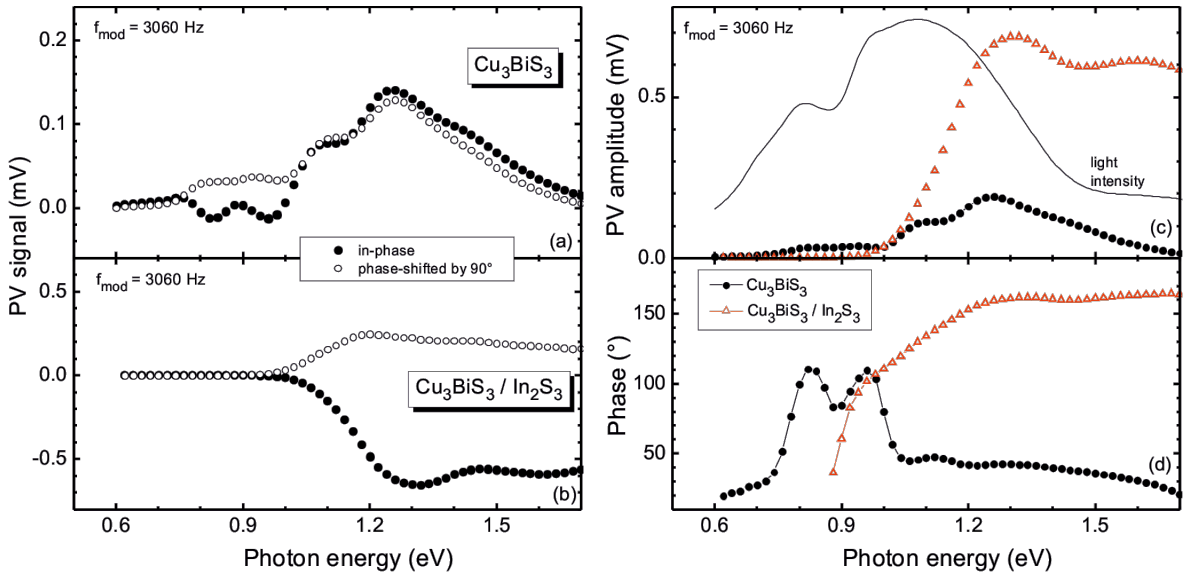

Figure 4: In-phase (solid circles) and 90°-phase-shifted (open circles) SPV spectra of (a) Cu_3BiS_3 and (b) Cu_3BiS_3/In_2S_3 samples at a modulation frequency of 3060 Hz. From these, spectra of the (c) PV amplitude and (d) phase angle for Cu_3BiS_3 (solid circles) and Cu_3BiS_3/In_2S_3 (open triangles) samples were derived. The solid line in (c) gives the light intensity.

The amplitude and phase-angle spectra are shown in Figure 4c and Figure 4d for the Cu_3BiS_3 and Cu_3BiS_3/In_2S_3 samples. Additionally, the spectrum of the light intensity is shown for comparison. There are distinct shoulders and peaks in the amplitude spectra, which are related to the onset of electronic transitions from which charge separation is possible and that depend also on the light intensity. A normalization of SPV spectra to the light intensity or to the photon flux is usually impossible due to the fact that different processes, even with opposite direction of charge separation, may contribute to the SPV signal, making its response highly nonlinear. We would like to point out here that the PV amplitude in the present measurements is much smaller than that found in [7], since the present measurements were performed with modulated light and with a different light source/intensity. On the other hand, the behavior of the phase angle can help to distinguish dominant processes of charge separation and recombination. The peaks in the phase-angle spectrum of the Cu_3BiS_3 sample at 0.83, 0.96 and 1.12 eV can be interpreted, for example, as charge separation from deep defect states with the respective energies above the valence-band edge (excitation of electrons into unoccupied surface states) or below the conduction band edge (excitation of electrons from occupied surface states).

The phase angle of the Cu_3BiS_3/In_2S_3 sample changes strongly from about 35° at 0.88 eV to 161° at 1.32 eV and remains rather constant at higher photon energies, while a change from 160 to 165° can be distinguished between 1.46 and 1.7 eV. A spectral range with a nearly constant value of the phase angle can be understood as a spectral range for which the mechanisms of charge separation, transport and recombination remain similar. This can be the case, for example, at photon energies above the mobility gap if the diffusion length of photogenerated charge carriers is significantly shorter than the absorption length of the exciting light, and if the unmodulated quasi Fermi levels are not very different. Therefore, we can conclude that the mobility gap of Cu_3BiS_3 is about 1.3 eV. Furthermore, photogeneration of charge carriers from defect states leads to the appearance of mobile and immobile charge carriers and therefore to a change of response times. Usually the response times become longer and therefore a change of the phase angle from values close to 180° toward 90° can be expected; this was observed for the Cu_3BiS_3/In_2S_3 sample between 1.3 and 0.94 eV.

Defect states appear differently in PV spectra depending on the modulation frequency, due to the role of response times for different processes. PV amplitude spectra are depicted in Figure 5 for different modulation frequencies. Usually, PV amplitudes decrease with increasing modulation frequency. For the Cu_3BiS_3 sample signatures of the three relatively broad, deep defect levels were observed at all frequencies. We remark that dips in the amplitude spectra could appear, for example, when the sign of SPV signals changed. For better interpretation a correlation of SPV with photocurrent measurements at Cu_3BiS_3 layers would be helpful. Three characteristic spectral regions were distinguished for Cu_3BiS_3/In_2S_3 samples below 0.9 eV (deep defect states), between 0.9 and 1.1 eV (exponential tail states), and above 1.1–1.3 eV (photogeneration of mobile electrons and holes). The PV amplitude of the deep defect states vanishes at frequencies above 1 kHz for the Cu_3BiS_3/In_2S_3 samples. Disorder in the material leads to states in the band gap close to the band edges, resulting in an exponential decay of the SPV. The characteristic energy of these exponential tails can be estimated at about 40 meV for Cu_3BiS_3/In_2S_3 samples at a modulation frequency of 3060 Hz, based on the solid fit line [20].

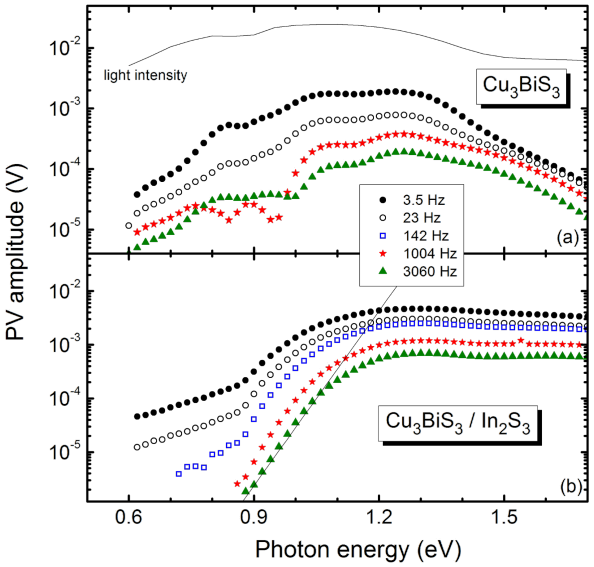

Figure 5: PV amplitude spectra of (a) Cu_3BiS_3 and (b) Cu_3BiS_3/In_2S_3 at modulation frequencies between 3.5 and 3060 Hz. The solid curve in the upper panel gives the light intensity. The straight line in the lower panel shows a fit to the data at 3060 Hz describing exponential tail states [20].

Conclusion

We have analyzed the formation of various buffer layers on Cu_3BiS_3 compound semiconductor films for applications as absorbers in solar cells. The In_2S_3, ZnS, and CdS buffer layers grow as small-grained films (grain size of 20–100 nm) on the Cu_3BiS_3 polycrystalline absorber. The deposition of In_2S_3 and CdS layers appears to charge the grain boundaries of the underlying Cu_3BiS_3 thin film negatively. In agreement with the narrow work-function distribution of the In_2S_3 buffer layer (width of 6–13 meV), the spectral surface photovoltage revealed a passivation of defect states at the absorber/buffer interface, evidenced by a reduction of the sub-band-gap SPV.

To develop the promising Cu_3BiS_3 semiconductor toward an efficient solar cell, future activities should include the investigation of the n-type window layer, i.e., ZnO. This additional n-type layer may also lead to an increased band bending at the pn-junction, thereby leading to better performing solar cells.

Experimental

Sample growth

Cu_3BiS_3 thin films were grown by coevaporation in two stages. In the first stage a Bi_xS_y layer is grown by simultaneous evaporation of Bi and S. In the second stage the Cu_3BiS_3 compound is formed by evaporation of Cu, in a sulfur environment, onto the Bi_xS_y layer, with the substrate temperature kept at 300 °C during the complete process [6]. Layers of Cu_3BiS_3 (thickness about 1 μm) were deposited on glass coated with Al, deposited by dc magnetron sputtering [21]. For analysis by Kelvin probe force microscopy (KPFM) [7], surface photovoltage (SPV), and X-ray photoemission spectroscopy (XPS), sample contact was established at the Al back contact.

CdS thin films were deposited onto the Cu_3BiS_3 layers from a solution containing thiourea (Scharlau) and cadmium chloride ($CdCl_2$) (Merck) as sources of S^{2-} and Cd^{2+}, respectively. The thickness of the films was ~80 nm, as measured with a Veeco Dektak 150 surface profiler. For specific experimental conditions see [22].

ZnS films were grown by coevaporation of metallic precursors evaporated from a tungsten boat for Zn and a tantalum effusion cell for sulfur. The substrate was heated to ~250 °C. A thickness monitor (Maxtec TM-400) with a quartz-crystal sensor was used to measure the deposition rate of Zn. The thickness of the films was ~120 nm, as measured with a Veeco Dektak 150 surface profiler. Details of the ZnS film preparation are given in [23].

In_2S_3 buffer layers were deposited by coevaporation of In and S on the substrate heated to ~300 °C. The deposition system consists of the same components mentioned above for the growth of films of ZnS. The thickness of the films was ~150 nm. Both, the ZnS and the In_2S_3 buffer layers were deposited on NH_3-etched Cu_3BiS_3 films.

X-ray photoelectron spectroscopy

The chemical surface condition of the as-prepared Cu_3BiS_3 and Cu_3BiS_3 etched with NH_3 was analyzed in an ultrahigh-vacuum (UHV) chamber ("CISSY" at Helmholtz-Zentrum Berlin) by X-ray photoelectron spectroscopy [24]. Mg Kα (1253.6 eV) radiation from a SPECS XR 50 X-ray gun served as the excitation source. The emitted photoelectrons were detected by a CLAM 4 electron spectrometer from Thermo VG Scientific. For surface cleaning, the sample was etched in a 3% aqueous NH_3 solution for 150 s at room temperature and transferred through air into the UHV system within less than 5 min.

Kelvin probe force microscopy

Kelvin probe force microscopy measurements were performed in a modified Omicron UHV AFM/STM operating at room temperature and a base pressure $<10^{-10}$ mbar [25], by using the amplitude-modulation technique (AM mode). We used PtIr-coated cantilevers (Nanosensors) with a first resonance frequency of ~75 kHz, measuring the contact potential difference (CPD) using the second resonance mode at ~450 kHz and an ac voltage of 100 mV. For detection of the cantilever oscillation a laser with λ = 980 nm was used, thus avoiding any excitation of the investigated samples. The work function of the surfaces was obtained from the measured CPD by calibration of the tip against a sample of highly oriented pyrolytic graphite with a known work function. The surface photovoltage was determined by illuminating the samples with red laser light (λ = 675 nm, 70 mW/cm^2) and subtracting the work function in the dark [26]. Also for KPFM, samples were NH_3 etched and transferred through air into the UHV system within less than 5 min.

Spectral surface photovoltage

Spectral dependent SPV measurements were performed at −186 °C in the fixed-parallel-plate-capacitor arrangement [27]. A quartz prism monochromator with a halogen lamp was used for modulated excitation (mechanical chopper frequencies between 3.5 Hz and 3 kHz). SPV signals were measured by means of a high-impedance buffer with a dual-phase lock-in amplifier. Spectral SPV experiments were performed on untreated Cu_3BiS_3 samples.

References

1. Jackson, P.; Hariskos, D.; Lotter, E.; Paetel, S.; Wuerz, R.; Menner, R.; Wischmann, W.; Powalla, M. *Progress in Photovoltaics: Research and Applications* **2011,** *19,* 894. doi:10.1002/pip.1078
2. Wu, X. *Sol. Energy* **2004,** *77,* 803. doi:10.1016/j.solener.2004.06.006
3. Gerein, N. J.; Haber, J. A. *Chem. Mater.* **2006,** *18,* 6297. doi:10.1021/cm061453r
4. Estrella, V.; Nair, M. T. S.; Nair, P. K. *Semicond. Sci. Technol.* **2003,** *18,* 190. doi:10.1088/0268-1242/18/2/322
5. Mesa, F.; Calderón, C.; Bartolo-Peréz, P.; Gordillo, G. Study of Cu3BiS3 Thin Films Prepared by Co-Evaporation. In *Proceedings of the 24th European Photovoltaic Solar Energy Conference,* EU PVSEC, Hamburg, Germany, Sept 21–25, 2009; WIP: München, Germany, 2009; pp 243 ff. doi:10.4229/24thEUPVSEC2009-1CV.3.3
6. Mesa, F.; Dussan, A.; Gordillo, G. *Phys. Status Solidi C* **2010,** *7,* 917. doi:10.1002/pssc.200982860
7. Mesa, F.; Gordillo, G.; Dittrich, T.; Ellmer, K.; Baier, R.; Sadewasser, S. *Appl. Phys. Lett.* **2010,** *96,* 082113. doi:10.1063/1.3334728
8. Hariskos, D.; Spiering, S.; Powalla, M. *Thin Solid Films* **2005,** *480,* 99. doi:10.1016/j.tsf.2004.11.118

9. Naghavi, N.; Abou-Ras, D.; Allsop, N.; Barreau, N.; Bücheler, S.; Ennaoui, A.; Fischer, C.-H.; Guillen, C.; Hariskos, D.; Herrero, J.; Klenk, R.; Kushiya, K.; Lincot, D.; Menner, R.; Nakada, T.; Platzer-Björkman, C.; Spiering, S.; Tiwari, A. N.; Törndahl, T. *Progress in Photovoltaics: Research and Applications* **2010,** *18,* 411. doi:10.1002/pip.955
10. Rau, U.; Taretto, K.; Siebentritt, S. *Appl. Phys. A* **2009,** *96,* 221. doi:10.1007/s00339-008-4978-0
11. Hafemeister, M.; Siebentritt, S.; Albert, J.; Lux-Steiner, M. C.; Sadewasser, S. *Phys. Rev. Lett.* **2010,** *104,* 196602. doi:10.1103/PhysRevLett.104.196602
12. Mönig, H.; Smith, Y.; Caballero, R.; Kaufmann, C. A.; Lauermann, I.; Lux-Steiner, M. C.; Sadewasser, S. *Phys. Rev. Lett.* **2010,** *105,* 116802. doi:10.1103/PhysRevLett.105.116802
13. Persson, C.; Zunger, A. *Phys. Rev. Lett.* **2003,** *91,* 266401. doi:10.1103/PhysRevLett.91.266401
14. Yan, Y.; Jiang, C.-S.; Noufi, R.; Wei, S.-H.; Moutinho, H. R.; Al-Jassim, M. M. *Phys. Rev. Lett.* **2007,** *99,* 235504. doi:10.1103/PhysRevLett.99.235504
15. Rusu, M.; Glatzel, T.; Neisser, A.; Kaufmann, C.; Sadewasser, S.; Lux-Steiner, M. C. *Appl. Phys. Lett.* **2006,** *88,* 143510. doi:10.1063/1.2190768
16. Glatzel, T.; Rusu, M.; Sadewasser, S.; Lux-Steiner, M. C. *Nanotechnology* **2008,** *19,* 145705. doi:10.1088/0957-4484/19/14/145705
17. NIST X-ray Photoelectron Spectroscopy Database, Version 3.5. National Institute of Standards and Technology: Gaithersburg, 2003; http://srdata.nist.gov/xps/ (accessed Feb 1, 2012).
18. Sadewasser, S. *Thin Solid Films* **2007,** *515,* 6136. doi:10.1016/j.tsf.2006.12.134
19. Dittrich, T.; Bönisch, S.; Zabel, P.; Dube, S. *Rev. Sci. Instrum.* **2008,** *79,* 113903. doi:10.1063/1.3020757
20. Urbach, F. *Phys. Rev.* **1953,** *92,* 1324. doi:10.1103/PhysRev.92.1324
21. Gordillo, G.; Mesa, F.; Calderón, C. *Braz. J. Phys.* **2006,** *36,* 982. doi:10.1590/S0103-97332006000600049
22. Rieke, P. C.; Bentjen, S. B. *Chem. Mater.* **1993,** *5,* 43. doi:10.1021/cm00025a012
23. Romero, E.; Vallejo, W.; Gordillo, G. Comparative study of ZnS thin films deposited by CBD and coevaporation. In *Proceedings of the 33rd IEEE Photovoltaic Specialist Conference,* San Diego, USA, May 11–16, 2008; IEEE: Piscataway, NJ, 2008. doi:10.1109/PVSC.2008.4922880
24. Lauermann, I.; Bär, M.; Ennaoui, A.; Fiedeler, U.; Fischer, C.-H.; Grimm, A.; Kötschau, I.; Lux-Steiner, M. C.; Reichardt, J.; Sankapal, B. R.; Siebentritt, S.; Sokoll, S.; Weinhardt, L.; Fuchs, O.; Heske, C.; Jung, C.; Gudat, W.; Karg, F.; Niesen, T. P. *Mater. Res. Soc. Symp. Proc.* **2003,** *763,* No. B4.5. doi:10.1557/PROC-763-B4.5
25. Sommerhalter, C.; Matthes, T. W.; Glatzel, T.; Jäger-Waldau, A.; Lux-Steiner, M. C. *Appl. Phys. Lett.* **1999,** *75,* 286. doi:10.1063/1.124357
26. Sadewasser, S. *Phys. Status Solidi A* **2006,** *203,* 2571. doi:10.1002/pssa.200669573
27. Duzhko, V.; Timoshenko, V. Yu.; Koch, F.; Dittrich, T. *Phys. Rev. B* **2001,** *64,* 075204. doi:10.1103/PhysRevB.64.075204

Beilstein Journal of Nanotechnology

Dipole-driven self-organization of zwitterionic molecules on alkali halide surfaces

Laurent Nony[1], Franck Bocquet[1], Franck Para[1], Frédéric Chérioux[2], Eric Duverger[2], Frank Palmino[2], Vincent Luzet[2] and Christian Loppacher[*1]

Full Research Paper

Open Access

Address:
[1]Aix-Marseille Univ, IM2NP, Faculté des Sciences de St. Jérome, F-13397 Marseille France; CNRS, IM2NP, Faculté des Sciences de St. Jérome, F-13397 Marseille France and [2]Institut FEMTO-ST, Université de Franche-Comté, CNRS, ENSMM, 32, Avenue de l'Observatoire, F-25044 Besancon Cedex, France

Email:
Christian Loppacher[*] - Christian.Loppacher@im2np.fr

* Corresponding author

Keywords:
alkali halide surface; noncontact atomic force microscopy; organic molecule; self-organization; zwitterion

Beilstein J. Nanotechnol. **2012,** *3,* 285–293.
doi:10.3762/bjnano.3.32

Received: 21 November 2011
Accepted: 17 February 2012
Published: 27 March 2012

This article is part of the Thematic Series "Noncontact atomic force microscopy".

Guest Editor: U. D. Schwarz

Abstract

We investigated the adsorption of 4-methoxy-4′-(3-sulfonatopropyl)stilbazolium (MSPS) on different ionic (001) crystal surfaces by means of noncontact atomic force microscopy. MSPS is a zwitterionic molecule with a strong electric dipole moment. When deposited onto the substrates at room temperature, MSPS diffuses to step edges and defect sites and forms disordered assemblies of molecules. Subsequent annealing induces two different processes: First, at high coverage, the molecules assemble into a well-organized quadratic lattice, which is perfectly aligned with the <110> directions of the substrate surface (i.e., rows of equal charges) and which produces a Moiré pattern due to coincidences with the substrate lattice constant. Second, at low coverage, we observe step edges decorated with MSPS molecules that run along the <110> direction. These polar steps most probably minimize the surface energy as they counterbalance the molecular dipole by presenting oppositely charged ions on the rearranged step edge.

Introduction

The adsorption of organic molecules on a crystalline substrate surface is governed by a delicate balance between the molecule–molecule (MM) and the molecule–substrate (MS) interaction. The latter can strongly depend on the registry between the organic layer and the inorganic substrate, especially if coincidences between the two lattices are possible (for an overview of the different epitaxial ordering see, for example, [1,2]). On the one hand, for metallic and semiconducting substrate surfaces, there often exists quite a strong MS interaction, which can either be caused by covalent binding or by weak overlap between the π-orbitals of the organic molecule and the electronic states of the surface. On the other hand, for insulating

substrates, the vertical MS interaction is often much weaker than, for example, the intermolecular π-stacking of the organic molecules. Although for certain molecules π-stacking can lead to the formation of one-dimensional wires [3], in general, for organic–inorganic heteroepitaxy (OIHE) on insulating substrates the growth mode is often governed by a dewetting process [4] as the MM interaction dominates.

In the last few years, many studies have been focused on alkali halide surfaces as model systems for the study of OIHE on insulating substrates (for an overview see, for example, [5]). These surfaces are nonreactive, easy to prepare by cleavage of single crystals or by vapour deposition of thin films on metal substrates, and they are atomically well-defined. Different routes have been proposed to circumvent the problem of dewetting since it is the control of a few, down to even single, homogeneous and well-ordered molecular layers that is desired for many applications in molecular (opto-)electronic devices.

As has been shown by Loppacher et al. [6], large and ordered structures are obtained if either the MM or the MS interaction dominates. In the former case, the structures mostly grow in three-dimensional crystallites [7-10]. Only for systems in which the MM interaction was directional, as for example by H-bonding [11] or by covalent bonding [12,13], layer-by-layer growth or even one-dimensional growth [14] was observed. When the MS interaction dominates, monolayer (ML) growth can be obtained more easily. For example, a few systems have been reported in which a metastable phase with a point-on-point epitaxy [15,16] or other well-defined epitaxies [17] were found and single molecular layers were observed. Furthermore, structured monolayer growth was obtained on a nanostructured surface [18].

In our work we study the influence of the molecular dipole on the adsorption of zwitterionic molecules on ionic-crystal (100) template surfaces. The crystals chosen (NaCl, KCl, RbCl, and KBr) all show the same structure (face-centered cubic, or rock salt) and thus provide an identical quadratic pattern of alternating electric charges on the surface, but with a different lattice constant (see below in Table 1). In other heteroepitaxial systems it was often observed that the orientation of an incompressible overlayer depended not only on the parameters during the sample preparation (substrate temperature, evaporation rate), but also on the lattice mismatch between the two structures [9,19]. Therefore, we have chosen the above-mentioned model substrates in order to verify whether the electrostatic MS interaction between the molecular charge distribution and the ions on the substrate surface could be used to force the molecular arrangement along equally charged ⟨110⟩ oriented substrate lines, regardless of the substrate lattice constant.

Experimental

The molecule we used is the zwitterion 4-methoxy-4′-(3-sulfonatopropyl)stilbazolium (MSPS). MSPS molecules were synthesized in accordance with the method previously described by Serbutoviez et al. [20] and Makoudi et al. [21]. MSPS is composed of a sulfonato endgroup (SO_3^-), which carries a negative charge and which is linked via an alkyl-chain to a pyridinum ring carrying a positive charge (N^+). MSPS molecules adopt two main conformations corresponding to the cis/trans isomerization of the C–C double bond. Cis (agraffe-like) and trans (scorpion-like) are described in Figure 1. However, only the scorpion-like isomer is obtained after the synthesis, because it is more stable than the cis isomer. The permanent electric dipole of the trans isomer is 16.8 D, the total length of this isomer is 1.28 nm. Due to the isomerization of the C–C double bond, the cis isomer is shorter than the trans isomer (0.53 vs 1.28 nm).

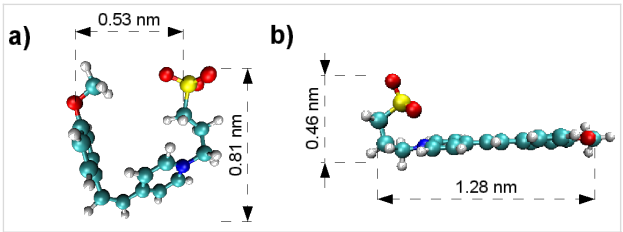

Figure 1: MSPS can have two conformations, namely the agraffe-like cis (a) and the scorpion-like trans (b) isomerization.

The ionic single-crystal substrates (MaTecK GmbH, Jülich, Germany) were cleaved ex situ and annealed in situ (UHV conditions) to 150–250 °C in order to obtain clean terraces and well-defined step edges.

The molecules were deposited from home-built pyrolytic boron nitride crucibles with the substrate kept at room temperature. The deposition rate was monitored by a quartz micro balance and set to approximately 0.5 ML/min. Large-scale ordering of the deposited molecular layers could only be achieved after subsequent annealing of the substrate to ≈110 °C for 15–30 min. Annealing to lower temperatures only affected the substrate surface a little; choosing higher temperatures resulted in desorption of the molecules.

Noncontact atomic force microscopy (NC-AFM) measurements were performed in situ under UHV conditions ($<2\cdot10^{-10}$ mbar) by means of a variable temperature AFM (VT-AFM, Omicron Nano Technology GmbH, Taunusstein, Germany) equipped with RHK electronics (SPM1000, RHK Technology, Troy, MI 48083, USA). Cantilevers used are PPP-NCL (Nanosensors, Neuchâtel, Switzerland) with resonance frequencies of ≈150 kHz, spring constants of ≈50 N/m, and

quality factors of ≈35,000. Typical oscillation amplitudes were 5–10 nm (10–20 nm peak-to-peak). The cantilevers were heated in situ to ≈150 °C for one hour in order to remove contaminants from the tip. In NC-AFM, the oscillation amplitude of the cantilever is kept constant by an oscillation feedback controller and the topography is regulated by keeping the frequency shift Δf constant. The contact potential difference between the tip and the sample was compensated by applying the corresponding bias voltage to the tip (static, no feedback). For image evaluation we used the WSxM software [22].

Results and Discussion

The topography image of ≈0.2 ML MSPS deposited on a clean KCl substrate surface is depicted in Figure 2a. MSPS diffuses to step edges and impurities and forms disordered amorphous islands, but with a more or less uniform height, and no formation of larger clusters or double layers. Most probably, the strong electrostatic MS interaction hinders both a three-dimensional growth and a reorganization into closely packed ordered islands on a large scale. It is only after a subsequent annealing cycle (110 °C for 15 min) to temperatures close to the sublimation temperature of MSPS (≈120 °C) that large-scale ordering of MSPS into rectangular islands is observed (Figure 2b). These islands are all oriented along the ⟨110⟩ direction of the substrate (see inset of Figure 2b for substrate orientation) and show a regular, quadratic Moiré pattern, several nanometers large, parallel to the island boundaries. With the annealing cycle, we also observe a rearrangement of the KCl substrate surface, which will be discussed at the end of this section. For the moment we would just like to mention that the diffusion of MSPS, with its strong electric dipole, on an ionic surface can create atomic-scale defects (see for example the upper part of Figure 3b).

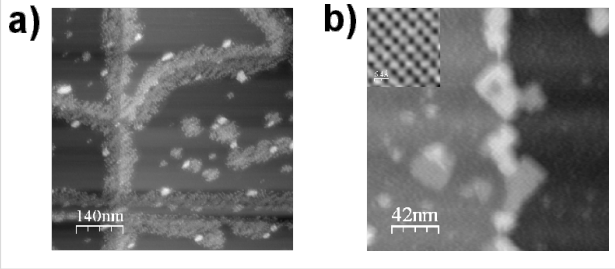

Figure 2: 0.2 ML of MSPS evaporated onto KCl. (a) displays the NC-AFM topography after deposition at RT (Δf = −59 Hz, A_0 = 7 nm), (b) shows the surface after annealing to 110 °C for 15 min (Δf = −40 Hz, A_0 = 7 nm). The substrate orientation is shown in the inset.

For a detailed investigation of the lattice parameters of both the molecular protrusions in the MSPS islands and the Moiré pattern respectively, we proceeded as follows: first, atomic-resolution images of the substrate surface (e.g., inset of Figure 2b) were used to determine the substrate orientation and to calibrate the scanner; second, the MSPS islands (and, if possible, simultaneously the substrate surface) were imaged on the molecular length scale; and third, large-scale images of the islands with the Moiré pattern were acquired. All images were drift corrected and evaluated in order to give the most accurate values for the experimentally determined lattice constant of MSPS $c_{\mathrm{msps,exp}}$ as well as for the Moiré pattern $l_{\mathrm{Moiré,exp}}$.

Figure 3a shows the topography image of ≈1 ML of MSPS on KCl. The image was taken after the annealing cycle, which

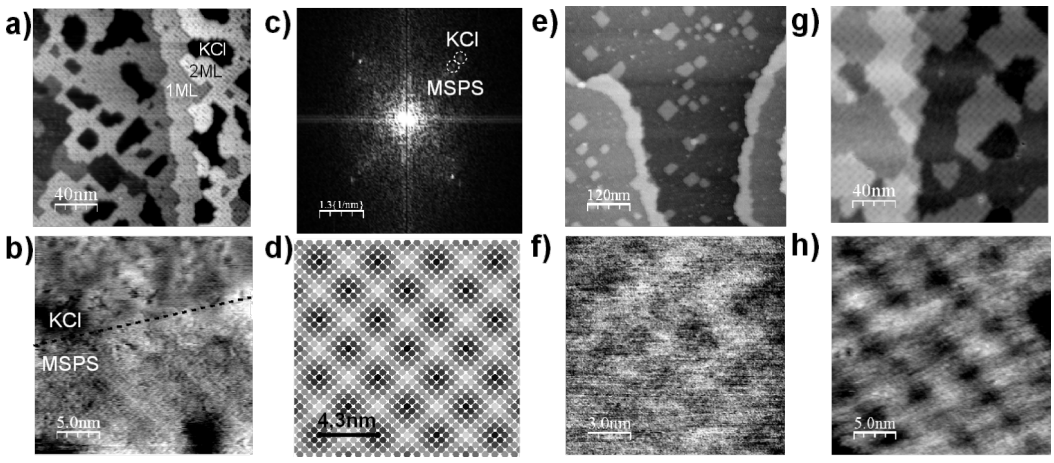

Figure 3: (a) Topography image of ≈1 ML of MSPS adsorbed on KCl (Δf = −75 Hz, A_0 = 7 nm); (b) shows a close up view on an MSPS island boundary with both, the MSPS and the KCl substrate imaged with molecular resolution (Δf = −17 Hz, A_0 = 5 nm). (c) Fourier transform of the image displayed in (b), two quadratic and parallel lattices are observed; MSPS has a slightly larger lattice constant. (d) simulation of a Moiré pattern obtained by superimposing the lattices of KCl and MSPS. (e) Topography image of ≈0.3 ML MSPS on RbCl (Δf = −60 Hz, A_0 = 7 nm) with a close up view of an MSPS island in (f) (Δf = −230 Hz, A_0 = 7 nm). (g) Topography image of ≈0.5 ML MSPS on KBr (Δf = −25 Hz, A_0 = 10 nm) with a close up view on an MSPS island in (f) (Δf = −30 Hz, A_0 = 10 nm).

induced the self-organization of the molecules. A large-scale ordering into islands one and two ML thick with a regular quadratic Moiré pattern of $l_{\text{Moiré,exp}} = 30 \pm 2$ Å is observed. On a molecular length scale, quadratic lattices are measured for both the molecular protrusions as well as for the substrate (Figure 3b). A Fourier-transform of the image in Figure 3b reveals two equally oriented quadratic lattices with the MSPS lattice measuring $c_{\text{msps,exp}} = 5.1 \pm 0.1$ Å (Figure 3c).

As mentioned above, MSPS has several conformational degrees of freedom and thus it is difficult to determine its exact conformation in the well-ordered islands observed on KCl. Makoudi et al. [23] used scanning tunneling microscopy (STM) to measure MSPS on Au(23 23 21) and observed a parallelogram unit cell with dimensions of 1.1 × 0.5 nm^2, and the molecules were adsorbed in the so-called scorpion-like conformation. The dipole moment of the molecule, which in this conformation is oriented perpendicular to the substrate surface, could only be imaged with low contrast, or not at all, by STM, due to its reduced conductivity and the fact that it is flexible.

In order to draw conclusions about the most probable conformation of the molecule adsorbed on the surface, we compare the experimentally determined parameters with the possible molecular conformations (the so-called scorpion- or agraffe-like conformation obtained by numerical simulation of a single molecule in vacuum, see Figure 1). Note that the comparison between the apparent size of the quadratic molecular unit cell (5.1 × 5.1 Å^2) and the distance between the ends of the molecule in the two former conformations (1.28 or 0.53 nm, respectively) requires each molecule to be imaged as (at least) two protrusions to account for the experimental images. To illustrate this issue, we have sketched the two adsorption conformations of the molecule on KCl(001) in Figure 4. In the case of the agraffe-like conformation, one might be tempted to consider a single protrusion (0.53 vs 0.51 nm) per molecule. However, in this situation, it is not possible to account for the experimental molecular unit cell as there would be a huge steric hindrance due to the molecular aspect ratio. From the fact that the molecular islands grow in a twofold symmetry, we conclude that one molecule must be represented by exactly two protrusions.

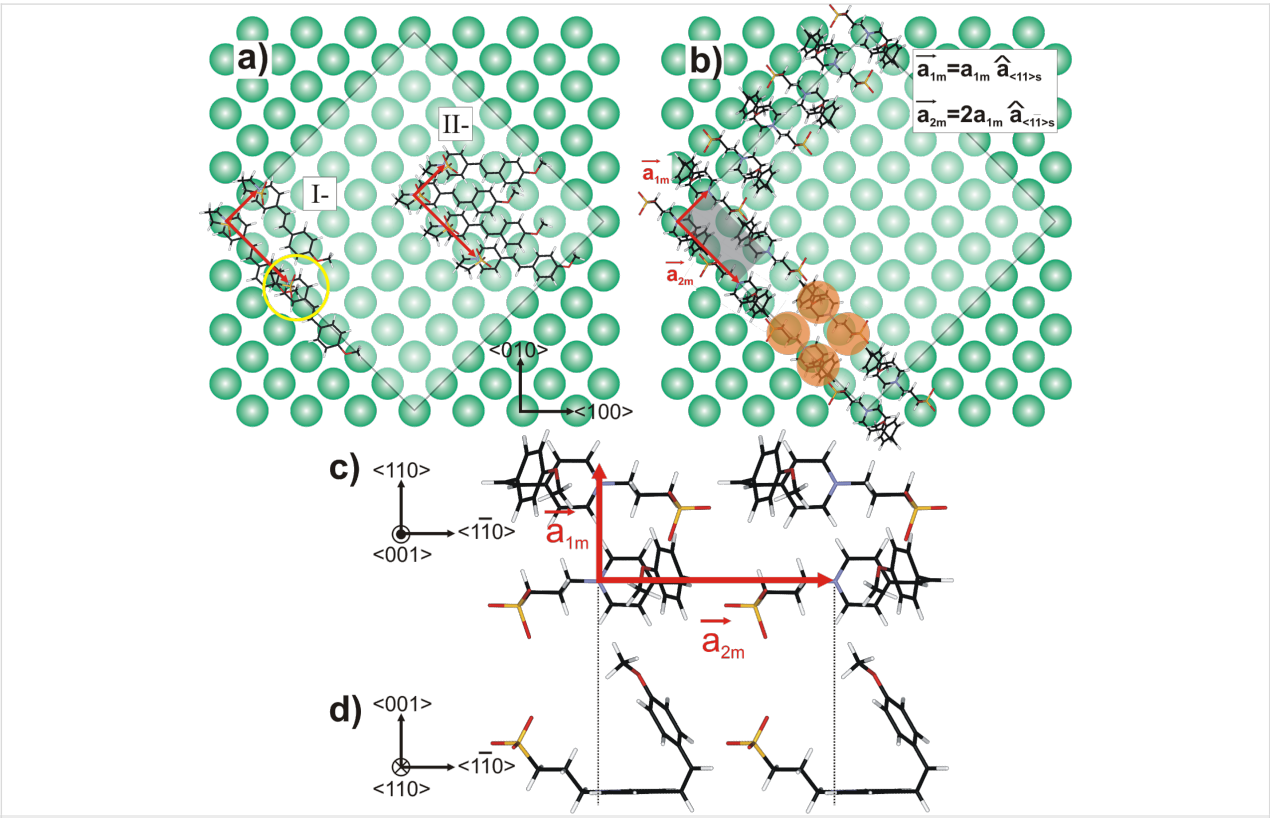

Figure 4: Conformations of MSPS on KCl(001). Only the positions of the substrate anions have been drawn. In (a) and (b), the white area depicts one patch of the molecular Moiré, as experimentally derived on KCl(001): $7a_{\langle 11\rangle s} \times 7a_{\langle 1\bar{1}\rangle s} = 31 \times 31$ Å^2, $a_{\langle 11\rangle s} = a_{\langle 1\bar{1}\rangle s} = 4.65$ Å being the interionic distances along the ⟨110⟩ and ⟨1$\bar{1}$0⟩ directions, respectively. (a) MSPS adsorbed in the scorpion-like conformation with molecular rows parallel to the ⟨1$\bar{1}$0⟩ direction (I) and to the ⟨100⟩ direction (II). Arrangements (I) and (II) do not match the experimental findings (see text). (b) MSPS in the agraffe-like conformation with the corresponding rectangular unit cell: $a_{1m} \times a_{2m} = 5.1 \times 10.2$ Å^2 aligned along the ⟨110⟩ and ⟨1$\bar{1}$0⟩ directions, respectively. Note that a_{2m} is twice as large, which reflects the fact that each molecule is composed of two protrusions along this molecular axis (orange areas). In the agraffe-like conformation, the MM interaction is increased due to the interaction between the zwitterionic part of one molecule and the dipole moment of the anisyl part of the neighboring molecule, as illustrated in the top view (c) and in the side view (d).

For the scorpion-like conformation, similar to the STM experiments [23], the two protrusions observed in the experimental pattern must be the aromatic rings, which are separated by 6.5 Å. This distance is too large to fit the experimentally observed pattern when the molecules are aligned along the $\langle 1\,\bar{1}0\rangle$ direction of the substrate (Figure 4a, I). When aligned along the ⟨100⟩ direction (Figure 4a, II), there is steric hinderance between the aromatic rings and a molecular film can only be formed when the aromatic rings are tilted by ≈40 °C with respect to the substrate surface. To our knowledge, such a film would only organize on a large scale if there was a significant MM interaction, as is, for example, the case for molecules with strong H-bonding [11]. It is therefore very unlikely that the molecules adopt the scorpion-like conformation, as first the molecular distances do not fit the experimental ones, and second, the formation of a homogeneous layer would not be promoted by MM interaction.

In contrast, for the agraffe-like conformation, the distance between the two ends of the molecule (i.e., 5.3 Å as depicted in Figure 1) is close to the experimentally observed value of 5.1 Å. The molecule adsorbs with its pyridine ring parallel to the surface and the N^+ charge on a line of substrate anions (see Figure 4b). Furthermore, if the molecules are rotated alternately by 180°, along the $\overrightarrow{a_{1m}}$ direction, a MM interaction can be established in both directions of the molecular unit cell. This interaction is formed between the zwitterionic part of one molecule and the anisyl part (i.e., methoxyphenyl) of the neighboring molecules (Figure 4c and Figure 4d). An additional indication in favor of the agraffe-like conformation is the fact that the highly ordered organic layers are only formed after subsequent annealing cycles up to 110 °C. This temperature is sufficiently high to induce the isomerization of MSPS on the surface, as the isomerization energy for stilbene (i.e., a molecule that represents the central part of MSPS only) is estimated to be ≈0.2 eV [24]. We therefore think that it is the agraffe-like conformation that the molecules adopt in our experiment and that the molecular unit cell must be rectangular, measuring 5.1 Å × 10.2 Å along the $\overrightarrow{a_{1m}}$ and $\overrightarrow{a_{2m}}$ directions, respectively. In our images, although the two ends of the molecule are chemically different, they appear with equal contrast.

In order to completely understand the self-organization of MSPS on KCl there are two additional points that must be clarified: First, is the observed Moiré pattern an effect of coincidences between the quadratic lattices of molecules and substrates, and can the molecular lattice be regarded as being incompressible (i.e., the intermolecular interactions are much stronger than the molecule–substrate interactions)? Second, is the orientation of the molecular layers along the ⟨110⟩ directions of the substrate due to a registry between the lattices of the substrate and the molecule (i.e., the gain in adsorption energy for a *point-on-line* coincidence as described in [9,19]), or is it due to the electrostatic interaction between the molecular dipole and the rows of charges present along the ⟨110⟩ direction?

The first question of whether the Moiré pattern is formed due to coincidences between the two quadratic lattices of the substrate c_{KCl} and the molecules $c_{msps,exp}$ can be easily answered as follows: The MSPS lattice is overlaid on the lattice of KCl with parallel orientation as observed in the experiment. Figure 3d shows a schematic representation (SPlot by Stefan C. B. Mannsfeld, Stanford Synchrotron Radiation Lightsource, Menlo Park, CA, USA) in which each circle corresponds to a protrusion in the MSPS lattice. Its color is varied as a function of the distance between its center and the position of the underlaying substrate ion. The darker the spot, the better the coincidence between the adsorbed molecule and the underlying substrate ion. Only one type of substrate ion is considered, as the electric charge of the N^+ close to the surface (see Figure 1a) will most probably adsorb on an anion Cl^- and not on a cation K^+. Figure 3d clearly shows that the experimental Moiré pattern is perfectly reproduced and, thus, the observed pattern can be explained by a simple coincidence between two parallel quadratic lattices. Note that the closer the two lattice parameters of MSPS and the substrate are, the larger the scale of the Moiré pattern will be. In order to verify if the organic layer is incompressible, we deposited and annealed sub-ML of MSPS on the NaCl, RbCl, and KBr substrates, which present significantly different lattice constants compared to KCl (Table 1). As can be seen from the values of the measured MSPS lattice constant $c_{msps,exp}$ in Table 1, for the substrates KCl, RbCl, and KBr, all measured $c_{msps,exp}$ are within ±1% error of 5.15 Å. The fact that no large-scale ordering is found for NaCl will be discussed below.

In order to answer the second question of whether the orientation of the organic overlayer is determined by a pure topographic effect of the quadratic substrate lattice or if it is the

Table 1: Experimental and calculated MSPS lattice constants c_{msps} and Moiré pattern distances $l_{Moiré}$. For the calculated values a 2-D coincidence is assumed for (n − x) MSPS/n ionic distances; x = 1 or 2.

substrate	NaCl	KCl	RbCl	KBr
c_{sub}	3.98 Å	4.44 Å	4.62 Å	4.67 Å
$c_{msps,exp}$	—	5.13 ± 0.1 Å	5.2 ± 0.1 Å	5.2 ± 0.3 Å
$l_{Moiré,exp}$	—	30 ± 3 Å	38 ± 4 Å	50 ± 5 Å
c_{msps}/c_{sub}	11/9	7/6	9/8	11/10
$c_{msps,calc}$	5.12 Å	5.18 Å	5.2 Å	5.14 Å
$l_{Moiré,calc}$	44 Å	31 Å	42 Å	51 Å

lines of equal charges on the ionic substrate orient along the ⟨110⟩ direction, we have to further evaluate the adsorption of MSPS on the substrates of KCl, RbCl, and KBr. If it is not the electrostatic MS interaction but a pure geometric effect that dominates the adsorption of MSPS on ionic substrates, one would expect that the orientation of the rectangular MSPS islands should vary for the different substrates (see Introduction and [9,19]).

Figure 3e,f and Figure 3g,h show large-scale and molecular-scale topography images for MSPS adsorbed and annealed on RbCl and KBr surfaces, respectively. On both substrates, the alignment of the molecular islands is parallel to the ⟨110⟩ direction of the substrate, which clearly indicates that it is the electrostatic MS interaction between a molecular charge distribution and the substrate surface that dominates the self-organization of these molecules. A detailed evaluation of the observed lattice constants $c_{msps,exp}$ for the different substrates as well as the Moiré pattern $l_{Moiré,exp}$ is depicted in Table 1. It should be remembered that the rectangular molecular unit cell $\overrightarrow{a_{1m}} \times \overrightarrow{a_{2m}}$ measures two $c_{msps,exp}$ distances along $\overrightarrow{a_{2m}}$ and one along $\overrightarrow{a_{1m}}$ (see Figure 4).

A comparison of the experimentally determined values $c_{msps,exp}$ and $l_{Moiré,exp}$ with the ones calculated assuming that there is an exact coincidence for $(n-1)$ molecular protrusions with n substrate ions, shows that the calculated $c_{msps,calc}$ maintains an almost constant value within 5.15 Å ± 1% and that the calculated parameters of the Moiré pattern are in excellent agreement with the experimental values for the substrates of KCl, RbCl, and KBr, respectively (see Table 1).

For NaCl, however, there is no coincidence for $(n-1)$ distances c_{msps} with n substrate distances, which would result in a lattice constant c_{msps} of close to 5.15 Å (rigid monolayer of MSPS as observed on the other substrates), but only for $(n-2)$ molecular protrusions (11 interionic distances for 9 molecular distances would give $c_{msps,calc}$ = 5.12 Å; see Table 1). In order to illustrate why an $n-1$ coincidence, but not an $n-2$ coincidence, would show large-scale ordering, we used the following one-dimensional model for the cases of KBr (i.e., 10 c_{msps} for 11 substrate distances) and NaCl (i.e., 9 c_{msps} for 11 substrate distances) along both molecular axis directions as depicted in Figure 4.

First, we assume that the adsorption energy E_{ads} varies laterally following the Madelung surface potential of the substrate, i.e., a sinusoidal potential, and we position the molecules according to the two coincidences (Figure 5a and Figure 5d). Along the short molecular axes, each molecular protrusion corresponds to an anchoring site (i.e., the dipolar end with the pyridine ring and its positive charge N^+ adsorbed on an anion Cl^-). The case for the long molecular axes, in which only every second molecular protrusion corresponds to an anchoring point, will be discussed below. Second, we calculate the lateral force that would act on a molecule within that potential (i.e., the derivative $-\partial E_{ads}/\partial x$) for

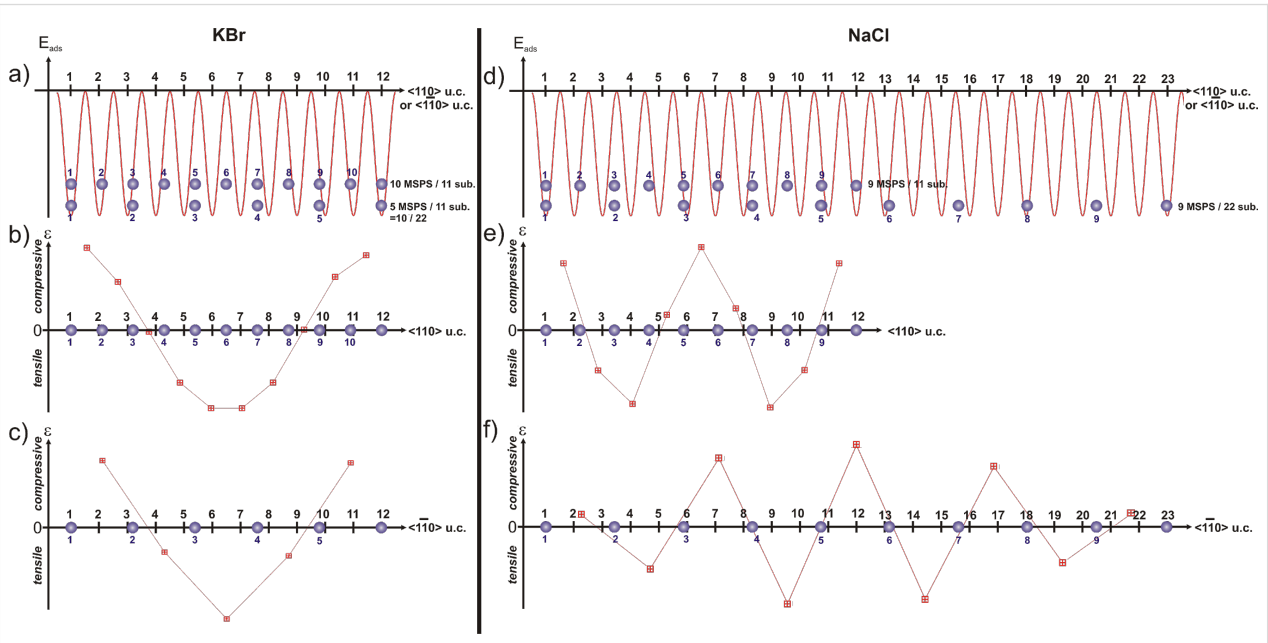

Figure 5: Model for the lateral stress ε in a MSPS film adsorbed on KBr (left) and NaCl (right). (a) and (d) display the position of the adsorbed molecule with respect to the sinusoidally shaped E_{ads} potential; (b) and (e) indicate if there is tensile or compressive stress within the film along the short molecular axes a_{1m} (i.e., the ⟨110⟩ direction), and (c) and (f) along the long molecular axes a_{2m} (⟨1$\bar{1}$0⟩ direction).

each discrete molecular position. Finally, we plot the difference of these discrete forces between two neighboring molecules in order to get an estimate for the local stress ε within that intermolecular bond. This stress competes with the stabilizing MM interaction. Although the film is incompressible, we assume that it can be pulled apart by tensile stress under certain circumstances as explained below.

For KBr we observe one area of tensile stress, which is centered between two areas of compressive stress. The latter are anchored on the substrate, as the first and last molecule of the row are above their preferred adsorption sites, at which the positive charge of the zwitterion would be strongly adsorbed on an anion Cl^- (Figure 5a and Figure 5b). For NaCl there is a double modulation of the stress ε within the film along the ⟨110⟩ direction (Figure 5e). In contrast to the case of KBr described above, these areas of tensile stress are only anchored on one side. The area of compressive stress in the middle is not anchored to the substrate as the molecules are not above their preferred adsorption site but only close to it. Therefore, for MSPS adsorbed on NaCl, the intermolecular bonds will be locally ruptured and the long-range ordering will be perturbed, and thus no Moiré pattern will be visible. All the same, we assume that the strong electrostatic MS interaction will still force small domains or lines of molecules to arrange along the Cl^- lines upon annealing; however, there are too many dislocations, such that only small areas with a more or less uniform height can be observed (not shown).

Along the long molecular axes (i.e., the $\langle 1\bar{1}0\rangle$ direction), only every second molecular protrusion could act as an anchoring point. As depicted in Figure 5c for KBr, this does not change the shape, with a single modulation of the stress compared to the short molecular axes for the substrates with an even number of molecular protrusions per $l_{\text{Moiré}}$. However for the NaCl substrate with an odd number of protrusions per $l_{\text{Moiré}}$, the N^+ charge would be on site only after two distances $l_{\text{Moiré}}$, and thus, the stress along this direction shows a very inhomogeneous modulation as depicted in Figure 5f.

The experimental results on the four ionic crystal surfaces described above clearly indicate that it is the coincidence between lines of dense molecular rows and the ⟨110⟩ direction of the substrate that dominates the adsorption of the zwitterionic MSPS on ionic-crystal surfaces. The fact that the ⟨110⟩ direction of the substrate presents lines of equally charged ions underlines the fact that it is the electrostatic MS interaction that determines the self-organization of MSPS, with its electric dipole moment perpendicular to the substrate surface. We therefore conclude that the observed overlayer is a *coincidence II* epitaxy, when we follow the classification scheme by Hooks et al. [2]. The characteristics of such a type of epitaxy are that only some of the overlayer lattice points lie on primitive substrate lattice lines and that a supercell can be constructed. The condition for a supercell in our case requires that the reciprocal-space lattice vectors for the substrate $\boldsymbol{a}^*$ and the molecular layer $\boldsymbol{b}^*$ satisfy the following criterion $\boldsymbol{b}^* = f\boldsymbol{a}^*$, with f being a fractional number (see the Fourier transform in Figure 3c). Finally, the fact that the molecular lattice constant almost does not change on the different investigated surfaces is clear proof that the molecular layer is incompressible and that the lateral molecule–molecule (MM) interaction is quite strong.

As mentioned above, we observe a rearrangement of the substrate surface during the annealing cycle. The observed effect is especially significant for surfaces with low MSPS coverage. It is most likely that, during the annealing cycle, as the molecules prefer to adsorb at step edges and as the steps are not completely decorated, the molecules diffuse along the steps and do not self-organize but, rather, modify the sample topography. In order to observe in more detail how the molecules rearrange the step edges, we prepared a KCl surface with quadratic holes (produced by electron-beam irradiation, see references in [5]) shown in Figure 6a. After deposition of ≈0.1 ML of MSPS and subsequent annealing, the substrate exhibited holes in KCl with many of the step edges oriented along ⟨110⟩ directions and which were most probably decorated with MSPS molecules (visible as black dots, Figure 6b). ⟨110⟩ oriented steps are polar and thus energetically unfavorable; we therefore assume that the originally ⟨100⟩ and ⟨010⟩ oriented step edges change their orientation to the ⟨110⟩ and $\langle 1\bar{1}0\rangle$ direction in order to compensate for the strong electric dipole moment of the adsorbed MSPS. A similar rearrangement of an ionic surface was observed for truxenes on KBr by Trevethan et al. [25]. In these experiments, the restructuring of rectangular edges to round structures is attributed to the fact that these molecules interact more strongly with kink and inner corner sites of a certain polarity.

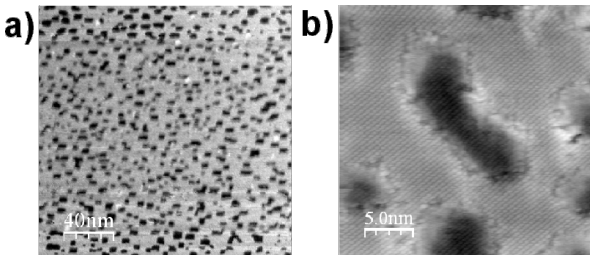

Figure 6: (a) Large-scale topography image of electron-bombarded KCl showing the characteristic holes (Δf = −12 Hz, A_0 = 5 nm); (b) topography image after deposition of ≈0.1 ML MSPS and subsequent annealing (Δf = −24 Hz, A_0 = 3 nm). ⟨110⟩ oriented step edges are visible, which are decorated with a few molecules (black dots).

Conclusion

In summary, we have shown that zwitterionic MSPS adsorbs most probably in an isomerized agraffe-like conformation on ionic-crystal surfaces, with its electric dipole moment perpendicular to the substrate surface. We observe homogeneous and incompressible monolayers of MSPS on KCl, RbCl, and KBr substrates. Our experiments clearly indicate that it is the electrostatic molecule–substrate (MS) interaction between the positive charge of the zwitterion and the negatively charged anion of the substrate surface that determines the adsorption of MSPS in a large-scale quadratic supercell (type II coincidence [2]). For all three substrates, dense molecular rows follow the ⟨110⟩ and ⟨1 $\bar{1}$0⟩ directions of the substrate, with every sixth (KCl) to tenth (KBr) molecule in coincidence with a corresponding substrate ion. It is this coincidence together with the large-scale organization that creates the experimentally observed Moiré pattern. Although, the electrostatic MS interaction dominates the adsorption mechanism, a large-scale organization of MSPS can only take place if a reasonable coincidence is possible along the ⟨110⟩ direction of the substrate, which was not the case for NaCl substrates on which the inhomogeneous stress within the molecular layer made a large-scale organization impossible. Finally, the strong molecular dipole moment can interact with the substrate in such a way that during annealing, molecules diffuse along substrate step edges and induce a reorientation of the steps in order to compensate for the electrostatic field of the adsorbed molecular dipole.

Acknowledgements

We acknowledge financial support from ANR grant *Nanokan* (ANR-11-BS10-004) and the use of the SPlot software provided by Stefan Mannsfeld.

References

1. Mannsfeld, S. C. B.; Fritz, T. *Mod. Phys. Lett. B* **2006,** *20,* 585. doi:10.1142/S0217984906011189
2. Hooks, D. E.; Fritz, T.; Ward, M. D. *Adv. Mater.* **2001,** *13,* 227. doi:10.1002/1521-4095(200102)13:4<227::AID-ADMA227>3.0.CO;2-P
3. Glatzel, T.; Zimmerli, L.; Kawai, S.; Meyer, E.; Fendt, L.-A.; Diederich, F. *Beilstein J. Nanotechnol.* **2011,** *2,* 34. doi:10.3762/bjnano.2.4
4. Burke, S. A.; Topple, J. M.; Grütter, P. *J. Phys.: Condens. Matter* **2009,** *21,* 423101. doi:10.1088/0953-8984/21/42/423101
5. Bennewitz, R. *J. Phys.: Condens. Matter* **2006,** *18,* R417. doi:10.1088/0953-8984/18/26/R01
6. Loppacher, C.; Zerweck, U.; Eng, L. M.; Gemming, S.; Seifert, G.; Olbrich, C.; Morawetz, K.; Schreiber, M. *Nanotechnology* **2006,** *17,* 1568. doi:10.1088/0957-4484/17/6/006
7. Kunstmann, T.; Schlarb, A.; Fendrich, M.; Wagner, T.; Möller, R.; Hoffmann, R. *Phys. Rev. B* **2005,** *71,* 121403(R). doi:10.1103/PhysRevB.71.121403
8. Resel, R.; Haber, T.; Lengyel, O.; Sitter, H.; Balzer, F.; Rubahn, H.-G. *Surf. Interface Anal.* **2009,** *41,* 764. doi:10.1002/sia.3095
9. Smilgies, D.-M.; Kintzel, E. J., Jr. *Phys. Rev. B* **2009,** *79,* 235413. doi:10.1103/PhysRevB.79.235413
10. Fremy, S.; Schwarz, A.; Lämmle, K.; Prosenc, M.; Wiesendanger, R. *Nanotechnology* **2009,** *20,* 405608. doi:10.1088/0957-4484/20/40/405608
11. Pawlak, R.; Nony, L.; Bocquet, F.; Oison, V.; Sassi, M.; Debierre, J.-M.; Loppacher, C.; Porte, L. *J. Phys. Chem. C* **2010,** *114,* 9290. doi:10.1021/jp102044u
12. Bombis, C.; Kalashnyk, N.; Xu, W.; Lægsgaard, E.; Besenbacher, F.; Linderoth, T. R. *Small* **2009,** *5,* 2177. doi:10.1002/smll.200900301
13. Abel, M.; Clair, S.; Ourdjini, O.; Mossoyan, M.; Porte, L. *J. Am. Chem. Soc.* **2011,** *133,* 1203. doi:10.1021/ja108628r
14. Kittelmann, M.; Rahe, P.; Nimmrich, M.; Hauke, C. M.; Gourdon, A.; Kühnle, A. *ACS Nano* **2011,** *5,* 8420. doi:10.1021/nn2033192
15. Dienel, T.; Loppacher, C.; Mannsfeld, S. C. B.; Forker, R.; Fritz, T. *Adv. Mater.* **2008,** *20,* 959. doi:10.1002/adma.200701684
16. Burke, S. A.; Ji, W.; Mativetsky, J. M.; Topple, J. M.; Fostner, S.; Gao, H.-J.; Guo, H.; Grütter, P. *Phys. Rev. Lett.* **2008,** *100,* 186104. doi:10.1103/PhysRevLett.100.186104
17. Hinaut, A.; Lekhal, K.; Aivazian, G.; Bataillé, S.; Gourdon, A.; Martrou, D.; Gauthier, S. *J. Phys. Chem. C* **2011,** *115,* 13338. doi:10.1021/jp202873f
18. Barth, C.; Gingras, M.; Foster, A. S.; Gulans, A.; Félix, G.; Hynninen, T.; Peresutti, R.; Henry, C. R. *Adv. Mater.*, in press.
19. Mannsfeld, S. C. B.; Fritz, T. *Phys. Rev. B* **2004,** *69,* 075416. doi:10.1103/PhysRevB.69.075416
20. Serbutoviez, C.; Nicoud, J.-F.; Fisher, J.; Ledoux, I.; Zyss, J. *Chem. Mater.* **1994,** *6,* 1358. doi:10.1021/cm00044a039
21. Makoudi, Y.; Arab, M.; Palmino, F.; Duverger, E.; Ramseyer, C.; Picaud, F.; Chérioux, F. *Angew. Chem., Int. Ed.* **2007,** *46,* 9287. doi:10.1002/anie.200702794
22. Horcas, I.; Fernández, R.; Gómez-Rodríguez, J. M.; Colchero, J.; Gómez-Herrero, J.; Baro, A. M. *Rev. Sci. Instrum.* **2007,** *78,* 013705. doi:10.1063/1.2432410
23. Makoudi, Y.; Didiot, C.; Palmino, F.; Duverger, E.; Kierren, B.; Malterre, D.; Chérioux, F. *Surf. Sci.* **2010,** *604,* 27. doi:10.1016/j.susc.2009.10.012
24. Kwasniewski, S. P.; Claes, L.; François, J.-P.; Deleuze, M. S. *J. Chem. Phys.* **2003,** *118,* 7823. doi:10.1063/1.1563617
25. Trevethan, T.; Such, B.; Glatzel, T.; Kawai, S.; Shluger, A. L.; Meyer, E.; de Mendoza, P.; Echavarren, A. M. *Small* **2011,** *7,* 1264. doi:10.1002/smll.201001910

Beilstein Journal of Nanotechnology

Wavelet cross-correlation and phase analysis of a free cantilever subjected to band excitation

Francesco Banfi and Gabriele Ferrini*

Full Research Paper

Open Access

Address:
Interdisciplinary Laboratories for Advanced Materials Physics (i-LAMP) and Dipartimento di Matematica e Fisica, Università Cattolica del Sacro Cuore, I-25121 Brescia

Email:
Gabriele Ferrini* - gabriele@dmf.unicatt.it

* Corresponding author

Keywords:
AFM; band excitation; force; wavelet transforms

Beilstein J. Nanotechnol. **2012,** *3,* 294–300.
doi:10.3762/bjnano.3.33

Received: 01 December 2011
Accepted: 07 February 2012
Published: 29 March 2012

This article is part of the Thematic Series "Noncontact atomic force microscopy".

Guest Editor: U. D. Schwarz

Abstract

This work introduces the concept of time–frequency map of the phase difference between the cantilever response signal and the driving signal, calculated with a wavelet cross-correlation technique. The wavelet cross-correlation quantifies the common power and the relative phase between the response of the cantilever and the exciting driver, yielding “instantaneous” information on the driver-response phase delay as a function of frequency. These concepts are introduced through the calculation of the response of a free cantilever subjected to continuous and impulsive excitation over a frequency band.

Introduction

Atomic force microscopy (AFM) has made important progresses towards the characterization of material properties at the nanoscale (elastic constants, force interactions, friction, molecular interactions, to name only a few) by means of dynamic techniques that extended the microscope capabilities well beyond simple topographic measurements [1,2]. Among the techniques developed in dynamic AFM, multimode excitation and the so called band-excitation methods have been put forward recently [3-5]. All of these techniques are based on the frequency, amplitude and phase response around one or more cantilever oscillation modes when the tip interacts with the sample surface. The temporal evolution of the amplitude, phase or frequency response is in many cases a fundamental parameter. The implementation of these techniques is based on the continuous excitation of multiple flexural cantilever modes [3,4], impulsive cantilever excitation [5] or thermal-noise excitation [6-9].

Thermal noise analysis has been performed, with the aid of wavelet transforms, to characterize the time–frequency response of a thermally excited cantilever in dynamic force spectroscopy [10-12]. In these previous works, the focus was on the time

evolution of the brownian power spectral density of the tip when it is in contact with the force field of the sample surface (e.g., van der Waals, adhesion, Hertz interaction regime). However, wavelet analysis, in analogy with the classical Fourier transform, also provides *phase* information when complex functions are used as a wavelet basis.

The scope of this work is to introduce the idea that a time–frequency map of the phase difference between the cantilever response signal and the driving signal can be extracted with a wavelet cross-correlation (WCC) technique, based on the inherent phase information residing within the complex Gabor transform. This analysis has been exploited principally in the field of meteorology, oceanography and geophysical studies [13-15]. Since, to the best of our knowledge, there are no examples of WCC used in AFM, we will illustrate some examples based on the response of a damped harmonic oscillator, which in many situations is a good model for an oscillating cantilever, to different kinds of driving forces. Through the wavelet cross-correlation it is possible to quantify the power correlation and the relative phase between the cantilever response and the driving signal under reasonable assumptions [15]. In the last few years, the investigation of phase-analysis techniques [16,17] contributed to the understanding of energy-dissipation processes and elastic response in heterogeneous samples, an important topic in biological research, where the liquid environment is principally of interest. In liquids the typical cantilever Q-factor ranges from 5 [18] up to 40, for this reason we will focus our attention on the simulation of low-Q oscillators.

Wavelet cross-correlation

The wavelet transform has shown great potential in various scientific disciplines, but it is not widespread in the context of noncontact AFM. This may be due to the absence of discussions of the practical and technical aspects of wavelet analysis relating to noncontact AFM. This article shows the use of wavelet cross-correlation by means of two simple but paradigmatic examples: The continuous and the impulsive band excitation of a free cantilever.

Before introducing the cross-correlation concept, we give a brief introduction to wavelet transform theory [19]. Wavelet analysis is based on the projection (convolution) of a discrete time series $f(t)$ (the signal), where t is the time index, onto a set of continuous functions $\Psi_{s,d}(t)$ derived from the translations and dilations of a *mother wavelet* $\Psi(t)$, where

$$\Psi_{s,d}(t) = \frac{1}{\sqrt{s}}\Psi\left(\frac{t-d}{s}\right) \tag{1}$$

s and d are real parameters and $s > 0$. Any set of functions constructed as in Equation 1 and meeting the fundamental requirements of zero average, implying that $\Psi(t)$ is an oscillating function, and rapid decay at infinity (technically $\Psi(t)$ must be continuous and have a compact support; this is called the admissibility condition), are called *wavelets*.

The convolution of $f(t)$ with $\Psi_{s,d}(t)$, at the scale s and delay d, is the *wavelet transform* (WT) of the signal $W^f(s,d)$:

$$\begin{aligned} W^f(s,d) &= \int_{-\infty}^{+\infty} f(t)\Psi^*_{s,d}(t)\,\mathrm{d}t \\ &= \int_{-\infty}^{+\infty} f(t)\frac{1}{\sqrt{s}}\Psi^*\left(\frac{t-d}{s}\right)\mathrm{d}t \end{aligned} \tag{2}$$

This is a continuous wavelet transform, because the parameters s and d vary continuously. The translation parameter d corresponds to time and the dilation parameter s corresponds to temporal period (or its inverse, frequency). Equation 2 expands the time series $f(t)$ into a bidimensional parameter space (s,d) and gives a local measure of the relative resemblance of the wavelet to the signal.

The complex mother wavelet (also called Gabor wavelet or Gaussian wavelet) used in this work, as described in [10], is represented as

$$\Psi(t) = \frac{1}{(\sigma^2\pi)^{1/4}}\exp\left(-\frac{t^2}{2\sigma^2} + i\eta t\right)$$

where σ controls the amplitude of the Gaussian envelope, and thus its time–frequency resolution, and η is the carrier frequency. Since the intrinsic time–frequency resolution in WT is determined by the wavelet set over which the signal is expanded, we chose a Gaussian wavelet basis because it is particularly adapted to follow signals in time, having the least spread in both the frequency and time domain and thus the best time–frequency resolution. The temporal parameter t in the expression of the Gabor wavelet can be regarded as a (dimensionless) discrete index and likewise σ and η are dimensionless wavelet parameters defining the wavelet shape over the discrete sampling string. The Gabor wavelet (dimensionless) center frequency at scale s is given by $f = \eta/(2\pi s)$. It is possible to associate a pseudofrequency F (in Hz) at a scale s by considering that f is sampled with a time interval T, such that $F = f/T$. Therefore, the wavelet dilations set by the scale parameter s are inversely proportional to the frequency F. In the following analysis, the dimensionless wavelet parameters are chosen as

σ = 1 and η = 6. This choice of parameter gives an adequate balance between time and frequency localization, which in wavelet analysis are subjected to a classical Heisenberg-like principle of indetermination (for details see [10]).

Given two time series $f(t)$ and $g(t)$, with wavelet transforms $W^f(s,d)$ and $W^g(s,d)$, the cross-wavelet spectrum is defined as:

$$W^{fg}(s,d) = W^f(s,d)W^g(s,d)^* \tag{3}$$

where * denotes the complex conjugate. Since the cross-correlation coefficients are complex numbers, they can be represented as $W^f(s,d) = |W^f(s,d)|\exp(\Phi^f(s,d))$. $|W^f(s,d)|$ represents the wavelet amplitude, $\Phi^f(s,d)$ is the absolute phase. Both amplitude and phase are relative to the "point" (s,d) in the frequency–time plane. The cross-wavelet power, $|W^{fg}(s,d)|$, shows regions in time–frequency space where the time series have a high common power. The relative phase difference between the two time series ($\Phi^f(s,d)$ = phase of f; $\Phi^g(s,d)$ = phase of g), can be calculated as:

$$\Phi^{fg}(s,d) = \Phi^f(s,d) - \Phi^g(s,d) = \tan^{-1}\left(\frac{\mathrm{Im}\left(<s^{-1}W^{fg}(s,d)>\right)}{\mathrm{Re}\left(<s^{-1}W^{fg}(s,d)>\right)}\right) \tag{4}$$

where < > represents a smoothing operator. It must be noted that this definition depends essentially on the action of the smoothing operator on the various wavelet spectra. The same situation in found in the definition of optical coherence, see [20]. For a discussion of this fundamental but rather technical aspect, see [15,21]. In general terms, a high correlation between two time series does not necessarily imply that there is any kind of connection or cause-and-effect relationship. This means that the time series can have high common power at a given time and frequency and still being uncorrelated, a problem which arises also when analyzing the correlation of signals with standard Fourier transform techniques. As an example, a correlation peak will be always present in the cross correlation between white noise and a sinusoidal signal, without implying any causal connection between the two time series. For this reason it is important to observe the phase relationship: A strong causal connection implies that the oscillations of the two series must be phase locked.

Results

As an example to highlight the characteristics of wavelet cross-correlation, consider the case of a damped cantilever with a displacement $z(t)$ that obeys the classical mass–spring equation

$$\ddot{z} + \frac{\omega_0}{Q}\dot{z} + \omega_0^2 z = f(t) \tag{5}$$

where $f(t)$ is the driving force per unit mass.

The above equation of motion is integrated numerically with a free resonant frequency of $f_0 = \omega_0/(2\pi) = 1$ MHz, a quality factor $Q = 4$ and an excitation driving frequency that linearly sweeps the frequency interval $0.1f_0 < \Delta f < 0.9f_0$ in 50 μs (chirped driver). The driving function is $f(t) = z_d\cos(\nu_d(t)t)$, where z_d is the driving amplitude and $\nu_d(t)$ the driving frequency that is linearly chirped: $\nu_d(t) = A + Bt$, $A = 0.1$ MHz and $B = 0.016$ MHz/μs. Note that the actual instantaneous driver frequency as a function of time is the time derivative of the total driver phase, i.e., $A + 2Bt$. As a consequence, the resonance at f_0 is excited when the instantaneous driving frequency sweeps through f_0, which does *not* coincide with the frequency $\nu_d(t)$. In Figure 1 the result of the numerical integration is shown and is compared with the driving frequency, which sweeps through the frequency band at a constant rate.

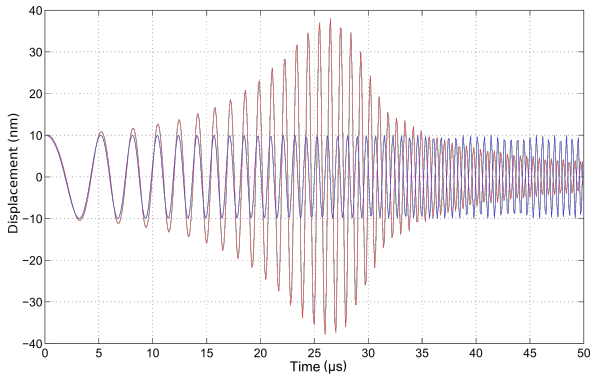

Figure 1: The response of a damped harmonic oscillator (red line) to a chirped driver (blue line) whose frequency is linearly swept in the interval $0.1f_0 < \Delta f < 0.9f_0$ over 50 μs, where $f_0 = \omega_0/(2\pi) = 1$ MHz is the resonant frequency of the oscillator. The quality factor is $Q = 4$ and the initial conditions are 10 nm amplitude and zero velocity.

The wavelet cross-correlation analysis in Figure 2 evidences the oscillator phase relationship to the driving frequency (arrows), simultaneously with the cross-wavelet power spectral density (represented in the color scale, identifying the time-series common power), as a function of time and the instantaneous frequency [22]. The figure shows the magnitude of the wavelet cross-correlation between the two signals, $W^{zf}(\omega,t) = W^z(\omega,t)W^f(\omega,t)^*$ and the relative phase (arrows). Phase arrows indicate the phase relationship of the oscillator to the driving sinusoid (pointing right: in-phase; left: anti-phase; up: oscillator lagging behind driver by 90°). The edge effects are delimited by continuous lines. We note that the representation in terms of the cross-correlation between the damped

harmonic oscillator and the chirped driver allows us to capture more intuitively the evolution of the spectral content of the cantilever oscillations, in a way that is not possible with a traditional Fourier transform. However, the utility of this technique is even more relevant when we deal with impulsive excitation.

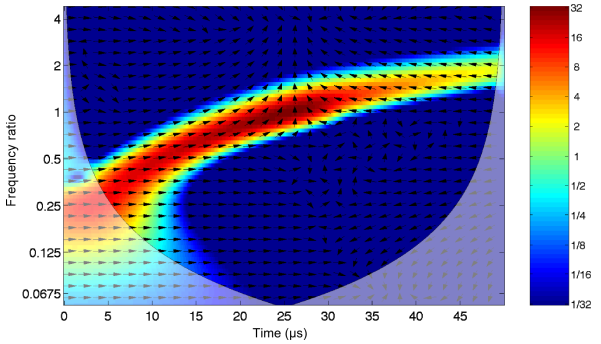

Figure 2: Wavelet cross-correlation between the chirped driver and the response of the damped harmonic oscillator (quality factor Q = 4), as shown in Figure 1. The wavelet cross-correlation coefficients (reported in the color scale) evidence the common power between the two time series in the time–frequency plane. Note that the frequency axis is represented in octaves as the base-2 logarithm of the ratio of the oscillator frequency to the resonant frequency. The color scale is proportional to the wavelet cross-correlation power and is represented in octaves. The arrows superimposed on the representation given by the color scale show the local phase difference between the oscillator and the driver. Arrow pointing right: in-phase; left: anti-phase; up: oscillator lagging behind driver by 90°. The area where edge artifacts may distort the picture are delimited by a lighter shade.

An excitation signal that can be used in AFM band excitation is the sinc function. It is defined as

$$\mathrm{sinc}(t) = \frac{\sin(\pi t)}{\pi t},\ t \neq 0 \quad \mathrm{sinc}(t) = 1,\ t = 0 \qquad (6)$$

This function is the continuous inverse Fourier transform of the rectangular pulse of width 2π and height 1. It is used as a simultaneous excitation over a limited frequency range. The time response of the damped cantilever to a properly scaled sinc function is shown in Figure 3. The response of the oscillator starts abruptly from nearly zero deflection with a finite velocity: A dynamic that is typical of impulsive forces. The wavelet cross-correlation analysis is shown in Figure 4. The spectral components have a temporal evolution peaked around the excitation pulse, as expected. To extract information from these signals, it is interesting to follow the "local" phase difference between driver and oscillator around the oscillator resonance. Below resonance the spectral components of the oscillator are in-phase with the driver, above resonance they are in anti-phase, and while at resonance they show a phase lag of $\pi/2$ with respect to the spectral components of the driver. It is important to note that the phase relations just described refer to a

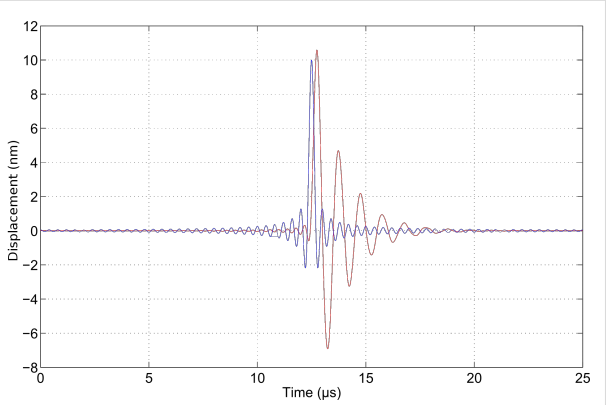

Figure 3: The response of a damped harmonic oscillator (red line, quality factor Q = 4) to a sinc driver (blue line) with an amplitude of 10 nm and a flat excitation bandwidth up to 2.5 MHz. Initial conditions are zero amplitude and zero velocity.

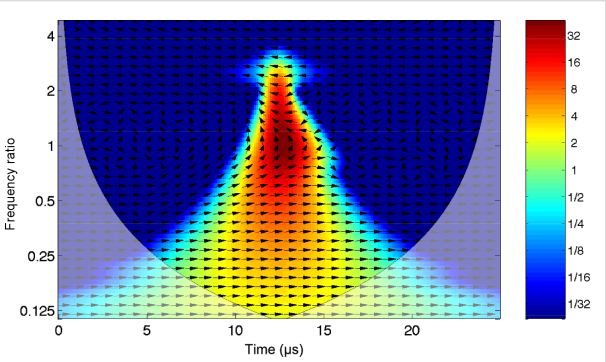

Figure 4: Wavelet cross-correlation between the sinc driver and the response of the damped harmonic oscillator (quality factor Q = 4), as shown in Figure 3.

frequency band that has been simultaneously excited and encompasses the resonant frequency.

Although the above description of the spectral phase appears intuitive, it would not be possible to obtain it by means of a classical Fourier analysis. If the signal is not stationary, as is the case in band excitation, the squared magnitude of the Fourier coefficients measure the average energy contained in a spectral interval without tracing its effective time evolution. In this case the phase relative to each spectral component is not "local" in time, preventing its interpretation in terms of a causality relationship with a specific perturbing agent.

It is interesting to note that the cross-correlation analysis allows us to separate those spectral components that are directly influenced by the driver and those relative to the subsequent evolution of the oscillator response, when the impulsive driver action has died down. We consider the same excitation as in Figure 3, but with an oscillator that has a much higher Q-factor, Q = 40.

The time evolution is shown in Figure 5. We note that the initial displacement is not amplified in proportion to the Q-factor, as one would have anticipated on the basis of standard resonance amplification, as can be seen from the comparison with Figure 3. The higher Q-factor manifests as a response of the oscillator that now extends over a longer time span, well beyond the driver pulse. The wavelet cross-correlation is similar to that seen in Figure 4, because the cross-correlation is zero when the driver has decayed down and thus independent of the temporal extension of the oscillator, see Figure 6. In this case the time extent of the spectral components near resonance is increased in comparison to Figure 4 due to a less abrupt damping of the oscillaton motion.

Since the oscillator signal extending beyond the driver pulse can carry useful information but is not visible in the cross correlation, an *artificial* signal can be used as a reference. The phase of the oscillator can be tracked by correlating it with a reference harmonic signal at the resonant frequency, as we demonstrate in Figure 7. In this case the oscillator phase is leading that

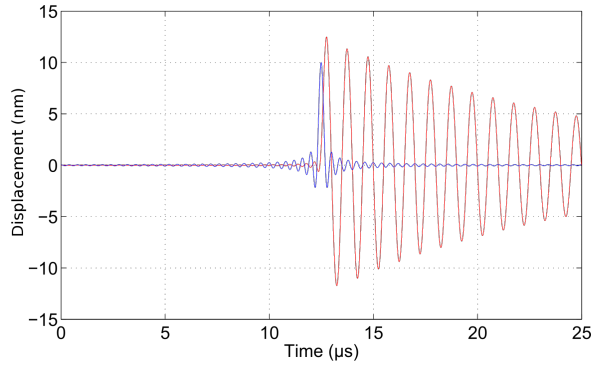

Figure 5: The response of a damped harmonic oscillator (red line, quality factor Q = 40) to a sinc driver (blue line) identical to that specified in Figure 3.

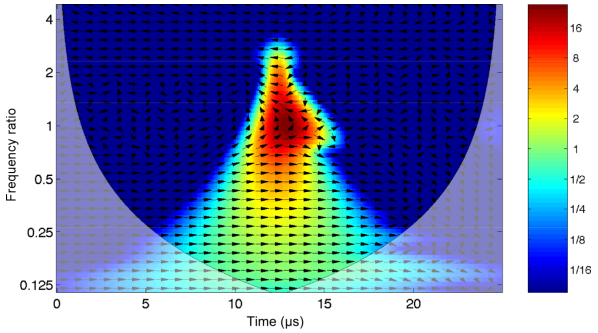

Figure 6: Wavelet cross-correlation between the sinc driver and the response of the damped harmonic oscillator (quality factor Q = 40), as shown in Figure 5.

of the reference by $\pi/2$. It is important to note here that the value of the phase difference depends on the choice of the reference signal, but its evolution in time can carry information on the interactions of the oscillator with the environment. The obvious implication that this analysis mode has on band-excitation techniques is the separation of the cantilever response into two distinct periods: An initial stage during the active driving that set the cantilever in motion and a following stage in which the undriven cantilever decays to a steady state.

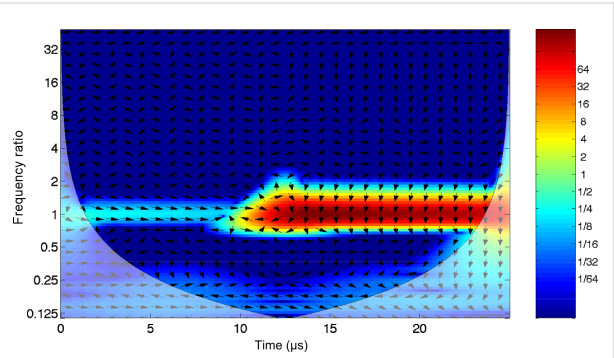

Figure 7: Wavelet cross-correlation between a sinusoidal reference signal at resonance and the damped harmonic oscillator response (quality factor Q = 40), to a sinc driver, as shown in Figure 5.

Discussion

In this section we would like to comment on how to exploit WCC and wavelet phase analysis in a practical AFM experiment, discussing the implications for the real cantilever dynamics as opposed to modeling a harmonic oscillator. A fundamental feature of wavelet phase analysis consists of measuring the phase response of the cantilever with respect to complex excitation signals (band excitations, frequency sweeps, structured pulses), and displaying the results in the time–frequency plane, with a resolution set by the Heisenberg principle, as shown in the simulations reported in Figure 2, Figure 4, and Figure 6 for a damped harmonic oscillator. This is in contrast to standard phase measurements, in which the phase response is mapped with respect to a continuous single-frequency excitation. A strategy to gain information from wavelet phase analysis relies on taking a reference "phase carpet", corresponding to a free cantilever, for a given excitation signal. This is a time–frequency map of the phase difference between the cantilever response signal and the driving signal when the cantilever is *not* engaged in interaction. Successive excitation of the interacting cantilever provides the interaction "phase carpet". Subtracting the interacting phase carpet from its reference, allows us to retrieve the local phase rotation, that is a function of the tip–surface interaction and the chosen excitation/driving signal. With this approach the phase rotation is measured at each frequency that resides within the excited

band around a cantilever resonance and it is possible to follow its time evolution. The advantage with respect to single-frequency techniques is a more robust all-frequency characterization of the phase rotation and the possibility of connecting this information with the amplitude variation at each point in the time–frequency plane. With respect to traditional analysis, in which the spectral information is extracted with a Fourier transform, the wavelet representation disentangles the interaction spectra in the time domain. The spectral components acquire an interaction causality that is absent in the Fourier spectrum, revealing the time succession in which the phase or the amplitude at a specified frequency has been altered by the interaction. In certain cases this information may be of great utility, for example to enable correlation of phase-jumps with the interaction processes, that usually have time-scales that are a fraction of the oscillation period. It is foreseen that in similar cases the wavelet analysis could track dynamics otherwise not visible in a Fourier spectrum because of the superposition of spectral contributions generated at different times.

In amplitude-modulation AFM (tapping mode) wavelet analysis is useful to track the time evolution of the nonlinearities in tip–surface dynamics. The wavelet analysis allows one to follow more than a single flexural mode simultaneously [10,11] and the eventual harmonics due to a nonlinear response, characterizing their time evolution. Regarding the phase response, we expect that nonlinear interaction will produce phase discontinuities in the WCC between the driving signal and the cantilever response, whose temporal dynamics should be accessible. As an example, the spectral response of a cantilever in liquid excited at its first flexural resonance, and which impacts on a sample, is controlled by the elastic parameters of the sample and determines the degree of excitation of the higher flexural modes [17]. The cantilever spectral distribution upon impact, captured with wavelet amplitude and phase analysis, is thus a fingerprint of the material properties. This information can be used, at the very least, to determine compositional contrast.

A final remark is due concerning the effect of noise (thermal and environmental noise) on wavelet analysis while processing data collected under normal AFM operating conditions. One might expect noise to be a limiting factor when performing wavelet analysis, due to the fact that the wavelet analyzes the signals for a shorter time and therefore loses the averaging effect present in traditional Fourier spectra. Regarding environmental noise, it has been demonstrated that by using only thermal excitation it is possible to retrieve useful information from force spectroscopy [11] with a *single* approach curve under standard operating conditions. Regarding the thermal noise, the excitation signals must have amplitudes exceeding that of the thermal noise, because averaging is limited or absent. In this case, the choice of the excitation amplitude depends on the type of cantilever, on its quality factor and on the parameters to be measured. We anticipated that only extremely low amplitude excitations should have portions of the time–frequency map rendered useless below the noise floor. Further (ongoing) studies will be necessary to gain insights into the limitations of wavelet analysis.

Conclusion

The application of wavelet analysis to interacting cantilevers is a promising route to the characterization of material properties on the nanoscale. The wavelet correlation technique allows one to measure the phase relationship between driver force and cantilever response in complex excitation schemes. The complete time–frequency picture of the phase evolution can be exploited as an important tool to characterize material response and tip–sample interactions. The wavelet correlation analysis sets into a different perspective the AFM techniques, which have been analyzed so far only in terms of Fourier transform.

Acknowledgements

This work has been partially supported by the Università Cattolica del Sacro Cuore through D.2.2 grants.

References

1. Garcia, R. *Amplitude modulation atomic force spectroscopy;* Wiley-VCH: Weinheim, 2010.
2. Morita, S.; Wiesendanger, R.; Meyer, E., Eds. *Noncontact Atomic Force Microscopy;* Springer: Berlin, 2002.
3. Lozano, J. R.; Garcia, R. *Phys. Rev. B* **2009,** *79,* 014110. doi:10.1103/PhysRevB.79.014110
4. Solares, S. D.; Hölscher, H. *Nanotechnology* **2010,** *21,* 075702. doi:10.1088/0957-4484/21/7/075702
5. Jesse, S.; Kalinin, S. V.; Proksch, R.; Baddorf, A. P.; Rodriguez, B. J. *Nanotechnology* **2007,** *18,* 435503. doi:10.1088/0957-4484/18/43/435503
6. Cleveland, J. P.; Schäffer, T. E.; Hansma, P. K. *Phys. Rev. B* **1995,** *52,* R8692. doi:10.1103/PhysRevB.52.R8692
7. Heinz, W. F.; Antonik, M. D.; Hoh, J. H. *J. Phys. Chem. B* **2000,** *104,* 622. doi:10.1021/jp993394t
8. Drobek, T.; Stark, R. W.; Heckl, W. M. *Phys. Rev. B* **2001,** *64,* 045401. doi:10.1103/PhysRevB.64.045401
9. Malegori, G.; Ferrini, G. *J. Vac. Sci. Technol., B: Microelectron. Nanometer Struct.* **2010,** *28,* C4B18. doi:10.1116/1.3305452
10. Malegori, G.; Ferrini, G. *Beilstein J. Nanotechnol.* **2010,** *1,* 172. doi:10.3762/bjnano.1.21
11. Malegori, G.; Ferrini, G. *Nanotechnology* **2011,** *22,* 195702. doi:10.1088/0957-4484/22/19/195702
12. Malegori, G.; Ferrini, G. *e-J. Surf. Sci. Nanotechnol.* **2011,** *9,* 228. doi:10.1380/ejssnt.2011.228
13. Meyers, S. D.; Kelly, B. G.; O'Brien, J. J. *Mon. Weather Rev.* **1993,** *121,* 2858. doi:10.1175/1520-0493(1993)121<2858:AITWAI>2.0.CO;2
14. Kumar, P.; Foufoula-Georgiou, E. *Rev. Geophys.* **1997,** *35,* 385. doi:10.1029/97RG00427

15. Torrence, C.; Compo, G. P. *Bull. Am. Meteorol. Soc.* **1998,** *79,* 61. doi:10.1175/1520-0477(1998)079<0061:APGTWA>2.0.CO;2
16. Martínez, N. F.; García, R. *Nanotechnology* **2006,** *17,* S167. doi:10.1088/0957-4484/17/7/S11
17. Melcher, J.; Carrasco, C.; Xua, X.; Carrascosa, J. L.; Gómez-Herrero, J.; de Pablo, P. J.; Raman, A. *Proc. Natl. Acad. Sci. U. S. A.* **2009,** *106,* 13655. doi:10.1073/pnas.0902240106
18. Fukuma, T.; Jarvis, S. P. *Rev. Sci. Instrum.* **2006,** *77,* 043701. doi:10.1063/1.2188867
19. Mallat, S. G. *A Wavelet Tour of Signal Processing,* 2nd ed.; Academic Press: San Diego, 1999.
20. Born, M.; Wolf, E. *Principles of Optics,* 7th ed.; Cambridge University Press: Cambridge, 1999.
21. Grinsted, A.; Moore, J. C.; Jevrejeva, S. *Nonlinear Proc. Geophys.* **2004,** *11,* 561. doi:10.5194/npg-11-561-2004
22. The software for wavelet cross correlation used in this work was developed by A. Grinsted, see [21]

Beilstein Journal of Nanotechnology

Graphite, graphene on SiC, and graphene nanoribbons: Calculated images with a numerical FM-AFM

Fabien Castanié[1,2], Laurent Nony[3,4], Sébastien Gauthier[1] and Xavier Bouju[*1]

Full Research Paper

Open Access

Address:
[1]CEMES-CNRS, Centre d'élaboration des matériaux et d'études structurales, 29 rue Jeanne-Marvig, BP 94347, F-31055 Toulouse Cedex 4, France, [2]Université de Toulouse, UPS, 29 rue Jeanne-Marvig, BP 94347, F-31055 Toulouse Cedex 4, France, [3]Aix Marseille Université, IM2NP, Centre scientifique de Saint-Jérôme, Service 151, Avenue Escadrille Normandie-Niemen, F-13397 Marseille Cedex 20, France and [4]CNRS, IM2NP (UMR 7334), Marseille, France

Email:
Xavier Bouju[*] - bouju@cemes.fr

* Corresponding author

Keywords:
calculations; FM-AFM; graphene; graphite; image; nanoribbon

Beilstein J. Nanotechnol. **2012,** *3,* 301–311.
doi:10.3762/bjnano.3.34

Received: 05 December 2011
Accepted: 02 March 2012
Published: 02 April 2012

This article is part of the Thematic Series "Noncontact atomic force microscopy".

Guest Editor: U. D. Schwarz

Abstract

Background: Characterization at the atomic scale is becoming an achievable task for FM-AFM users equipped, for example, with a qPlus sensor. Nevertheless, calculations are necessary to fully interpret experimental images in some specific cases. In this context, we developed a numerical AFM (n-AFM) able to be used in different modes and under different usage conditions.

Results: Here, we tackled FM-AFM image calculations of three types of graphitic structures, namely a graphite surface, a graphene sheet on a silicon carbide substrate with a Si-terminated surface, and finally, a graphene nanoribbon. We compared static structures, meaning that all the tip and sample atoms are kept frozen in their equilibrium position, with dynamic systems, obtained with a molecular dynamics module allowing all the atoms to move freely during the probe oscillations.

Conclusion: We found a very good agreement with experimental graphite and graphene images. The imaging process for the deposited nanoribbon demonstrates the stability of our n-AFM to image a non-perfectly planar substrate exhibiting a geometrical step as well as a material step.

Introduction

In the family of atomic force microscopy (AFM) techniques, the frequency-modulation (FM) mode provides subatomic and submolecular resolution [1-4]. Since the pionnering work performed by Giessibl [5], a large variety of surfaces have been observed at the atomic scale. For example, atomic features were imaged on Si [6-12], InSb [13], GaAs [14], Ge [15], NiAl [16,17], MgO [18-20], NaCl [21-25], $CaCO_3$ [26], TiO_2 [27-29], NiO [30], KBr [21,31-35], CaF_2 [36], and graphite [37-44] to mention just a few. Moreover, from monolayer to single molecules, submolecular resolution has been obtained on various molecular systems [3,45-59]. Recently, impressive results were shown with single pentacene $C_{22}H_{14}$ and $C_{16}H_{10}N_2O_2$ molecules adsorbed on a thin NaCl film deposited on a Cu(111) surface [52,53]. These breakthroughs were possible with a functionalized tip, that is, with a CO molecule attached to the tip apex acting as a supertip [60]. Most of the mentioned studies were based on a technical improvement consisting of the use of a tuning fork of the qPlus sensor type [61]. This sensor is an AFM tip that is fixed to one branch of a quartz tuning fork and provides a stiff probe capable of being approached close enough to the sample without touching the surface [62]. When the probe is oscillating above the sample, one of the characteristics of an experimental FM-AFM setup is the presence of several feedback loops to pilot the probe based on the dynamic behavior of the oscillator. Briefly speaking, an important element of the FM-AFM experimental apparatus is the frequency detection by demodulation performed with the aid of a phase-locked loop (PLL). This allows measurement of the frequency shift Δf from the fundamental resonance frequency of the free cantilever due to the tip–sample interactions. Moreover, two controllers are involved in the FM-AFM, namely the amplitude-controller (AC) and the distance-controller (DC) modules. The first one deals with the control of the oscillation amplitude of the probe, maintaining it at a constant value, and giving at the end an image representing a dissipation measurement. The second one keeps the resonance frequency shift Δf due to the probe–surface interaction constant, hence providing the topographic image. The complexity of the two entangled loops of the FM-AFM, each with different gain parameters to be adapted to the experimental conditions, has been tackled through analytical and numerical solutions. Different approaches have been proposed to theoretically describe the FM-AFM [63-66]. The numerical FM-AFM described in this paper is based on the development already described by Nony et al. [67], and the details of the adaptation and the improvement will be described elsewhere [68]. All the blocks constituting the experimental FM-AFM setup were translated into numerical blocks in the overall n-AFM.

Graphene is a material that is now widely tackled in the condensed-matter community due to its fascinating prospects related to its particular electronic properties [69-72]. Many papers report on the growth process, which occurs mainly on metallic surfaces or on the silicon carbide surface, and on the characterization at the atomic scale by scanning tunneling microscopy (STM) or Raman spectroscopy [73-79]. Recently, the ability to create nanoribbons of graphene [80-82] arises because such a system exhibits a gap opening, thus providing a semiconducting behavior to the material. Actually, the structure of the edge of these nanoribbons of few nanometers in width plays a role in the expected electronic properties due to the confinement effect and due to the reactivity of the carbon atoms at the edges [79,83]. It is thus important to control and to determine the atomic structure of these edges, especially if one wants to functionalize them with molecules to tune their electronic properties [83].

Here, we propose a reliable numerical FM-AFM tool to study the imaging process with a good flexibility in terms of parameter choice. The efficiency of this numerical AFM is showed through model systems of three graphitic structures, namely a graphite substrate, a graphene surface on a SiC substrate, and the edges of graphene nanoribbons, in frozen-atom and free-atom modes.

Technical details of the numerical AFM (n-AFM)

n-AFM in frequency-modulation mode

The n-AFM simulates the behavior of a frequency-modulation AFM with parameters compatible with an ultrahigh-vacuum environment. The probe oscillates at or close to its fundamental resonance frequency $\tilde{f}_0$. In this mode, the amplitude of oscillation is kept constant. When the oscillator is far enough from the sample, it can be considered as a free oscillator with $f_0 = \tilde{f}_0$. Upon approach toward the sample, an interaction between the tip and the sample appears and disturbs the oscillator motion, which leads to an almost instantaneous frequency shift, $\Delta f = \tilde{f}_0 - f_0$. The frequency shift varies depending on the tip–sample distance. This is a critical parameter of FM-AFM.

As already mentioned and described in previous contributions [65,67,84], a FM-AFM is composed of several blocks dedicated to AC and DC modules, and also the PLL. The PLL block has as input signal, i.e., the normalized signal depicting the oscillator motion. This block is used as a frequency demodulator and as a synchronized signal generator. Indeed, the input signal is demodulated in order to compute the frequency shift and a signal synchronized with the input is generated in order to

be used as the new normalized excitation signal. In this way, the excitation signal remains coherent with the oscillation of the probe.

The AC keeps the oscillation amplitude constant and equal to a predefined setpoint. Large-amplitude (typically 10–20 nm) to small-amplitude (of the order of 0.02 nm to mimic a qPlus sensor [62]) settings are available with the n-AFM. The DC allows the regulation of the tip–sample distance based on minimizing the difference between Δf and the frequency setpoint. This regulation yields the sample topography. Each block was transposed into a numerical program and included in a general code written in Fortran 90 language. Just a few parameters are needed as input for the oscillator: stiffness constant k, quality factor Q, resonance frequency f_0, amplitude A.

The versatility of the n-AFM allows the production of two types of image. In constant-height mode, the tip is approached toward the surface up to the point where the predefined setpoint, Δf_{set}, corresponding to a tip–surface separation, H_{set}, is reached. Then, the DC is disengaged, the XY-scan is engaged and the Δf variations around Δf_{set} are recorded. In this situation, the scan is therefore performed at nearly constant height, H_{set} (subject to vertical drift, which is obviously to be reduced as much as possible). Conversely, in constant-Δf mode, the DC remains engaged. Then, the image depicts the regulation of the tip–surface separation that is required to maintain constant Δf_{set}. Therefore, beyond the known influence of (i) the tip–surface interaction regime (attractive versus repulsive; the attractive regime is such that $H > H_{min}$, and the repulsive regime is such that $H < H_{min}$, where H_{min} corresponds to H at Δf_{min}, i.e., the minimum in the frequency shift versus tip–surface separation (H) curve) and (ii) the chemical nature of the tip–surface interaction on the contrast formation of the resulting images, the measured images may as well depend on the acquisition mode. To illustrate this point, let us consider two situations illustrated in Figure 1.

First, we consider a reactive or inert tip interacting with two identical atoms, one on an atomically flat lower terrace, and the other on a nearby upper terrace. Owing to the similar chemical nature of the atoms, Δf versus H curves measured on top of each of them exhibit similar features, and notably similar Δf minima. The curves are simply H-shifted with respect to each other (Figure 1a). This will correspond to the case of the reconstructed graphene discussed hereafter. Second, we consider a less reactive or inert tip above two different surface sites lying at almost the same height on the surface (e.g., a top and hollow site on a graphite surface, as explained hereafter, Figure 1b). In the case of the corrugated surface, it can be seen in Figure 1a that an image recorded in constant-height mode in the attractive regime will yield an inverted contrast compared to an image

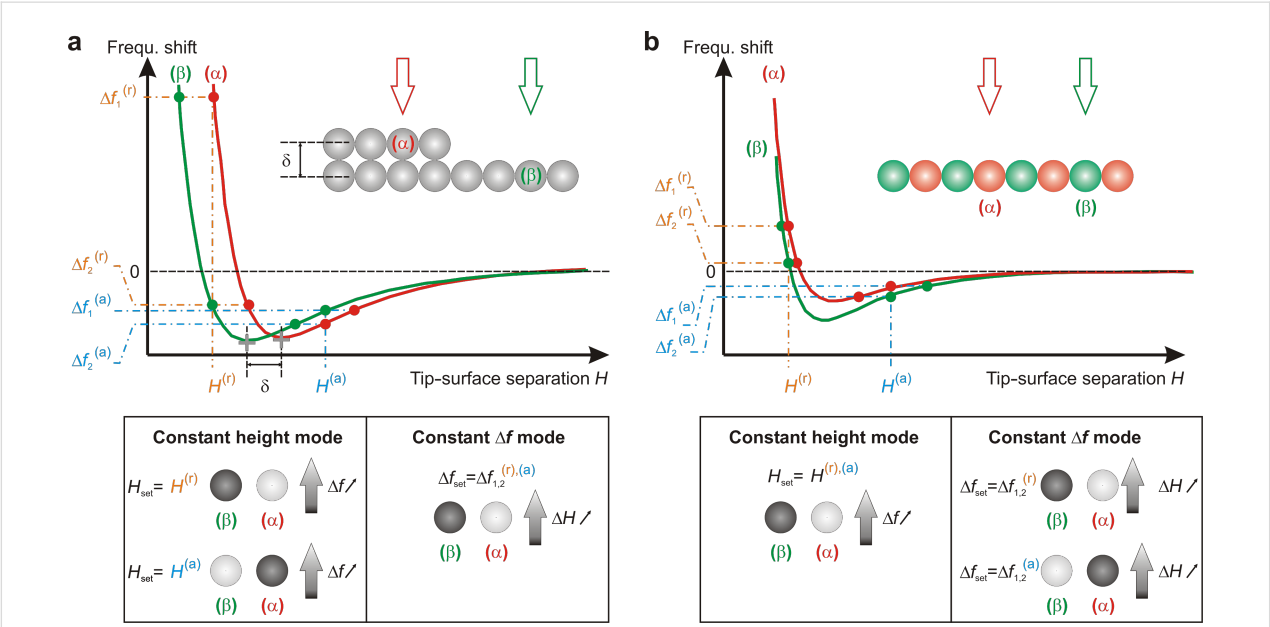

Figure 1: Illustration of constant-height and constant-Δf imaging modes in nc-AFM. We consider, as an illustrative situation, the cases of a homogeneous and atomically corrugated surface with a step (a) and a heterogeneous, but still atomically corrugated surface (b). In each situation frequency shift versus tip–surface separation (H) curves are presented above α and β surface sites. The tables below the curves illustrate the resulting imaging contrast (from white to dark grey, standing for large to small values of the variable) above each type of site depending upon the imaging mode. Contrast-inversion situations may appear depending on (i) the imaging mode, (ii) the interaction regime between the tip and the surface and (iii) the nature of the interaction between the tip and the surface atoms.

recorded in constant-Δf mode, whatever the value of Δf_{set} is (attractive or repulsive regime). In the case of the heterogeneous surface, an inversion contrast will be observed between a constant-Δf mode image acquired in the attractive regime and a constant-height mode image, whatever the interaction regime is.

Moreover, a molecular dynamics (MD) module is added by linking the n-AFM to the MD code DL_POLY [85]. This MD module can be implemented when it is necessary to take temperature conditions and/or deformations of the tip and the sample upon interaction into account. One of the main difficulties here is to handle the different time scales that characterize the different dynamic behaviors of the oscillator and the AFM junction atoms. Finally, a Kelvin probe force microscopy module (KPFM) [86-88] will be included in a near future. It should be mentioned also that when the tip interacts chemically with the substrate through bond creation between the tip apex atom and surface atoms, the choice of the force-field method may be difficult to justify. In that case, although reactive force fields exist [89-91] and may be implemented with the n-AFM, advanced first-principles methods [92] are well adapted to deal with local changes of electronic structure when the tip interacts with the sample surface, especially for KPFM [93,94]. For weak chemical interactions and van der Waals forces, theoretical studies have demonstrated accurate results for carbon-based systems [95-97], but are too slow and too computationally expensive compared to semiempirical models in the context of the n-AFM. The overall n-AFM system will be described elsewhere [68].

The settings used for this study are similar to the ones in [52], which correspond to a qPlus sensor: A_{set} = 0.2 Å, f_0 = 23165 Hz, k_c = 1800 N·m^{-1}, Q = 50000.

An important input is the tip–sample interaction, which will be described in the following section for the three graphitic structures.

Description of the interaction forces

In this study, the used model for the tip is composed of a nanosphere to mimic the probe body supporting a cluster of atoms for the tip apex. The sphere has a radius R of 4 nm and its force of interaction with a surface $F_{vdW}^{sphere-surface}$ is well described by

$$F_{vdW}^{sphere-surface}(r) = -\frac{H_k R}{6}\frac{1}{(r-R)^2}, \quad (1)$$

if $(r - R) \ll R$ [98]. H_k is the Hamaker constant (1 eV) and r the sphere–surface distance.

The cluster has a pyramidal diamond-like structure and is composed of 29 atoms [99]. The external interactions, that is between the atoms of the tip cluster and the atoms of the sample, are described by a Buckingham pairwise potential:

$$E_{vdW}^{cluster}(r) = A e^{-r\cdot a} - B\frac{b^6}{r^6}, \quad (2)$$

where a, b, A and B are constants depending on the type of atoms and are chosen in the data file of the MM4 force field [100,101].

When the MD module is switched on, the atoms of the tip and of the substrate are free to move under the constraints of internal and external interactions, and of a thermostat accounting for the external temperature. This constitutes the so-called free-atoms mode. In this case, the n-body Tersoff potential [89,102] was used for the internal interactions between atoms of each of the subsystems (the tip apex and the sample). This potential is designed to reproduce the covalent systems of the group IV elements in the periodic table (carbon, silicon, germanium, etc). Recent improvements of this potential [103] do not modify the results presented below.

In the case of graphite, the van der Waals interaction between two layers is described by a standard Lennard-Jones potential:

$$E_{LJ}(r) = 4\varepsilon\left[\left(\frac{\sigma}{r}\right)^{12} - \left(\frac{\sigma}{r}\right)^{6}\right], \quad (3)$$

with ε = 0.011 eV and σ = 3.2963 Å.

Results and Discussion

Graphite surface imaging

AFM imaging of the graphite surface is a difficult task because the interaction between the tip and the sample is generally weak. Following Hembacher et al. [41], the normalized frequency shift $\gamma = kA^{3/2}\Delta f/f_0$ is estimated to be $|\gamma| < 1$ fN·m$^{1/2}$. With the parameters used with the n-AFM, one gets $\gamma \approx 7 \times 10^{-18}\ \Delta f$ N·m$^{1/2}$, that is $\gamma \approx -0.1$ fN·m$^{1/2}$ with $\Delta f = -13$ Hz. From an experimental point of view, such a low value explains why graphite imaging is tedious and so challenging.

There are several previous studies that tackle the atomic determination of the graphite surface by FM-AFM [37-44,104-106]. Indeed, there is a discrepancy in the interpretation of the brightest features on the surface. By coupling STM and FM-AFM [41,44], one may identify the actual graphite struc-

ture observed in the images. Nevertheless, the role played by the tip (structure and composition) seems to impact directly upon the imaging process [44,107,108].

Here, we consider a graphite (0001) sample consisting of three graphene layers stacked with the abab structure each separated by 3.34 Å [109] and with 1792 carbon atoms each. The carbon atoms on the uppermost layer of the sample may be classified into two types, *A* with another neighboring atom just underneath, and *B* above a hollow site *h*. The tip is composed of 29 carbon atoms with a diamond-like organization. Results are presented in Figure 2 (in all the presented images, the scanning is from the left to right alternately, and from the bottom to the top). Force–distance spectra above different surface sites show a rather small variation due to the softness of the interaction, as sketched and enhanced in Figure 1b and similar to the Figure 2c (black and open symbols) in [44]. Figure 2a shows an image of the graphite surface in the frozen-atoms mode and at constant height, H_{set} = 4.3 Å, where *H* is the distance between the topmost surface plane and the terminating atom of the tip apex. At this distance, the tip oscillates in the attractive part of the tip–surface interaction force curve. This is the reason why the frequency shift exhibits a negative value. The maximum of corrugation is about 0.12 Hz, which is very weak. Such a low value is measured with the n-AFM because it works ideally without external noise sources and with no atomic vibration in the frozen-atoms mode. The *A* atoms appear brighter than the *B* atoms and the *h*-sites show a depression.

Nevertheless, a numerical noise remains due to the approximation made, which induces the fuzzy aspect of the image. The amplitude of the numerical noise is about 0.01 Hz on the frequency shift.

In the repulsive regime, the tip is scanned with a height H_{set} = 2.75 Å, and the corresponding image is shown in Figure 2b. Notice that the input parameters are the same as those previously used, but now the frequency shift is positive. Because the slope of the curve of the interaction force is much more abrupt in the repulsive part than in the attractive part, the maximum of corrugation is larger and reaches 87 Hz. The numerical noise is hidden by such values of frequency shift and the image looks much sharper. During the oscillation and the scanning, the tip experiences a maximal force of about 1.43 nN.

The relative atomic contrast in the two images at constant height in the attractive and repulsive regimes remains the same (Figure 1b): The *A* atoms appear brighter than the *B* sites.

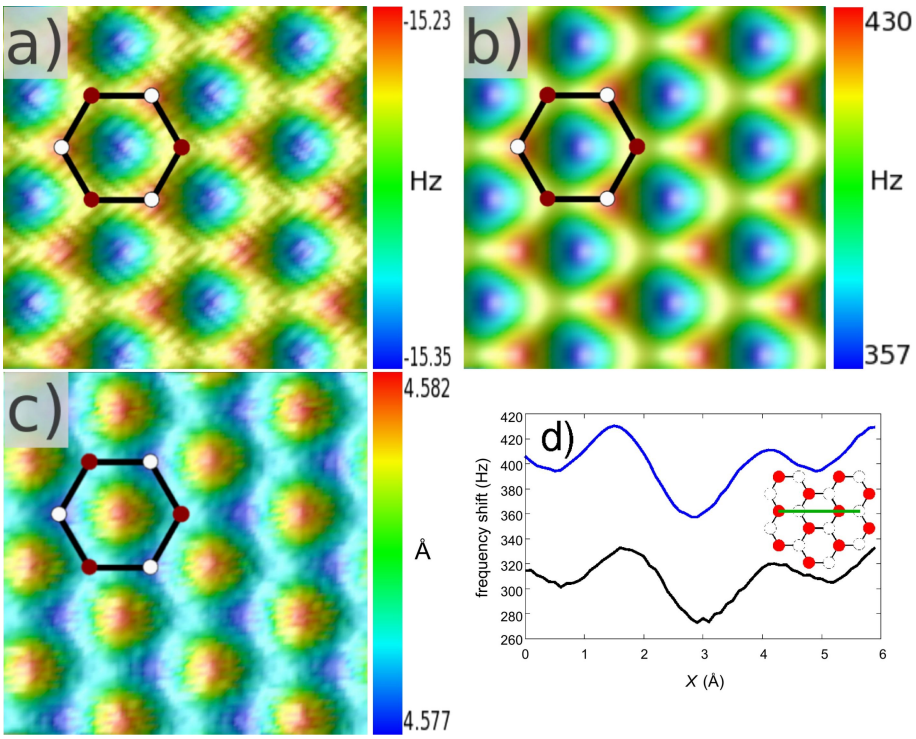

Figure 2: (a) Constant-height FM-AFM image of the graphite surface with H_{set} = 4.3 Å. White and dark circles correspond to *A* and *B* atoms, respectively. (b) Same as in (a) with H_{set} = 2.75 Å. (c) Constant-frequency-shift FM-AFM image of the graphite surface with Δf_{set} = −13 Hz. The size of these three images is 9 × 9 Å^2. (d) Scanlines above the green line shown in inset in the constant-height mode (H_{set} = 2.75 Å) for the frozen-atoms (blue) and free-atoms (black) regimes.

Indeed, the images exhibit a honeycomb pattern, with the most attractive and the least repulsive force above the hollow site in Figure 2a and in Figure 2b, respectively. This is in qualitative agreement with experiments [38,40,42,43] and calculated results [38,44]. Quantitative comparison may be tricky because parameters are different (working parameter set, reactive or inert tip, etc.). In [38], a tip–sample interaction model is based on a Lennard-Jones potential and gives similar results if one compares the scan line in Figure 2d. Of course, such a pairwise potential (Lennard-Jones or Buckingham potential) is not able to describe a reactive tip, and the contrast is explained in terms of the Pauli repulsion in the repulsive region.

For the constant-frequency-shift mode at $\Delta f_{set} = -13$ Hz, the result in the frozen-atoms mode is shown in Figure 2c. Here too, the tip explores the attractive range of the tip–surface interaction force with H around 4.58 Å and the tip experiences a minimal force of about −0.5 nN. One can see a contrast inversion compared to the previous cases in the constant-height mode (see Figure 1b and the corresponding table) but the bright spot above the hollow site has the same physical origin as previously, and it reflects the most attractive force as well. It is interesting to note that the maximum of corrugation is extremely small, about 0.004 Å which shows the consistent stability of the numerical distance controller. One may note that the chosen model of interactions gives a minimal Δf of about −14 Hz. To keep the tip in the attractive regime and to avoid an instable regime in which the controller is not able to prevent a tip crash on the surface, we have taken the Δf_{set} value mentioned above. Even if the corrugation is very low to be easily measured experimentally, one sees the difference between the *A* and *B* top sites and these results are qualitatively in agreement with experiments reported in the literature.

The results of the free-atoms mode at constant height (H_{set} = 2.75 Å) are shown in Figure 2d through a scanline above the graphite surface (see inset) corresponding to a condition at T = 4.9 K. Compared to the frozen-atoms result, the dynamic behavior induces a diminution of the corrugation (around 13 Hz) and a slight lateral shift due to the small motions of the carbon atoms during the scanning. Even a tiny out-of-plane displacement of the graphite atoms (<0.05 Å) generates a variation of about 90 Hz due to the abrupt slope of the $\Delta f(H)$ curve in the repulsive zone.

Supported graphene on a silicon carbide substrate

We consider here a graphene sheet on a Si-terminated 6H-SiC surface (5284 C atoms for the graphene sheet and three SiC layers for the substrate with 1332 Si and 1332 C atoms each giving in total a system of 13276 atoms). First, one has to consider the relaxation of the graphene layer with respect to the atomic structure of the substrate. By performing a full energy minimization of the system with DL_POLY-4 using periodic boundary conditions and with a Tersoff potential to connect the graphene and the SiC substrate, we found a buckling of the graphene sheet that is due to the incommensurability between the graphene and the SiC surfaces. The results shown in Figure 3a are similar to those obtained by DFT [74] or by using a more sophisticated empirical potential [110]: A quasi-hexagonal superstructure with a 6 × 6 periodicity is revealed with more or less long edges and a corrugation of about 1.2 Å. Such a soft corrugation of the moiré patterns is an interesting system for the n-AFM.

We performed FM-AFM calculations at constant height with H_{set} = 3.8 Å and at constant frequency shift with Δf_{set} = −12.5 Hz after relaxation of the graphene layer on SiC. The results are presented in Figure 3b and Figure 3c, respectively. On both images in the frozen-atoms mode, one recognizes the graphene reconstruction with distinct edges, and sharp nodes at the crossing points of the edges. Indeed, the Δf corrugation ranges from −20.0 Hz to 275.9 Hz in Figure 3b. This clearly indicates a rather strong repulsive regime at some points (yellow-red) due to the reduction of the tip–atom surface distance. Moreover, one can easily distinguish the long edges, which are two rows of C atoms higher than the narrow ones. The 6 × 6 periodicity was observed in noncontact mode AFM [111] but with smoother edges obtained in the constant-frequency-shift mode. In the attractive regime shown in Figure 3c, we observe a corrugation of 0.4 Å which may be measurable experimentally. Notice that there is no contrast inversion for the graphene hexagons on the ridges, whereas there is an inversion for hexagons in the center of the superstructure (Figure 1a and the corresponding table). This arises from a crossing between $\Delta f(H)$ curves as shown in Figure 1. At the center of the superstructure, one recovers the previous case of the graphite surface. The red (green) curve in Figure 1b could illustrate a tip–surface approach curve above a top (hollow) site: In the constant-frequency-shift mode, it is mandatory to work with a Δf_{set} higher than the minimum Δf (the red curve in the figure). As illustrated in Figure 1b, there is no intersection between the two typical curves. This thus implies a contrast inversion. On the contrary, and with the same requirement for the Δf setpoint, if $\Delta f(H)$ curves have a crossing point, as illustrated in Figure 1a, there is no contrast inversion. In this figure, the red characteristics should represent an approach curve above a surface atom that sits slightly out of the plane compared to the green one, corresponding to an approach above an atom in the surface plane. This shift can occur due to the local relaxation of the carbon atom network, as is the case for the graphene ripples.

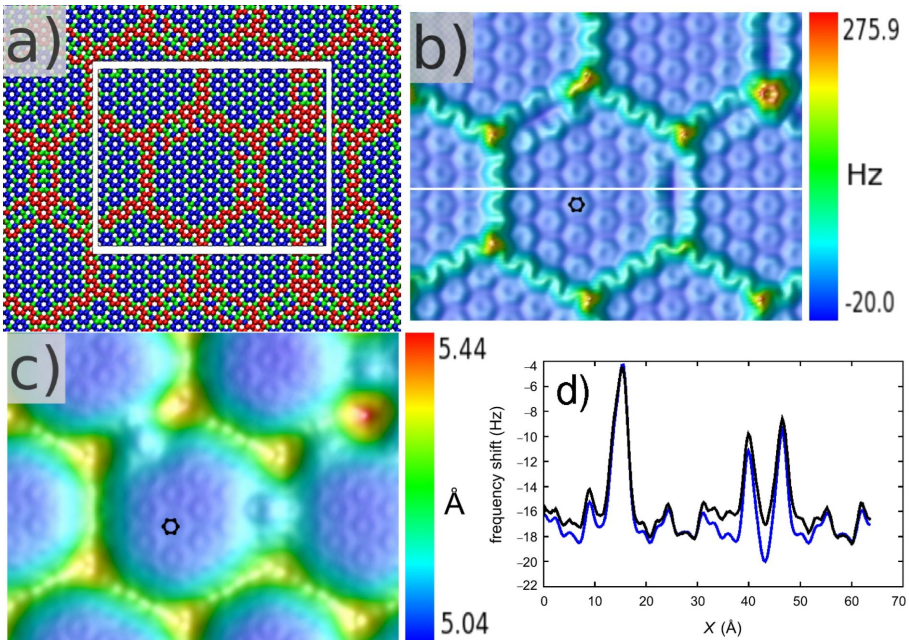

Figure 3: (a) Atomic structure of the buckled graphene on SiC with the height of graphene atoms classified in three categories: red, blue and green are the colors for the highest, the intermediate and the lowest carbon atoms, respectively. (b) Calculated graphene FM-AFM image with H_{set} = 3.8 Å along the white box in (a). The Δf corrugation is 295.9 Hz. The image size is 63.9 × 50.1 Å^2. The small black hexagon corresponds to a carbon ring of the surface. (c) FM-AFM calculated graphene image with Δf_{set} = −12.5 Hz along the white box in (a). The height corrugation is 0.4 Å (5.44 Å to 5.04 Å). The image size is 63.9 × 50.1 Å^2. (d) Scanlines above the white line in (b) for the frozen-atoms (blue) and free-atoms (black) regimes.

To go further, one needs to estimate the actual influence of the tip and of the temperature at T = 4.9 K in the free-atoms mode. By comparing the scan lines presented in Figure 3d, one sees that the system governed by MD exhibits, in some respects, a lower corrugation in the large ridge zones but a similar signal around the middle of the superhexagon. It appears also that the displacement of carbon atoms under these conditions is not homogeneous regarding their positions in the quasi-hexagonal superstructure. For rings on the higher ridge and at the center of the superhexagon, the mobility is reduced at T = 4.9 K. This is not the case for the other carbon rings, which induce a change in the frequency shift signal (almost 2 Hz at this temperature). This effect could be related to the local constraints of the carbon rings in the buckled graphene sheet.

Graphene nanoribbon edges

In the recent literature in the graphene community, there is a vivid interest in graphene nanoribbons (GNR), because one may tune their electronic structure through chemical edge modification. Before reaching this stage, precise characterization of the structure of the edges has to be tackled experimentally by transmission electronic microscopy, scanning tunneling microscopy (STM) or calculations [79,82,112-118]. Generally, GNRs show a zigzag or armchair configuration. It was also demonstrated that the zigzag edge may reconstruct to a configuration with Stone–Wales-like defects consisting of alternate pairs of pentagons and heptagons. Nevertheless, a recent theoretical contribution shows that the zigzag edges are found to be dominant for graphene nanoribbons obtained with proper etching [119].

Actually, as far as we know, there are no experimental FM-AFM imaging studies that reveal the edge structures of GNR. Nevertheless, some STM images succeed in identifying the edge conformation, although with a mixing of structural and electronic contributions [79]. As we are mainly interested in the capability of the n-AFM to image a GNR deposited on a SiC surface, we chose to start calculations with a GNR exhibiting a pristine zigzag edge [119]. The GNR consists of 684 carbon atoms forming a ribbon with a width of 18.38 Å. The SiC substrate is the same as previously used and the total system has 8676 atoms. Periodic boundary conditions are imposed along the main axis of the GNR. After a full energy relaxation, the GNR is slightly buckled and similar patterns to those seen in the graphene layer are obtained (Figure 4c). These patterns were also observed experimentally by STM on GNR or on graphene quantum dots [79,114,115]. A calculated FM-AFM image acquired with the n-AFM in the frozen-atoms regime is shown in Figure 4a. Here, the setpoint is H_{set} = 3.8 Å and the Δf corrugation is 81.7 Hz.

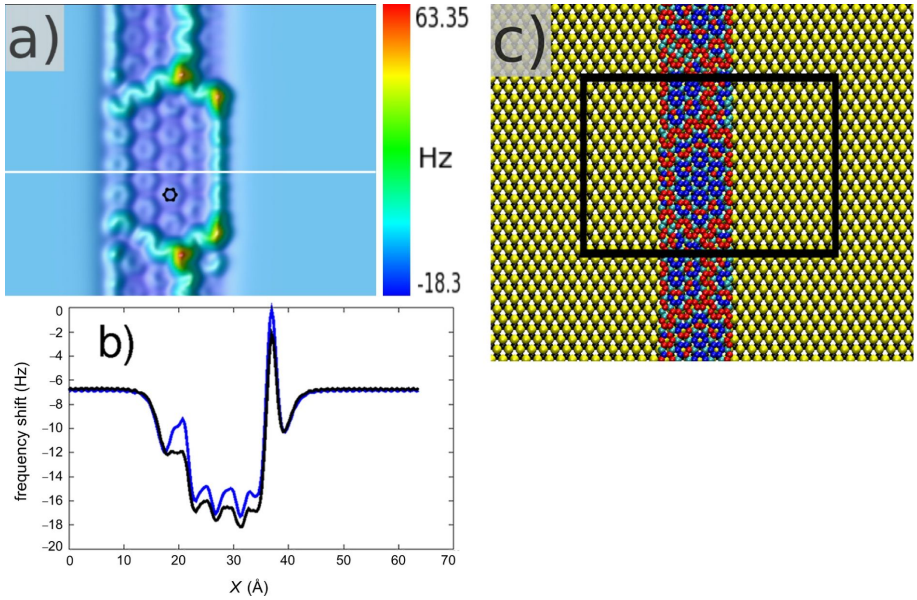

Figure 4: (a) FM-AFM calculated image of a graphene nanoribbon with H_{set} = 3.8 Å. The Δf corrugation is 81.68 Hz. The image size is 63.9 × 50.1 Å^2, which corresponds to the black area in (c). (b) Scan lines above the white line in (a) for the frozen-atoms (blue) and free-atoms (black) regimes. (c) Atomic model of the reconstructed GNR (same color code as in Figure 3d) on the SiC substrate (yellow, silicon atoms; black, carbon atoms).

At this setpoint, it is not possible to resolve the atomic structure of the SiC substrate, and the GNR appears globally darker due to the increase in attraction below the tip. If one compares the extremal values of the graphene and the GNR images, one remarks that the maximum Δf is more than four times smaller for the GNR. It means that repulsion is less important due to smaller deformations of the network of carbon atoms in the GNR. This is consistent with the reduced size of the GNR in which the mechanical constraints are less important at the borders. One may also notice that the stability of the n-AFM is satisfactory during the scanning. Indeed, the tip oscillator experiences, first, a geometrical step due to the presence of the GNR on the SiC surface (the average distance between the GNR and the SiC surface plane is about 2.1 Å), and second, an interaction step between the bare SiC surface and the "SiC substrate plus the GNR". These two steps are well accepted by the numerical DC of the n-AFM.

Finally, we compare the frozen-atoms and the free-atoms regimes along a scanline above the GNR in Figure 4b. The carbon atoms relax more freely generating a larger shift than in the case of graphene (1.5–2.0 Hz). One observes that the presence of the tip locally affects the structure at 4.9 K. It should also be mentioned that the lateral extension of the tip apex has a rather limited influence on the atomic behavior due to the limited size of the tip cluster. In order to take into account the interaction due to the lateral facets of the whole probe, one either discretizes the tip body by small volume elements and calculates a pairwise potential between each element and the atoms of the sample [120], or one adapts a self-consistent formalism to calculate the interactions between a dielectric probe of arbitrary shape and a corrugated surface [121-123].

Conclusion

We have proposed calculated images with the help of a numerical AFM (n-AFM) working in the FM-AFM mode. This n-AFM is a reliable numerical tool to address different conditions of use, from large to small (qPlus) amplitudes, either at constant height or at constant frequency shift. Moreover, the coupling of a molecular dynamics module allows us to take into account an external temperature as well as the mechanical pressure of the tip during the sample scanning. We have shown three examples on graphitic structures: (i) a flat graphite surface, (ii) smooth corrugated ripples of a graphene sheet relaxed on a silicon carbide substrate, and (iii) a corrugated transition of a graphene nanoribbon supported by a SiC surface. Improvements remain to be made for the prospective study of single molecule imaging and/or manipulation processes and related physical problems, such as dissipation [66,124,125] and the influence of noise perturbations [126].

Acknowledgements

Authors acknowledge the Agence Nationale de la Recherche with the PNANO project MolSiC (ANR-08-P058-36). This

researchers were granted access to the HPC resources of CALMIP under the allocation 2011-[P0832]. F.C. thanks N. Renon (CALMIP) for helpful discussions.

References

1. Giessibl, F. J. *Rev. Mod. Phys.* **2003,** *75,* 949. doi:10.1103/RevModPhys.75.949
2. Barth, C.; Foster, A. S.; Henry, C. R.; Shluger, A. L. *Adv. Mater.* **2011,** *23,* 477. doi:10.1002/adma.201002270
3. Gross, L. *Nat. Chem.* **2011,** *3,* 273. doi:10.1038/nchem.1008
4. Lauritsen, J. V.; Reichling, M. *J. Phys.: Condens. Matter* **2010,** *22,* 263001. doi:10.1088/0953-8984/22/26/263001
5. Giessibl, F. J. *Science* **1995,** *267,* 68. doi:10.1126/science.267.5194.68
6. Giessibl, F. J.; Hembacher, S.; Bielefeldt, H.; Mannhart, J. *Science* **2000,** *289,* 422. doi:10.1126/science.289.5478.422
7. Giessibl, F. J. *Mater. Today* **2005,** *8,* 32. doi:10.1016/S1369-7021(05)00844-8
8. Giessibl, F. J.; Herz, M.; Mannhart, J. *Proc. Natl. Acad. Sci. U. S. A.* **2002,** *99,* 12006. doi:10.1073/pnas.182160599
9. Sugimoto, Y.; Pou, P.; Abe, M.; Jelinek, P.; Pérez, R.; Morita, S.; Custance, Ó. *Nature* **2007,** *446,* 64. doi:10.1038/nature05530
10. Morita, K.; Sugimoto, Y.; Sasagawa, Y.; Abe, M.; Morita, S. *Nanotechnology* **2010,** *21,* 305704. doi:10.1088/0957-4484/21/30/305704
11. Sugimoto, Y.; Nakajima, Y.; Sawada, D.; Morita, K.-i.; Abe, M.; Morita, S. *Phys. Rev. B* **2010,** *81,* 245322. doi:10.1103/PhysRevB.81.245322
12. Sugimoto, Y.; Yi, I.; Morita, K.-i.; Abe, M.; Morita, S. *Appl. Phys. Lett.* **2010,** *96,* 263114. doi:10.1063/1.3457997
13. Kolodziej, J. J.; Such, B.; Szymonski, M.; Krok, F. *Phys. Rev. Lett.* **2003,** *90,* 226101. doi:10.1103/PhysRevLett.90.226101
14. Kolodziej, J. J.; Such, B.; Szymonski, M. *Phys. Rev. B* **2005,** *71,* 165419. doi:10.1103/PhysRevB.71.165419
15. Eguchi, T.; Fujikawa, Y.; Akiyama, K.; An, T.; Ono, M.; Hashimoto, T.; Morikawa, Y.; Terakura, K.; Sakurai, T.; Lagally, M. G.; Hasegawa, Y. *Phys. Rev. Lett.* **2004,** *93,* 266102. doi:10.1103/PhysRevLett.93.266102
16. Hamm, G.; Barth, C.; Becker, C.; Wandelt, K.; Henry, C. R. *Phys. Rev. Lett.* **2006,** *97,* 126106. doi:10.1103/PhysRevLett.97.126106
17. Heyde, M.; Kulawik, M.; Rust, H.-P.; Freund, H.-J. *Phys. Rev. B* **2006,** *73,* 125320. doi:10.1103/PhysRevB.73.125320
18. Barth, C.; Henry, C. R. *Phys. Rev. Lett.* **2003,** *91,* 196102. doi:10.1103/PhysRevLett.91.196102
19. Heyde, M.; Simon, G. H.; Rust, H.-P.; Freund, H.-J. *Appl. Phys. Lett.* **2006,** *89,* 263107. doi:10.1063/1.2424432
20. Bieletzki, M.; Hynninen, T.; Soini, T. M.; Pivetta, M.; Henry, C. R.; Foster, A. S.; Esch, F.; Barth, C.; Heiz, U. *Phys. Chem. Chem. Phys.* **2010,** *12,* 3203. doi:10.1039/b923296f
21. Hoffmann, R.; Kantorovich, L. N.; Baratoff, A.; Hug, H. J.; Güntherodt, H.-J. *Phys. Rev. Lett.* **2004,** *92,* 146103. doi:10.1103/PhysRevLett.92.146103
22. Barth, C.; Henry, C. R. *Phys. Rev. Lett.* **2008,** *100,* 096101. doi:10.1103/PhysRevLett.100.096101
23. Hoffmann, R.; Weiner, D.; Schirmeisen, A.; Foster, A. S. *Phys. Rev. B* **2009,** *80,* 115426. doi:10.1103/PhysRevB.80.115426
24. Langewisch, G.; Fuchs, H.; Schirmeisen, A. *Nanotechnology* **2010,** *21,* 345703. doi:10.1088/0957-4484/21/34/345703
25. Kawai, S.; Canova, F. F.; Glatzel, T.; Foster, A. S.; Meyer, E. *Phys. Rev. B* **2011,** *84,* 115415. doi:10.1103/PhysRevB.84.115415
26. Schütte, J.; Rahe, P.; Tröger, L.; Rode, S.; Bechstein, R.; Reichling, M.; Kühnle, A. *Langmuir* **2010,** *26,* 8295. doi:10.1021/la904706p
27. Lauritsen, J. V.; Foster, A. S.; Olesen, G. H.; Christensen, M. C.; Kühnle, A.; Helveg, S.; Rostrup-Nielsen, J. R.; Clausen, B. S.; Reichling, M.; Besenbacher, F. *Nanotechnology* **2006,** *17,* 3436. doi:10.1088/0957-4484/17/14/015
28. Rahe, P.; Bechstein, R.; Schütte, J.; Ostendorf, F.; Kühnle, A. *Phys. Rev. B* **2008,** *77,* 195410. doi:10.1103/PhysRevB.77.195410
29. Yurtsever, A.; Sugimoto, Y.; Abe, M.; Morita, S. *Nanotechnology* **2010,** *21,* 165702. doi:10.1088/0957-4484/21/16/165702
30. Hoffmann, R.; Lantz, M. A.; Hug, H. J.; van Schendel, P. J. A.; Kappenberger, P.; Martin, S.; Baratoff, A.; Güntherodt, H.-J. *Phys. Rev. B* **2003,** *67,* 085402. doi:10.1103/PhysRevB.67.085402
31. Hoffmann, R.; Lantz, M. A.; Hug, H. J.; van Schendel, P. J. A.; Kappenberger, P.; Martin, S.; Baratoff, A.; Güntherodt, H.-J. *Appl. Surf. Sci.* **2002,** *188,* 238. doi:10.1016/S0169-4332(01)00915-1
32. Venegas de la Cerda, M. A.; Abad, J.; Madgavkar, A.; Martrou, D.; Gauthier, S. *Nanotechnology* **2008,** *19,* 045503. doi:10.1088/0957-4484/19/04/045503
33. Kawai, S.; Glatzel, T.; Koch, S.; Such, B.; Baratoff, A.; Meyer, E. *Phys. Rev. Lett.* **2009,** *103,* 220801. doi:10.1103/PhysRevLett.103.220801
34. Ruschmeier, K.; Schirmeisen, A.; Hoffmann, R. *Phys. Rev. Lett.* **2008,** *101,* 156102. doi:10.1103/PhysRevLett.101.156102
35. Such, B.; Glatzel, T.; Kawai, S.; Koch, S.; Meyer, E. *J. Vac. Sci. Technol., B: Microelectron. Nanometer Struct.–Process., Meas., Phenom.* **2010,** *28,* C4B1. doi:10.1116/1.3382230
36. Hoffmann, R.; Barth, C.; Foster, A. S.; Shluger, A. L.; Hug, H. J.; Güntherodt, H.-J.; Nieminen, R. M.; Reichling, M. *J. Am. Chem. Soc.* **2005,** *127,* 17863. doi:10.1021/ja055267i
37. Allers, W.; Schwarz, A.; Schwarz, U. D.; Wiesendanger, R. *Appl. Surf. Sci.* **1999,** *140,* 247. doi:10.1016/S0169-4332(98)00535-2
38. Hölscher, H.; Allers, W.; Schwarz, A.; Schwarz, U. D.; Wiesendanger, R. *Phys. Rev. B* **2000,** *62,* 6967. doi:10.1103/PhysRevB.62.6967
39. Hölscher, H.; Schwarz, A.; Allers, W.; Schwarz, U. D.; Wiesendanger, R. *Phys. Rev. B* **2000,** *61,* 12678. doi:10.1103/PhysRevB.61.12678
40. Hembacher, S.; Giessibl, F. J.; Mannhart, J.; Quate, C. F. *Proc. Natl. Acad. Sci. U. S. A.* **2003,** *100,* 12539. doi:10.1073/pnas.2134173100
41. Hembacher, S.; Giessibl, F. J.; Mannhart, J.; Quate, C. *Phys. Rev. Lett.* **2005,** *94,* 056101. doi:10.1103/PhysRevLett.94.056101
42. Albers, B. J.; Schwendemann, T. C.; Baykara, M. Z.; Pilet, N.; Liebmann, M.; Altman, E. I.; Schwarz, U. D. *Nat. Nanotechnol.* **2009,** *4,* 307. doi:10.1038/nnano.2009.57
43. Kawai, S.; Kawakatsu, H. *Phys. Rev. B* **2009,** *79,* 115440. doi:10.1103/PhysRevB.79.115440
44. Ondráček, M.; Pou, P.; Rozsíval, V.; González, C.; Jelínek, P.; Pérez, R. *Phys. Rev. Lett.* **2011,** *106,* 176101. doi:10.1103/PhysRevLett.106.176101
45. Loppacher, C.; Guggisberg, M.; Pfeiffer, O.; Meyer, E.; Bammerlin, M.; Lüthi, R.; Schlittler, R.; Gimzewski, J. K.; Tang, H.; Joachim, C. *Phys. Rev. Lett.* **2003,** *90,* 066107. doi:10.1103/PhysRevLett.90.066107

46. Nony, L.; Gnecco, E.; Baratoff, A.; Alkauskas, A.; Bennewitz, R.; Pfeiffer, O.; Maier, S.; Wetzel, A.; Meyer, E.; Gerber, C. *Nano Lett.* **2004,** *4,* 2185. doi:10.1021/nl048693v
47. Yoda, T.; Ichii, T.; Fukuma, T.; Kobayashi, K.; Yamada, H.; Matsushige, K. *Jpn. J. Appl. Phys.* **2004,** *43,* 4691. doi:10.1143/JJAP.43.4691
48. Ashino, M.; Schwarz, A.; Behnke, T.; Wiesendanger, R. *Phys. Rev. Lett.* **2004,** *93,* 136101. doi:10.1103/PhysRevLett.93.136101
49. Burke, S. A.; Mativetsky, J. M.; Hoffmann, R.; Grütter, P. *Phys. Rev. Lett.* **2005,** *94,* 096102. doi:10.1103/PhysRevLett.94.096102
50. Fendrich, M.; Kunstmann, T.; Paulkowski, D.; Möller, R. *Nanotechnology* **2007,** *18,* 084004. doi:10.1088/0957-4484/18/8/084004
51. Ashino, M.; Obergfell, D.; Haluška, M.; Yang, S.; Khlobystov, A. N.; Roth, S.; Wiesendanger, R. *Nat. Nanotechnol.* **2008,** *3,* 337. doi:10.1038/nnano.2008.126
52. Gross, L.; Mohn, F.; Moll, N.; Liljeroth, P.; Meyer, G. *Science* **2009,** *325,* 1110. doi:10.1126/science.1176210
53. Gross, L.; Mohn, F.; Moll, N.; Meyer, G.; Ebel, R.; Abdel-Mageed, W. M.; Jaspars, M. *Nat. Chem.* **2010,** *2,* 821. doi:10.1038/nchem.765
54. Schütte, J.; Bechstein, R.; Rahe, P.; Langhals, H.; Rohlfing, M.; Kühnle, A. *Nanotechnology* **2011,** *22,* 245701. doi:10.1088/0957-4484/22/24/245701
55. Pawlak, R.; Kawai, S.; Fremy, S.; Glatzel, T.; Meyer, E. *ACS Nano* **2011,** *5,* 6349. doi:10.1021/nn201462g
56. Mohn, F.; Gross, L.; Meyer, G. *Appl. Phys. Lett.* **2011,** *99,* 053106. doi:10.1063/1.3619829
57. Kawai, S.; Pawlak, R.; Glatzel, T.; Meyer, E. *Phys. Rev. B* **2011,** *84,* 085429. doi:10.1103/PhysRevB.84.085429
58. Hinaut, A.; Lekhal, K.; Aivazian, G.; Bataillé, S.; Gourdon, A.; Martrou, D.; Gauthier, S. *J. Phys. Chem. C* **2011,** *115,* 13338. doi:10.1021/jp202873f
59. Chiutu, C.; Stannard, A.; Sweetman, A. M.; Moriarty, P. *Chem. Commun.* **2011,** *47,* 10575. doi:10.1039/c1cc14147c
60. Guillermet, O.; Gauthier, S.; Joachim, C.; de Mendoza, P.; Lauterbach, T.; Echavarren, A. *Chem. Phys. Lett.* **2011,** *511,* 482. doi:10.1016/j.cplett.2011.06.079
61. Giessibl, F. J. *Appl. Phys. Lett.* **2000,** *76,* 1470. doi:10.1063/1.126067
62. Giessibl, F. J.; Pielmeier, F.; Eguchi, T.; An, T.; Hasegawa, Y. *Phys. Rev. B* **2011,** *84,* 125409. doi:10.1103/PhysRevB.84.125409
63. Couturier, G.; Boisgard, R.; Nony, L.; Aimé, J. P. *Rev. Sci. Instrum.* **2003,** *74,* 2726. doi:10.1063/1.1564274
64. Couturier, G.; Aimé, J. P.; Salardenne, J.; Boisgard, R. *Eur. Phys. J.: Appl. Phys.* **2001,** *15,* 141. doi:10.1051/epjap:2001175
65. Polesel-Maris, J.; Gauthier, S. *J. Appl. Phys.* **2005,** *97,* 044902. doi:10.1063/1.1841462
66. Trevethan, T.; Kantorovich, L.; Polesel-Maris, J.; Gauthier, S. *Nanotechnology* **2007,** *18,* 084017. doi:10.1088/0957-4484/18/8/084017
67. Nony, L.; Baratoff, A.; Schär, D.; Pfeiffer, O.; Wetzel, A.; Meyer, E. *Phys. Rev. B* **2006,** *74,* 235439. doi:10.1103/PhysRevB.74.235439
68. Castanié, F.; Nony, L.; Gauthier, S.; Bouju, X. **2012**. (to be submitted for publication).
69. Geim, A. K. *Rev. Mod. Phys.* **2011,** *83,* 851. doi:10.1103/RevModPhys.83.851
70. Novoselov, K. S. *Rev. Mod. Phys.* **2011,** *83,* 837. doi:10.1103/RevModPhys.83.837
71. Avouris, P. *Nano Lett.* **2010,** *10,* 4285. doi:10.1021/nl102824h
72. Rümmeli, M. H.; Rocha, C. G.; Ortmann, F.; Ibrahim, I.; Sevincli, H.; Börrnert, F.; Kunstmann, J.; Bachmatiuk, A.; Pötschke, M.; Shiraishi, M.; Meyyappan, M.; Büchner, B.; Roche, S.; Cuniberti, G. *Adv. Mater.* **2011,** *23,* 4471. doi:10.1002/adma.201101855
73. Varchon, F.; Mallet, P.; Magaud, L.; Veuillen, J.-Y. *Phys. Rev. B* **2008,** *77,* 165415. doi:10.1103/PhysRevB.77.165415
74. Varchon, F.; Mallet, P.; Veuillen, J.-Y.; Magaud, L. *Phys. Rev. B* **2008,** *77,* 235412. doi:10.1103/PhysRevB.77.235412
75. Li, G.; Luican, A.; Andrei, E. Y. *Phys. Rev. Lett.* **2009,** *102,* 176804. doi:10.1103/PhysRevLett.102.176804
76. Allen, M. J.; Tung, V. C.; Kaner, R. B. *Chem. Rev.* **2011,** *110,* 132. doi:10.1021/cr900070d
77. Sakai, K.-i.; Takai, K.; Fukui, K.-i.; Nakanishi, T.; Enoki, T. *Phys. Rev. B* **2010,** *81,* 235417. doi:10.1103/PhysRevB.81.235417
78. Phark, S.-h.; Borme, J.; Vanegas, A. L.; Corbetta, M.; Sander, D.; Kirschner, J. *ACS Nano* **2011,** *5,* 8162. doi:10.1021/nn2028105
79. Yang, H.; Mayne, A. J.; Boucherit, M.; Comtet, G.; Dujardin, G.; Kuk, Y. *Nano Lett.* **2010,** *10,* 943. doi:10.1021/nl9038778
80. Tapasztó, L.; Dobrik, G.; Lambin, P.; Biró, L. P. *Nat. Nanotechnol.* **2008,** *3,* 397. doi:10.1038/nnano.2008.149
81. Cai, J.; Ruffieux, P.; Jaafar, R.; Bieri, M.; Braun, T.; Blankenburg, S.; Muoth, M.; Seitsonen, A. P.; Saleh, M.; Feng, X.; Mullen, K.; Fasel, R. *Nature* **2010,** *466,* 470. doi:10.1038/nature09211
82. Park, C.; Yang, H.; Mayne, A. J.; Dujardin, G.; Seo, S.; Kuk, Y.; Ihm, J.; Kim, G. *Proc. Natl. Acad. Sci. U. S. A.* **2011,** *108,* 18622. doi:10.1073/pnas.1114548108
83. Sun, Z.; Pint, C. L.; Marcano, D. C.; Zhang, C.; Yao, J.; Ruan, G.; Yan, Z.; Zhu, Y.; Hauge, R. H.; Tour, J. M. *Nat. Commun.* **2011,** *2,* 559. doi:10.1038/ncomms1577
84. Morita, S.; Giessibl, F. J.; Wiesendanger, R., Eds. *Noncontact Atomic Force Microscopy;* NanoScience and Technology, Vol. 2; Springer: Berlin, Heidelberg, 2009. doi:10.1007/978-3-642-01495-6
85. Todorov, I. T.; Smith, W.; Trachenko, K.; Dove, M. T. *J. Mater. Chem.* **2006,** *16,* 1911. doi:10.1039/B517931A
86. Bocquet, F.; Nony, L.; Loppacher, C.; Glatzel, T. *Phys. Rev. B* **2008,** *78,* 035410. doi:10.1103/PhysRevB.78.035410
87. Nony, L.; Foster, A. S.; Bocquet, F.; Loppacher, C. *Phys. Rev. Lett.* **2009,** *103,* 036802. doi:10.1103/PhysRevLett.103.036802
88. Sadewasser, S.; Glatzel, T., Eds. *Kelvin Probe Force Microscopy - Measuring, Compensating Electrostatic Forces;* Springer Series in Surface Sciences, Vol. 48; Springer: Berlin, Heidelberg, 2012. doi:10.1007/978-3-642-22566-6
89. Tersoff, J. *Phys. Rev. B* **1989,** *39,* 5566. doi:10.1103/PhysRevB.39.5566
90. van Duin, A. C. T.; Dasgupta, S.; Lorant, F.; Goddart, W. A., III. *J. Phys. Chem. A* **2001,** *105,* 9396. doi:10.1021/jp004368u
91. Bosson, M.; Grudinin, S.; Bouju, X.; Redon, S. *J. Comput. Phys.* **2012,** *231,* 2581. doi:10.1016/j.jcp.2011.12.006
92. Lewis, J. P.; Jelínek, P.; Ortega, J.; Demkov, A. A.; Trabada, D. G.; Haycock, B.; Wang, H.; Adams, G.; Tomfohr, J. K.; Abad, E.; Wang, H.; Drabold, D. A. *Phys. Status Solidi B* **2011,** *248,* 1989. doi:10.1002/pssb.201147259
93. Sadewasser, S.; Jelinek, P.; Fand, C.-K.; Custance, O.; Yamada, Y.; Sugimoto, Y.; Abe, M.; Morita, S. *Phys. Rev. Lett.* **2009,** *103,* 266103. doi:10.1103/PhysRevLett.103.266103
94. Tsukada, M.; Masago, A.; Shimizu, M. *J. Phys.: Condens. Matter* **2012,** *24,* 084002. doi:10.1088/0953-8984/24/8/084002
95. Dappe, Y. J.; Basanta, M. A.; Flores, F.; Ortega, J. *Phys. Rev. B* **2006,** *74,* 205434. doi:10.1103/PhysRevB.74.205434

96. Dappe, Y. J.; Scipioni, R. *Phys. Rev. B* **2011,** *84,* 193409. doi:10.1103/PhysRevB.84.193409
97. Seydou, M.; Dappe, Y. J.; Marsaudon, S.; Aimé, J.-P.; Bouju, X.; Bonnot, A.-M. *Phys. Rev. B* **2011,** *83,* 045410. doi:10.1103/PhysRevB.83.045410
98. Argento, C.; French, R. H. *J. Appl. Phys.* **1996,** *80,* 6081. doi:10.1063/1.363680
99. Tang, H.; Bouju, X.; Joachim, C.; Girard, C.; Devillers, J. *J. Chem. Phys.* **1998,** *108,* 359. doi:10.1063/1.475383
100. Allinger, N. L.; Chen, K.; Lii, J.-H. *J. Comput. Chem.* **1996,** *17,* 642. doi:10.1002/(SICI)1096-987X(199604)17:5/6<642::AID-JCC6>3.0.CO;2-U
101. Allinger, N. L. *J. Comput.-Aided Mol. Des.* **2011,** *25,* 295. doi:10.1007/s10822-011-9422-4
102. de Brito Mota, F.; Justo, J. F.; Fazzio, A. *J. Appl. Phys.* **1999,** *86,* 1843. doi:10.1063/1.370977
103. Lindsay, L.; Broido, D. A. *Phys. Rev. B* **2010,** *81,* 205441. doi:10.1103/PhysRevB.81.205441
104. Kawai, S.; Glatzel, T.; Koch, S.; Such, B.; Baratoff, A.; Meyer, E. *Phys. Rev. B* **2010,** *81,* 085420. doi:10.1103/PhysRevB.81.085420
105. Wright, C. A.; Solares, S. D. *Nano Lett.* **2011,** *11,* 5026. doi:10.1021/nl2030773
106. Sun, Z.; Hämäläinen, S. K.; Sainio, J.; Lahtinen, J.; Vanmaekelbergh, D.; Liljeroth, P. *Phys. Rev. B* **2011,** *83,* 081415. doi:10.1103/PhysRevB.83.081415
107. Campbellová, A.; Ondráček, M.; Pou, P.; Pérez, R.; Klapetek, P.; Jelínek, P. *Nanotechnology* **2011,** *22,* 295710. doi:10.1088/0957-4484/22/29/295710
108. Canova, F. F.; Foster, A. S. *Nanotechnology* **2011,** *22,* 045702. doi:10.1088/0957-4484/22/4/045702
109. Kolmogorov, A. N.; Crespi, V. H. *Phys. Rev. B* **2005,** *71,* 235415. doi:10.1103/PhysRevB.71.235415
110. Lampin, E.; Priester, C.; Krzeminski, C.; Magaud, L. *J. Appl. Phys.* **2010,** *107,* 103514. doi:10.1063/1.3357297
111. Filleter, T.; Bennewitz, R. *Phys. Rev. B* **2010,** *81,* 155412. doi:10.1103/PhysRevB.81.155412
112. Girit, C. O.; Meyer, J. C.; Erni, R.; Rossell, M. D.; Kisielowski, C.; Yang, L.; Park, C.-H.; Crommie, M. F.; Cohen, M. L.; Louie, S. G.; Zettl, A. *Science* **2009,** *323,* 1705. doi:10.1126/science.1166999
113. Koskinen, P.; Malola, S.; Häkkinen, H. *Phys. Rev. B* **2009,** *80,* 073401. doi:10.1103/PhysRevB.80.073401
114. Coraux, J.; N'Diaye, A. T.; Engler, M.; Busse, C.; Wall, D.; Buckanie, N.; Meyer zu Heringdorf, F. J.; Van Gastel, R.; Poelsema, B.; Michely, T. *New J. Phys.* **2009,** *11,* 023006. doi:10.1088/1367-2630/11/3/039801
115. Hämäläinen, S. K.; Sun, Z.; Boneschanscher, M. P.; Uppstu, A.; Ijäs, M.; Harju, A.; Vanmaekelbergh, D.; Liljeroth, P. *Phys. Rev. Lett.* **2011,** *107,* 236803. doi:10.1103/PhysRevLett.107.236803
116. Koskinen, P.; Malola, S.; Häkkinen, H. *Phys. Rev. Lett.* **2008,** *101,* 115502. doi:10.1103/PhysRevLett.101.115502
117. Kroes, J. M. H.; Akhukov, M. A.; Los, J. H.; Pineau, N.; Fasolino, A. *Phys. Rev. B* **2011,** *83,* 165411. doi:10.1103/PhysRevB.83.165411
118. Rodrigues, J. N. B.; Gonçalves, P. A. D.; Rodrigues, N. F. G.; Ribeiro, R. M.; Lopes dos Santos, J. M. B.; Peres, N. M. R. *Phys. Rev. B* **2011,** *84,* 155435. doi:10.1103/PhysRevB.84.155435
119. Guo, Y.; Guo, W. *J. Phys. Chem. C* **2011,** *115,* 20546. doi:10.1021/jp205671r
120. Touhari, F.; Bouju, X.; Girard, C.; Devel, M.; Cohen-Solal, G. *Appl. Surf. Sci.* **1998,** *125,* 351. doi:10.1016/S0169-4332(97)00504-7
121. Bouju, X.; Girard, C.; Labani, B. *Ultramicroscopy* **1992,** *42–44,* 430. doi:10.1016/0304-3991(92)90303-2
122. Girard, C.; Bouju, X.; Joachim, C. *Chem. Phys.* **1992,** *168,* 203. doi:10.1016/0301-0104(92)87155-3
123. Girard, C.; Bouju, X.; Martin, O. J. F.; Dereux, A.; Chavy, C.; Tang, H.; Joachim, C. *Phys. Rev. B* **1993,** *48,* 15417. doi:10.1103/PhysRevB.48.15417
124. Kantorovich, L. N. *J. Phys.: Condens. Matter* **2001,** *13,* 945. doi:10.1088/0953-8984/13/5/313
125. Trevethan, T.; Kantorovich, L. *Nanotechnology* **2004,** *15,* S44. doi:10.1088/0957-4484/15/2/010
126. Polesel-Maris, J.; Venegas de la Cerda, M. A.; Martrou, D.; Gauthier, S. *Phys. Rev. B* **2009,** *79,* 235401. doi:10.1103/PhysRevB.79.235401

License and Terms

Beilstein Journal of Nanotechnology

Models of the interaction of metal tips with insulating surfaces

Thomas Trevethan*[1,2,3], Matthew Watkins[4] and Alexander L. Shluger[1,2,4]

Full Research Paper

Open Access

Address:
[1]Department of Physics and Astronomy, University College London, Gower Street, WC1E 6BT London, United Kingdom, [2]WPI-AIMR, Tohoku University, 2-1-1 Katahira, Aoba, Sendai, 980-8577, Japan, [3]Department of Chemistry, University of Sussex, Brighton, BN1 9RH, United Kingdom and [4]The London Centre for Nanotechnology, University College London, 17–19 Gordon Street, WC1H 0AH London, United Kingdom

Email:
Thomas Trevethan* - t.trevethan@sussex.ac.uk

* Corresponding author

Keywords:
atomic force microscopy; density functional theory; ionic surfaces; metallic asperities; surface interactions

Beilstein J. Nanotechnol. **2012,** *3,* 329–335.
doi:10.3762/bjnano.3.37

Received: 12 December 2011
Accepted: 22 March 2012
Published: 13 April 2012

This article is part of the Thematic Series "Noncontact atomic force microscopy".

Guest Editor: U. D. Schwarz

Abstract

We present the results of atomistic simulations of metallic atomic-force-microscopy tips interacting with ionic substrates, with atomic resolution. Chromium and tungsten tips are used to image the NaCl(001) and MgO(001) surfaces. The interaction of the tips with the surface is simulated by using density-functional-theory calculations employing a mixed Gaussian and plane-wave basis and cluster-tip models. In each case, the apex of the metal cluster interacts more attractively with anions in the surfaces than with cations, over the range of typical imaging distances, which leads to these sites being imaged as raised features (bright) in constant-frequency-shift images. We compare the results of the interaction of a chromium tip with the NaCl surface, with calculations employing exclusively plane-wave basis sets and a fully periodic tip model, and demonstrate that the electronic structure of the tip model employed can have a significant quantitative effect on calculated forces when the tip and surface are clearly separated.

Introduction

The noncontact atomic force microscope (NC-AFM) is capable of imaging both conducting and insulating systems with true atomic resolution and has provided extraordinary contributions to surface science [1-3]. In NC-AFM the tip is prevented from jumping into mechanical contact with the sample surface due to the large restoring force of the cantilever at the turning point of the tip trajectory when it is closest to the surface. As a result, the instrument can probe all regions of the tip–surface interaction with high stability, in particular the “near contact” region of separation where the tip apex atom and surface are separated by only a few angstroms (i.e., the typical range of chemical bonds). However, the nature of the force between the tip and the surface is highly dependent on the exact atomic structure and chemical nature of the tip apex. In the case of ionic surfaces,

different terminating atoms can lead to completely inverted image contrasts [3,4], in which case it is not even possible to identify the polarity of surface ions corresponding to protrusions in the image. The control and characterization of the tip-apex termination is therefore critical for the reliable interpretation of images.

AFM tip–cantilever assemblies are usually fabricated from silicon, which is then exposed to air and will thus develop a native oxide layer with air-induced contaminants. This layer can be removed in situ inside the ultrahigh vacuum chamber, by sputtering and/or annealing. However there is no guarantee that the tip apex is pure silicon, and contaminant atoms or molecules may remain. The tip can also be contaminated by material from the surface during imaging; in fact, in many cases atomic-resolution images are only obtained after the tip has been deliberately crashed into the surface, implying that the tip apex is formed from surface species [1,2]. The development of NC-AFM based on a quartz tuning fork (qPlus sensor) instead of a silicon cantilever has led to more freedom in choosing the tip material, as a tip can be manually attached to the tuning-fork prong [5]. However, the problem of keeping the tip apex free of contaminants remains.

One approach to deal with the problem of tip–apex control is to employ a tip material that is easy to prepare and characterize in situ, i.e., in UHV and through the tip–surface interaction. The use of metal-coated tips meets both of these requirements. Firstly, coating a standard silicon tip with a layer of metal can be achieved in the UHV chamber by evaporation (assuming that the metal bonds effectively to the oxide layer) [6], resulting in a high confidence that the metallic tip apex is free from airborne contaminants. Secondly, it is possible to judge based on the conductivity of the tip as to whether the tip apex is metallic or terminated with contaminant atoms. This can be achieved by recording the resonant frequency while the bias voltage, applied between the tip and the sample holder, is varied. As described in [7], smooth parabolic curves that are independent of the scan direction indicate a metallic tip apex. On the other hand, discontinuities and hysteresis between scan directions indicate charge localization and reconfiguration and a tip apex that is not truly metallic.

It has been demonstrated that a chromium-coated tip is capable of imaging the bulk NaCl(001) surface with atomic resolution, at relatively large tip–surface separations (i.e., >5 Å), reducing the potential for the tip to become contaminated by the surface [7]. Plane-wave density-functional-theory (DFT) calculations employing a periodic metallic-tip model demonstrated that the Cr tip apex interacts most strongly with anions (Cl^-) in the surface, and that these ions correspond to protrusions in the image. Thus these experiments and the accompanying calculations suggest that properly characterized Cr coated tips can be used to unambiguously interpret the contrast in images of the NaCl(001) surface. The mechanism of contrast formation proposed is quite universal and involves the interaction of the polarized tip (due to the Smoluchowski effect) with the surface ions at large tip–surface separations and the hybridization of tip and anion states at smaller separations. Therefore it is reasonable to expect that similar mechanisms should apply both to other ionic surfaces and to other metals. A more general understanding of the interaction of metallic tips with ionic surfaces will help motivate experimental efforts and inform choices of tip material and tip-preparation methods.

In this paper we present the results of atomistic DFT calculations performed to investigate the interaction between metal tips and the typical binary ionic surfaces, NaCl(001) and MgO(001). The high symmetry of these surfaces makes their AFM images particularly difficult to interpret [3], although in the case of NaCl(001), there have been several approaches to successfully interpret atomic-resolution images [8-11]. We consider two types of metal tip, namely chromium and tungsten, which are chosen due to their common use in scanning-probe experiments. For several different combinations of tip and surface, we determine the tip–surface force field and the origin of the tip–surface interaction at close approach. These calculations employ cluster-tip models and localized Gaussian atomic basis sets, which result in a significantly lower computational cost when compared with fully periodic tips (which consist of a significantly greater number of atoms) and plane-wave calculations. We compare the results of these two approaches for the Cr/NaCl system and discuss the effect of the DFT methodology and the electronic structure of the tip model on the accuracy of the calculations of tip–surface forces. The plan of the rest of the paper is as follows: The next section describes the methodology employed; the third section describes the results of the calculations; and in the final section a discussion of the results and how they compare to other calculations is presented.

Results and Discussion

The calculations presented in this study were performed by using the DFT module of the CP2K code [12] and employing the PBE exchange-correlation functional [13]. Gaussian basis sets of DZVP quality were used with semicore GTH pseudopotentials [14-16]. The pseudopotentials included 9, 10, 14 and 18 valence electrons for Na, Mg, W and Pt. The auxiliary plane-wave basis, used to calculate the Hartree energy, had an energy cutoff of 4000 eV. To account for the metallic nature of the tip (i.e., a very small band gap) in the simulation, we also employ Fermi–Dirac smearing of the molecular-orbital occupation numbers, with an electronic temperature of 2500 K.

Both the NaCl(001) and MgO(001) surfaces were modeled using a periodic slab, 6 × 6 atoms in area and three atomic layers deep, where the bottom-most layer is frozen in bulk-like positions. For a direct comparison with the results of previous plane-wave calculations employing a periodic-tip model, the NaCl(001) surface was also modeled with a 5 × 5 primitive unit cell surface area, three atomic layers deep, which was chosen to match the *x*-*y* periodicity of the periodic tip model. The slabs are periodic in the *x*-*y* directions, and there is a vacuum gap of 30 Å in the *z*-direction. The lattice separation in the NaCl slab is 2.78 Å and in the MgO slab is 2.12 Å. When the geometries of the surface slabs are optimized they exhibit rumpling, with the anions protruding from the surface plane. The corrugation of the NaCl surface is approximately 0.1 Å and 0.04 Å in MgO. The one-electron band gaps for the NaCl surface at 4.9 eV, and for the MgO surface at 3.6 eV, are underestimated, which is typical for PBE calculations.

The tip models are shown in Figure 1. The cluster Cr and W tips consist of four-layered pyramids, cut from the body-centered-cubic (BCC) structure of the bulk crystals. The top two layers of the 30 atom tips are frozen, and the lower two layers are free to relax. For a direct comparison with the plane-wave calculations presented in [7], a periodic-tip model consisting of a three-layer BCC slab of Cr with symmetric pyramidal protrusions (Figure 1b) was also employed. It is well-known that the structure and morphology of the tip has a significant effect on the tip–surface interaction [17,18]; however, this type of pyramidal protrusion was shown to be the best match to the experimental measurements reported for this system [7]. The work functions for the Cr tips are calculated as being approximately 3.7 eV for both tip models, which is similar to previous calculations for the Cr surface [19] but slightly less (by 0.2–0.6 eV) than the experimental values [20,21]. For all of the tip models the Fermi energy lies well within the band gap of the ionic surface slabs.

To calculate the tip–surface force field, the frozen part of the tip is fixed at a position above the surface, the system relaxed, and the total energy calculated. The tip is then moved a small distance closer to the surface, and this is repeated to map out the energy as a function of the tip position. The gradient of this energy in the *z*-direction is then used to determine the tip force. The tip height is defined as the separation that would exist between the front atom of the tip and the surface plane if there were no relaxation in the tip (i.e., with the tip away from the surface). The DFT method is known to underestimate atomistic dispersion forces; however, these are not expected to contribute to the atomic-scale variation of the force on the tip above different atomic sites [3]. A macroscopic van der Waals attraction is added to the total force on the tip for simulated image calculations, as stated in the Experimental section.

To correct for the basis-set-superposition error (BSSE), which acts to increase the force on the tip originating from the interaction with the surface, due to the overlap of the basis functions of the surface and tip, we employ the counterpoise method to correct the total system energy for different tip positions relative to the surface [22]. Our calculations demonstrate that the BSSE is similar at a given tip height above both anions and cations (approximately 0.1 eV at 4 Å), and is therefore not likely to contribute to atomic-scale contrast. Furthermore, the BSSE is only present at tip–surface separations below 4.5 Å, as above this height there is no orbital overlap.

The total energy as a function of tip height, for the apex of the Cr cluster tip directly above both Cl^- and Na^+ ions in the NaCl

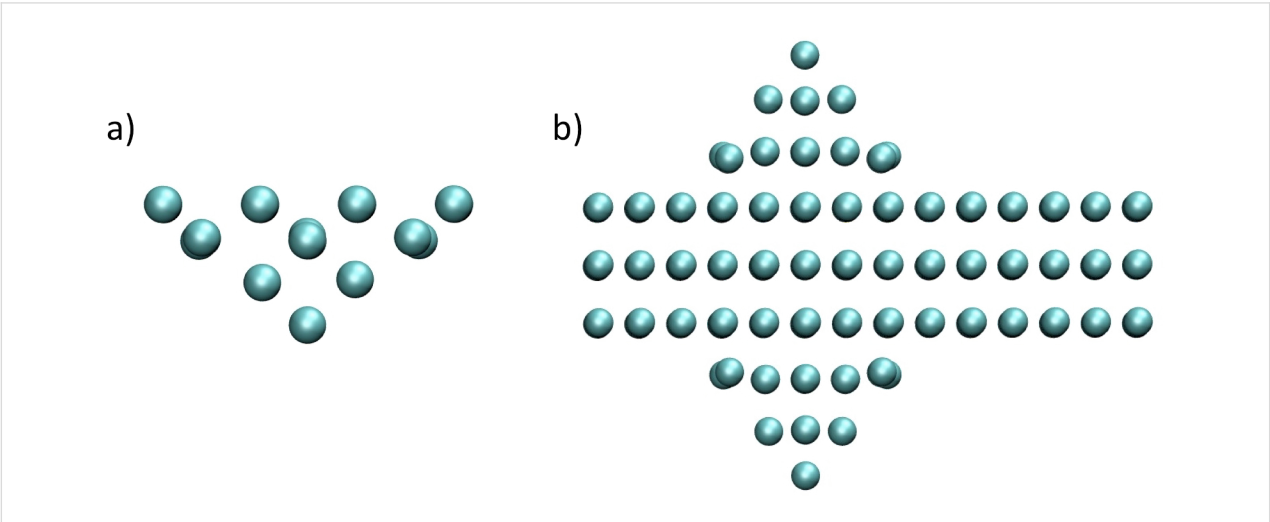

Figure 1: (a) Side-on view of the structure of the Cr and W cluster tip models. (b) The structure of the periodic Cr tip model.

surface, and above both O^{2-} and Mg^{2+} ions in the MgO surface, is shown in Figure 2. Here the energy change is relative to the energy of the tip and surface when they are completely separated. In each case it is clear that the force is largest directly above anions in the surface, significantly so in the range probed by noncontact imaging, i.e., 3–5 Å. For each tip above an anion in the surface, at close approach (approx. 3–4 Å) the force increases markedly due to a structural change consisting of strong displacement of an anion out of the surface to bond to the tip apex. This jump of a surface ion to the tip apex will result in hysteresis in the tip–surface force field and atomic-scale dissipation being measured by the NC-AFM instrument [23,24]. For the Cr tip interacting with the NaCl surface, the total charge on the tip at a separation of 6 Å is less than −0.01 $|e|$ (from a Mulliken population analysis); however, when the tip comes closer to the surface above a Cl^- ion, there is a small charge transfer to the tip (of −0.03 $|e|$ at a height of 4 Å and of −0.1 $|e|$ at 3 Å). For the tip above the MgO surface, a similar transfer occurs, but it is slightly more pronounced (a charge on the tip of −0.16 $|e|$ at 4 Å above an O^{2-} ion in the surface).

Figure 3 shows the total energy as a function of the tip height for the W tip directly above Cl^- and Na^+ ions in the NaCl(001) surface. As before, the interaction is strongest above the anion, and increases significantly below 4.5 Å (note this is not due to an instability caused by an atom jump). The charge transfer to the tip at close approach is similar to that in the case of the Cr tip interacting with this surface, which is to be expected due to the similar Fermi energies of the two clusters. In the case of both tips, the origin of the charge transfer at close approach and the increased tip force above the anions is due to the hybridization of the d states in the tip apex atom with the p states in the surface anion.

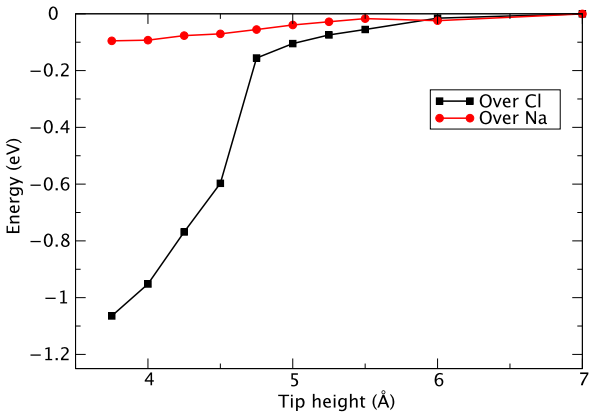

Figure 3: Energy as a function of tip height for the W tip interacting with the NaCl(001) surface.

In each of the tip–surface combinations, the calculated force fields would result in the anions being imaged as prominent protrusions in a constant-frequency-shift image of the surfaces. To demonstrate this, and show the extent of typical atomic scale corrugation, we simulated the imaging of the NaCl surface with the Cr cluster tip, using typical imaging parameters based on a traditional silicon cantilever (listed in the Experimental section). The force field used for these calculations was calculated on a lateral square grid with a spacing of 1/8 of the lattice constant between points (i.e., four points between adjacent surface ions), and between tip heights of 3 Å and 7 Å. Figure 4 shows a constant-Δf image (Δf = −60 Hz) of the NaCl surface, in which the distance of closest approach is 3.6 Å. The rumpling is approximately 0.6 Å with the protrusions corresponding to Cl^- ion lattice positions and depressions to Na^+ ion positions.

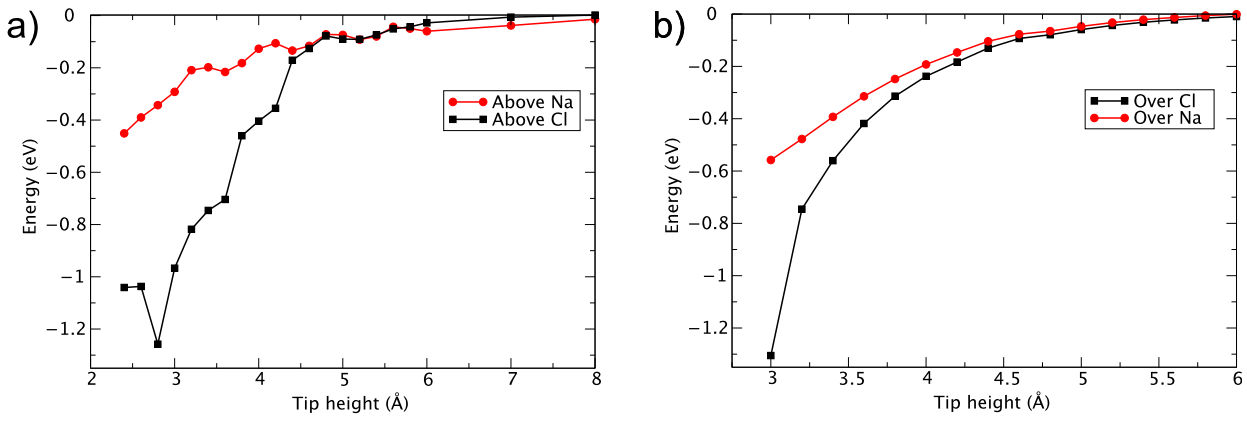

Figure 2: (a) Energy as a function of cluster Cr tip height above the NaCl(001) surface. (b) Energy as a function of tip height above the MgO(001) surface.

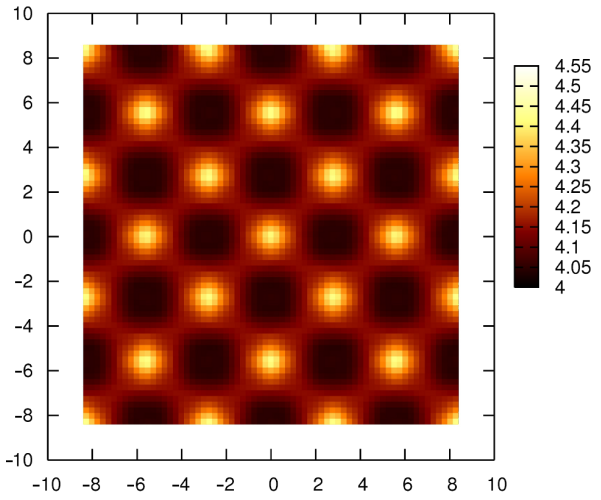

Figure 4: Constant-frequency-shift image (Δf = −60 Hz) of the NaCl surface imaged with the cluster Cr tip.

To investigate both the contribution of the electronic structure of the tip and the type of simulation method to the interaction between a metallic tip and an ionic surface, we calculated the changes in total energy as a function of tip position for the periodic Cr tip model interacting with the NaCl surface. We used the exact same system configurations as used in previous plane-wave DFT calculations, employing the VASP code [25] (as described above). The same PBE correlation-exchange functional employed in [7] was used here. The main difference in the model we apply is in the form of the basis functions, in which the wave function of the system is expanded: Here they are Gaussian and atom-based, as opposed to being plane waves.

Figure 5 shows the total energies (BSSE corrected) as a function of tip position (the exact same positions calculated in [7]). As in [7], Morse bond functions were fitted to these energies as a function of tip height for each position, in the noncontact range of 4–7 Å, where no instabilities occur. The derivative of this function gives the force on the tip due to the interaction with the surface, as a function of tip height, which is shown in Figure 6 in the range of 4–6 Å, along with the curves from the plane-wave calculations presented in [7], and fitted curves for the cluster Cr tip model discussed above. These forces show that the periodic tip model leads to an overall force that is quantitatively smaller than that in the cluster model for a given tip height, by approximately 10% in the 4.5–5.5 Å range.

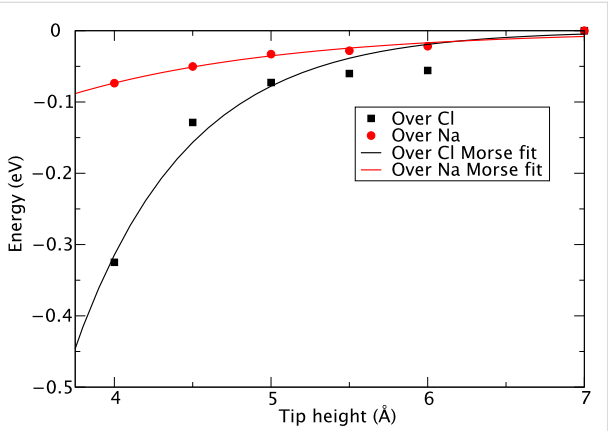

Figure 5: Total energy changes as a function of tip height for the periodic Cr tip interacting with the NaCl(001) surface, and Morse function curves fitted to the data points.

The absolute forces between the NaCl surface and the periodic tip model above both Cl^- and Na^+ ions, as calculated in this study, are larger than the forces calculated by using exactly the same setup in the previous plane-wave calculations: The forces are larger by approximately 50–100% in the 4.5–5.5 Å range.

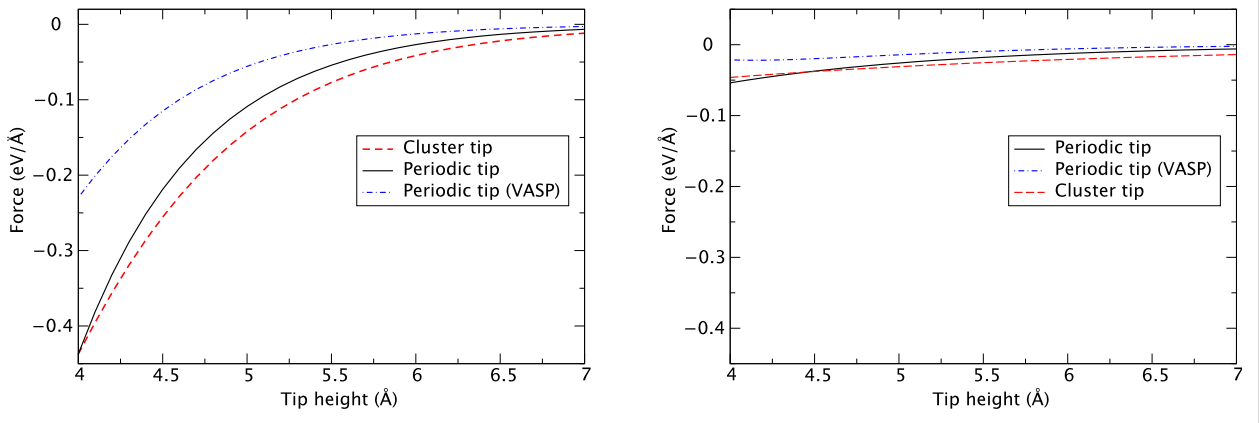

Figure 6: Tip force as a function of height directly above Cl^- (left) and Na^+ (right) ions in the NaCl(001) surface, for the cluster tip and periodic tip, and an identical periodic tip but with energies determined from plane-wave (VASP) calculations [7].

Conclusion

We have presented the results of calculations to determine how metal-cluster tips interact with two representative, model ionic surfaces at typical NC-AFM imaging distances. These calculations all unambiguously show that the attractive force on the tip will be strongest with the tip apex positioned directly above an anion in the surface, over the entire range of NC-AFM imaging distances (3–6 Å). As a result, the anion will always be imaged as elevated (bright) in NC-AFM images of these surfaces with these tip materials. The origin of the tip–sample interaction close to the surface is due to hybridization of the anion p states with the d states of the tip apex. This interaction mechanism does not give rise to contrast further from the surface (i.e., >4.5 Å); however, the force is still significantly greater above the anion beyond this distance. As was determined in [7], the interaction of the tip with the surface beyond this distance is purely electrostatic: In a truly metallic tip, the tip apex develops a small intrinsic dipole due to the Smoluchowski effect. The positive end of this dipole points to the surface and increases the interaction over the anions. In addition, anions move out from the surface due to the surface rumpling and are also, in general, more easily polarized than are cations. Both of these effects enhance the attractive tip–surface force above the anions. Here, the induction energy is $-1/2\ \alpha|E|$, where α is the atomic polarizability of the tip apex atoms and E is the electric field generated by the interaction, which is reproduced implicitly in the DFT calculations.

Each of the tip models employed in these calculations (cluster tip, periodic tip) give similar qualitative results, in so much that the force is strongest over the anion. This supports our previous conclusion that using well-characterized metallic tips may enable unambiguous chemical identification of image features [7]. It is not particularly surprising that quantitative differences between forces are obtained upon using different tip models and computational methods, as we push the accuracy of the calculations at large tip–surface separations. In particular, the cluster model leads to a slightly larger overall attractive force in the 4–6 Å distance range than does the periodic model, which may be due to an increased reactivity due its small size. For the periodic tip model, the tip–surface forces calculated in this study are also quantitatively different to in the calculations presented in [7], in which a plane-wave basis set was employed but with the same functional, even though again they qualitatively agree. Overall, the total attractive force at a given separation (in the near-contact range) is up to 100% larger, even when exactly the same atomic configuration is employed; although in absolute terms the difference in the forces is small. In this noncontact distance range, the asymptotic behavior of the electronic density (which may be significantly affected by the basis functions employed), the different treatment of the long-range electrostatics and periodic boundary conditions, and/or slight differences in the effective polarizabilities of the surface or tip ions may all contribute to the observed force difference. The polarizability could be affected by the quality of the basis set, k-point sampling and the pseudopotential used (the plane-wave code uses a pseudopotential constructed with Cr in a d^5s^1 state, whilst the present calculations include $s^2p^6d^5s^1$). At present, the full convergence of all the parameters in these calculations is at the limits of the available computational resources, and detailed investigations to disentangle the subtle differences between the calculations are not feasible. These results demonstrate that when calculating weak forces between a metallic tip and surface for a quantitative comparison with experimental results, care must be taken over the choice of both the tip model and the calculation method: Both the electronic structure of the tip and the method can have a significant effect on the calculated forces.

Experimental

Simulated image parameters

Elastic constant: 148.7 N/m; natural frequency: 189000.0 Hz; setpoint amplitude: 5 nm; Q-factor: 10000.0. Macroscopic van der Waals: Hamaker constant: 0.999 eV; Tip radius: 18.0 nm

Acknowledgements

MW would like to acknowledge funding from the Leverhulme Trust. The authors also acknowledge the use of the UCL Legion High Performance Computing Facility, and associated support services, in the completion of this work. They are grateful to G. Teobaldi for useful discussions and help in calculations.

References

1. Barth, C.; Foster, A. S.; Henry, C. R.; Shluger, A. L. *Adv. Mater.* **2011,** *23,* 477–501. doi:10.1002/adma.201002270
2. Giessibl, F. J. *Rev. Mod. Phys.* **2003,** *75,* 949–983. doi:10.1103/RevModPhys.75.949
3. Hofer, W. A.; Foster, A. S.; Shluger, A. L. *Rev. Mod. Phys.* **2003,** *75,* 1287–1331. doi:10.1103/RevModPhys.75.1287
4. Foster, A. S.; Barth, C.; Shluger, A. L.; Reichling, M. *Phys. Rev. Lett.* **2001,** *86,* 2373–2376. doi:10.1103/PhysRevLett.86.2373
5. Hembacher, S.; Giessibl, F. J.; Mannhart, J. *Appl. Surf. Sci.* **2002,** *188,* 445–449. doi:10.1016/S0169-4332(01)00976-X
6. Schwarz, A.; Kaiser, U.; Wiesendanger, R. *Nanotechnology* **2009,** *20,* 264017. doi:10.1088/0957-4484/20/26/264017
7. Teobaldi, G.; Lämmle, K.; Trevethan, T.; Watkins, M.; Schwarz, A.; Wiesendanger, R.; Shluger, A. L. *Phys. Rev. Lett.* **2011,** *106,* 216102. doi:10.1103/PhysRevLett.106.216102
8. Kawai, S.; Glatzel, T.; Koch, S.; Baratoff, A.; Meyer, E. *Phys. Rev. B* **2011,** *83,* 035421. doi:10.1103/PhysRevB.83.035421
9. Hoffmann, R.; Weiner, D.; Schirmeisen, A.; Foster, A. S. *Phys. Rev. B* **2009,** *80,* 115426. doi:10.1103/PhysRevB.80.115426
10. Lantz, M. A.; Hoffmann, R.; Foster, A. S.; Baratoff, A.; Hug, H. J.; Hidber, H. R.; Güntherodt, H.-J. *Phys. Rev. B* **2006,** *74,* 245426. doi:10.1103/PhysRevB.74.245426

11. Tang, H.; Bouju, X.; Joachim, C.; Girard, C.; Devillers, J. *J. Chem. Phys.* **1998,** *108,* 359. doi:10.1063/1.475383
12. VandeVondele, J.; Krack, M.; Mohamed, F.; Parrinello, M.; Chassaing, T.; Hutter, J. *Comput. Phys. Commun.* **2005,** *167,* 103–128. doi:10.1016/j.cpc.2004.12.014
13. Perdew, J. P.; Burke, K.; Ernzerhof, M. *Phys. Rev. Lett.* **1996,** *77,* 3865–3868. doi:10.1103/PhysRevLett.77.3865
14. VandeVondele, J.; Hutter, J. *J. Chem. Phys.* **2007,** *127,* 114105. doi:10.1063/1.2770708
15. Hartwigsen, C.; Goedecker, S.; Hutter, J. *Phys. Rev. B* **1998,** *58,* 3641–3662. doi:10.1103/PhysRevB.58.3641
16. Krack, M. *Theor. Chem. Acc.* **2005,** *114,* 145–152. doi:10.1007/s00214-005-0655-y
17. Sasaki, N.; Tsukada, M. *Phys. Rev. B* **1995,** *52,* 8471–8482. doi:10.1103/PhysRevB.52.8471
18. Tóbik, J.; Štich, I.; Terakura, K. *Phys. Rev. B* **2001,** *63,* 245324. doi:10.1103/PhysRevB.63.245324
19. Ossowski, T.; Kiejna, A. *Surf. Sci.* **2008,** *602,* 517–524. doi:10.1016/j.susc.2007.11.005
20. Aldén, M.; Skriver, H. L.; Mirbt, S.; Johansson, B. *Surf. Sci.* **1994,** *315,* 157–172. doi:10.1016/0039-6028(94)90551-7
21. Eastman, D. E. *Phys. Rev. B* **1970,** *2,* 1–2. doi:10.1103/PhysRevB.2.1
22. van Duijneveldt, F. B.; van Duijneveldt-van de Rijdt, J. G. C. M.; van Lenthe, J. H. *Chem. Rev.* **1994,** *94,* 1873–1885. doi:10.1021/cr00031a007
23. Trevethan, T.; Kantorovich, L. *Nanotechnology* **2005,** *16,* S79–S84. doi:10.1088/0957-4484/16/3/015
24. Trevethan, T.; Kantorovich, L. *Nanotechnology* **2006,** *17,* S205–S212. doi:10.1088/0957-4484/17/7/S18
25. Kresse, G.; Furthmüller, J. *Phys. Rev. B* **1996,** *54,* 11169–11186. doi:10.1103/PhysRevB.54.11169

License and Terms

Beilstein Journal of Nanotechnology

Drive-amplitude-modulation atomic force microscopy: From vacuum to liquids

Miriam Jaafar[1], David Martínez-Martín[*1], Mariano Cuenca[2], John Melcher[3], Arvind Raman[4] and Julio Gómez-Herrero[*1]

Full Research Paper

Open Access

Address:
[1]Departamento de Física de la Materia Condensada, Universidad Autónoma de Madrid, E-28049 Madrid, Spain, [2]Servicios generales de apoyo a la investigación, Universidad Autónoma de Madrid, E-28049 Madrid, Spain, [3]Department of Engineering Mathematics, University of Bristol, Bristol BS8 1TR, United Kingdom and [4]Birck Nanotechnology Center and School of Mechanical Engineering, Purdue University, West Lafayette, IN 47904-2088, USA

Email:
David Martínez-Martín[*] - davidmmo@gmail.com;
Julio Gómez-Herrero[*] - julio.gomez@uam.es

* Corresponding author

Keywords:
atomic force microscopy; control systems; dissipation; frequency modulation; noncontact

Beilstein J. Nanotechnol. **2012,** *3,* 336–344.
doi:10.3762/bjnano.3.38

Received: 20 January 2012
Accepted: 15 March 2012
Published: 18 April 2012

This article is part of the Thematic Series "Noncontact atomic force microscopy".

Guest Editor: U. D. Schwarz

Abstract

We introduce drive-amplitude-modulation atomic force microscopy as a dynamic mode with outstanding performance in all environments from vacuum to liquids. As with frequency modulation, the new mode follows a feedback scheme with two nested loops: The first keeps the cantilever oscillation amplitude constant by regulating the driving force, and the second uses the driving force as the feedback variable for topography. Additionally, a phase-locked loop can be used as a parallel feedback allowing separation of the conservative and nonconservative interactions. We describe the basis of this mode and present some examples of its performance in three different environments. Drive-amplutide modulation is a very stable, intuitive and easy to use mode that is free of the feedback instability associated with the noncontact-to-contact transition that occurs in the frequency-modulation mode.

Introduction

Dynamic atomic force microscopy (dAFM) [1,2] is a powerful yet versatile tool capable of operating in environments ranging from ultrahigh vacuum (UHV) to liquids [3,4], and imaging samples ranging from stiff inorganic materials [5] to soft biological matter [6], with nanoscale resolution. Amplitude-modulation AFM (AM-AFM) [7] and in particular its large-amplitude version, commonly known as tapping mode [8], is the most extended dAFM mode, but it has limitations: Its application to the vacuum environment is very difficult because of the long scanning times imposed by the high quality factor Q of the cantilevers in vacuum, which present a settling time given by $\tau_{cl} = Q/(\pi f_0)$. Frequency-modulation AFM (FM-AFM, also

known as noncontact AFM) [9] is the classical alternative to AM allowing atomic resolution in UHV chambers [10] at higher scanning rates. FM-AFM has recently been extended to operate in other media with lower Q, with remarkable success [11]. However, FM-AFM has a well-known drawback: The transition from noncontact to contact causes an instability in the feedback control [12], which is particularly important for inhomogeneous surfaces in which, for example, the adhesion changes abruptly. The curve in Figure 1a represents a typical curve of the tip–sample force versus distance in a vacuum or air environment. The FM feedback maintains the frequency shift, which is closely related to the force gradient, to infer the topography of the sample [13]. Since the frequency shift changes its sign (Figure 1a), stable feedback is only possible on a branch of the force curve where it is monotonic. For the case of AM, the transition between the contact and noncontact regimes can introduce bistabilities [14,15] but, as a general rule, AM can operate with similar feedback conditions in both regimes. In liquid, the absence of significant van der Waals forces results in a monotonic interaction [4] and the feedback in both FM and AM is often perfectly stable. However biological samples, such as viruses, tend to contaminate the tip and introduce attractive interactions causing FM to become unstable. As we shall see, in these cases imaging biological samples with FM is impractical. In an attempt to overcome this control instability, we have developed the method presented herein. In addition to the conservative interactions depicted in Figure 1a, there exist nonconservative or dissipative forces, that subtract energy from the oscillation [16,17]. The dissipation generally grows monotonically [18] as the tip approaches the sample surface (Figure 1b). However, the precise dependence of the dissipation on the tip–sample distance depends on the detailed atomic configuration of the tip involved in the experiment [19].

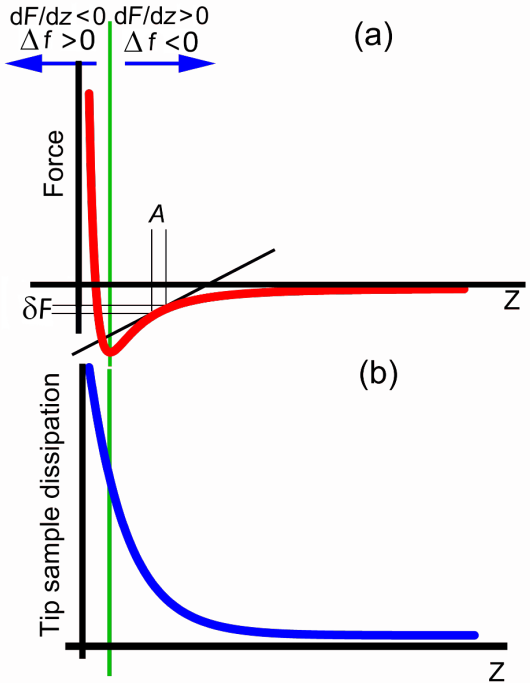

Figure 1: The interaction versus distance. (a) Conservative force versus distance interaction between an AFM tip and a surface. As the tip approaches the surface the interaction becomes first attractive and then repulsive. The frequency shift also varies from negative to positive. FM is only stable in one of the two branches. (b) In addition to the conservative interactions the tip also dissipates energy when interacting with the surface. The figure illustrates the monotonic tendency of this magnitude.

In this work we present a new AFM scanning mode, which we have called “drive amplitude modulation” (DAM-AFM) [20] and which takes advantage of the aforementioned monotonicity of the dissipation to obtain stable images in all environments from vacuum to liquids. Moreover, DAM has a similar settling time to FM, and consequently the scanning time is also very similar. The paper begins by describing the basics features of DAM and comparing them with AM and FM, following by a discussion of some experimental results in vacuum and liquids.

Results and Discussion

The basis of DAM-AFM

Figure 2 portrays the functional schemes for the three different AFM modes under consideration. The standard representation of a feedback loop and the corresponding icon used to simplify the different diagrams is shown in Figure 2a. For the case of AM (Figure 2b) a harmonic driving force with constant amplitude at (or near to) the free resonance frequency f_0 of the cantilever is used. The oscillation amplitude A is the controlled input for the topography feedback, and the scanner position in the z-direction (perpendicular to the sample surface plane, and which is closely related with the tip–sample distance) is the regulated variable; the variation of the phase is recorded in the phase image, which is used as a spectroscopic image. In FM (Figure 2c) three feedback loops are used; two nested loops for the topography and one additional loop working in parallel to keep the oscillation amplitude constant by adjusting the amplitude of the driving force. A phase-locked loop (PLL) tracks the effective resonance frequency of the cantilever as it varies as a consequence of the tip–sample interaction. In FM, the position of the scanner in the z-direction is adjusted to keep the frequency shift constant and generates a topography image. This topography image is usually interpreted as a map of constant force gradient. The amplitude of the driving force, which is controlled in the parallel feedback loop, represents the dissipation. Figure 2d shows the functional scheme for DAM. As in FM, two nested feedback loops give the topography in DAM. The first loop adjusts the driving force in order to main-

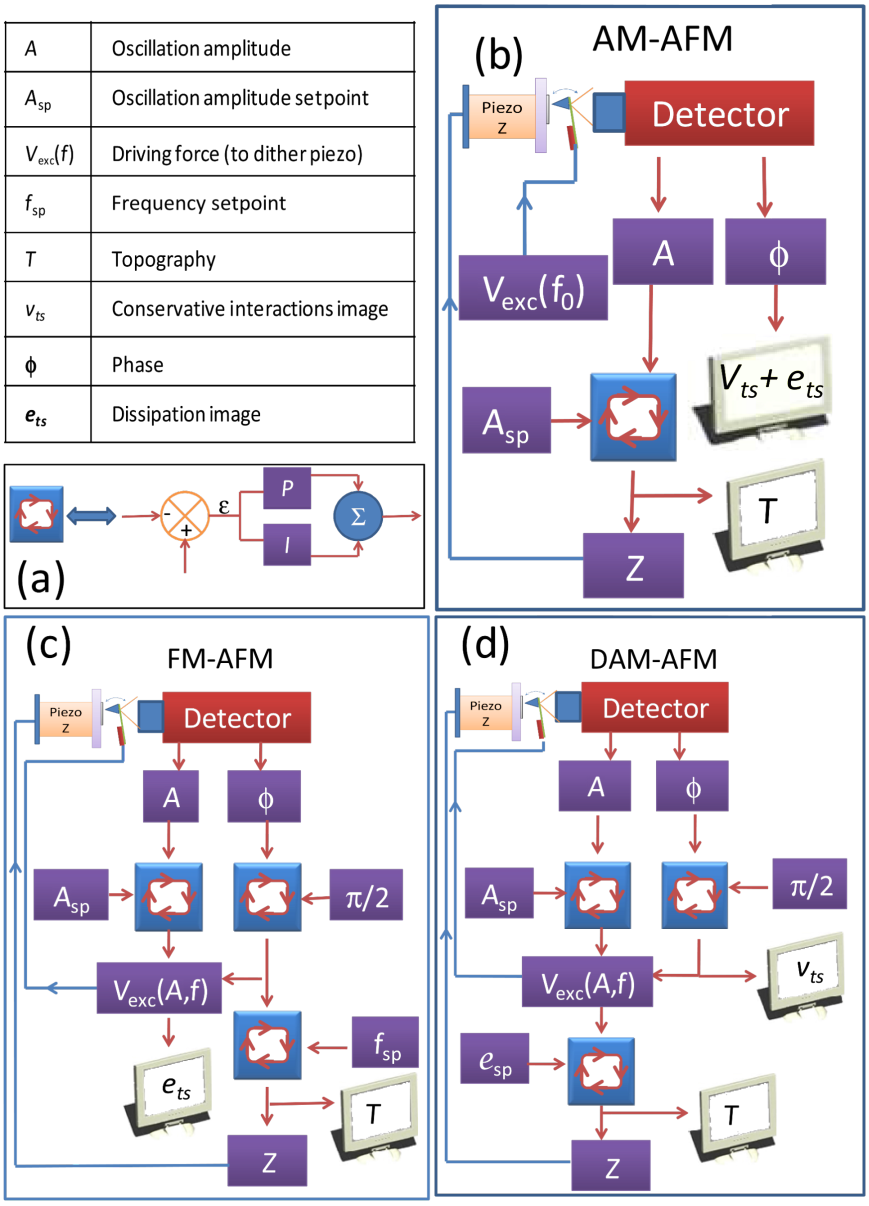

Figure 2: Feedback diagrams for different d-AFM modes. dAFM has three basic variables: The oscillation amplitude A, the phase ϕ and the driving force V_{exc}. (a) Expansion of the feedback icon used in the schemes. (b) Typical feedback scheme for AM. (c) FM feedback scheme. The short branch varies the driving force to keep the amplitude constant, hence producing a dissipation image (e_{ts}). The other branch is a phase-lock loop, which keeps the system at resonance according to the tip–sample interaction. The regulated variable of the PLL, the frequency, is used as the controlled input for the topography feedback. (d) In DAM the short branch is a PLL, which produces a map of the conservative force (v_{ts}). The long branch uses the amplitude as the process variable, and the regulated variable is the driving force, which is used as the controlled input for the topography feedback.

tain the oscillation amplitude. The driving force needed to sustain this oscillation amplitude is related to the energy dissipated in the system. By adjustment of the position of the scanner in the z-direction the driving force is kept constant at the setpoint value. A PLL, which tracks the effect resonance frequency, can operate as parallel feedback loop in DAM. Topography images in DAM represent maps of constant dissipation. The frequency shift controlled by the PLL provides a spectroscopic image. We note that a PLL can also be implemented in AM. In this configuration the topography images in both AM and DAM have a similar meaning. Strictly speaking DAM can work with or without a PLL. In either case, the scanning speed in vacuum is comparable to that in FM. Nevertheless, while omission of the PLL simplifies the acquisition setup, the topography images, as in AM, reflect both conservative and nonconservative forces.

Notice that, as reflected in the schemes, in both FM and DAM the amplitude A and frequency f of the driving force

$$V_{exc}(A, f; t) = A(\tau_1) \cdot \sin[2\pi f(\tau_2) \cdot t]$$

are modified by feedback loops that work with characteristic times τ_1 and τ_2 (not necessarily the same for frequency or amplitude) that depend on the details of the experimental setup but, as we will show, can be pushed well below the transient time of the free driven cantilever τ_{cl}. What defines the difference between these two modes is which of the feedback loops working on this driving signal (amplitude for DAM or frequency for FM) is used as the process variable for the topography feedback.

All of the experiments described in this work have been carried out with Nanotec Electronica (http://www.nanotec.es) microscopes controlled with the SPM software package WSxM [21]. However, this mode can be easily implemented in other commercial systems. Nanosensors PPP-NCH and Olympus OMCL-RC type probes were used for the experiments in vacuum and in liquid, respectively. For the sake of completeness, in Supporting Information File 1 we also include images taken with other cantilever types. The stiffness values for each cantilever were obtained in an air environment by using Sader's expression [22].

In vacuum DAM-AFM

The experimental setup consists of a home-made high-vacuum chamber with a base pressure of 10^{-6} mbar, equipped with an AFM head. The vacuum is achieved by using a conventional combination of a dry mechanical pump plus a turbopump. In order to avoid vibrations from the turbopump affecting the measurements, the microscope head is suspended by three viton cords. The quality factor of the cantilevers saturates at pressures below 10^{-3} mbar, and hence the dynamics of the cantilevers are similar to what is typically observed in UHV chambers at room temperature (the values of the Q factor in UHV operation are commonly between 8000 and 25000). All the experiments were carried out at room temperature.

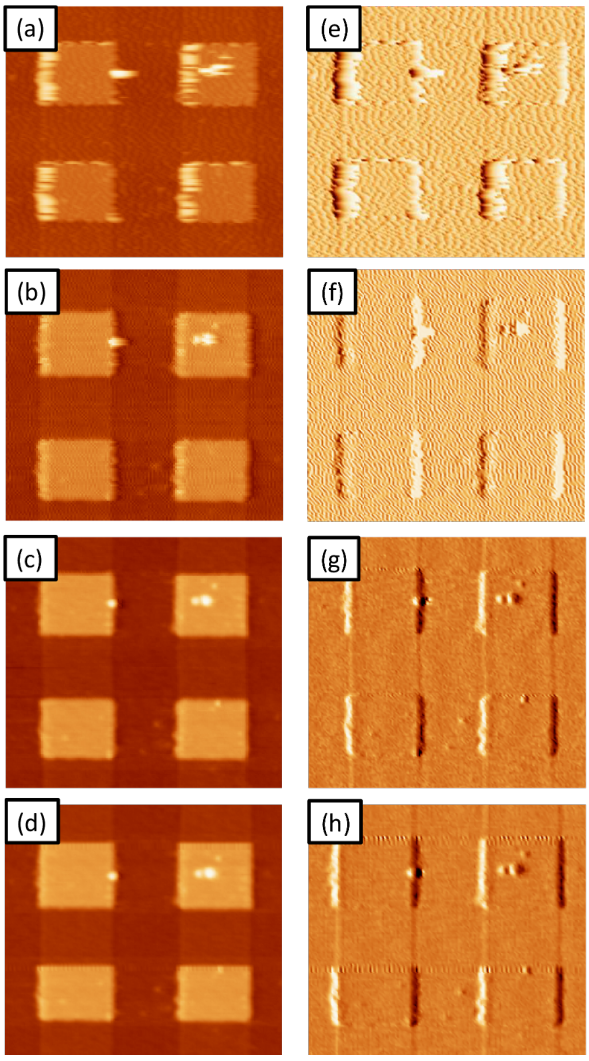

Figure 3: Testing the methods at high Q. Topography images of a calibration grid taken in vacuum in (a) AM (setpoint = 6.5 nm); (b) FM (setpoint = −50 Hz); (c) DAM in the attractive regime (setpoint = 1.2 pW; V_{exc} = 0.49 V); and (d) DAM in the repulsive regime (setpoint= 4.5 pW; V_{exc} = 0.77 V). (e–h) Corresponding error images: amplitude for AM, frequency shift for FM and dissipation for DAM. For all of the images: free amplitude A = 10 nm. K = 23 N/m, Q = 11800, line rate= 1.2 Hz, f_0 = 225 kHz. The height of the motifs is 20 nm and the structural period is 3 μm.

Figure 3a–d portrays four topography images of a calibration grid taken in AM, FM and DAM acquired in both the attractive and repulsive regimes, respectively. Figure 3e–h shows the corresponding error signals: Amplitude, frequency shift, and dissipation for the two DAM cases, respectively. We have chosen this sample because its surface conditions are similar to those found in many samples of technological interest, and which in many cases are difficult to scan in vacuum by using a conventional mode. Scanning with DAM overcomes these difficulties. Figure 3a (AM) shows clear traces of instabilities as expected for AM images acquired at high Q for which the settling time is $\tau_{cl} \approx 17$ ms, making this mode too slow for vacuum applications. In order to achieve higher scan rates the settling time can be reduced by increasing the tip–sample dissipation (diminishing the Q), which implies a large amplitude reduction and therefore higher applied forces during imaging. The frequency shift setpoint for Figure 3b (FM) is negative indicating that the topography image was taken in the attractive/noncontact regime (as is the usual case in FM). Imaging in FM

at low amplitude was unstable because of the high adhesion observed on the surface: The interaction passes from being attractive to repulsive. To avoid this effect, we have to increase the feedback gain resulting in the appearance of high-frequency components in the error signal. In order to stabilize the system we used the *tip safe* option in the WSxM software, which prevents tip–sample crashes by withdrawing the tip when the oscillation amplitude of the cantilever drops below a given threshold. As usual we tried to optimize the scanning conditions for the chosen amplitude; nevertheless we could not reduce the high-frequency artifacts observed in the image. Figure 3c and Figure 3d (DAM) were acquired by using dissipation setpoints of 1.2 pW and 4.5 pW, respectively, with the PLL enabled, as calculated following the expression [23,24]

$$P_{ts} = P_0\left(\frac{V_{exc}}{V_{exc,0}} - \frac{f}{f_0}\right) \quad (1)$$

where P_0 is the power dissipation caused by internal friction in the freely oscillating cantilever given by

$$P_0 = 2\pi f_0 \frac{1/2\,kA^2}{Q}. \quad (2)$$

Stable imaging in DAM does not require *tip safe* or any other kind of precaution. Acquiring images in DAM is easy and direct. It is also possible to select the optimum cantilever oscillation amplitude for each experiment, ranging from less than 1 nm up to tens of nanometers at high scan speeds.

It is known from control theory [25] that a feedback loop can modify the differential equation that describes the dynamic of a plant (in the present case, the plant is the cantilever). As a consequence, the new transient time can be reduced arbitrarily by changing the feedback gains. This is conveniently illustrated in Figure 4 (see a more detailed discussion in Supporting Information File 2). This figure portrays a MATLAB simulation in which a perturbation (Figure 4a) is applied to a free cantilever with Q = 15000. The response of the cantilever without any feedback shows the expected transient with a settling time of $\tau_{cl} = Q/(\pi f_0)$ (Figure 4b). Figure 4c displays the response of the cantilever with the amplitude and the frequency feedback loops enabled. Notice that the shape of the perturbation is a step function for both cases. However, for the open-loop case the perturbation is a sudden change in the amplitude of the driving force, whereas for the closed-loop configuration the perturbation is a sudden change in the amplitude setpoint. As shown in the charts, the response time in the second configuration is dramatically reduced with respect to the open-loop configuration.

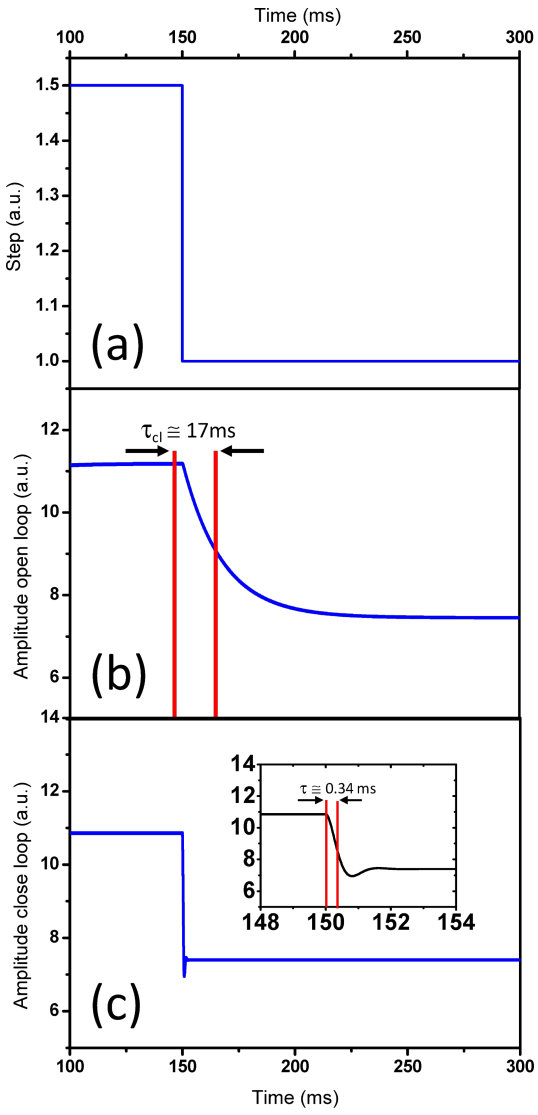

Figure 4: Response to a step perturbation under high Q. (a) Perturbation applied to the free cantilever. (b) Amplitude response for a free cantilever in the open-loop configuration. (c) Amplitude response for a free cantilever in the close-loop configuration. The inset shows a zoom in the step region, showing a characteristic time of 0.3 ms, which is much shorter that the one observed in the open-loop configuration. The MATLAB sequence diagram is shown in Supporting Information File 2.

The second consideration, closely related to the previous one, is the energy balance. Assuming a free cantilever at resonance, the power that has to be provided to the cantilever to achieve a given amplitude is inversely proportional to Q (Equation 2). The implication is that keeping the cantilever at resonance in air requires *r*-times more power than in vacuum (being that $r = Q_{vac}/Q_{air}$). This *r* factor is about 20 for the cantilevers used in this work, but it can be much higher. Figure 5 shows the total dissipation and the frequency shift (simultaneously acquired) as

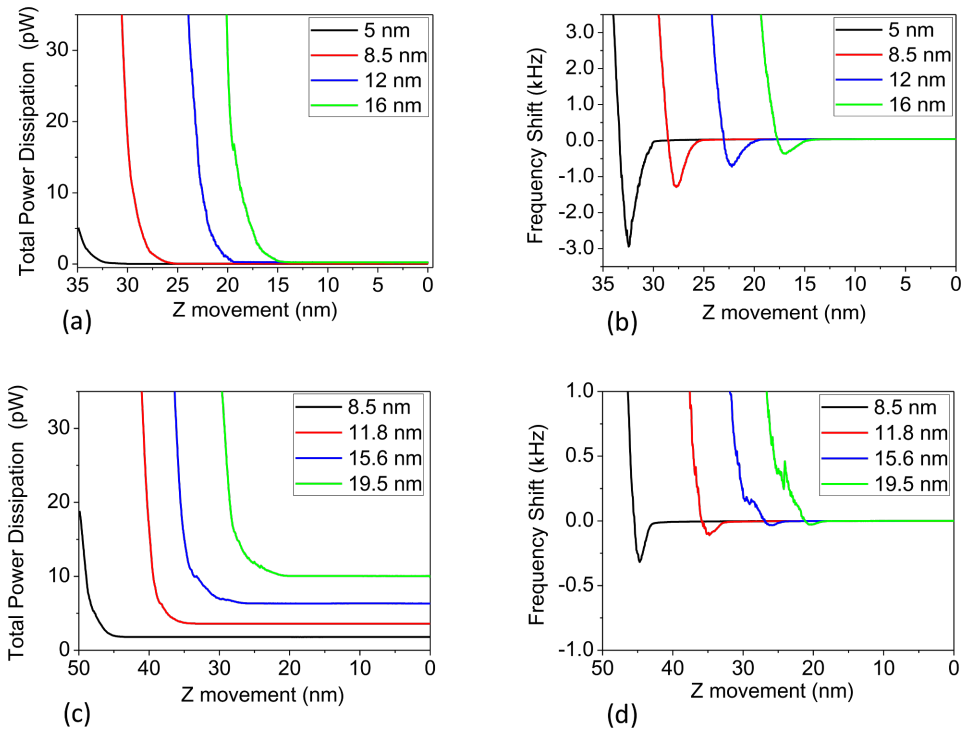

Figure 5: *In vacuum* total dissipation (a) and frequency shift (b) curves as a function of the z-scanner position for different amplitudes. (c) and (d) equivalent to the cases in (a) and (b) but *in air* (ambient conditions). The energy required to sustain the free oscillation in air is a factor of Q_{vacuum}/Q_{air} times the energy needed in vacuum. Cantilever parameters: k = 16.6 N/m, ω_0 = 230.97 kHz, Q_{vacuum} = 23900, Q_{air} = 468.

a function of the z-scanner position for experiments, in both *vacuum* (a,b) and *air* (c,d). As expected, the power required to sustain the cantilever oscillation is much higher for the *in air* case than for the *in vacuum* case. In addition, the charts are experimental illustrations of the force and dissipation trends shown in Figure 1. The onset of both frequency shift and dissipation depends on the cantilever oscillation amplitude for obvious reasons: As the amplitude grows the tip finds the sample surface at a lower z-scanner position. When the tip approaches the surface it encounters a potential well that is the combination of the harmonic potential of the cantilever plus the surface potential. In order to maintain the oscillation we have to provide a total energy to the cantilever that is high enough that the tip is not trapped by the surface potential. Since the system is not conservative this total energy varies with time.

The energy dissipated by a cantilever over one period *in vacuum* is, as a consequence of the tip–sample interaction, on the order of 10^{-20} J (see, for instance, [26]). The energy required to force a cantilever to oscillate in vacuum with an amplitude of 10 nm is about the same as the energy loss per oscillation period. *In air* the energy required by the cantilever to maintain a stable free oscillation is 20 times higher, so the energy loss due to the tip–sample interaction is usually negligible. As a general rule, in order to enhance the sensitivity, the cantilever oscillation amplitude should be comparable to the selected interaction length [1,2]. Since in AM the energy pumped into the cantilever is fixed, the tip gets easily trapped in the sample potential and the image becomes unstable. This effect is particularly relevant in vacuum. In air and liquids the cantilever dissipation originated by the environment is much higher than the dissipation due to tip–sample interaction. Thus, the energy required by the cantilever to maintain a stable oscillation amplitude is so high that the effect described above becomes irrelevant (Supporting Information File 3 contains experimental data of the instabilities when using conventional AM in vacuum).

In addition to the grid sample we imaged a number of surfaces of technological and fundamental relevance using DAM (Supporting Information File 1 includes a variety of images taken in different environments). Figure 6 shows a silicon substrate on which several motives have been fabricated by means of a conventional e-beam lithography technique. The preparation of these samples involves several steps including deposition and lift-off of a polymer layer. This layer is, in many cases, very difficult to remove completely, leaving the sample contaminated. During scanning in FM in vacuum, the tip easily passes from the attractive to the repulsive regime, in which it is contaminated by the polymer.

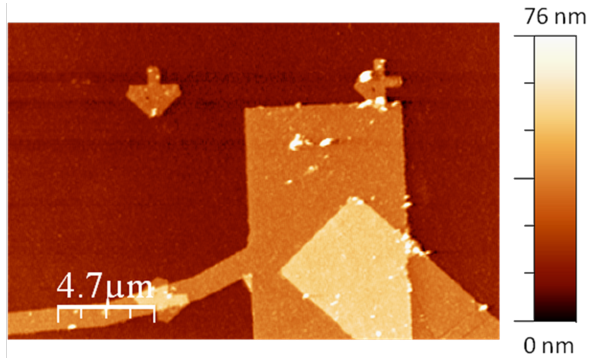

Figure 6: Gold electrodes fabricated by e-beam lithography. The DAM topography was acquired in vacuum with excellent stability despite the polymer contamination that is characteristic of the lithography process. Nanosensors PPP-FMR probe with: A = 24 nm; Q = 8600; f_0 = 61.1 kHz; k = 1.3 N/m; line rate = 0.9 Hz; setpoint = 3.8 pW.

DAM-AFM in liquids

Low quality factors are common when imaging in liquids due to the viscous hydrodynamic loading between the cantilever and the environment. This friction in some cases induces an overdamped dynamic of the cantilever, making it very difficult to apply low forces in AM, which are necessary to obtain stable virus images [27], for example. Since the demonstration of true atomic resolution in liquids by Fukuma et al. [11] using FM [28], this mode has attracted the attention of the AFM community in attempts to image biological samples with high resolution. FM is able to overcome the limitations of AM making it possible to obtain high-quality images of the viruses and other biological samples [29,30]. However, FM is only stable while the tip is clean and the conservative interaction is repulsive, but once the tip becomes contaminated, which is very common when measuring biological samples under physiological conditions, the interaction curve is not monotonic, resulting in instabilities in the FM feedback.

Figure 7a shows the dependence of the frequency shift and the dissipation for a clean AFM tip immersed in a buffer solution. Both magnitudes grow monotonically with the tip–sample distance. Figure 7b shows this dependence again with the same tip but this time contaminated after scanning a highly oriented pyrolytic graphite (HOPG) substrate with viruses adsorbed on it. While the dissipation is still monotonic, the frequency shift is not. This type of frequency-shift dependence makes scanning the surface impractical with FM. However, this is not an issue for DAM. Figure 7c displays an in-liquid DAM topography in which a ϕ29 bacteriophage [31] adsorbed on a HOPG surface can be seen. Figure 7d shows a height profile along the green line drawn in Figure 7c. Notice that the virus topography exhibits the nominal height for ϕ29 [32] implicating that the applied force is very low. By using Sader's expression [33] the applied force can be calculated from the frequency-shift data. This value is nearly 100 pN, which is remarkable taking into account the relative high stiffness of the cantilever (0.6 N/m). In

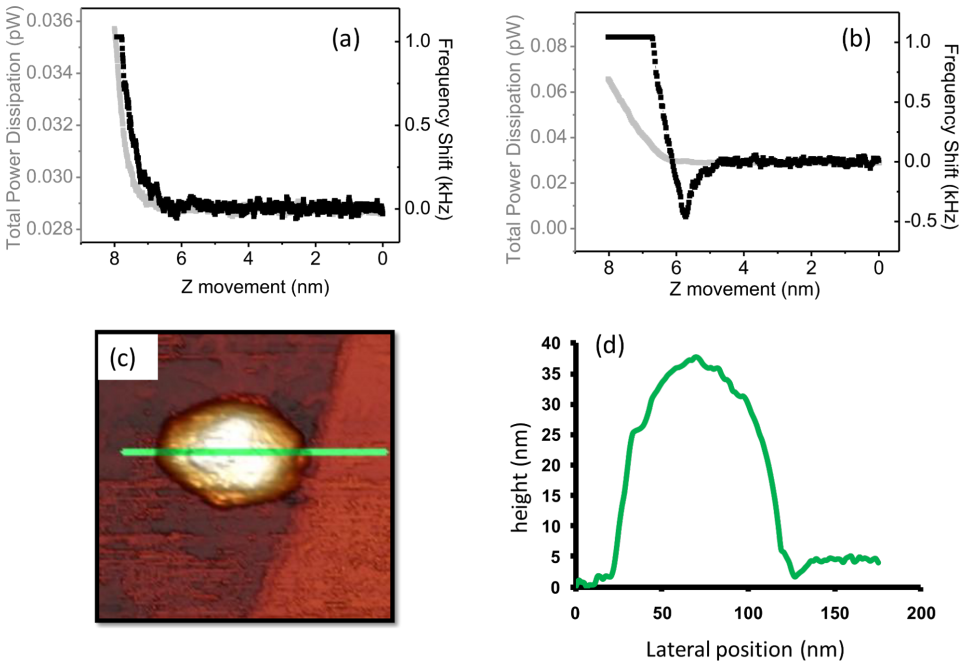

Figure 7: DAM in liquid. Frequency shift (black) and dissipation (light gray) for a clean tip (a) and after becoming contaminated (b). Note that the flat region of the frequency shift in (b) reflects the saturation of the PLL. (c) DAM topography showing a ϕ29 virus adsorbed on a HOPG substrate. (d) Height profile along the green line drawn in (c). Image parameters: A = 2 nm, k = 0.6 N/m, Q = 4, line rate = 2 Hz; f_0 = 16 kHz, setpoint = 33 fW.

this case, DAM prevails over AM because the adhesion (attractive forces) on the virus is always lower than on the substrate, as can be easily verified by performing force versus distance curves [30]. Scanning in AM implies fixing a total energy for the cantilever that is high enough to enable scanning of the substrate without being trapped by the attractive forces, but this energy is also high enough to damage the virus. In DAM the energy is automatically adapted at each point of the image to optimize the image conditions.

Conclusion

We have discussed the effects of the amplitude feedback on the transient times and energy balance, concluding that DAM is a suitable method for imaging in different environments ranging from vacuum to liquids and is useful for a variety of applications. DAM operation avoids the feedback instabilities associated with the transition between noncontact and intermittent-contact regimes. This feature translates to stable scanning of heterogeneous samples of technological relevance that are cumbersome to scan in vacuum, and which can be different to the standard samples used in UHV fundamental surface-science studies, e.g., atomically flat single crystals. Using DAM in liquids we have already been able to obtain true atomic resolution on a mica surface (see Supporting Information File 1) but atomic resolution in vacuum remains a challenge. DAM can also improve magnetic force imaging since it allows operating at smaller tip–sample distances than the conventional modes. Finally, since DAM reduces the settling time, it may be useful for high-speed scanning in air under ambient conditions.

Supporting Information

Supporting Information File 1

DAM images of relevant technological samples.
[http://www.beilstein-journals.org/bjnano/content/supplementary/2190-4286-3-38-S1.pdf]

Supporting Information File 2

Dynamic response in DAM-AFM.
[http://www.beilstein-journals.org/bjnano/content/supplementary/2190-4286-3-38-S2.pdf]

Supporting Information File 3

Handling instabilities with AM and DAM.
[http://www.beilstein-journals.org/bjnano/content/supplementary/2190-4286-3-38-S3.pdf]

Acknowledgements

The authors want to thank Pablo Ares and Dr. Jaime Colchero for stimulating discussions and Nanotec Electrónica SL for technical support. The authors acknowledge funding by the Spanish government grants MAT2010-20843-C02-02, PLE2009-0065, Consolider CSD2010-00024 and CAM project and the Comunidad de Madrid No. S2009/MAT-1467. M. J. gives thanks for the JdC contract.

References

1. García, R.; Pérez, R. *Surf. Sci. Rep.* **2002,** *47,* 197–301. doi:10.1016/S0167-5729(02)00077-8
2. Giessibl, F. J. *Rev. Mod. Phys.* **2003,** *75,* 949–983. doi:10.1103/RevModPhys.75.949
3. Hansma, P. K.; Cleveland, J. P.; Radmacher, M.; Walters, D. A.; Hillner, P. E.; Bezanilla, M.; Fritz, M.; Vie, D.; Hansma, H. G.; Prater, C. B.; Massie, J.; Fukunaga, L.; Gurley, J.; Elings, V. *Appl. Phys. Lett.* **1994,** *64,* 1738–1740. doi:10.1063/1.111795
4. Putman, C. A. J.; Van der Werf, K. O.; De Grooth, B. G.; Van Hulst, N. F.; Greve, J. *Appl. Phys. Lett.* **1994,** *64,* 2454–2456. doi:10.1063/1.111597
5. Ashino, M.; Schwarz, A.; Behnke, T.; Wiesendanger, R. *Phys. Rev. Lett.* **2004,** *93,* 136101. doi:10.1103/PhysRevLett.93.136101
6. Radmacher, M.; Fritz, M.; Hansma, P. K. *Biophys. J.* **1995,** *69,* 264–270. doi:10.1016/S0006-3495(95)79897-6
7. Martin, Y.; Williams, C. C.; Wickramasinghe, H. K. *J. Appl. Phys.* **1987,** *61,* 4723–4729. doi:10.1063/1.338807
8. Zhong, Q.; Inniss, D.; Kjoller, K.; Elings, V. B. *Surf. Sci.* **1993,** *290,* L688–L692. doi:10.1016/0039-6028(93)90582-5
9. Albrecht, T. R.; Grütter, P.; Horne, D.; Rugar, D. *J. Appl. Phys.* **1991,** *69,* 668–673. doi:10.1063/1.347347
10. Giessibl, F. J. *Science* **1995,** *267,* 68–71. doi:10.1126/science.267.5194.68
11. Fukuma, T.; Kobayashi, K.; Matsushige, K.; Yamada, H. *Appl. Phys. Lett.* **2005,** *87,* 034101. doi:10.1063/1.1999856
12. Gauthier, M.; Pérez, R.; Arai, T.; Tomitori, M.; Tsukada, M. *Phys. Rev. Lett.* **2002,** *89,* 146104. doi:10.1103/PhysRevLett.89.146104
13. Controlled input is the current status of a process under control. The setpoint is the desired value for the process variable. The regulated variable in process control is the variable that the controller action influences to keep the controlled input constant at the setpoint value.
14. García, R.; San Paulo, A. *Phys. Rev. B* **1999,** *60,* 4961–4967. doi:10.1103/PhysRevB.60.4961
15. Solares, S. D. *Meas. Sci. Technol.* **2007,** *18,* 592–600. doi:10.1088/0957-0233/18/3/007
16. Anczykowski, B.; Krüger, D.; Fuchs, H. *Phys. Rev. B* **1996,** *53,* 15485–15488. doi:10.1103/PhysRevB.53.15485
17. Cleveland, J. P.; Anczykowski, B.; Schmid, A. E.; Elings, V. B. *Appl. Phys. Lett.* **1998,** *72,* 2613–2615. doi:10.1063/1.121434
18. Kaggwa, G. B.; Kilpatrick, J. I.; Sader, J. E.; Jarvis, S. P. *Appl. Phys. Lett.* **2008,** *93,* 011909. doi:10.1063/1.2950324
19. Oyabu, N.; Pou, P.; Sugimoto, Y.; Jelinek, P.; Abe, M.; Morita, S.; Pérez, R.; Custance, Ó. *Phys. Rev. Lett.* **2006,** *96,* 106101. doi:10.1103/PhysRevLett.96.106101
20. Martínez-Martín, D.; Jaafar, M.; Gómez-Herrero, J. Procedimiento de control de un microscopio de barrido. Spanish patent P201131624.
21. Horcas, I.; Fernández, R.; Gómez-Rodríguez, J. M.; Colchero, J.; Gómez-Herrero, J.; Baro, A. M. *Rev. Sci. Instrum.* **2007,** *78,* 013705. doi:10.1063/1.2432410

22. Sader, J. E.; Chon, J. W. M.; Mulvaney, P. *Rev. Sci. Instrum.* **1999,** *70,* 3967–3969. doi:10.1063/1.1150021
23. Loppacher, C.; Bennewitz, R.; Pfeiffer, O.; Guggisberg, M.; Bammerlin, M.; Schär, S.; Barwich, V.; Baratoff, A.; Meyer, E. *Phys. Rev. B* **2000,** *62,* 13674–13679. doi:10.1103/PhysRevB.62.13674
24. Gotsmann, B.; Seidel, C.; Anczykowski, B.; Fuchs, H. *Phys. Rev. B* **1999,** *60,* 11051–11061. doi:10.1103/PhysRevB.60.11051
25. Khalil, H. K. *Nonlinear Systems,* 3rd ed.; Prentice Hall: Upper Saddle River, N.J., 2002.
26. Kawai, S.; Pawlak, R.; Glatzel, T.; Meyer, E. *Phys. Rev. B* **2011,** *84,* 085429. doi:10.1103/PhysRevB.84.085429
27. Xu, X.; Carrasco, C.; de Pablo, P. J.; Gomez-Herrero, J.; Raman, A. *Biophys. J.* **2008,** *95,* 2520–2528. doi:10.1529/biophysj.108.132829
28. As a benchmark of our instrument we have obtained state of the art images of mica surfaces in liquids using FM, achieving easily true atomic resolution comparable to that shown by Fukuma et al. [11].
29. Martínez-Martín, D.; Carrasco, C.; Hernando-Pérez, M.; de Pablo, P. J.; Gómez-Herrero, J.; Pérez, R.; Mateu, M. G.; Carrascosa, J. L.; Kiracofe, D.; Melcher, J.; Raman, A. *PLoS One* **2012,** *7,* e30204. doi:10.1371/journal.pone.0030204
30. Martinez-Martin, D.; Herruzo, E. T.; Dietz, C.; Gomez-Herrero, J.; Garcia, R. *Phys. Rev. Lett.* **2011,** *106,* 198101. doi:10.1103/PhysRevLett.106.198101
31. Melcher, J.; Carrasco, C.; Xu, X.; Carrascosa, J. L.; Gómez-Herrero, J.; de Pablo, P. J.; Raman, A. *Proc. Natl. Acad. Sci. U. S. A.* **2009,** *106,* 13655–13660. doi:10.1073/pnas.0902240106
32. Tang, J.; Olson, N.; Jardine, P. J.; Grimes, S.; Anderson, D. L.; Baker, T. S. *Structure* **2008,** *16,* 935–943. doi:10.1016/j.str.2008.02.024
33. Sader, J. E.; Jarvis, S. P. *Appl. Phys. Lett.* **2004,** *84,* 1801–1803. doi:10.1063/1.1667267

License and Terms